UNIVERSITAT
POLITÈCNICA
DE VALÈNCIA

DOCTORAL THESIS

EXPERIMENTS ON TURBOCHARGER COMPRESSOR ACOUSTICS

PRESENTED BY

D. Jorge García Tíscar

SUPERVISED BY

Dr. D. Alberto Broatch Jacobi

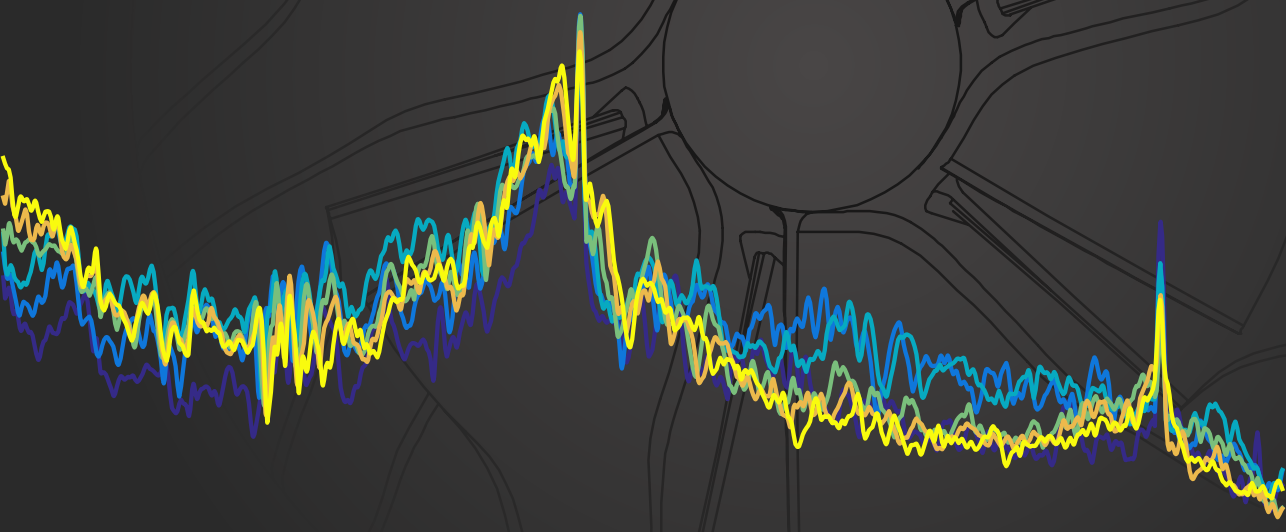

January 2017

DEPARTAMENTO DE MÁQUINAS Y MOTORES TÉRMICOS

UNIVERSITAT POLITÈCNICA DE VALÈNCIA
DEPARTAMENTO DE MÁQUINAS Y MOTORES TÉRMICOS

DOCTORAL THESIS

EXPERIMENTS ON TURBOCHARGER COMPRESSOR ACOUSTICS

PRESENTED BY

D. Jorge García Tíscar

SUPERVISED BY

Dr. D. Alberto Broatch Jacobi

FOR THE DEGREE OF

Doctor of Philosophy

JANUARY 2017

collection doctoral thesis
Experiments on turbocharger. Compressor acoustics

Author
Jorge García Tíscar

Publisher
2017, Editorial Universitat Politècnica de València
Venta: www.lalibreria.upv.es / Ref.: 6678_01_01_01

ISBN: 978-84-9048-993-2

DOCTORAL THESIS

"Experiments on turbocharger compressor acoustics"

Presented by: D. Jorge García Tíscar
Supervised by: Dr. D. Alberto Broatch Jacobi

THESIS EXAMINERS

Dr. D. Hans Rämmal
Dr. D. Richard Burke
Dr. D. Pedro Acisclo Rodríguez Aumente

DEFENSE COMITEE

Chairman: Dr. D. José Ramón Serrano Cruz
Secretary: Dr. D. Francisco Javier Martos Ramos
Member: Dr. D. Hans Rämmal

Valencia, January 2017

A Paula

Abstract

As turbocharging requirements raise to face an increasingly stricter environmental regulation of internal combustion engines, concerns regarding their acoustic emission become more pressing. Since downsized engines require higher boost pressures and lower mass flow rates, the turbocharger compressor is forced to work at more unstable regimes, where flow patterns become more complex and noise levels rise.

This thesis aims to thus to investigate these issues, proposing methodologies to characterize the acoustic emission of turbocharger compressors and implementing them in different experiments with a special focus on the link between acoustic emission and flow behaviour at unstable conditions.

A literature review is carried out in order to assess the state of the art principally regarding experimental techniques related to this issue but also including the latest developments in terms of understanding the flow characteristics through numerical simulations. Different methodologies are consequently proposed and implemented into a custom test rig inside an anechoic chamber as to experimentally measure and analyze the acoustic output of the compressor.

From this measurement campaign a characterization of the noise spectral content across the compressor map is obtained and described, identifying different acoustical phenomena such as blade passing tonal noise, low frequency content associated to deep surge, higher frequency broadband ascribed to tip clearance interaction, and broadband noise in the plane wave range known as *whoosh* in the literature, of special concern for automotive manufacturers. This particular phenomenon is detected even at more stable conditions at higher flow rate, and rising in level as flow rate is diminished to the point of being masked by lower frequency content.

After a validation of the selected procedure in realistic engine conditions, experimental data is compared against a numerical model of the compressor developed in a parallel work to assess its validity and propose different post-

processing techniques to extract additional insights about the behaviour of the flow at different conditions, hinting at the main generation mechanism for *whoosh* being located at the compressor diffuser.

Since numerical simulations predict a reduced amount of reversed unstable flow at conditions where *whoosh* noise is still measured, an experimental campaign is performed where detailed measures of local temperature near the compressor wheel are used to determine the evolution of reversed flow, with supplemental readings through pressure probes in the inducer and diffuser being used to link this evolution with the fluctuation of spectral content. Temperature results are also correlated with measurements of the velocity field through particle imaging, demonstrating a clear link between the reversed flow field and temperature readings.

Different experimental campaigns are then described where modifications of the inlet geometry immediately upstream the compressor are performed in order to assess how the air flow presentation can influence acoustic performance. Geometries featuring reservoirs, nozzles and guide vanes are shown to potentially reduce noise levels. A 90º elbow parametric study is performed, demonstrating how the inner radius of the elbow influences circumferential temperature differences and noise levels, leading to the hypothesis of geometry influence on *whoosh* noise being related to air presentation changes that promote lower or higher growth of reversed backflow, which in turns carries upstream the spectral content being generated in the compressor diffuser.

Lastly, additional experimental and numerical studies are proposed to further explore these issues, in order to provide a better understanding of how inlet designs may delay and mitigate the appearance and transmission of these adverse acoustical phenomena.

Resumen

A medida que los requerimientos de turbocompresión aumentan para afrontar una regulación de los motores de combustión interna cada vez más estricta, la preocupación respecto a su emisión acústica se hace más acuciante. Debido a que motores de menor tamaño requieren mayores aumentos de presión y menores gastos másicos, el compresor del turbogrupo se ve forzado a trabajar en regímenes más inestables, los patrones de flujo se hacen más complejos y los niveles de ruido aumentan.

Esta tesis tiene como objetivo investigar estas cuestiones, proponiendo metodologías para caracterizar la emisión acústica de compresores de turbogrupos, e implementándolas en diferentes experimentos enfocados especialmente en la relación entre emisión acústica y comportamiento del flujo en condiciones inestables.

Por tanto, se lleva a cabo una revisión bibliográfica para evaluar el estado del arte, especialmente en lo concerniente a técnicas experimentales relacionadas con el problema, pero incluyendo también los últimos desarrollos en términos de comprensión de las características del flujo mediante simulaciones numéricas. Como resultado, diferentes metodologías se proponen e implementan en un banco de ensayo hecho a medida dentro de una cámara anecoica para medir y analizar la producción sonora del compresor.

Mediante esta campaña de medida se obtiene y describe una caracterización acústica del contenido espectral del ruido a lo largo del mapa del compresor, identificando diferentes fenómenos sonoros tales como ruido tonal debido al paso de álabe, contenido de baja frecuencia asociado al bombeo profundo, contenido de banda ancha a alta frecuencia atribuido a la interacción del flujo en la holgura de punta de pala y ruido de banda ancha en el rango de onda plana, conocido como *whoosh* en la literatura y de especial interés para los fabricantes automovilísticos. Este fenómeno en

concreto se detecta incluso a condiciones más estables de alto gasto másico, y aumenta de nivel a medida que el gasto disminuye hasta llegar a ser enmascarado por el aumento del contenido de baja frecuencia.

Después de validar los procedimientos seleccionados en condiciones realistas de motor, se comparan los datos experimentales con un modelo numérico del compresor desarrollado en un trabajo paralelo a fin de evaluar su validez y proponer diferentes técnicas de postprocesado, con el objetivo de extraer información adicional acerca del comportamiento del flujo en diferentes condiciones, que sugieren que el mecanismo principal de generación de *whoosh* se encuentra localizado en el difusor del compresor.

Debido a que numerosas simulaciones predicen una cantidad reducida de inestable flujo inverso en condiciones donde el *whoosh* aparece en las medidas, se lleva a cabo una campaña experimental en la cual medidas detalladas de temperatura local cerca del rotor se usan para determinar la longitud del flujo inverso, con medidas suplementarias a través de sondas de presión usadas para relacionar esta evolución con la fluctuación de contenido espectral. Los resultados de temperatura se correlacionan también con medidas del campo de velocidad por imágenes de partículas, demostrando una clara relación entre el campo de flujo inverso y las medidas de temperatura.

Se describen a continuación diferentes campañas experimentales en las cuales se llevaron a cabo modificaciones de la geometría de entrada inmediatamente aguas arriba del compresor con el fin de evaluar cómo la presentación del flujo puede influenciar el rendimiento acústico. Geometrías incluyendo remansos, toberas y álabes guía demuestran una reducción de los niveles de ruido. Se ha realizado un estudio paramétrico de un codo de 90º, mostrando que el radio del codo influye en la distribución circunferencial de temperatura y los niveles de ruido, llevando a la hipótesis de que la influencia de la geometría en el ruido de *whoosh* está relacionada con cambios en la presentación del aire que promueven menor o mayor reflujo, que a su vez convecta aguas arriba el contenido espectral generado en el difusor del compresor.

Por último, se proponen estudios adicionales tanto experimentales como numéricos para explorar en profundidad estas cuestiones, a fin de proporcionar una mejor comprensión acerca de cómo el diseño de la entrada del compresor puede retrasar y mitigar la aparición y transmisión de estos fenómenos acústicos adversos.

Resum

A mesura que els requeriments de turbocompressió augmenten a fi d'afrontar una regulació dels motors de combustió interna cada vegada més estricta, la preocupació respecte a la seva emissió acústica es fa més urgent. Com que motors de dimensions més reduïdes requereixen majors augments de pressió i menors cabals màssics, el compressor del turbogrup es veu forçat a treballar a règims més inestables, els patrons de flux es fan més complexos, i els nivells de soroll augmenten.

Aquesta tesi té com a objectiu investigar aquestes qüestions, proposant metodologies per a caracteritzar l'emissió acústica de compressors de turbogrups, implementant-les en diferents experiments enfocats especialment a la relació entre emissió acústica i comportament del flux en condicions inestables.

Per tant, es duu a terme una revisió bibliogràfica per avaluar l'estat de l'art, especialment pel que fa a tècniques experimentals relacionades amb el problema, però incloent també els últims desenvolupaments en termes de comprensió de les característiques del flux mitjançant simulacions numèriques. Com a resultat, diferents metodologies es proposen i implementen en un banc d'assaig fet a mida dins d'una cambra anecoica per mesurar i analitzar la producció sonora del compressor.

Mitjançant aquesta campanya de mesura s'obté i descriu una caracterització acústica del contingut espectral del soroll al llarg del mapa del compressor, identificant diferents fenòmens sonors com ara soroll tonal a causa del pas d'àlep, contingut de baixa freqüència associat al bombeig profund, contingut de banda ampla a alta freqüència atribuït a la interacció del flux en la folgança de punta de pala i soroll de banda ampla en el rang d'ona plana, conegut com a *whoosh* en la literatura i d'especial interès per als fabricants automobilístics. Aquest fenomen en concret es detecta fins

i tot a condicions més estables d'alt cabal màssic, i augmenta de nivell a mesura que el cabal disminueix fins arribar a ser emmascarat per l'augment del contingut de baixa freqüència.

Després de validar els procediments seleccionats en condicions realistes de motor, es comparen les dades experimentals amb un model numèric del compressor desenvolupat en un treball paral·lel a fi d'avaluar la seva validesa i proposar diferents tècniques de post-processat, amb l'objectiu d'extraure informació addicional sobre el comportament del flux en diferents condicions, que suggereixen que el mecanisme principal de generació de *whoosh* es troba localitzat al difusor del compressor.

Pel fet que nombroses simulacions prediuen una quantitat reduïda d'inestable flux invers en condicions on el *whoosh* apareix en les mesures, es duu a terme una campanya experimental en la qual mesures detallades de temperatura local prop del rotor s'utilitzen per a determinar la longitud del flux invers, amb mesures suplementàries mitjançant sondes de pressió emprades per a relacionar aquesta evolució amb la fluctuació de contingut espectral. Els resultats de temperatura es correlacionen també amb mesures del camp de velocitat per imatges de partícules, demostrant una clara relació entre el camp de flux invers i les mesures de temperatura.

Es descriuen a continuació diferents campanyes experimentals en les quals es van realitzar modificacions de la geometria d'entrada immediatament aigües dalt del compressor a fi d'avaluar com la presentació del flux pot influenciar el rendiment acústic. Geometries incloent volums, toveres i àleps guia demostren una reducció dels nivells de soroll. S'ha realitzat un estudi paramètric d'un colze de 90º, mostrant que el ràdio del colze influïx en la distribució circumferencial de temperatura i els nivells de soroll, donant suport a la hipòtesi de que la influència de la geometria en el soroll de *whoosh* està relacionada amb canvis en la presentació de l'aire que promouen menor o major reflux, que aleshores convecta aigües dalt el contingut espectral generat en el difusor del compressor.

List of publications

Following the work performed in the framework of this doctoral thesis and its associated projects, the following journal papers have been published:

[1] A. Broatch, J. Galindo, R. Navarro, and J. García-Tíscar. "Methodology for experimental validation of a CFD model for predicting noise generation in centrifugal compressors". *International Journal of Heat and Fluid Flow* 50, 2014, pp. 134–144.

[2] A. Broatch, J. Galindo, R. Navarro, J. García-Tíscar, A. Daglish, and R. K. Sharma. "Simulations and measurements of automotive turbocharger compressor whoosh noise". *Engineering Applications of Computational Fluid Mechanics* 9 (1), 2015, pp. 12–20.

[3] A. Torregrosa, A. Broatch, R. Navarro, and J. García-Tíscar. "Acoustic characterization of automotive turbocompressors". *International Journal of Engine Research* 16 (1), 2015, pp. 31–37.

[4] A. Broatch, J. Galindo, R. Navarro, and J. García-Tíscar. "Numerical and experimental analysis of automotive turbocharger compressor aeroacoustics at different operating conditions". *International Journal of Heat and Fluid Flow* 61, Part B, 2016, pp. 245–255.

[5] A. J. Torregrosa, A. Broatch, X. Margot, and J. García-Tíscar. "Experimental methodology for turbocompressor in-duct noise evaluation based on beamforming wave decomposition". *Journal of Sound and Vibration* 376, 2016, pp. 60–71.

Additionally, two more manuscripts have been submitted to the journal *Experimental Thermal and Fluid Science* and are undergoing peer-review:

[6] A. J. Torregrosa, A. Broatch, X. Margot, J. García-Tíscar, Y. Narvekar, and R. Cheung. "Local flow measurements in a turbocharger compressor inlet". *Submitted to Experimental Thermal and Fluid Science*, 2016.

[7] A. J. Torregrosa, A. Broatch, J. V. Pastor, J. García-Tíscar, R. K. Sharma, and R. Cheung. "Measuring turbocharger compressor inlet backflow through laser particle image velocimetry". *Submitted to Experimental Thermal and Fluid Science*, 2016.

Division of work between authors

The work leading up to this thesis was done in collaboration with other researchers. The respondent is the co-author of all papers on which this thesis is based, with author signatures being in order of seniority in the Institute. The respondent implemented the proposed methodology into the different experimental setups, performed the measurements, processed the experimental results and extracted the presented conclusions. Discussions were also performed in collaboration with supervisor Prof. Broatch and the rest of the co-authors. Numerical simulations were not performed by the respondent, and are thus gratefully acknowledged.

Funding acknowledgements

The respondent wishes to acknowledge the financial support received through contract FPI-S2-2015-1530 of the *Programa de Apoyo para la Investigación y Desarrollo* (PAID) of Universitat Politècnica de València. The equipment used in this work has been partially supported through the following projects:

- Project nº TRA2012-36954 of the Spanish Ministerio de Economía y Competitividad: *Mecanismos de generación de ruido producido por turbo compresores de motores de combustión interna alternativos* (RUITUR).
- Project nº DPI2015-70464-R of the Spanish Ministerio de Economía y Competitividad: *Propagación y emisión de ruido de admisión en motores turbo-sobrealimentados* (EMITUR).
- FEDER project funds FEDER-ICTS-2012-06: *Dotación de infraestructuras científico técnicas para el Centro Integral de Mejora Energética y Medioambiental de Sistemas de Transporte* (CiMeT) framed in the operational program of unique scientific and technical infrastructure of the Spanish Ministerio de Economía y Competitividad.

Parts of the work presented in this thesis have been supported by different collaboration agreements with industry partner Jaguar Land Rover Limited, Abbey Road, Whitley, Coventry CV3 4LF, UK.

Acknowledgements

"Good company in a journey makes the way to seem the shorter", wrote Isaak Walton back in 1653 and, certainly, I could not have wished for a better company in this journey. I would like to express my gratitude, first and foremost, to my advisor Prof. Alberto Broatch for his guidance and support in the pursuit of this research.

A gratitude that I also must extend to Prof. Galindo and Dr. Navarro, not only for the development of the numerical model but for the many insightful discussions held along the development of this work.

Also included in this recognition are certainly the people of the Noise Control research line, specially Prof. Torregrosa, Bernardo Planells and Josep Gómez. My sincere appreciation also goes to my colleagues at CMT – Motores Térmicos, starting with Profs. Payri and Desantes and including the professors, researchers, technicians, students, etc., with whom I shared so many good times. Special thanks as well to the administrative staff, Teresa, Amparo, Julia, for their help navigating the fearsome seas of paperwork.

I also wish to thank Profs. Mats Åbom, Susann Boij and Inés López for welcoming me as a visiting researcher in the Marcus Wallenberg Laboratory at the KTH – Royal Institute of Technology, and of course to Luck, Juan Pablo, Romain, Luca, Mathieu, and the many others who offered me their hospitality in Stockholm. I am indebted as well to the people at Jaguar Land Rover with whom we have made so many fruitful collaborations.

Last but not least, I wish to thank my friends and family for their everlasting support, specially my parents from whom I inherited the appreciation for mathematics and science. And finally, thank you, Paula, for sharing this journey, and those that may follow.

Valencia, 2017

"Hundreds of noises wove themselves into a wiry texture of sound with barbs protruding here and there, smart edges running along it and subsiding again, with clear notes splintering off and dissipating. By this noise alone, whose special quality cannot be captured in words, a man returning after years of absence would have been able to tell with his eyes shut that he was back in the Imperial Capital and Royal City of Vienna."

Robert Musil, *The Man Without Qualities.*

Contents

List of Figures

List of Tables

List of Symbols

Latin

A	Area	m^2
a	Speed of sound	$\mathrm{m\,s}^{-1}$
c_p	Specific heat capacity at constant pressure	$\mathrm{J\,kg}^{-1}\,\mathrm{K}^{-1}$
D	Duct diameter	m
D_o	Compressor outer diameter	m
d_s	Sensor separation	m
f	Frequency	Hz
He	Helmholtz number	—
I	Sound Intensity	$\mathrm{W\,m}^{-2}$
k	Turbulent kinetic energy	$\mathrm{m}^2\,\mathrm{s}^{-2}$
L	Level (SPL, SIL or PVL)	dB
$\dot{m}$	Mass flow rate	$\mathrm{kg\,s}^{-1}$
M	Mach number	—
N	Compressor rotational speed	rpm
p	Pressure	Pa
R	Specific gas constant	$\mathrm{J\,kg}^{-1}\,\mathrm{K}^{-1}$
r	Duct radius	m
Re	Reynolds number	—
St	Strouhal number	—
T	Temperature	K
T_d	Sensor time interval	s
t	Time	s
U	Mean velocity	$\mathrm{m\,s}^{-1}$
w_n^*	Beamformer weight factor of sensor n	—
W_u	Compressor specific work	$\mathrm{m}^2\,\mathrm{s}^{-2}$
x_n	Pressure signal of transducer n	Pa
X_n	Pressure signal of transducer n in the frequency domain	Pa
y^+	Non-dimensional boundary layer distance	—

Greek

$\Delta f, t$	Frequency or time step	Hz or s
γ	Ratio of specific heats	—
ε_R	Relative error	%
η_s	Isentropic efficiency	%
θ	Direction of arrival	rad
λ	DMD eigenvalue	—
Π	Pressure ratio	—
ρ	Density	$\mathrm{kg\,m^{-3}}$
σ	Standard deviation	—
τ	Compressor torque	$\mathrm{kg\,m^2\,s^{-2}}$
Φ	DMD mode	—
φ	Flow coefficient	—
ψ	Generic variable	—
Ω	Rotational speed	$\mathrm{rad\,s^{-1}}$
ω	Specific turbulence dissipation rate	$\mathrm{s^{-1}}$

Sub- and superscripts

$+$	Forward-travelling variable
$-$	Backward-travelling variable
$*$	Corrected variable
$1, 2, 3$	Related to $1^{\mathrm{st}}, 2^{\mathrm{nd}}$ or 3^{rd} downstream sensor
a	(Freq.) related to an asymmetric acoustic mode
back	Backward travelling wave
CFD	Variable simulated through CFD
c	(Freq.) related to a circular acoustic mode
d	Related to sensor spacing
exp	Variable measured experimentally
H	Hermitian transpose
in	Related to the inlet duct
k	Discrete time step
forw	Forward-travelling wave
n	(Freq.) related to the spatial Nyquist criterion
out	Related to the outlet duct
s	Isentropic
ref	Reference value
rms	Root mean squared
T	(Sub.) Total or stagnation variable | (Sup.) Transposed
TT	Total to total ratio
tip	Related to the blade tip
W, A, S	Wall, axis or cross-section monitor, respectively

Acronyms

AMF	Air Mass FLow
BPF	Blade Passing Frequency
CAD	Computer-Aided Design
CCD	Charge-coupled device
CFD	Computational Fluid Dynamics
DAQ	Data Acquisition
DES	Detached Eddy Simulation
DMD	Dynamic Mode Decomposition
DOA	Direction Of Arrival
ECU	Engine Control Unit
FFT	Fast Fourier Transform
HWA	How Wire Anemometry
IGV	Inlet Guide Vanes
LDA	Laser Doppler Anemometry
LCMV	Linearly-Constrained Minimum Variance
LE	Leading edge
LES	Large Eddy Simulation
MEMS	Micro Electro-Mechanical System
MoC	Method of Characteristics
Nd:YAG	Neodymium-doped Yttrium Aluminium Garnet
NRBC	Non-Reflecting Boundary Condition
NSD	Non-dimensional Spectral Density
NVH	Noise, Vibration & Harshness
PIV	Particle Image Velocimetry
POD	Proper Orthogonal Decomposition
PS	Pressure Side
PSD	Power Spectral Density
PR	Pressure Ratio
PVL	Particle Velocity Level
RANS	Reynolds-Averaged Navier-Stokes
RO	Rotating Order
ROI	Region Of Interest
RPM	Revolutions Per Minute
TCN	Tip Clearance Noise
TMM	Two Microphone Method
SIL	Sound Intensity Level
SLS	Selective Laser Sintering
SPL	Sound Pressure Level
SST	Shear Stress Transport
SS	Suction Side
SVD	Singular Value Decomposition
VGT	Variable Geometry Turbine

CHAPTER 1

Introduction

> *"The story is set in the year 1922 and has its main character, Mr Engelbert, moving to Prague from the countryside to live out his retirement years and struggling to cope with the aggressive modernity of the city. The horror is not the power of money or the arrogance of the people, but the noise; not the age-old noise of a thunderstorm or a hammer, but the new noise of engines, especially of automobiles and motor-cycles, the explosive internal combustion monsters."*
>
> **Milan Kundera**, *The Curtain.*

As Milan Kundera so eloquently wrote, the noise produced by internal combustion vehicles has radically changed the way we understand cities; even many decades before we understood the dangers that chemical emissions pose to the environment and our health, noise emissions were without a doubt a commotion for urban inhabitants worldwide: an horrific, roaring hallmark of accelerated progress.

Nowadays, no one is surprised anymore by the sound of an automobile or a "motor-cycle". Even the mere absence of this familiar, background urban sound is unsettling to many. Road traffic is, however, the main source of noise pollution in cities. As an example, Fig. 1.1 depicts global noise levels in the city of Valencia.

It can be clearly seen how automotive vehicles define the noise environment in our cities; high-traffic roads appear as higher level sources of noise that propagates towards less travelled areas. The traffic-restricted campus of Universitat Politècnica de València, where this thesis has been developed, appears as a blue, quieter island at the upper right part of the figure.

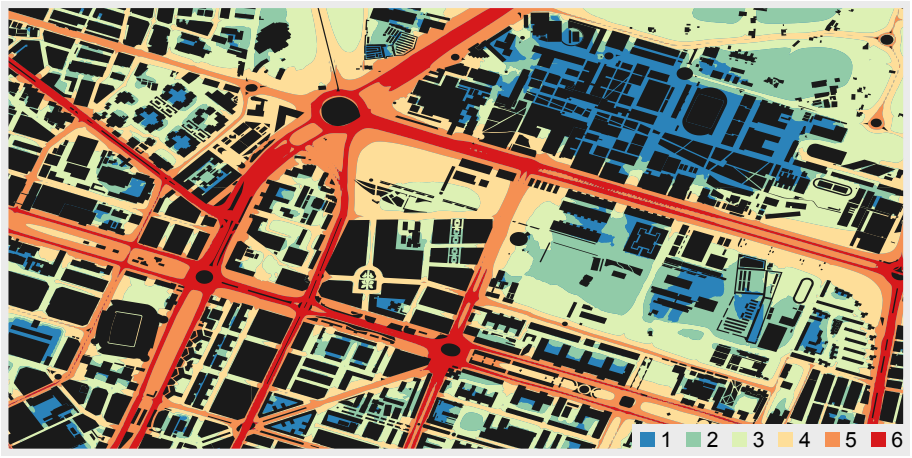

Figure 1.1: *Global noise levels of the city of Valencia around Universitat Politècnica (upper right), showing the importance of road traffic as a source of urban noise pollution. Scale shows normalized levels from quieter (1) to noisier (6). Data courtesy of the Valencia City Council.*

Noise emission by automotive vehicles is, however, a sum of very complex phenomena. One could consider, intuitively, that the dominant factor of this sum must be the combustion noise itself: several explosions going off every second of operation, their vibration propagating through the metallic engine block and radiating through the air.

However, many of other sources of noise exist in a vehicle: aerodynamic noise produced as air flows around the structures and through the intake and exhaust pipes, friction noise of the tires against the asphalt of the road, mechanical noise of the engine parts working together, auxiliary systems such as fuel injection, pumps and, increasingly important, the noise produced by the turbocharger group.

1.1. Turbochargers

The idea of using a compressor to increase the density of air available in the combustion chamber of an engine is now more than a century old. While Gottlieb Daimler's 1885 patent [8] included a supercharging mechanical pump, and Louis Renault's 1902 patent [9], featured a centrifugal supercharger, the first design for a turbocharger (this is, a supercharging compressor driven by the exhaust gasses) was presented in Alfred Büchi's patent N°204630 from the Imperial Patent Office of the German Reich [10], in the year 1905.

While some early racing and luxury sport cars featured supercharged engines (the popular Mercedes *Kompressor* series started in 1921), most mass produced cars still relied on simpler, naturally aspirating engines.

During the first half of the XX century, the primary areas of application of turbocharging were marine and, specially, aviation engines. The addition of turbocharging to aircraft engines allowed them to counter the diminishing air density at high altitude, increasing the available power and operating ceiling. For instance, the first product made by Cliff Garrett's corporation was a supercharged air cooler for the B-17 Flying Fortress.

It was not until the sixties that turbocharging made its appearance into the popular automotive market, with the Chevrolet Corvair Monza and the aptly named Oldsmobile Jetfire. However, technology was still not very reliable, and they were quickly retired from the dealerships.

The scene changed radically during the seventies. Several factors (the oil crisis, enhanced reliability, stringent emission requirements, turbocharged cars winning Formula 1 and Le Mans races) made possible the first successful turbocharged passenger cars, that grew during the 80s and 90s to dominate the diesel automotive market.

To illustrate this evolution, Fig. 1.2 shows how expressions like "turbocharger" and "traffic noise" started to appear in English literature. We can see a sudden bump of "turbocharger" mentions following the start of WWII (where turbocharging aircraft quickly became norm), but the peak of popularity appears in the 80s. Concern for "traffic noise" on the other hand suddenly boosts from 1965 to 1975.

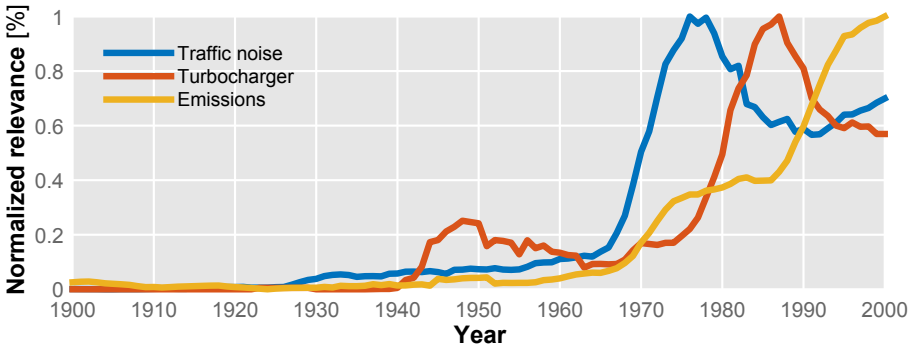

Figure 1.2: *Normalized relevance of selected English terms in literature, as indexed by Google Books. Data licensed under CC-BY 3.0 license terms.*

This figure also shows how, from the last years of the XX century, social concern for the nocive effects of pollutant emissions has grown steadily. These include NO_x, CO, CO_2, particulate matter (PM) and so on. In a bid to lower emissions, a trend of *downsized* engines has become popular, aiming to increase efficiency and lower contaminants by reducing the displacement and cylinder count, in both petrol and diesel markets. Upcoming regulations are even more stringent [11], so this tendency is expected to continue.

As power and torque must be maintained in these reduced displacement engines, turbocharging requirements increase, becoming more and more popular in the petrol market as well. Further information on the relationship between stringent emissions policies, downsizing and turbocharging can be found in the work of Schumann et al. [12]

1.2. Noise emissions

Another important aspect of increasing concern for both regulators and consumers is the so-called NVH (Noise, Vibration and Harshness) problem that opened this chapter. While in some cases the addition of a turbocharger to a downsized engine can be useful to attenuate noisy exhaust pulsations [13] and improve knocking resistance [14], it has also been shown [15] that at certain operating conditions, a downsized engine will radiate higher noise levels than an equivalent engine of larger displacement.

Increased turbocharging requirements also imply that the compressor must work near its limiting conditions, such as the *surge* limit [16], where compressor airflow is so low that it reverses, allowing air to escape the compressor upstream instead of downstream. Auriel Stodola [17] wrote in 1927:

"A phenomenon which, as a mysterious difficulty, has in the beginning given the builders of centrifugal compressors no end of worry is 'surging'; that is, a periodic sudden sending back of the compressed air through the compressor into the atmosphere [...]. The cause of the surging is the instability of the dynamic equilibrium on the rising branch of the characteristic curve."

As he correctly pointed out, this potentially destructive condition is preceded by flow instabilities while the pressure ratio is still rising, that are also linked to increased noise output. This link that will be further explored along this work with the aid of noise maps and spectrograms.

Another factor that must be taken into account during the analysis of acoustical emissions is that noise *quantity* (overall level) is not the only concern, as noise *quality* is also an important problem, regarding both the possibilities of attenuation and the psychoacoustic perception of the customer, as shown in [18] and the work of Nor et al. [19]

1.3. State of the art

These concerns have led to a thriving research effort regarding turbocharging efficiency, usefulness to reduce pollution and contribution to noise emissions.

Several approaches to this problem are being tested. Some researchers conduct experimental analysis of the internal flow patters in the compressor. Others focus their interest in the externally radiated acoustic field. Computational fluid dynamic (CFD) simulations are carried out in order to visualize the different flow phenomena inside and near the compressor.

Aside from experimental or numerical characterization of the acoustic problem, its mitigation is also being actively investigated. Options range from the modification of inlet or casing geometries, to the addition of different silencers and resonators on the compressor pipes.

Through this research, different acoustical phenomena have been identified. While some of them, like the tonal noise produced by the blade pass (known as Blade Passing Frequency or BPF) have a clear, straightforward explanation, others are not yet fully understood.

For example, a certain wideband noise known as *whoosh* in the literature has been lately of interest, with explanations for its generation ranging from turbulent vorticity to fluid interaction with tip clearance (the gap between the wheel blades and the casing wall). Further research is currently ongoing on this particular phenomenon.

1.4. Objectives

The objective of this thesis is threefold, covering not only the experimental acoustic analysis itself but also its methodological and application aspects. To sum up, the different but related objectives can be enumerated as:

- Enlarging the corpus of published experimental results of turbocharger compressor acoustic measurements across its different operating conditions: as the literature is still reduced, expanding it will improve not only understanding of known phenomena but will also identify other areas that may be of interest for further research.

- Presenting a comprehensive experimental methodology, from instrumentation to measuring procedures and signal processing, in order to consistently and reliably characterize acoustic emissions, ensuring at the same time the robustness of these techniques when faced with real engine conditions.

- Exploring how this experimental methodology can be applied not only to the characterization of the internal sound field, but also to the initialization and validation of numerical simulations, the analysis of the influence of unstable flow phenomena at marginal surge conditions and the study of the effect of different inlet geometries on noise generated by the compressor.

1.5. Thesis outline

After this introduction that constitutes chapter 1, a comprehensive literature review on turbocharger compressor noise research will be carried out in chapter 2. This review will introduce relevant developments regarding not only experimental compressor testing, but also some literature concerning numerical simulations that are of vital importance to improve the understanding of the flow field causing the acoustical emission.

Chapter 3 will present the different methodologies used in the experimental campaign performed during this thesis, along with the facilities and equipment used to this effect. These methodologies mainly include procedures for the characterization of the internal sound field, but also some for measuring external sound radiation will be introduced. Theoretical background, limitations and best practices regarding the use of the presented techniques will be also discussed.

The results of the experimental campaign carried out using the described methodology will constitute chapter 4. Pressure spectra will be used to identify relevant acoustic phenomena, and noise maps and spectrograms will be used to analyze the evolution of these phenomena across the different operating conditions of the compressor.

On chapter 5, procedures described on chapter 3 will then be implemented on an engine test cell in order to assess their performance in real engine conditions. This performance will be compared to established methods such as the two-microphone method and the pressure-pressure intensity probe. While external measurements are difficult in a non-anechoic environment such as the engine test cell, an example of the acoustical particle velocity method will be tested to overcome this limitation.

Chapter 6 will explore how the obtained experimental results can be used to initialize and validate numerical simulations. In turn, these simulations can provide insight into particularities of the flow field by using different post-processing techniques, and also suggest further experimental measurements that can be relevant for the understanding of the phenomena involved in the generation of noise.

Detailed characterization of the flow field and its thermodynamic variables in the inducer and final section of the compressor inlet duct will enable further comprehension of how stalled flow cells reverse and reintegrate into the main flow, and the relation of this phenomenon with the acoustic emission. Chapter 7 will be devoted to the measurement and analysis of this issue.

As influence of the inlet geometry immediately upstream of the compressor wheel has been proved of significant relevance in both compressor performance and noise emission, chapter 8 will present experimental studies of different geometries and their influence on the the compressor behaviour, with special emphasis on noise emission.

Finally, chapter 9 will offer the conclusions that have been reached through the experimental campaign and analysis of results, along with suggestions of future works that could be carried out to advance knowledge of the topic.

CHAPTER 2

Literature review

In order to provide a better context for the development of this work, a literature review has been carried out, where special emphasis has been put into existing experimental research of automotive turbocharger acoustics, although techniques and results from related fields of turbomachinery and fluid mechanics were also considered when applicable.

For instance, numerical simulations on the topic are becoming more numerous. They offer further insight into the underlying flow structures even if clear, causal correlations have not yet been demonstrated. As such, these studies merit their own specific section.

Another point related to these flow structures that deserves interest is the analysis of how the particularities of the inlet geometry immediately upstream of the compressor wheel influence the performance and the noise emission of the system. Not only this influence offers clues of which mechanisms are responsible for certain acoustic phenomena, but they also present an interesting possibility of mitigation.

2.1. Experimental research

While the acoustical emission of axial compressors has been a subject of extensive research since more than fifty years ago [20, 21], studies performed on centrifugal turbocharger are comparatively more scarce.

Of the existing literature dealing with centrifugal turbomachinery, many efforts were directed at large fans or centrifugal pumps, with small turbochargers have begun only recently to be more relevant.

Among the first it is worth to mention the extensive research carried out at Pennsylvania State University, where at least since the nineties [22] an instrumented centrifugal pump was installed in an anechoic flow bench to characterize its acoustical performance.

This setup allowed several researchers to conduct experiments analysing not only in-duct noise, as in the works of Mongeau et al. [22, 23] and radiated noise, as shown by Choi et al. [24, 25], but also pressure distribution on the blade surface [22, 24].

A related experimental campaign, starting at least from the turn of the millennium, was carried out at the University of Siegen. Here, Wolfram and Carolus [26] used again a centrifugal pump inside an anechoic chamber.

In this case, measurements were done relying in anemometers directed at the blades that could be rotated at will in order to analyse azimuthal rotating modes [27]. Radiated noise could be also measured using a single microphone [28].

Both Penn State and Siegen campaigns show significant aspects of interest such as the identification of Blade Passing Frequency (BPF) peaks on the acoustic spectrum and hints on the link between stall and noise [22]. Relevant dimensionless numbers such as the Strouhal and Helmholtz numbers are also suggested [23].

However, it is important to notice that there are important differences between these large centrifugal pumps and small turbocharger compressor for automotive purposes.

These differences are found not only in the geometrical design aspect but also in the order of rotational speed. While the considered pumps do not exceed 3600 rpm, small automotive turbochargers can exceed 200 krpm.

Also, they are affected by the pulsating flow of the reciprocating engine, which will be present in the acoustic signature as well. This later aspect will be shown in chapter 5.

In order to address these differences and focus the literature review in the specific issues presented by turbocharger compressors, selected works from the literature will be reviewed in the following subsections, placing special attention in both the measurement techniques and the acoustical results obtained.

2.1.1. Methods for turbocharger noise characterization

Although not numerous, acoustical research works on small, centrifugal turbocharger compressors can be found in the literature. Many of them are published by automotive or compressor manufacturers, who are among the most concerned about compressor noise emissions.

Starting from the work of Trochon [29] and Evans and Ward [30, 31] up to more recent investigations such as those of Åbom, Kabral and Rammal [32, 33] at the Swedish Royal Institute of Technology (KTH), several different methodologies for characterising the acoustical emission of automotive turbochargers can be found.

A first division can be made between those studies aiming to measure *internal* flow noise, placing sensors inside the compressor housing or inlet and outlet ducts, and those works based on external measurements of the *radiated* noise.

Evans and Ward [30, 31] opted for a simple setup of four microphones to measure sound radiation. These four microphones were situated on the same plane and directed to a turbocharger-equipped engine. They were distributed at 90º with a separation of one meter from the engine. From the pressure readings of these four microphones, Sound Pressure Level (SPL)[1] was computed and then averaged among them, in order to get a single signal from which spectrograms and sound spectra could be derived.

A similar setup was used by Teng and Homco [16] (see specially Fig. 1 of this reference) in order to test different countermeasures for *whoosh* noise mitigation, such as engine calibration, resonators in the compressor inlet/outlet, compressor trim variation and a swirl generation device.

This kind of averaging four spatially-distributed microphones method was implemented in the anechoic chamber in order to characterize the far-field radiated sound of the turbocharger group during the experimental campaign; further information will provided on subsection 3.4.2 of chapter 3.

Apart from the far-field radiation, another acoustic problem of interest is that of *orifice noise*, this is, the noise created by the ingestion of the air stream into the opening of the turbocharger inlet duct.

Lee et al. [34] used a Brüel & Kjær free field type microphone pointed at the compressor inlet as seen in Fig. 8 of this reference. It can also be noted that in order to avoid "flow effects", the microphone was located 0.8 away from the inlet.

[1] Usually defined as $10\log_{10}\left(\bar{p}^2/p_{\text{ref}}^2\right)$, with $\bar{p}$ being the root mean square (RMS) sound pressure and $p_{\text{ref}} = 20\,\mu\text{Pa}$ being the threshold of human hearing.

The setup selected by Guillou et al. [35] to measure ingestion noise was very similar. Here, a single microphone was positioned aligned with the axis of the turbocharger at a distance of 0.4 m, again facing directly to the compressor inlet bell mouth.

Another solution was implemented by Figurella et al. in [36]. In this case, a Brüel & Kjær type 2235 Sound Level Meter was positioned 0.25 m from the inlet duct orifice, at a 45º angle from the inlet axis. In [37] Figurella et al. opted instead to rely on a ¼" microphone affixed at the same position, 0.25 m away from the orifice and 45º from the axis. Both instruments appear in Fig. 1 of the cited work [37].

During the experimental campaign that was carried out for the development of this thesis, two free field microphones were situated at a distance of 10 and 20 cm from the inlet pipe orifice. This will be expanded in detail in subsection 3.4.1 of chapter 3.

Finally, a third approach for the characterization of compressor noise is based on measuring the sound field inside the inlet and outlet ducts, usually by means of fast pressure sensors. This has the advantage of not needing to ensure anechoic conditions in the test cell. Another remarkable advantage is that, by analysing the flow field alone, one can avoid the influence of the radiative properties of the duct material and geometry.

As these advantages make this last approach specially interesting for a research centred on the sources of aero-acoustical generated noise, emphasis has been put in reviewing existing literature dealing with internal flow noise.

Early work by Trochon [29] dealt with the acoustic characterization of turbocharger noise measuring in-duct airborne noise at the compressor exit (see Fig. 1 of this reference) during engine operation.

Gaudé et al. [38] from Honeywell Turbo Technologies presented an extensive review of different vibro-acoustic sources of turbocharger noise. Both accelerometers and pressure sensors affixed to the pipes were used, and their use to identify some vibro-acoustic phenomena was demonstrated. While this work omits a proper, referenced methodology description, it indeed mentions that acoustic noise intensity was calculated using wave decomposition by means of three sensors, and it indicates the range of plane wave frequencies for the installed ducts.

Raitor and Neise [39] used different methods, taking into account the presence of acoustic modes in the duct. The first one consisted on a ½" microphone equipped with a turbulence screen and mounted in a rotatable section of the duct. This allows the measurement of circumferentially

averaged sound pressure level (SPL), in accordance with ISO 5136. This rotatable section can also be fitted with four consecutive rings, each with four flush-mounted condenser microphones for analysis of acoustic modes.

This last technique is similar to that used in the previously mentioned work by Guillou et al. [35], where four Kulite model XCS-190-5D miniature pressure sensors were mounted on the compressor inlet adaptor, equally separated 90º. In this work, a single Kulite model XTEL-160-50G was also used in the outlet duct.

A single in-duct fast pressure sensor was also the technique selected by Figurella et al. [36, 37]. In this case Kistler piezoresistive transducers were used, both in the compressor inlet duct (model 4045A2) and in the outlet duct (model 4045A2 or 4045A5).

Pai et al. [40, 41] opted as well for a single sensor (in this case labelled as a microphone) to measure sound pressure level inside the compressor inlet duct. An ambient microphone was present as well, but its readings are not included in their work.

A different approach was taken by Tiijoka et al. [42], who describe the use of an array of three pressure transducers in both inlet and outlet pipes of their compressor setup (see Figs. 1-3 of the reference). In order to estimate the strength of the propagating nodes, a cross-spectra averaging technique was used.

Table 2.1: *Synthesis of different measurement techniques for the acoustical characterization of turbocharger compressors found in the literature, including type of measurement and location.*

Reference	Measurement	Type	Location
Trochon [29]	1 in-duct sensor at the outlet	SPL	Out
Evans [30]	4-microphone averaging around engine	SPL	External
Gaudé [38]	2 × 3-sensor arrays (wave decomp.)	SIL	In+Out
Raitor [39]	1 mic or 4 × 4 mic sections + up to 5 outlet sensors	SPL	In+Out
Teng [16]	4-microphone averaging around engine	SPL	External
Guillou [35]	4 Kulite (inlet) + 1 Kulite (outlet) + 1 mic at 0.4 m	SPL	In+Out+Orifice
Lee [34]	1 microphone at 0.8 m from orifice	SPL	Orifice
Tiikoja [42]	2 × 3-sensor arrays (cross spectra avg.)	SPL	In+Out
Figurella [36]	2 × piezores. transducers + SLM at 0.25 m and 45º	SPL	In+Out+Orifice
Figurella [37]	2 × piezores. transducers + 1 mic at 0.25 m and 45º	SPL	In+Out+Orifice
Pai [41]	1 microphone (inlet) + 1 microphone (ambient)	SPL	In+External

In table 2.1 a synthesis of the information compiled in this subsection is presented. It can be seen how only one reference [38] used sound intensity, which is inherently a more robust magnitude. Sound pressure level, on the other hand, is easily influenced by the particular geometric setup and measurement location. It is also apparent that, while measurements have been presented regarding inlet, outlet, orifice and external noise, no study as far (as the author knows) has been presented regarding all four options simultaneously.

2.1.2. Relevant results

After reviewing the different methods available in the literature regarding turbocharger noise, a selection of relevant acoustical results from these works is analyzed in this subsection. It is worth noting that while some of the referred research was directly aimed at characterizing noise output, other works had different objectives and only used noise measurement as a metric, without discussing its characteristics or generation process.

An interesting introduction is provided by Gaudé et al. whose work collects a variety of different noise-generating phenomena in turbochargers [38]. Table 2.2 reproduces this classification. Several tone sources are proposed,

Table 2.2: *Classification of turbocharger noise phenomena, including frequencies and source mechanisms, as proposed by Gaudé et al. [38].*

Name	Spectrum	Frequency range	Source mechanism
Oil whirl	Tone	0 – 1000 Hz (function of oil temp.)	Rotor-dynamics vibration of rotating group caused by oil film.
Synchronous vibration	Tone synchronous to turbocharger speed	0 – 4000 Hz	Rotor-dynamics - Residual unbalance of the rotor.
Synchronous pulsation	Tone synchronous to turbocharger speed	1000 – 4000 Hz (Depends on wheel outer diameter)	Aerodynamics: Pressure fluctuations induced by lack of symmetry of compressor wheel.
Harmonics	Tone = number of irregularities × speed	0 – 20 kHz	Rotor-dynamics or aerodynamics due to irregularities.
Turbine BPF	Tone = number of blades × speed	→ 20 kHz	Aerodynamics.
Compressor BPF	Tone = number of full blades × speed	→ 20 kHz	Aerodynamics.
Hiss	broadband noise	0 – 20 kHz	Aerodynamics due to turbulence in the compressor stage.

mainly linked to the imbalance of the rotor and irregularities and lack of symmetry of the compressor wheel. Another source of tones is the passing of the blades of both turbine and compressor, in special the main ones in the case of the later.

Besides the different tones and their associated harmonics, a broadband noise is identified as "hiss", whose source mechanism is listed as related to turbulence in the compressor stage. The frequency range of this turbulence-related phenomenon is proposed as 0 – 20 kHz, but no further insight is given.

A similar division was anticipated by Trochon [29], who classified turbocharger compressor noise in "pulsation noise" (the tonal noise caused by the blade rotation) and "blow noise", a broadband noise (named this way for its resemblance to noise produced by a leakage). It is attributed by the author to aerodynamic turbulence "inside the compressor" at high mass flow and low shaft speed. By examining Fig. 1 of the reference we can assess the presence of such a broadband noise between 1.5 and 2.5 kHz.

Evans and Ward [30] address explicitly the issue of a so-called *whoosh* noise. This noise is identified as being "in general" of the broadband type. The authors state that this noise is typically present from 750 Hz to in excess of 10 kHz. they note however that most of the energy is apparently distributed between 1.5 and 3 kHz. This appears to be similar to the "hiss" noise mentioned in the previous reference, but in this case the authors point out that the occurrence of *whoosh* appears to be specifically associated with operation close to surge. In this situation, blade stall, reverse flow and recirculation of intake air generate increased turbulence, which the authors point as possible source .

Raitor and Neise [39] mention instead the so-called "tip clearance noise" (TCN), referring to a noise with broadband spectral content below the blade passing frequency (BPF). A similarity is drawn with the work of Kameier and Neise [43] regarding axial turbo compressors, where a rotating instability linked to stall cell propagation is discussed. This TCN is marked in Fig. 8 of the reference as located between 3 kHz and 5.5 kHz in the inlet duct.

BPF is also marked in the figure, including its harmonics. An intense "buzz-saw" multi-tonal noise is apparent at higher speeds in the inlet, but not so in the outlet (see Fig. 10 of the reference). TCN appears in the outlet duct as well. Mach number at the impeller tip is also highlighted as signalling the transition between TCN vs. BPF dominance. Furthermore, broadband content seems to appear between 1.2 – 2 kHz, with a smaller one at 2 – 2.8 kHz, both being similar to the aforementioned *whoosh* noise.

In Fig. 2.1 an idealized representation of the a sample SIL spectrum is offered for reference, showcasing the most relevant acoustic phenomena that have been reported in the literature and will be investigated along this work. *Whoosh* is shown as a smaller broadband effect at plane wave range frequency, TCN as a higher frequency broadband and BPF and its harmonics as tonal noise peaks.

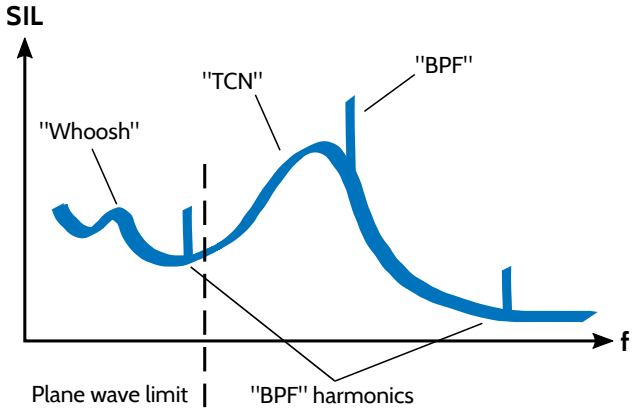

Figure 2.1: *Idealized representation of a characteristic SIL spectrum in a turbocharger compressor outlet, featuring the most commonly identified acoustic phenomena according to the literature.*

Following the work of Evans and Ward, Teng and Homco [16] obtained further insight on the precise location of the *whoosh* noise for their setup. Especially, in Fig. 5 of the reference the authors identify *whoosh* noise as appearing in the 4.5 to 7 kHz band. BPF tone is not seen on the figure, which is limited to a maximum frequency of 10 kHz. However, amplitude and frequency of this band, and its abrupt lower frequency cut-off, could suggest that it is more related to the TCN identified by other authors.

Inspection of the spectrogram that the authors present in Fig. 2 appears to show a certain broadband content between 1 – 2 kHz along all conditions of the full-load test, which would be more consistent with other reports of *whoosh*. In order to confirm the relation between broadband noise and surge inception, a type K thermocouple was affixed very close to the compressor inlet. An apparent correlation between temperature rise and 5 to 7 kHz sound pressure content is found in Fig. 7 of the reference, with the authors suggesting that the presence of hot backflow due blade stall is related to the identified broadband noise.

Guillou et al. [35] do not directly address the noise spectra in their study. Nonetheless, the authors plot the pressure FFT in the outlet duct for various flow regimes. It can be seen in their Fig. 7, specially in the lower right plot (stable regime), how a clear broadband appears between 2 and 3.5 kHz. This phenomenon continues to be present in both stall and surge regimes, but in those conditions it becomes masked by the strong low frequency signals that are typical of surge.

Lee et al. [34] focus their work on "pulsation noise", asserting that it is caused by unbalance of shaft and blades, and BPF noise, caused by the cyclic motion of the blades. Its harmonics are also observed and mentioned (see Figs. 9 and 10 of the reference). The authors also observe a noticeable "hump" in the same figures, but they argue that, since it was not reported by the turbocharger manufacturer, it can be dismissed as caused by the experimental setup. Note that this broadband noise, which could be related to *whoosh*, appeared in this case between 3 and 4.5 kHz. Interestingly, it was also present even when the compressor was running without inlet and outlet ducts (see Fig. 11 of the reference), suggesting an internal source.

Tiikoja et al. [42] revisit the topic making again a distinction between two contributing phenomena. Stationary distortions are identified as leading to periodic tones. Given an absence of inflow disturbances these tones are referred to as rotor-alone tonal noise. Fluctuating pressure fields caused by the interaction of inlet and outlet guide vanes and the rotor is regarded as a secondary source which will introduce tonal noise at harmonics of the BPF.

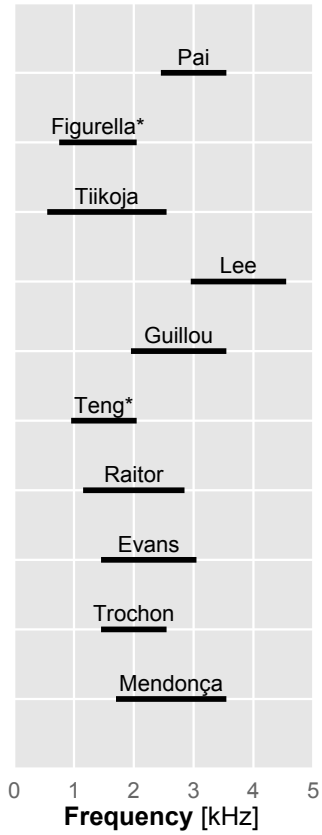

Figure 2.2: *Frequency range of lower frequency broadband noise found in selected turbocharger compressor literature, by principal author. Authors marked with * identify* whoosh *at higher frequencies, apparently conflating the issue with TCN.*

On the other hand, a "wide band noise" is ascribed to non-stationary disturbances (turbulence), but its importance for turbochargers is dismissed. Denomination of "buzz-saw noise" for the tonal phenomena is used and attributed to rotating shock waves attached to the blades whose tips reach

supersonic conditions. TCN is also named and marked as such in the results, appearing in this case between 5 and 10 kHz in the outlet and between 4 and 7.5 kHz in the inlet.

A smaller broadband is visible but not marked by the authors. This broadband is located between 0.6 and 2.5 kHz, in a way more consistent with the aforementioned reports of *whoosh* noise at these lower frequencies.

Similar results were obtained by Figurella et al. [36]. Discrete sound peaks (tones) were cited as the dominant phenomena, located at synchronous (rotor) speed and blade pass frequencies (rotor speed times number of main blades). A "broadband flow noise" is named as "*whoosh* or blow noise". Results were presented aggregating this content between 4 and 12 kHz. However, inlet sound pressure level spectra presented on Figs. 4 and 5 of the reference seem to indicate a more broadband elevation, only between 5 and 7 kHz.

This broadband content, however, seems more related to the aforementioned TCN phenomenon rather than to *whoosh*. Smaller broadbands near the synchronous frequency are shown in Fig. 5 of the reference, between 0.8 – 2 kHz, which would be more consistent with previous observations of *whoosh*. Later work by Figurella et al. [37] continued to make use of the 4 – 12 kHz band and no further individual spectra were presented. Inspection of the sound maps of the compressor presented in this work show a clear increase of noise in this band at conditions close to "marginal surge", where the gradient of isospeed lines is close to zero, suggesting again a relation with the onset of recirculating backflows.

In the work of Pai et al. [41], *whoosh* noise is mentioned only as a "broadband noise" but no specific frequency band is proposed. Again it is linked at operation near surge, for instance in transient conditions such as throttle tip-in or tip-in tip-out, but also to certain steady driving condition in petrol engines. A mechanism is proposed where acoustic radial mode resonance may be acting as amplifier for pressure perturbations in the 3 – 4 kHz band. Inspection of the spectrogram in Fig. 6 of the reference seems to suggest, however, that if an isolated noise broadband was indeed present at the proposed frequency range, it was rather located between 2.5 and 3.5 kHz, with further broadband content between 4 and 5 kHz.

In synthesis, two different kinds of phenomena are consistently identified in the literature regarding turbocharger compressors. One consists of the tonal noises linked to the rotation of the wheel. In order to work, compressor blades must maintain a pressure difference between their pressure and suction sides. This creates rotating pressure differences, being the rotation

of the blades the mechanism imposing the frequency. Harmonics of this frequency may appear, especially in transonic or supersonic conditions where shock waves attach to the blades, thus creating more rotating pressure gradients.

On the other hand, there is sufficient evidence of recurrent broadband noise at frequencies below the BPF, having been identified in the literature between 0.6 and 12 kHz. While it appears that *whoosh* noise and TCN are separate issues in terms of frequency range and location, some authors seem to conflate the two phenomena. In Fig. 2.2 some of the most clear lower frequency broadband noise identified in this literature review are represented, marking the authors that, however, identify *whoosh* at a higher frequency more typical of TCN.

As a conclusion, two different phenomena (lower frequency *whoosh* between approximately 1 – 4 kHz and so-called TCN at higher frequencies) seem to exist in turbocharger compressors. In contrast with BPF tonal noise, there is no clear mechanism proposed as being the cause of these broadband noises. As seen above, some authors vaguely ascribe these phenomena to "turbulence", others to stalled backflow interaction (including modal resonance), tip clearance effects, etc. Further research is thus needed to clarify the problem.

2.2. Numerical simulations

Given the clues about the relationship between this broadband noise and three-dimensional flow effects in and near the compressor impeller, and at the same time the difficulties of their accurate experimental characterization, it is worth considering the numerical simulation of the problem through Computational Fluid Dynamics (CFD).

The previously mentioned work by Lee et al. [34] included a CFD simulation of the compressor, matching experimentally measured operating conditions. However no agreement was found between predicted and measured noise spectra (see Figs. 17 and 18 of the reference), possibly due to reuse of only a single-revolution simulation. Karim et al. [44] successfully used experimental results to confirm a CFD prediction of *whoosh* noise diminishing, achieved by reducing length of leading edge step. However, only overall results are shown, not noise spectra.

Plausible noise spectra of turbocharger compressor were shown by Mendonça et al. [45]. By examining Fig. 7 of their work, it is possible to recognize the two aforementioned leading noise phenomena: BPF tonal

noise and its harmonics, and a broadband noise at a lower frequency (which would be consistent with *whoosh*) accompanied by another broadband at higher frequency near the BPF (which could correspond to TCN). The later one seems to shift in frequency between the inlet and outlet ducts.

In this case, the most noticeable broadband, that would be the one corresponding to *whoosh* noise, is expressed as percentage of rotation order (RO[2]), being located approximately at 0.5 to 0.9 RO (50% to 90% of shaft rotating frequency). This broadband has been included in Fig. 2.2. BPF peaks are noticeable only in the outlet ducts.

This last work appears to demonstrate that CFD simulations are indeed able to reproduce noise phenomena whose existence was experimentally assessed. However, caution should be exercised since (as shown for instance by the results of Lee [34]) it is possible to produce CFD results that accurately predict overall or averaged variables (efficiency, compression ratio, mass flow) or even overall noise levels, but whose frequency content does not match with experimental observations at all.

As a consequence, while plenty of works regarding turbocharger CFD simulation exist in the literature, only those that present plausible validation against *acoustic* experimental measurements (and not only against overall or averaged thermodynamic measurements) can be relied upon in order to extract insights about noise generation.

For instance, Hellstrom [46] presented CFD simulation results related to the experimental visualization work done by Guillou [47], where qualitative agreement is found between the predicted and measured flow structures. Of special interest when considering CFD results is data such as the isosurface of negative axial velocity shown in Fig. 10 of the reference, showing a spiral-like backflow structure that would be more difficult to identify experimentally.

However, it is also possible to consider research works that, while not specifically acoustic in nature, offer experimentally validated information about the flow field near the compressor inlet, specially if simulated operating conditions were chosen with the intention of analysing stall or surge phenomena. The work of Margot et al. [48] demonstrates how deep surge can be numerically predicted and how low pressure zones upstream of the compressor wheel lead to reversed flow in the periphery of the impeller (see Fig. 11 of the reference).

[2]Rotation order (RO) is frequency normalized by shaft speed (Hz/rotations per second) so that RO = 1 is the frequency of shaft rotation and RO of BPF is equal to the number of main blades.

Numerical analysis of this kind of flow reversion was carried out by Lang[49]. Unsteady simulations of the compressor, including the outlet duct with a throttle valve (replicating that of the experimental facility that was used for validation) were performed, decreasing valve area to reduce flow from stable to surge operating conditions. Good agreement was found between predicted and measured instantaneous pressure.

Furthermore, three different inlet geometries were simulated: a straight duct, an elbow and a reservoir. In the straight inlet case, a slight tapering of the duct is present. Even in this case, reversed flow seems to extend up to ∼2.5 inducer diameters from the wheel leading edge. Different patterns for reversed flow are attested for each geometry. Influence in surge margin is clearly demonstrated both numerically and experimentally.

Regarding the higher frequency broadband phenomenon referred to as TCN in the aforementioned works, a numerical analysis of the influence of tip clearance was performed by Galindo et al. [50] where different tip clearance ratios were simulated, resulting in no significant change in the acoustic signature. Therefore, the precise flow mechanism behind this particular phenomenon is not yet fully identified.

2.3. Local inlet flow field

Accurate characterization and modelling of the aforementioned unstable reversed flows is thus necessary to validate CFD results and evaluate the effect of corrective measures. Some indirect measurements have been made taking advantage of the temperature rise that the inlet experiences because of the high temperature of the compressed flow [36, 51]. Low frequency content and standard deviation of the pressure signals have also been used to track the onset and growth of these unstable phenomena [52].

Other tests have been performed to directly measure the flow velocity fields through different velocimetry techniques such as Laser Doppler Anemometry (LDA) [53], hot-wire anemometry (HWA) [54, 55] and Particle Imaging Velocimetry (PIV) [53, 56, 57].

The latter technique is desirable for CFD validation as it allows the measurement of whole sections of the field instead of a single point such as in the HWA and LDA techniques. Regarding the use of PIV in turbomachinery, many of the studies available in the literature have been performed on large centrifugal pumps [53, 58, 59], axial fans [54, 60] and axial compressors [56, 57, 61, 62], usually with the aim to study the evolution of the flow through the passages and the interaction with the diffuser vanes.

In the case of the works presented by Liu et al. [57] and Wernet [56, 61] an effort was also made to analyze the distribution of flow in planes perpendicular to the channel direction so that the transversal velocity field could be observed.

Even when proper centrifugal compressors were studied, attention was still put in the diffuser passages, such as in the works of Voges et al. [63], Ohuchida et al. [64] and Cukurel et al. [65]. In the three cases a small transparent window is placed in the diffuser casing to record the passage flow and interaction with the impeller wake.

The most relevant studies that instead of the diffuser considered the compressor inlet and the aforementioned backflow issue are those published by Guillou, Gancedo et al. [35, 66–68] who used a test rig where a turbocharger compressor was fitted with a bell mouth open inlet so that images of the flow could be taken directly without any barrier as the seeded ambient air was ingested. Hellström et al. [46] also used this setup to perform a comparison with numerical CFD simulations.

During these experimental campaigns measurements of the transversal velocity fields were conducted by illuminating the flow outside of the inlet with a laser sheet perpendicular to the compressor axis and close to the bell mouth. An interesting development of this approach was made in [68] where a short polycarbonate ported shroud was fitted between the bell mouth and the compressor. The laser sheet was then made to pass at different planes through this transparent shroud.

On the other hand, axial velocity fields were measured in [35, 67] by aligning the laser sheet with the compressor axis, and taking the snapshots not perpendicular to it but at an angle, as the bell mouth was not transparent. By doing this with two cameras an stereoscopic algorithm could be used to reconstruct the true axial velocity field as if the camera were indeed perpendicular to the illuminated plane.

However, it must be noted that in real world automotive applications the compressor inlet is not open in this fashion but attached to a long duct that houses the filter and flow meter. These ducts confine the reversed flow and force its reintegration into the main flow. And since has also been proved that the inlet geometry close to the compressor holds special relevance regarding onset and frequency of the deep surge instabilities [69] effort should be put into a characterization where the reversed flow is confined in he duct.

2.4. Influence of inlet geometry

Besides the aforementioned investigation of Lang [49], this influence of the inlet geometry modification immediately upstream of the compressor wheel (and thus, air presentation) on the performance and surge margin has been demonstrated on the literature, as seen for example in Galindo et al. [70], Serrano et al. [71] and Wang et al. [72].

Nonetheless, research has been focused on the improvement of surge margin and efficiency, while information about the influence of air presentation on turbocharger compressor noise is scarce, with studies often centered only in the analysis of deep surge dynamics [73, 74].

Consequently, one of the objectives of the present work is to experimentally assess this acoustical influence and analyze the features of the flow field that may be related to this acoustic emission.

This assessment must consider inlet modifications that are relevant to recent industry developments and requirements, while at the same time being simple enough to allow the establishment of general guidelines instead of conclusions limited to very specific devices.

Reviewing published works, one of the most simple modifications consists of the installation of an elbow upstream of the compressor inlet. These elbows are used sometimes to overcome packaging limitations. However, they cause pressure loss [75, 76] and flow distortion [71] that have adverse impact on compressor efficiency.

Concerning the acoustical influence, Li et al. [76] do consider the influence of the elbow over pressure spectral content at various locations. Of special interest is the analysis of BPF amplitude variation, which is attested experimentally (see Figs. 16 and 18 of the reference).

The authors concluded that some interaction between elbow-induced flow non-uniformity and the volute tongue was indeed affecting acoustic output, at least regarding tonal BPF noise, but also that more research was needed.

Other geometries of interest that have been tested in the literature are tapered ducts [49, 77] and reservoirs [49]. As mentioned earlier, Lang appreciated up to 15% improvement in surge margin optimizing reservoir volume, a figure similar to that reported by Galindo et al. [77] regarding improvement achieved by tapered ducts.

Similarly, a convergent-divergent nozzle was proposed by Desantes et al. [78], improving surge margin up to 25% at the cost of decreased maximum air flow. However, impact of these solutions on noise output was not considered.

More sophisticated options to enhance surge margin have been also proposed. For instance, a large amount of authors have researched the use of swirl generator devices placed upstream of the compressor inlet [79, 80].

The aforementioned work by Karim et al. [44] showed how a certain combination of swirl vanes could diminish overall SPL over the 6 – 12 kHz band. Furthermore, Galindo et al. [70] considered both positive and negative rotation devices, assessing their impact on surge margin and efficiency. Still, acoustic output was not taken into account.

Addition of a ported shroud has also been reported as an effective method of improving surge margin [35, 81]. In this solution, flow bleed slots are introduced on the impeller wall, connecting with the compressor inlet.

The objective of this approach is that reversed flow should recirculate through the slots as they present lower pressures due to the Venturi effect, instead of causing the usual flow disturbance by reversing across the tip clearance. At high mass flow rate these slots act as bypasses, thereby improving the choke limit.

Regarding the acoustical influence of these solutions, Chen and Yin [82] evaluated the influence of different ported shroud geometrical aspects, including the effect of splitter blades on the compressor wheel. The authors reported that full bladed compressors (as opposed of those with full and splitter blades) equipped with a ported shroud exhibited a decrease in both BPF (tonal) and overall noise.

2.5. Conclusions

After reviewing several works concerning diverse aspects of turbocharger compressor noise generation, some general conclusions can be drawn about the state of the art:

- While axial compressors have been subject to aero-acoustical studies since more than fifty years ago, noise generation in small centrifugal compressors has been comparatively more scarce.
- Several different methods for experimental acoustical characterization of turbochargers can be found in the literature. Among others, variations include instrumentation, measured variables, sensor location, etc.

- Studies consistently identify two main acoustical phenomena types: tonal noises related to a blade passing frequency (BPF) and its harmonics, and broadband noise at frequencies lower than BPF. The later kind is usually linked to stalling blades and correspondent back flows, but a clear mechanism is not yet firmly established.

- Sometimes broadband noise at higher frequencies is ascribed to tip clearance effects and referred to as TCN. Other authors refer to certain broadband humps as *whoosh* noise, more related to unstable flow in the inlet and being usually detected at lower frequencies, but other authors do not distinguish between the two.

- Computational Fluid Dynamics (CFD) simulations offer relevant insights about these stalling and recirculation issues, offering at the same time the capacity of testing different geometries to mitigate them. However, consistent and accurate prediction of measured noise spectra is still difficult to achieve.

- Characterization of the unstable flow phenomena in the compressor inducer and inlet has been performed using temperature and pressure indicators. More complete velocity field measurements using PIV are usually performed at compressors fitted with an open bell mouth, without confining the reversed flow in a straight pipe.

- Modification of compressor inlet geometry immediately upstream of the compressor wheel has a demonstrated effect on surge margin and compressor efficiency, but its influence on noise generation has been scarcely analyzed.

CHAPTER 3

Noise measurement methodology

As stated in the prior chapter, one of the main objectives of the present work has been to develop and implement robust measurement methodologies for the acoustical characterization of turbocharger compressors. In this chapter the theoretical background of these methodologies will be presented, along with the details of their practical implementation and a brief review of the facilities at where they have been implemented.

Apart from the purely experimental implementation, the step-by-step signal processing required to produce final, compiled results will be introduced as well, including sample results in order to illustrate each step. Special care will be put in considering the different theoretical and practical limitations and restrictions of experimental measurements and processing techniques, to ensure that results are significant and robust.

3.1. Facilities

Most of the experimental work presented in this thesis has been carried out at laboratory 5K of Universitat Politècnica de València. This facility is equipped with two main installations.

The first one is a flow bench powered by a Diesel engine linked to an asynchronous dynamometer and a screw compressor. This flow bench can be configured to function as a turbocharger test stand or to provide air flow to other facilities. Subsection 3.1.1 will be dedicated to an extended description of this installation.

Work on this chapter has been partly published in the following paper:

- *Experimental methodology for turbocompressor in-duct noise evaluation based on beamforming wave decomposition* [5]

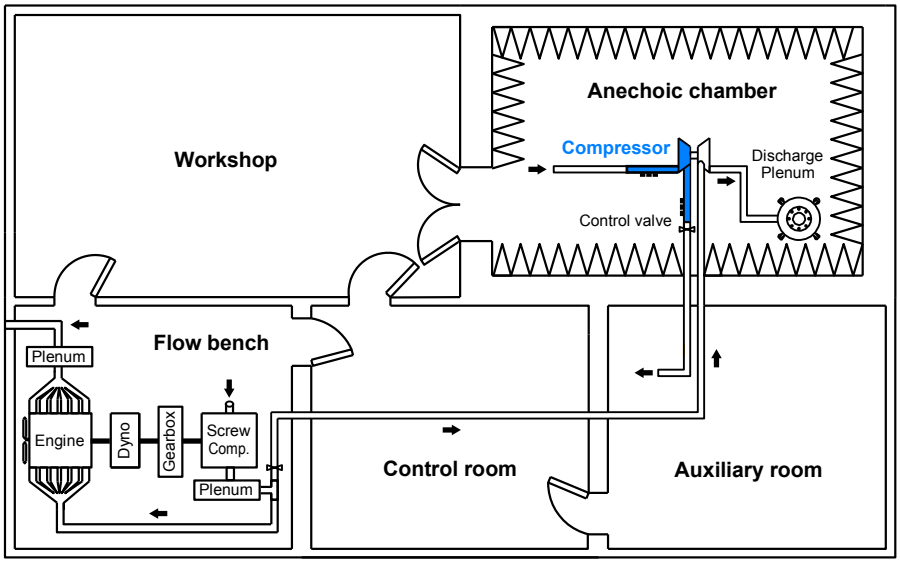

Figure 3.1: *Floor plan of lab 5K, containing a flow rig and its associated turbocharger installation inside an anechoic chamber with their auxiliary systems.*

Next to the flow bench, there is a large anechoic chamber that can be configured to either receive external air flow from the flow bench or to host a standalone engine by itself. For this project, air was provided by the flow bench when the turbocharger test stand was installed inside the chamber. This arrangement is illustrated by Fig. 3.1, while subsection 3.1.2 will describe in detail this particular chamber.

Additionally, an engine test cell located on laboratory 6D has been used for the on-engine validation tests described on chapter 5, where the inlet intake of a commercial engine was modified to measure the compressor acoustic emission. This installation is described in subsection 3.1.3.

Other relevant facilities that were used in this work include an impulse test bench that was used for piezoelectric sensor calibration, and a workshop were the required customized parts for measuring and instrumenting were manufactured.

3.1.1. Flow test rig

The flow test rig has been used as flow provider to power the turbocharger turbine both directly, with the turbocharger installed in the flow rig cell itself and, as shown in Fig. 3.1, with the turbocharger mounted in a supporting frame inside the anechoic chamber.

At the core of the rig there is a heavy duty MIDR 06.20.45 Diesel engine able to provide up to 260 kW of power. This engine is linked to an asynchronous dynamometer and, through a coupling gear, to an Atlas Copco ZA 110-3.5 volumetric screw compressor. An overview of the whole installation can be seen in Fig. 3.2. A detailed description of this facility is available in [83].

The purpose of this compressor is twofold. First, it supercharges the Diesel engine as its original turbocharger group was removed. Second, compressed flow can be routed to either a turbocharger installed in the same cell or to the adjacent chambers.

Another possibility of this test rig is to directly feed the exhaust gases of the engine to an external turbocharger. This is the reason why the original turbocharger was removed during installation. Direct flow will contain the pulsating content of the engine, allowing simulation of real engine conditions. The number of cylinders firing can be selected from 1 to 6 in

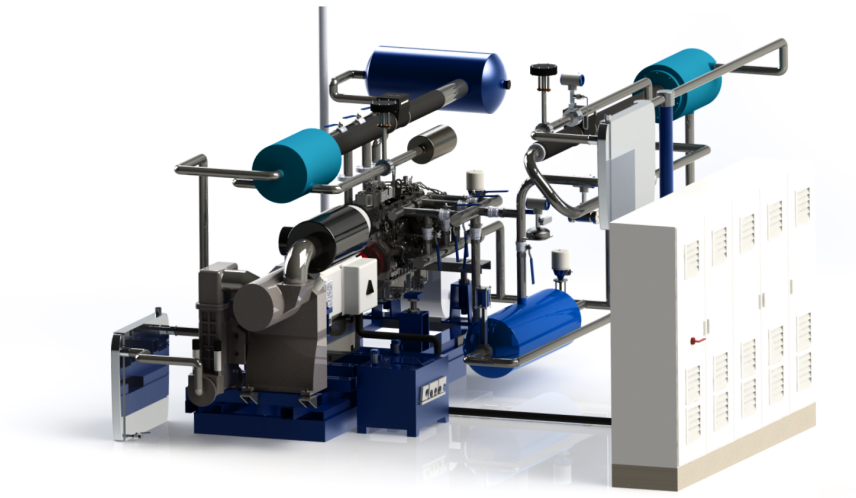

Figure 3.2: *Render of the flow rig showing the engine core, asynchronous dynamometer with its support cabinet, screw compressor and air distribution system, including control valves and reservoirs.*

order to simulate different pulsating content. Also, if the hot exhaust gas is desired but the pulsations are not, flow can be routed through a settling tank that will smooth them out, resulting in continuous flow.

For the studies carried out in this facility during the development of this thesis, pulsating flow was not selected. Continuous flow was used in both the test rig and the anechoic chamber. However, work presented in chapter 5 used real engine conditions to validate the proposed techniques and obtained results.

As for the flow control, another reservoir equipped with a discharging valve can be used to distribute the compressed air between the engine inlet manifold and the external circuit, which can be either directed to another chamber or vented to the outside ambient through a silencer.

If cold flow is desired, a water intercooler can be used to lower the temperature produced by the compression process. This temperature, along with the rest of flow properties like mass flows, pressures and other temperatures, are recorded through a dedicated control system.

Engine and dynamometer are controlled though their own independent instrumentation, while the instantaneous turbocharger variables, including those needed for acoustical characterization, are recorded through the dedicated high speed Yokogawa DL716 DAQ system.

3.1.2. Anechoic chamber

The anechoic chamber at laboratory 5K is a solid $9.5 \times 9 \times 7.2$ m reinforced concrete structure, isolated from the rest of the building and resting on a waterproof support that dampens outside vibrations.

The internal walls of the chamber are completely covered in fiberglass wedges of 0.8 m of longitude and a square base of 0.2×0.2 m. These wedges leave an interior space of $7.5 \times 6.5 \times 6$ m. Usually a further 1 m in each direction is left as an additional safety margin, the rest of the volume being equivalent to acoustic free field conditions.

Such free field conditions, where no acoustic reflection of the walls occurs, are certified in this chamber up to a cut-off frequency of 100 Hz. Low frequency waves may start to reflect below this limit.

A lightweight, acoustically-transparent, grated metallic floor is situated over the floor wedges, supporting personnel and light equipment. Four round steel pillars affixed to the concrete floor are available to support heavy loads such as engines.

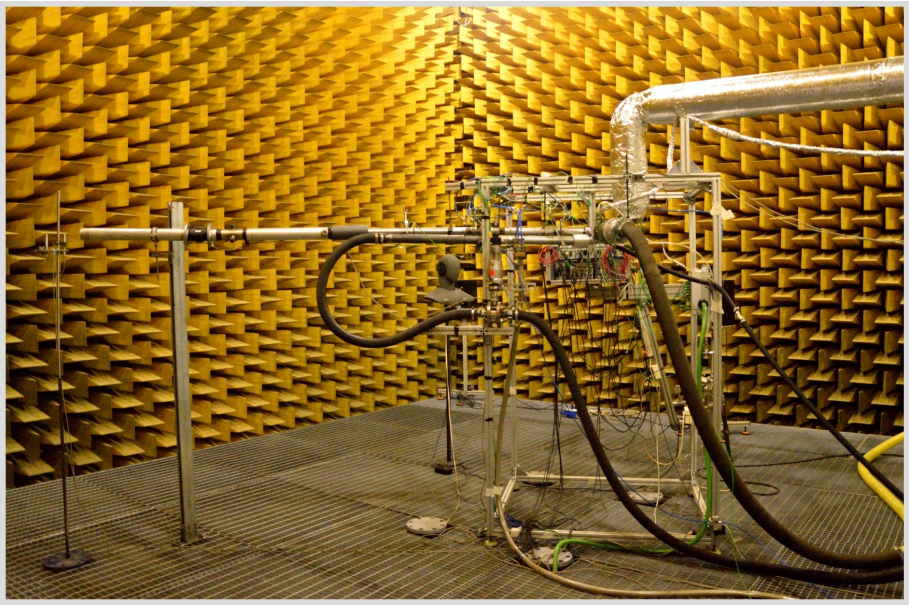

Figure 3.3: *View of the inside of the anechoic chamber, showing the turbocharger setup with the mounting frame and the pipes required to operate the installation.*

During the work described in this thesis, the load-bearing pillars were unused, since the turbocharger frame was lightweight enough to be supported by the grated floor. Figure 3.3 shows the tested turbocharger installed in this frame.

In order to allow the operation of the turbocharger, compressed air flow is fed to the turbine from the flow rig described in the prior subsection. The turbine discharges to a reservoir equipped with a conical nozzle that decreases velocity and acoustic emissions.

Meanwhile, the compressor takes ambient air from the chamber, while its exhaust is redirected to the adjacent auxiliary room for discharging, as seen in Fig 3.1. A closed-loop lubricating oil system is also present. Water is also provided to the cooling jackets of the sensors that require it, specially those located on the turbine pipes and the compressor outlet.

A control system similar to that of the flow rig monitors the operation of the system and gathers operational data (pipe temperatures, pressures, mass flow, compressor speed, etc.), allowing regulation of oil temperature, and compressor operation settings (speed and mass flow). Scientific data (mainly dynamic pressure) is recorded with a Yokogawa DL716 DAQ system.

3.1.3. Engine test cell

As mentioned early in the chapter, while most of the experimental work was carried out using the two facilities described already, the measurement methodology was later put to the test on an engine test cell to verify its reliability on real engine conditions.

The test cell, described in more detail in [69], is equipped with an asynchronous electromagnetic dynamometer that allows both steady and transient automatic testing. Operative parameters and control for the engine and dyno are integrated into a custom system, including gravimetric fuel consumption sensors, hot plate anemometers, emission measurements and temperature and pressure control of the air pipes and coolant flows.

Access and online control of the engine ECU is also available, and a special pneumatic system can be used to inject compressed air into the inlet manifold downstream of the compressor.

This air injection reduces the air that the compressor ingests, thus lowering compressor air flow and allowing the control of this relevant parameter independently of the engine necessities. The system was used to bring the compressor to surge and near-surge conditions during our research.

In order to implement and validate the in-duct acoustical measurement methodology presented in this chapter, additional sensors and equipment were fitted into the test cell, including a Yokogawa DL716 high speed DAQ system and a Brüel & Kjær PULSE^{TM} DAQ system with a type 4197 pressure-pressure sound intensity probe used as reference.

Figure 3.4: *View of the inside of the engine test cell with the engine in its default configuration, before being modified for the acoustic measurements described in chapter 5.*

3.2. Tested turbochargers

Different turbochargers have been used in the development of the investigation, as dictated by the requirements of the different projects and facilities that this thesis comprises. All of them are however similar, small to medium sized automotive turbochargers. The most relevant model is the Garrett GT17 model that was used in chapters 3, 4, 6 and section 8.1.

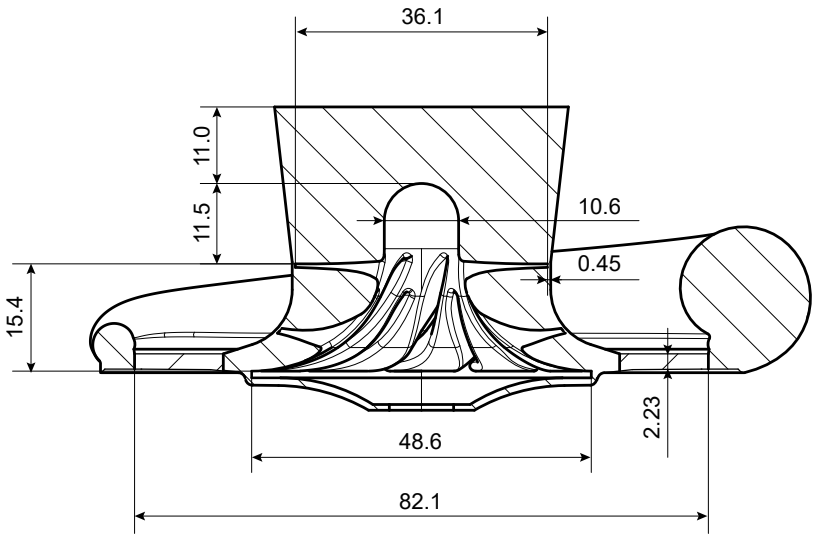

Figure 3.5: *Dimensional drawing of the compressor used in most of the development of the investigation, including some relevant dimensions.*

This particular model, featuring six main and six splitter blades, with a vaneless diffuser, was digitized to obtain its detailed geometry, which is shown in Fig. 3.5 along with its most relevant dimensions. A similar turbocharger was used for engine tests on chapter 5 and section 8.2 and another for chapter 7 and section 8.3, both of them modified in order to fit different inlet geometries.

3.3. In-duct noise measurement

In this section, a methodology is proposed to evaluate the noise emission of the compressor through its inlet and outlet pipes across selected zones of the compressor map of operating conditions. It allows a simple and clear visualization of noise phenomena and their frequency distributions at all possible operation points of the turbocharger system.

Although compressor manufacturers sometimes provide these kind of "noise maps" [38], they usually refrain from providing an adequately referenced and step-by-step methodology to reproduce them.

Reviewing the existing literature on turbocompressor noise a variety of very different measurement techniques can be found, from the two-sensor, in-duct approach of Tiikoja et al [42] to simple single-sensor pressure levels and external commercial noise-meters [36].

However, these works focus on the research of different phenomena (transmission loss [42], effect of flow incidence angle [36], sound generation by rotating stall [22], source characterization [23], etc.), not on the acoustical methodology itself nor on the particular setup considerations and restrictions that each measurement technique imposes.

In this chapter these shortcomings in existing literature are addressed by proposing a suitable experimental methodology and discussing the details of its theoretical background, its implementation, restrictions and processing required to produce useful results.

3.3.1. Theoretical background

The first step is thus to review the theoretical background of the determination of acoustic output in the specific situation of ducts with mean flow, and decide techniques to experimentally obtain the required data for their implementation.

3.3.1.1. Sound intensity in flow ducts

While it is possible [36] to rely on a single sensor to measure the scalar *sound pressure level* (SPL) of the flow at a certain location of a duct, more sophisticated approaches are needed to estimate the *sound intensity level* (SIL) that is propagating through the duct.

It is important to consider that the scalar magnitude of sound pressure level at a point can be influenced by the precise geometry of that section and by nodes and reflections that may occur in the duct, whereas sound intensity is a vectorial magnitude that remains almost constant along the duct (except for small dissipation losses), making it a more robust indicator of noise emission.

The basis of such intensity measurement methods is to consider that the pressure signal $x(t)$ measured at a given point of a duct is the linear superposition of a pressure wave x^+ travelling downstream and another pressure wave x^- travelling upstream (sometimes referred to as forward and backward waves, respectively [84]) so that:

$$x(t) = x^+(t) + x^-(t) \tag{3.3.1}$$

Comparing the pressure information at two or more spatial positions it is thus possible to infer how the waves are propagating along the duct in each direction, a possibility unavailable by means of a single sensor.

When using this wave decomposition approach, the sound intensity can be estimated following the expression proposed by Morfey [85] and successfully derived by Dokumaci [86] from physical principles:

$$I = \frac{1}{\rho a}\left(|\mathbf{X}^+|^2(1+M)^2 - |\mathbf{X}^-|^2(1-M)^2\right) \tag{3.3.2}$$

Here $\mathbf{X}^+$ and $\mathbf{X}^-$ are, respectively, the complex spectra of the downstream and upstream pressure waves, ρ is the mean density, a the mean sound speed, and M the mean Mach number of the flow.

3.3.1.2. Beamforming wave decomposition

For a more intuitive comprehension of the beamformer, one can consider its transmitting equivalent: a phased array emitter where the same signal $x(t)$, with its phase shifted by a quantity w_n^*, is fed to an n-element linear array of fixed transmitters, forming a plane wave emitted in the θ direction which can be steered at will adjusting each w_n^*. The beamforming method provides a way to mathematically tune the sensitivity of the overall system in order to isolate the downstream and upstream information of the acquired signal. A scheme for a narrowband beamformer can be found in Fig. 3.6.

The approach in this case is the inverse: by tuning the weights w_n^* that multiply each recorded pressure signal $x_n(t)$ the pressure wave coming from the direction of arrival (DOA) θ that we are interested in may be resolved. Details can be found in [87].

The extension to a wideband beamformer is relatively straightforward [88]. First the Fast Fourier Transform (FFT, denoted by $\mathscr{F}$) of the recorded pressure signals is computed:

$$\mathbf{X}_n(f_k) = \mathscr{F}\{x_n(t_k)\} \tag{3.3.3}$$

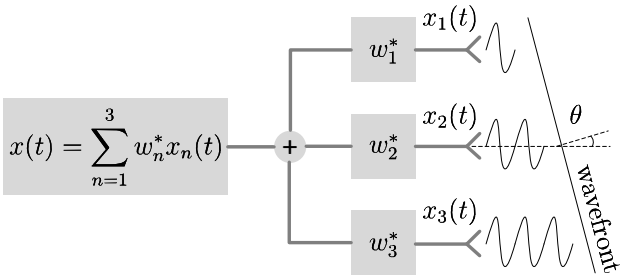

Figure 3.6: *Diagram of a narrowband beamformer with three elements tuned to a Direction of Arrival (DOA) of θ.*

Subscript k indicates that the signal is acquired at discrete time steps. The described narrowband procedure is then followed for each discrete frequency to finally obtain the desired signal through the inverse transform:

$$x(t) = \mathscr{F}^{-1}\left\{\mathbf{w}^H(f_k)\,\mathbf{X}(f_k)\right\} \tag{3.3.4}$$

Here, $\mathbf{X}(f_k)$ is the $k \times n$ matrix of transformed signals and $\mathbf{w}^H(f_k)$ is the matrix of weights for each frequency. In order to compute the optimal weights for the desired DOAs ($\theta = -90^o$ for downstream and $\theta = 90^o$ for upstream waves, assuming a typical flow DOA of $\theta = 90^o$), several schemes can be used.

For this study a Linearly Constrained Minimum Variance (LCMV) beamformer was used, a well established procedure, which aims at minimizing the overall output power (variance) of the signal, while maintaining unitary gain in the precise desired direction.

While several beamforming strategies and implementations are available, annex 3.A offers a simple guide on how to compute $\mathbf{w}^H(f_k)$ and thus $\mathbf{X}^+$ and $\mathbf{X}^-$ using this particular approach. Figure 3.7 shows the result of this decomposition in the time domain.

Further information on its application, including a comparison of various of these schemes against simulated and experimental data is available in the work of Piñero et al. [84].

3.3.2. Experimental procedure

Once that a suitable in-duct noise measurement technique was selected, it is necessary to analyze how to implement the procedure in the experimental setup, perform the measurements, and process the resulting data.

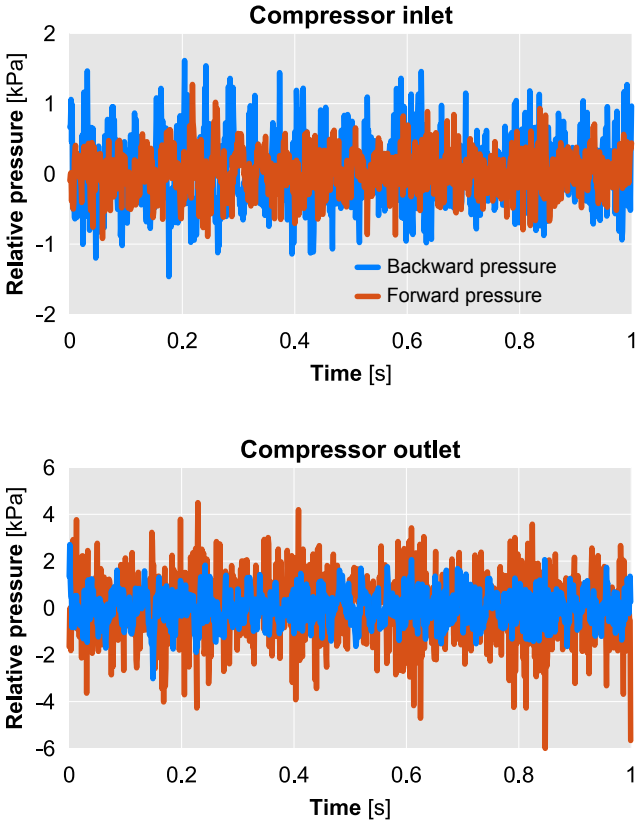

Figure 3.7: *Sample result of the decomposed pressure; at the inlet the amplitude of the pressure wave travelling forward (towards the compressor) is smaller than the one coming from the compressor; the reverse situation occurs at the outlet.*

3.3.2.1. Turbocharger instrumentation

The correct design and installation of the fast pressure sensor arrays is a critical part of the experimental setup. Ideally, the sensors should be mounted flush (with water-cooled adapters if necessary) in straight pipes, with diameters adjusted to preserve the cross sectional area of the adjacent duct in order to avoid complex structures caused by singularities. A sample of the expected pressure spectra results can be seen in Fig. 3.8.

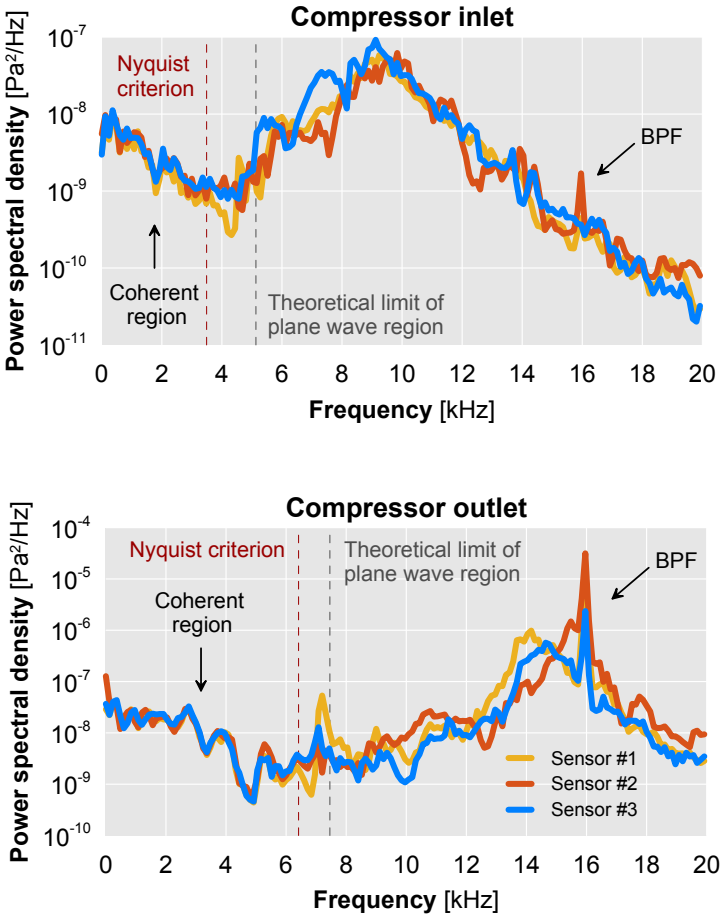

Figure 3.8: *Sample of raw inlet and outlet pressure power spectral densities (at 160 krpm and 60 g/s), including frequency limitations described in equations 3.3.6 and 3.3.7. The characteristic Blade Passing Frequency (BPF) can also be identified, specially in the outlet spectra.*

As a further measure, enough straight clearance should be left before and after the array (as shown on figure 3.9), to ensure essentially plane wave flow at the measurement section [89]. There should be a minimum of 6 diameters upstream of the array and a further 4 diameters downstream, as recommended by Torregrosa et al. [90].

When placing the transducers, it is important that the 1/5 and 1/3 nodes of the established standing wave pattern are avoided [91]. Also, a compromise in the spacing d_s between them must be reached, taking into consideration errors in the low-frequency [92] and high-frequency [93] bands.

Specially, it should be noted that spatial aliasing effects will occur above the Nyquist frequency imposed by the spacing d_s. The time of arrival of a wave with DOA θ and speed a to two consecutive sensors spaced by a distance d_s is:

$$T_d = \frac{d_s \sin\theta}{a} \tag{3.3.5}$$

This imposes a Nyquist-type frequency criterion, as the measured wave frequency f_n should be maximum half the frequency $f_d = 1/T_d$ naturally associated with T_d to ensure that no high frequency spatial aliasing effects are present:

$$f_n \leq \frac{f_d}{2} = \frac{1}{2T_d} = \frac{a}{2d_s \sin\theta} = \frac{a}{2d_s} \tag{3.3.6}$$

A further restricting phenomenon is the acoustic mode propagation. As the beamforming method proposed is based on the assumption of one-dimensional wave propagation, it will become unreliable with the onset of 3D effects.

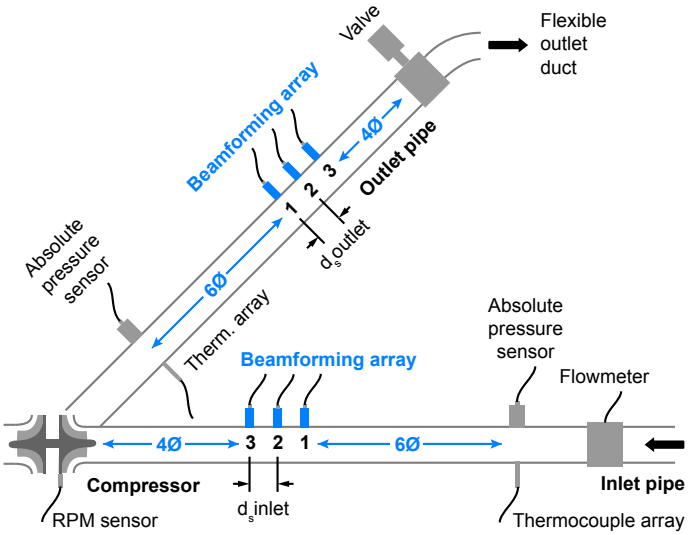

Figure 3.9: *Scheme of the proposed turbocharger instrumentation setup, highlighting in color the three-sensor beamforming arrays and their clearance requirements.*

According to Eriksson [94], it may be assumed that waves in a circular duct propagate in a planar fashion (i.e., pressure is constant in every cross-sectional area of the duct) below a cut-off frequency of:

$$f_a = 1.84 \frac{a}{\pi D} \sqrt{1 - M^2} \tag{3.3.7}$$

Here, a is the sound speed, D the duct diameter and M the mean Mach number. At higher frequencies, the so-called first asymmetric mode will start to propagate, thus rendering the assumption of one-dimensional propagation invalid. The first circular mode will in turn propagate beyond a cut-off frequency of:

$$f_c = 3.83 \frac{a}{\pi D} \sqrt{1 - M^2} \tag{3.3.8}$$

Special care should be taken when computing limiting frequencies f_n, f_a as they are not constant but dependent on the operating condition, since some of their components vary with temperature and mass flow. Figure 3.8 shows both limits for a certain operating point.

As the figure shows, the Nyquist criterion accurately pinpoints where differences between sensors start to grow, and it is clearly a more restrictive criterion than the acoustic mode onset. This limit should be properly computed for each condition when multi-sensor decomposition techniques are used.

Also, figure 3.8 shows other phenomena, for instance the Blade Passing Frequency (BPF) tonal noise that is identified in many of the works presented in chapter 2. As shown in table 2.2, the main BPF can be estimated by taking into account the shaft speed and the number of main blades:

$$\text{BPF} \sim 160\,\text{krpm} / 60 \frac{\text{s}}{\text{min}} \times 6\,\text{main blades} \sim 16\,\text{kHz} \tag{3.3.9}$$

It is also important to note that the closer the sensors are mounted together for increasing the f_n limit, the poorer the spatial resolution of low frequency waves will be, as the wavelengths $\lambda = a/f$ become too long and the difference between consecutive sensors decreases below the noise threshold. This effect is intrinsically related to each particular sensor model, but it must be considered if very low frequencies are of interest.

Finally, it is essential to ensure that the response of the three sensors of each array is coherent. Before mounting the sensors in the final linear array form, they should be mounted radially in the same section of a duct and individually calibrated, to ensure that the difference between sensors is not due to individual transducer differences, but only to wave propagation.

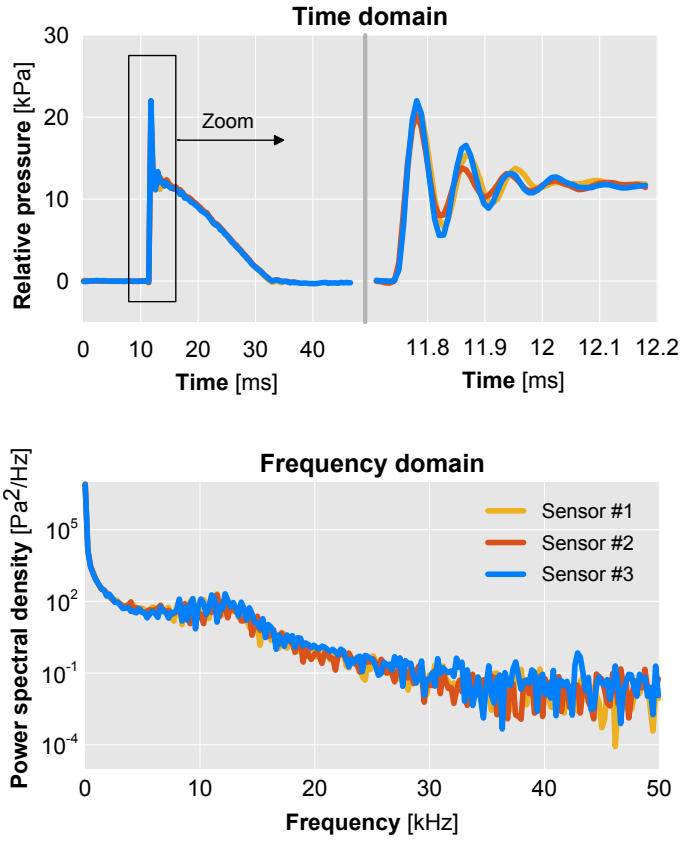

Figure 3.10: *Results of the calibration of the outlet sensors in an impulse test rig, showing a pressure measurement match in both time and frequency domains.*

In this case, the calibration is performed in an impulse test rig (described in detail in Payri et al. [95]) so as to obtain a clear reference pressure wave in all sensors. Both the time and frequency responses are observed, and both the amplifier offset and gain are adjusted to find the best match. An example can be seen on figure 3.10.

In addition to the fast pressure sensors data, more information is required to compile the compressor operating conditions map. These maps are usually presented as plots of the operation points on a total-to-total pressure ratio (Π_{TT}) versus corrected air mass flow ($\dot{m}^*$) axes.

3.3.2.2. Steady state measurements

The usual approach for measuring the operating points of the compressor map involves reducing the air flow by progressively closing the back-pressure valve (shown in figure 3.9) until the desired air mass flow is reached, while the turbine power is adjusted to preserve a given corrected compressor speed (N^*) and to achieve stable operation conditions.

Eventually the compressor blades will begin to stall, until a deep surge condition is reached, as shown in the top plot of figure 3.11. In order to avoid this destructive condition, the valve will be opened again and another constant corrected regime line will be measured, until the desired region of the compressor map is completely covered.

Several reference conditions can be selected when correcting the speed and the air mass flow; in this study the mean sea level standard day (defined as one of 15ºC of temperature and 1 atm of pressure) of the International Standard Atmosphere will be used:

$$\dot{m}^* = \dot{m}\frac{101325}{p_T}\sqrt{\frac{T_T}{288.15}} \qquad N^* = N\sqrt{\frac{288.15}{T_T}} \tag{3.3.10}$$

Here, p_T and T_T refer to the compressor inlet total pressure and temperature, respectively. These are calculated with the air mass flow and the cross sectional area of the inlet duct, using the continuity and ideal gas relations and assuming adiabatic flow:

$$\rho = \frac{p}{RT} \quad U = \frac{\dot{m}}{\rho A} \quad T_T = T + \frac{U^2}{2c_p} \quad p_T = p\left(\frac{T_T}{T}\right)^{\frac{\gamma}{\gamma-1}} \tag{3.3.11}$$

In this case R denotes the air-specific ideal gas constant and ρ, p, T and U the density, pressure, temperature and flow speed in the duct, respectively. Also, A denotes the cross sectional area, and c_p the air-specific heat capacity.

Figure 3.11 (bottom) shows the recorded data points of the compressor map, after computing the total-to-total pressure ratio and applying the standard day correction.

3.3.2.3. Surge limit characterization

When measuring a turbocharger operation map, it is particularly important to characterize accurately the surge limit, especially when an acoustic evaluation is sought out [96].

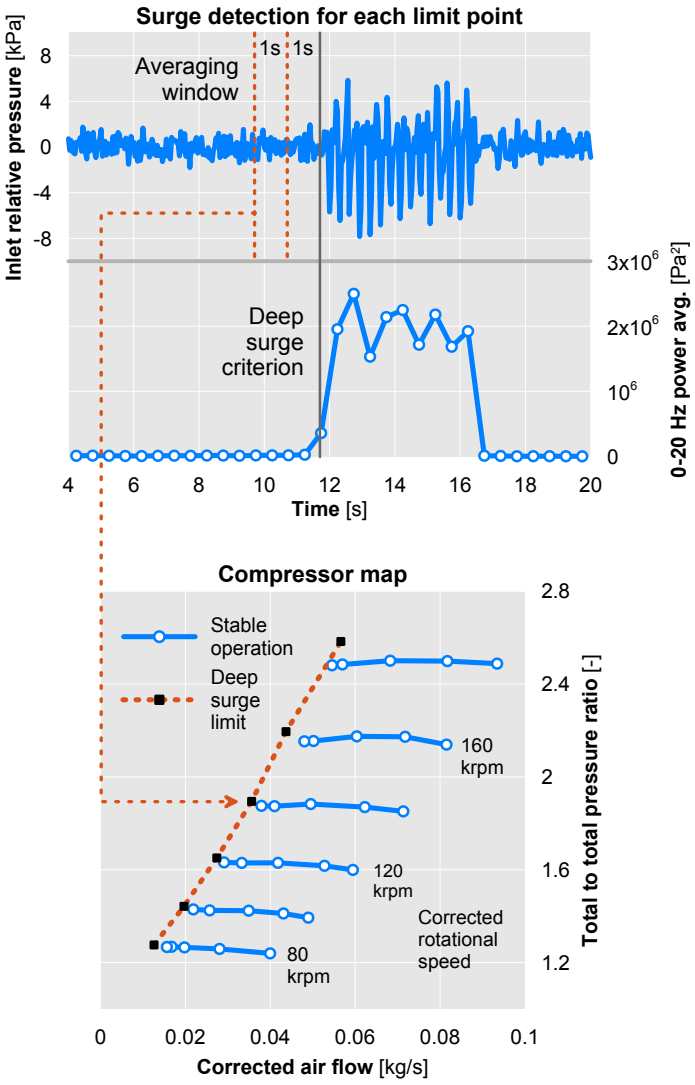

Figure 3.11: *Operating conditions for each measured data point (right plot), including the precise determination of the deep surge limit: top plot on the left shows the temporal evolution of the raw relative pressure recorded by one piezoelectric sensor; bottom plot on the left depicts the correlation between the frequency content in the 0-20 Hz band and deep surge onset.*

In order to measure different mass flows, the back-pressure valve is usually closed slowly until a certain surge criterion is met, and then opened to avoid damaging the turbocharger. Several surge criteria for centrifugal turbomachinery have been proposed in the literature, for tests on flow benches [96] and on engine test rigs [69].

An average of power spectrum of a single pressure sensor in the 0 to 20 Hz range, shown by Galindo et al [96] to be a good surge indicator, was computed once for discrete time steps k of 0.5 seconds, providing a clear indication of deep surge onset, as marked in figure 3.11 (top) with a solid line.

$$\mathbf{X}_k = |\mathscr{F}\{x(t)\}|^2,\ t \in [t_k, t_{k+1}] \tag{3.3.12}$$

To obtain the required near-surge data points to be displayed on the map, represented by small squares (▪) in the bottom plot of figure 3.11, a 1 second average of all recorded data was computed 1 second before surge as indicated by the dashed lines of the left plot, in order to calculate the map coordinates of the point.

3.3.2.4. Signal postprocessing: maps and spectrograms

In addition to the intensity spectra determined for each operating point, further results can be obtained by applying an interpolation procedure to the spectra associated with all the points tested.

For instance, it is possible to calculate the overall level of sound intensity for a given frequency range at each operating point i of the compressor operating map. The sound intensity level at a characteristic band (between f_1 and f_2) can be calculated for each point as:

$$L_i = 10\log_{10}\left(10^{12}\sum_{f=f_1}^{f_2} I(f)\right) \tag{3.3.13}$$

Once that several L_i levels have been measured for different conditions of a selected map region, a cubic spline interpolation function $\Phi_{f_1-f_2}$ is used to project the data onto a much more fine and regularly spaced grid, allowing the representation of a map of noise intensity across the measured region of the compressor map, as shown in figure 3.12.

These “noise maps” synthesize the information of the acoustic output of a frequency band of interest in a simple and visual result, allowing an easy estimation of the noise emission through desired operating conditions even if these have not been specifically measured.

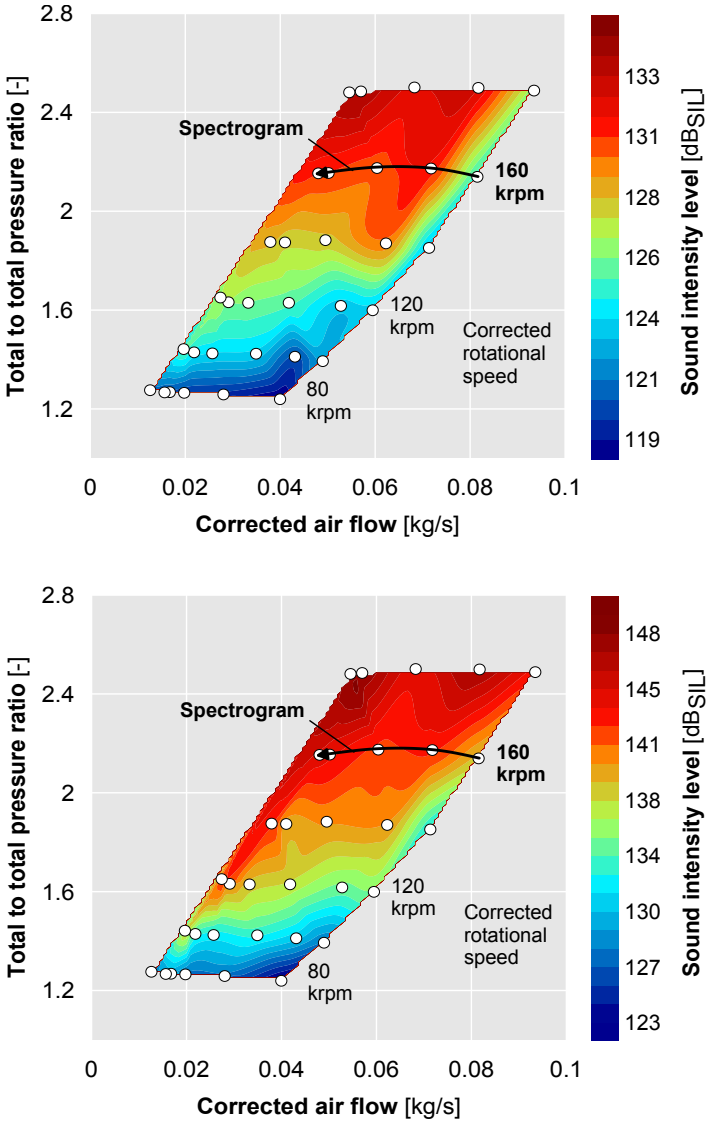

Figure 3.12: *Sample of noise level in the 1 – 3 kHz band obtained through the processing described in subsection 3.3.2.4, including the measured data points (∘) and the paths later expanded as spectrograms shown in figure 3.13. The top map represents the inlet duct, whereas the bottom map represents the outlet duct.*

Expanding on the necessity of analysing the frequency content evolution as the operating conditions of the compressor change, a different approach can be used, where the measured discrete information can be compiled to estimate a continuous spectrogram.

This is accomplished by sequentially performing the previous map processing for a number N of much smaller frequency bands of width Δf, resulting in a collection of N interpolation functions $\Phi_{f_j - f_{j+1}}$, where $f_{j+1} - f_j = \Delta f$.

Using these functions, the intensity levels $\mathbf{L}$ on each small frequency band k are interpolated for a set of M pairs of the compressor map coordinates, such that:

$$\mathbf{L}_j = \Phi_{f_j - f_{j+1}}(\dot{\boldsymbol{m}}^*, \boldsymbol{\Pi}_{\mathrm{TT}}) \tag{3.3.14}$$

An estimation of the spectrogram $\mathbf{S}$ that would be obtained in a quasi-stationary measurement by following the set of operation conditions $(\dot{\boldsymbol{m}}^*, \boldsymbol{\Pi}_{\mathrm{TT}})$ pairs can then be compiled gathering the levels $\mathbf{L}_j$. Choosing one coordinate of the set of pairs (in this case $\dot{m}^*$) as reference for the X axis:

$$\mathbf{S}(f_j, \dot{m}^*) = \begin{bmatrix} \mathbf{L}_1(\dot{m}_1^*) & \dots & \mathbf{L}_1(\dot{m}_M^*) \\ \vdots & \ddots & \vdots \\ \mathbf{L}_N(\dot{m}_1^*) & \dots & \mathbf{L}_N(\dot{m}_M^*) \end{bmatrix} \tag{3.3.15}$$

Thus the sound intensity level value $\mathbf{S}$ for each $\dot{m}^*$ and each frequency band j can be plotted. An example of this processing for frequencies between 50 and 5000 Hz binned with $\Delta f = 50$ Hz is presented on figure 3.13, where coordinates $(\dot{\boldsymbol{m}}^*, \boldsymbol{\Pi}_{\mathrm{TT}})$ correspond to the 160 krpm iso-speed line highlighted in Fig. 3.12.

3.3.3. Preliminary results

In order to illustrate the presented methodology along this section, experimental data was obtained by performing a measurement of the selected turbocharger in the flow bench that is used to provide flow to the anechoic chamber, configured as shown in figure 3.9. Since in this case the only concern was the validation of the in-duct methodology, installation in the anechoic chamber was not required.

Kistler type 7031 piezoelectric transducers were used for the inlet duct; the outlet duct was fit with type 6031 transducers due to available stock. An array spacing $d_s = 32$ mm for the outlet and $d_s = 50$ mm for the inlet

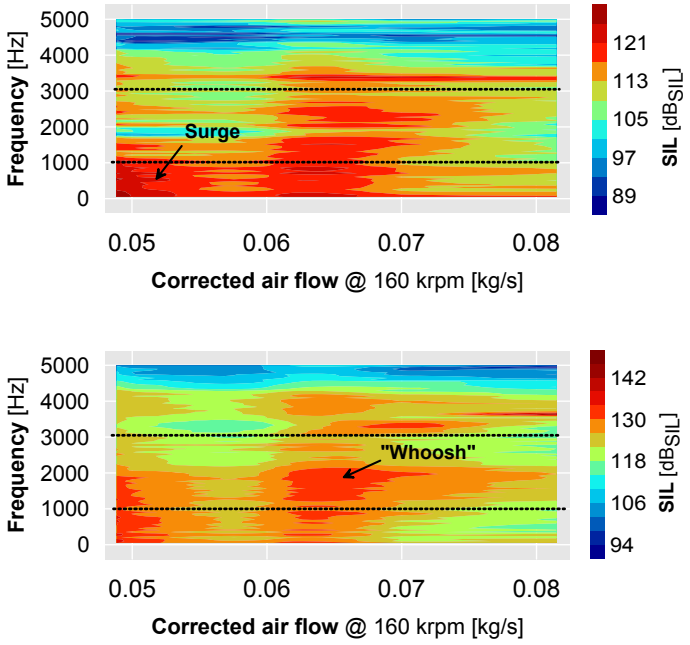

Figure 3.13: *Sample of spectrograms (top: inlet; bottom: outlet) calculated using the procedure outlined in subsection 3.3.2.4, following the 160 krpm paths marked in figure 3.12. The 1 – 3 kHz band selected for the maps in figure 3.12 is highlighted, along with some particular flow phenomena discussed in section 3.3.3.*

was selected, allowing for a safe upper limit in terms of the spatial Nyquist criterion f_n of ∼6 and ∼3.5 kHz respectively (precise values depend on the conditions of each point).

The variables needed in order to characterize the operating condition (mass flow, speed, temperatures and pressures) were averaged during 30 seconds using the in-house DAQ system, while the six piezoelectric sensors acquired 10^5 pressure samples during 1 second using the Yokogawa DAQ system. This acquisition settings were kept for the rest of the work.

Pressure signals on recorded points (shown in figure 3.11) were then processed according to the proposed methodology. Samples of the final results are presented in figures 3.12 and 3.13.

Figure 3.12 shows the 1 – 3 kHz sound intensity level distribution across selected operating conditions, approximately between maximum efficiency and the measured surge limit. As shown in chapter 2, noise in this frequency is often known as *whoosh*.

Another point of concern that has been identified in the results is that the relevance of this particular phenomenon extends far from the surge region and well into the expected engine operation region.

Looking at either the 160 krpm line on figure 3.12 or at the expanded spectrograms of this line in figure 3.13 where this band has been marked, there is a local maximum in this band between 60 and 70 g/s. For the 180 krpm points on the map of figure 3.12, the *whoosh* noise may be heard even for up to 80 g/s mass flow rate.

Apart from *whoosh*, both spectrograms show a clear rise in low frequency content when the mass flow is reduced and surge conditions start to appear, even if deep surge conditions have not yet been reached. This is consistent with spectrograms measured experimentally by Galindo et al [97] and indicates that the methodology proposed in this section provides results that are consistent with previous literature. These results will be expanded upon in the following chapter.

3.4. External noise measurements

While the accurate characterization of the internal sound field is crucial to understand the different phenomena, the transmission of the noise to the ambient is also relevant as external acoustic radiation is ultimately the main concern of the automotive industry.

To that extent, different external measurements have been carried out as part of the experimental campaign. Noise data has been captured in the orifice of the compressor inlet, around the far field of the turbocharger, and along the radiating surfaces near field.

This section will describe how these measurement were made, while results and discussion will be presented in section 4.2 of chapter 4, including a correlation of orifice noise and in-duct results and the discussion on the contribution to the overall noise produced by each part of the system.

Also included is a brief description of an acoustic particle velocity measurement procedure that was tested during the development of this thesis and could be of interest for the characterization of near-field sound emission

even in non-anechoic test cells. A sample of the results that this method can achieve will be shown in chapter 5, which deals with measurements in these conditions.

3.4.1. Orifice noise

The noise emitted by the open end of the compressor inlet duct is of special concern, as it is the point where the internal sound field meets the exterior ambient. Furthermore, the compressor may not act as the only source of noise in this case, as the noise produced by the flow interaction with the duct orifice during the aspiration process can be relevant as well.

However, when measuring external noise care should be taken to avoid reflections and perturbations that may interfere with the results. This is why it was decided to install the turbocharger inside the anechoic chamber, so that free-field conditions could be recreated and external noise measurements could be taken and compared against in-duct results.

In this chamber, instrumentation consisted of two 1/2" Brüel & Kjær type 4190 free-field microphones, fitted with type 2669C pre-amplifiers and placed next to the compressor inlet orifice, separated 10 cm and 20 cm, respectively. These are shown as "Mic 1" and "Mic 2" in Fig. 3.14.

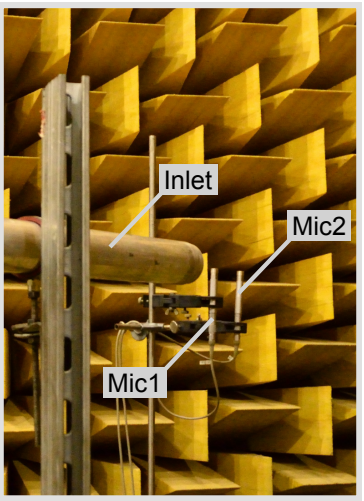

Figure 3.14: *Image of the two free-field microphones placed at 10 mm (Mic 1) and 20 mm (Mic 2) from the orifice of the compressor inlet duct.*

These microphones were calibrated before the measurements with a Brüel & Kjær type 4228 pistonphone. Both the calibration and the data acquisition were performed with a Brüel & Kjær PULSE system.

As the conditions inside the anechoic chamber can be regarded as being equivalent to those of an acoustic free field, we can estimate the magnitude of the sound intensity at each microphone i as:

$$|I_i| = \frac{p^2_{\mathrm{rms,i}}}{\rho c} \tag{3.4.1}$$

Here, $p^2_{\mathrm{rms,i}}$ is the root mean squared pressure recorded by microphone i, ρ is the ambient density and c the ambient sound speed. These are calculated from pressure and temperature sensors available in the anechoic chamber.

3.4.2. Far field

Taking advantage of the free-field conditions of the chamber, additional microphones were installed around the turbocharger group to estimate the far field sound radiation, in a manner similar of the setup used by Teng and Homco for measurements of the whole [16] engine.

To obtain a better estimation of the sound field, four free-field microphones of the same type 4190 were distributed around the the central point of the installation, at a radial distance of 1 m from it, as Fig. 3.15 shows.

Data from all microphones was captured using a Brüel & Kjær PULSE^{TM} DAQ system, composed by types 3560D, 7536, 2826 and 2 × 3032A (hardware) and types 7700, 7702, 7705 and 7755 B (software). In order to provide a global metric to compare against orifice noise, results for the four far-field microphones were averaged to compute the overall sound pressure level radiated by the turbocharger system.

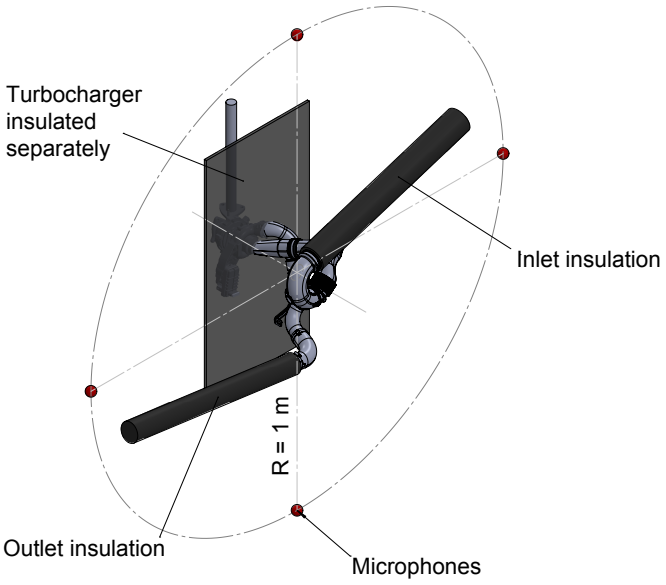

Figure 3.15: *Radiated noise microphones installed around the turbocharger, featuring a commercial set of compressor inlet and outlet pipes that will be sequentially insulated for evaluating the contribution of each part.*

3.4.3. Near field

While useful to characterize the far field sound information emitted by the turbocharger, successful measurement through free-field microphones depend on the acoustic characteristics of the test ambient being suitable. As standard turbocharger test rigs and engine test cells are usually not acoustically conditioned, reflections and interferences make measurements of external noise difficult.

These issues increase when the objective is to analyze the acoustic field near the tested turbochargers, as near-field measurements can be adversely impacted by diffuse background noise and reactive sound fields [98, 99].

A technique that could be useful in order to address these issues is the direct measurement of acoustic particle velocity level (PVL). A probe featuring a MEMS sensor[1] enabling these kind of measurements in air has been made commercially available by Microflown [100].

This probe has been used to perform acoustic intensity measurements, demonstrating some advantages against pressure-based probes [101]. Applications include acoustic holography for near-field situations [102] and panel-based noise evaluation in automotive cabins [103]. In chapter 5 one of these probes will be used to perform a test in a standard engine cell in order to assess its usefulness in identifying the near-field acoustic signature generated by the turbocharger.

3.5. Conclusions

In this chapter a detailed experimental methodology for the noise evaluation of turbocharger compressors in flow benches or engine test cells has been proposed. It includes a description of the kind of turbochargers tested in this thesis and the facilities where the experimental work has been developed.

The characterization method is based on a robust in-duct acoustical beamforming technique that resolves the plane wave range sound intensity, by decomposing the total pressure signal into its upstream and downstream components.

[1] MEMS refers in general to Micro Electro-Mechanical Systems, in this particular case consisting of two thin parallel used as micro hot-wire anemometers.

In addition to resolving intensity, another advantage of the wave decomposition technique is the possibility of isolating the pressure data coming from the compressor, in order to enhance the spectral content of interest in situations where actual anechoic setups are not feasible, due to valves, filters, and other elements.

This isolated pressure information is also useful to validate or initialize CFD simulations where the model boundary conditions have to be defined as anechoic because simulating accessories (valves, flexible ducts, etc.) is not worthy or desirable. Such a validation methodology was presented in [1] and is discussed in chapter 6 of this work.

When used to evaluate the acoustic intensity of the noise generated by the compressor, the proposed signal processing allows to easily understand visual representations in the form of noise maps of selected frequency bands of interest and estimated spectrograms of operating paths. This can provide guidelines for the evaluation of strategies to counter or avoid certain adverse noise phenomena.

The examples presented above illustrate how this technique allows detecting known acoustical phenomena of a centrifugal compressor, such as medium frequency *whoosh* noise and low frequency surge onset, as well as mapping its distribution and relevance across different operating conditions of the turbocharger.

In addition to offering the detailed measurement and signal processing steps, this chapter stresses the importance of taking into account restrictive factors such as calibration, sensor setup clearances and locations, frequency aliasing effects and ranges in which theoretical assumptions hold in order to obtain robust and reproducible results.

Additionally, and taking advantage of the anechoic chamber where the turbocharger was installed, instrumentation added to measure external noise (both orifice noise and the noise radiated to the far field by the system surfaces) is described. Finally, the application of an acoustic particle velocity probe to measure the near-field emission of a turbocharger in engine conditions is proposed.

3.A. Appendix: LCMV beamforming procedure

This appendix to chapter 3 shows a short step by step guide to compute the desired $\mathbf{X}^+$ and $\mathbf{X}^-$ decomposed spectra required in equation 3.3.2, using a LCMV (Linearly Restricted Minimum Covariance) strategy as presented by Verdú [104]. Recall that decomposed signals for each frequency f_k are obtained by weighting the transformed measurement matrix $\mathbf{X}(f_k) = [X_1 X_2 X_3] = \mathscr{F}\{[x_1 x_2 x_3]\}$ as follows:

$$\begin{aligned} \mathbf{X}^+(f_k) &= \mathbf{w}^{+H}\mathbf{X}(f_k) \\ \mathbf{X}^-(f_k) &= \mathbf{w}^{-H}\mathbf{X}(f_k) \end{aligned} \tag{3.A.1}$$

It can be shown that the corresponding weights for filtering the forward and backward signals are obtained for each frequency f_k by:

$$\begin{aligned} \mathbf{w}^+ &= \mathbf{g}^+\left[\Sigma_x^{-1}\,\mathbf{A}^H(\Theta)\left[\mathbf{A}^H(\Theta)\,\Sigma_x^{-1}\,\mathbf{A}^H(\Theta)\right]^{-1}\right] \\ \mathbf{w}^- &= \mathbf{g}^-\left[\Sigma_x^{-1}\mathbf{A}^H(\Theta)\left[\mathbf{A}^H(\Theta)\,\Sigma_x^{-1}\,\mathbf{A}^H(\Theta)\right]^{-1}\right] \end{aligned} \tag{3.A.2}$$

Where $g^+ = [1\ 0]^T$ and $g^- = [0\ 1]^T$ are the desired response vectors (unitary gain in one direction and zero gain in the opposite). Σ_x denotes the covariance matrix. For certain discrete frequencies f_k it can be reduced to:

$$\Sigma_x(f_k) = [\mathbf{X}(f_k)\,\mathbf{X}^H(f_k)] \tag{3.A.3}$$

The constraints matrix $\mathbf{A}(\Theta) = [\mathbf{a}^+(\theta)\,\mathbf{a}^-(\theta)]^T$ contains the beamformer response array (signal lags) in both directions:

$$\begin{aligned} \mathbf{a}^+(\theta) &= \mathbf{a}(-90°) = \left[1, \exp(j\beta^+ d_s), \exp(j\beta^+ 2d_s)\right]^T \\ \mathbf{a}^-(\theta) &= \mathbf{a}(90°) = \left[1, \exp(-j\beta^- d_s), \exp(-j\beta^- 2d_s)\right]^T \end{aligned} \tag{3.A.4}$$

Here d_s is the distance between sensors and $\beta^\pm$ are complex wave numbers corrected for attenuation and mean flow:

$$\beta^+ = \frac{k + \alpha(1-j)}{1+M} \quad \text{and} \quad \beta^- = \frac{k + \alpha(1-j)}{1-M} \tag{3.A.5}$$

M represents the Mach number, $k = \omega/c$ the acoustic wave number and α the viscothermal attenuation coefficient, which can be computed as:

$$\alpha = \frac{1}{r\,a}\left(\frac{\nu\,\omega}{2}\right)^{1/2}\left[1 - (\gamma - 1)Pr^{-0.5}\right] \tag{3.A.6}$$

Duct radius is denoted here by r, a is the speed of sound, ν the cinematic viscosity, $\omega = 2\pi f_k$ the angular frequency and Pr is the Prandtl number.

CHAPTER 4

Noise measurements

This chapter is devoted to the results of applying the described acoustic measurement methodology to the selected turbocharger compressor. A first section of the chapter will deal with in-duct results, regarding both the full spectrum of the turbocharger noise output and the plane wave frequency range, the later being analyzed in detail with the help of the wave decomposition technique described in the previous chapter.

Externally radiated noise produced by the turbocharger group will also be discussed, results comprising both inlet orifice noise and the acoustic radiation around the system generated by the turbocharger itself and its inlet and outlet ducts. Additionally, a correlation will be obtained between the internal and orifice noise levels, that could be useful to estimate these external noise levels without the need to test the system in a large anechoic environment.

4.1. Internal noise field

The first part of the experimental campaign consisted of gathering sufficient acoustic data across several operating conditions of the compressor, in order to compute not only the acoustic signature in the most typical operating points but also how this signature varied at different conditions.

Data for this in-duct noise analysis was recorded using the previously described piezoelectric sensor arrays in both inlet and outlet ducts. This data was then processed in the form of pressure and sound intensity and

Work on this chapter has been partly published in the following paper:

- *Simulations and measurements of automotive turbocharger compressor* whoosh *noise* [2]

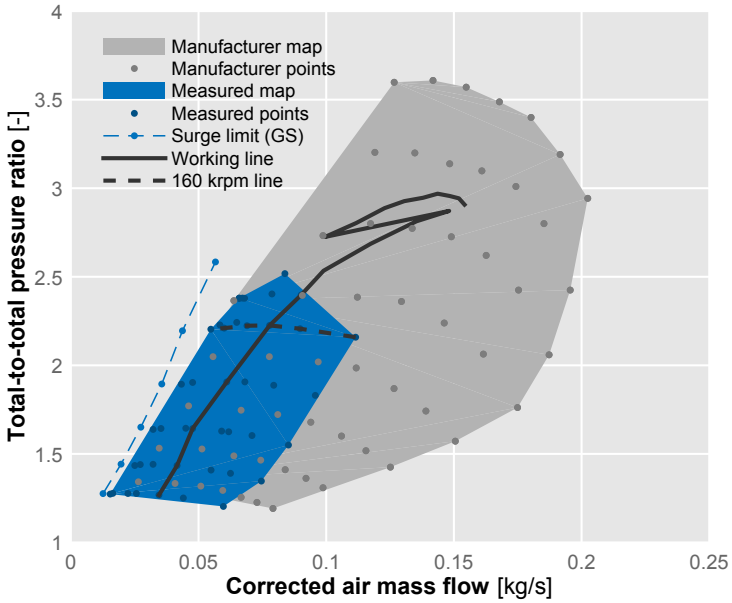

Figure 4.1: *Comparison of the compressor map provided by the manufacturer and the critical operating points measured in the experimental campaign, including the deep surge limit measured in the gas stand, the approximate working line with the target engine and the 160 krpm speed line.*

pressure spectra, noise maps, and spectrograms to show different aspects of the turbocharger acoustic behaviour and its evolution across different operating conditions.

These operating conditions at which measurements were performed were selected taking into account the full compressor map provided by the manufacturer and the approximate working line[1] of the engine operating points in real-life conditions and the capabilities of the compressor test bench.

Regarding air mass flow, conditions were measured from approximately the maximum efficiency point to a limit slightly beyond the conservative deep surge line indicated by the manufacturer. Pressure ratios were measured up to the maximum capability of the available screw compressor to provide continuous flow.

[1]Note that at shaft speeds grater than 190 krpm a second turbocharger is activated in this engine, creating a shift in the working line noticeable in the range between 2.5 and 3 pressure ratio.

The two limits conform a measurement subset of the compressor map depicted in Fig. 4.1 in color. This subset encompasses the working line up to a shaft speed of 170 krpm. In addition, the deep surge limit was measured in a separate gas stand to locate more accurately the true limit.

These surge measurements were performed with a tapered duct in the compressor inlet line to match the gas stand pipe diameter, which has an influence on the surge margin. Although, these tests confirmed that the manufacturer margin was close enough to the deep surge measured according to the methodology of low frequency content increase described in chapter 3.

As it can be seen in Fig. 4.1 for most of the measured shaft speed lines the last data point (the one with less air mass flow) was situated approximately in between the conservative limit established by the manufacturer and the limit experimentally measurable in the gas stand.

This allowed the comparison between optimum compressor operating points situated at near the maximum thermodynamic efficiency conditions and the most critical conditions near deep surge, passing through the unstable mild surge (or marginal surge) region between the two extremes.

4.1.1. Spectral content

Inlet and outlet pressure spectra were measured at each one of the selected points, allowing a comparison in terms of frequency content of the pressure signals and distribution of acoustic intensity across the measured compressor map. In this subsection results will be divided between plane wave frequency range, where the wave decomposition algorithm based on beamforming can be applied to the array signals to compute the forward and backward waves, and the higher frequencies where acoustic modes are present and thus the decomposition cannot be performed.

To provide a better insight on how the spectral content of the pressure signals changes across the different operating conditions two subsets of the measured map have been highlighted.

The first of these subsets is a constant shaft speed line at 160 krpm where the air mass flow is progressively reduced from approximately highest efficiency. This will allow the analysis of how the spectral content changes with mass flow from relatively stable conditions to unstable ones.

A second subset forms a distribution of data points following the working line of the real engine which is depicted in Fig. 4.1. Since this line is situated at an approximately constant distance from the surge limit it allows to track the evolution of spectral content given by the change in shaft speed while keeping similarly mild surge operating conditions.

4.1.1.1. Plane wave range

Though dependent on pipe diameter, flow temperature and velocity, typical automotive turbocharger compressor setups can maintain plane wave conditions up to 5 – 7 kHz [38]. It is specially relevant because it comprises the frequencies of relevant acoustic phenomena such as *whoosh* noise, tonal noise induced by BPF harmonics, deep surge, etc.

From the research point of view, this frequency range is interesting because considering the pressure change constant along each pipe section allows for easier analytical and numerical modelling.

Working in this range allows the use of wave decomposition procedures to isolate the contributions coming forward or backward through the compressor inlet and outlet pipes. These decomposed pressure waves can also be used together to compute the acoustic intensity through the duct.

From chapter 3 it can be recalled that in a circular duct with mean flow, the cut-off frequency at which the plane wave assumption cannot be considered to be valid any longer is given by equation 3.3.7. At higher frequencies, the first asymmetric acoustic mode starts propagating.

In the case of the pipes considered in this study, evaluation of this expression led to cut-off frequencies of approximately 4.7 kHz for the inlet duct and 7.4 kHz in the case of the outlet duct, due to differences in flow conditions and pipe diameter. Also, it must be taken into account that this limit varied slightly because of changes in velocity and temperature at different operating conditions.

The spatial Nyquist-like criterion related to the separation of the sensors of the decomposition array described by equation 3.3.6 was more restrictive than the first asymmetric mode limit, leading to maximum cut-off frequencies for plane wave propagation of 3.4 kHz for the inlet and 6.4 kHz for the outlet. This limit is marked as a dashed line in the following figures.

In Fig. 4.2 the Power Spectral Density (PSD, referenced to 20 μPa as in the case of SPL) of the raw pressure signals captured by one piezoelectric sensor of each array is shown. For both inlet and outlet ducts, spectra are plotted at different shaft speeds along the working line depicted in Fig. 4.1. It can be seen in this figure how, generally, spectra on the plane wave range

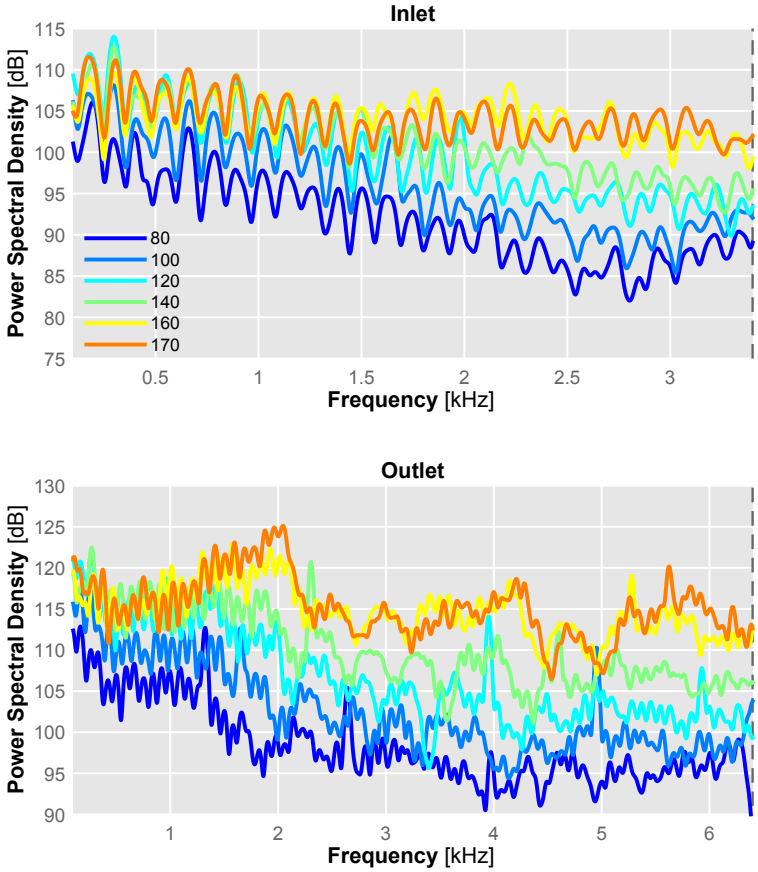

Figure 4.2: *Comparison of pressure spectra along the working line plotted in Fig. 4.1 in the plane wave frequency range, for both inlet (top) and outlet (bottom) ducts. Legend shows the different shaft speeds in krpm.*

feature higher levels at lower frequencies. Higher speed points in the outlet feature a distinctive broadband between 1 and 2.5 kHz, described as *whoosh* noise in the literature.

In Fig. 4.3 the same procedure has been carried out for the 160 krpm shaft speed line marked with a dashed line in Fig. 4.1, in order to evaluate the evolution of spectral content as air mass flow is reduced through the mild surge conditions. In the outlet where the *whoosh* phenomenon can be seen between 1 kHz or less and up to 3 kHz with greater clarity. Again, spectral content below approximately 3 kHz appear more "jagged" that at higher frequencies.

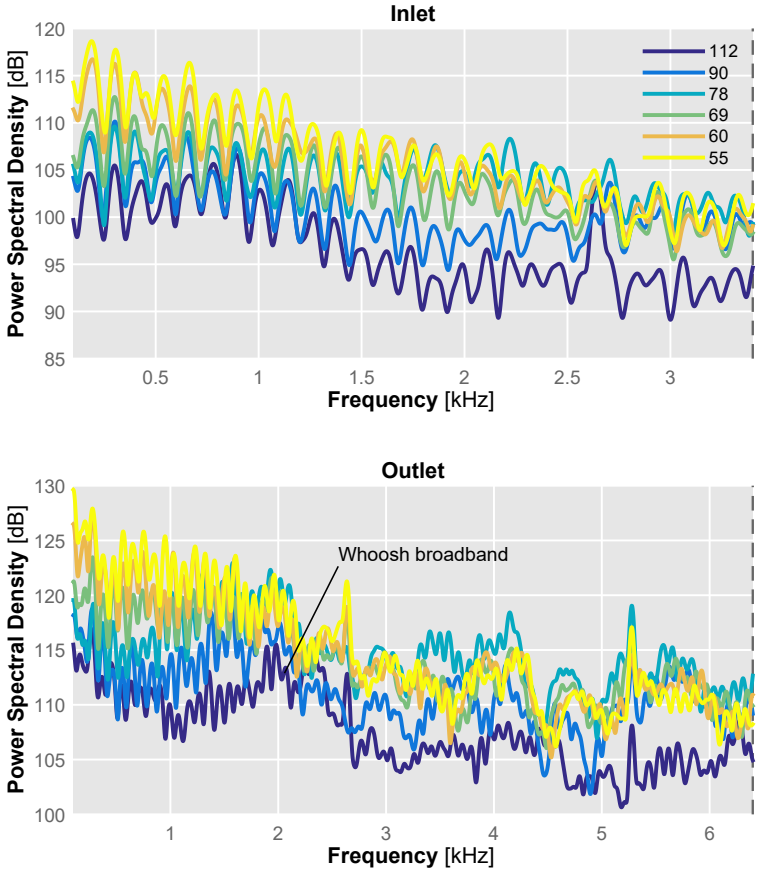

Figure 4.3: *Comparison of pressure spectra along the 160 krpm speed line plotted in Fig. 4.1 in the plane wave frequency range, for both inlet (top) and outlet (bottom) ducts. Legend shows the different mass flow rates in g/s.*

It is also apparent, specially examining the spectra at 60 g/s and 55 g/s that the broadband is not so apparent at the lowest flow conditions not because it decreases in level but because of the increase in the surrounding frequency content that matches the broadband level, thereby masking it.

Moreover, it should be remarked that this broadband phenomena at typical *whoosh* noise frequencies can be identified even at the operating point with higher air mass flow, which is located near the maximum efficiency region of the compressor map; a zone which is presumed to be stable.

4.1.1.2. Decomposed pressure waves

In order to better isolate the spectral content coming from the compressor from the reflections and interferences of the upstream and downstream ducting and components, the wave decomposition algorithm based on LCMV beamforming presented in chapter 3 was applied to the aforementioned pressure data recorded by the three-sensor arrays while following the working line and 160 krpm line operating conditions.

The differences in spectral content between the decomposed pressure waves and the reconstructed total pressure signal can be seen in Fig. 4.4 where the three are plotted for two opposite operating conditions: higher flow at lower speed and lower flow at higher speed.

It can be seen how, as previously mentioned, the decomposed signal coming from the compressor (backward wave in the inlet, forward wave in the outlet) are almost coincident with the total pressure spectra along the plane wave range, smoothing out the buzz-saw noise at the lower frequencies.

In contrast, the opposite-travelling wave presents lower amplitudes, specially between 1 and 3 kHz in the high speed, lower flow plot where there is a difference of approximately 10 dB between 2 and 3 kHz.

Fig. 4.5 shows the PSD of this decomposed pressure signal. In the case of the top plot that contains the information from the inlet duct, PSD from the backward travelling wave is presented, since it is the one coming from

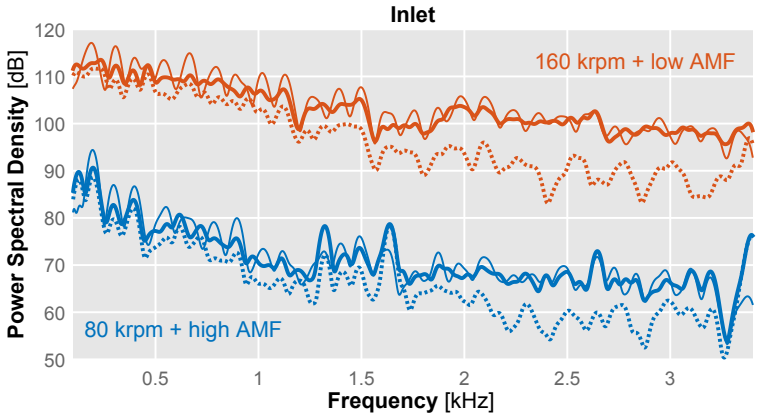

Figure 4.4: *Comparison of total (solid, thin line) and decomposed pressure spectra (coming from the compressor in solid thick line, going towards the compressor in dotted line) for two extreme points: 80 krpm and highest mass flow and 160 krpm and lower mass flow.*

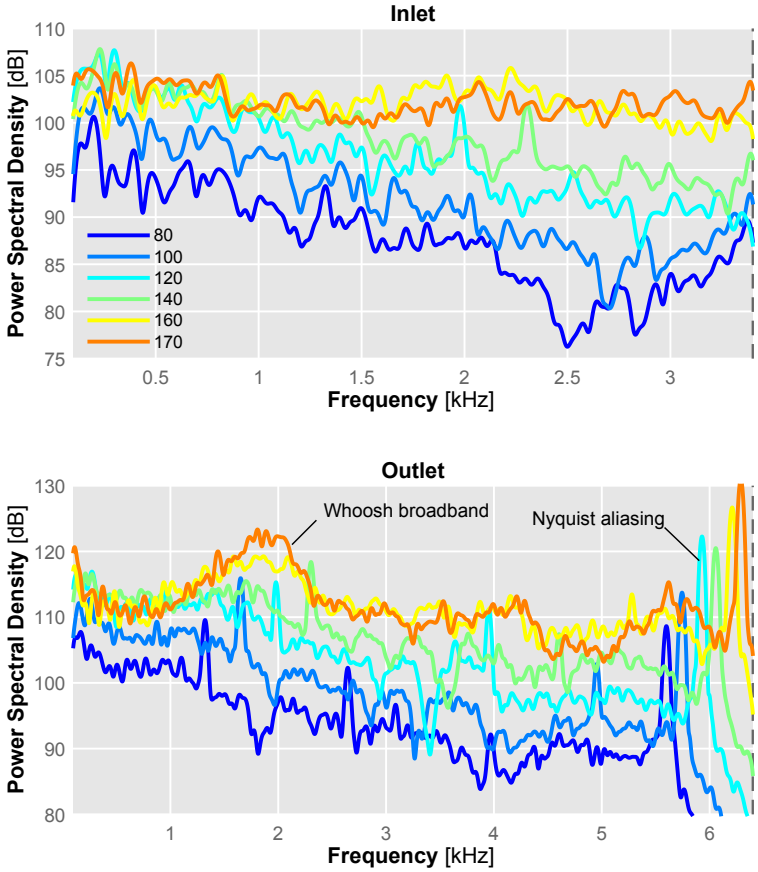

Figure 4.5: *Comparison of decomposed pressure spectra along the working line plotted in Fig. 4.1 for both the inlet duct (top plot, backwards travelling waves) and outlet duct (bottom plot, forwards travelling waves).*

the compressor. Conversely, the forward travelling wave PSD is plotted in the case of the bottom plot depicting outlet duct data. Note the spurious aliasing peaks as the spatial Nyquist limit is reached for each condition.

It can thus be seen in Fig. 4.5 that the decomposition algorithm allows a clearer representation of the signal, since it is not affected by the buzz-saw effect at lower frequencies (lower than 3 kHz), specially visible in the inlet spectra (see also Fig. 4.4 for a comparison).

A similar result can be seen in Fig. 4.6, where the decomposed pressure waves are plotted for the data points in the 160 krpm, from higher to lower air mass flows. It shows a clear identification of the *whoosh* broadband

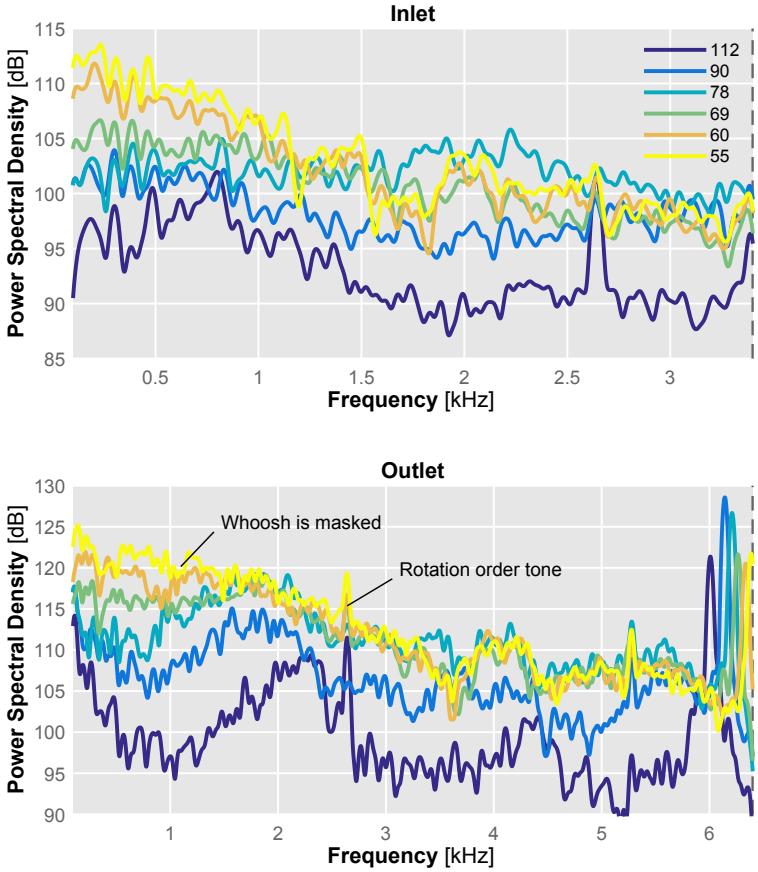

Figure 4.6: *Comparison of decomposed pressure spectra along the 160 krpm speed line plotted in Fig. 4.1 for both the inlet duct (top plot, backwards travelling waves) and outlet duct (bottom plot, forwards travelling waves).*

phenomenon between 1 kHz and 3 kHz and how it becomes masked by the rise in lower and higher content as air mass flow diminishes. A rotation order tone at 160 krpm/60 s = 2.66 kHz is also noticeable in both ducts.

4.1.1.3. Higher frequencies

Beyond the previously mentioned cut-off frequencies, the propagation of acoustic modes invalidates the plane wave assumption that it is made in the wave decomposition process, thereby rendering this treatment unusable. It is however interesting to consider at least the raw pressure PSD as it contains relevant acoustic content.

In Fig. 4.7 the PSD of the pressure signals recorded by one sensor of the array is presented, for both inlet and outlet ducts. It can be seen how, in the case of the inlet pressure spectra, amplitude increases with shaft speed along the whole frequency range. Inlet spectra also feature a broadband elevation that starts at 12 kHz and collapses with plane wave propagation at 5 kHz, which could be related to the TCN mentioned in the literature as described in chapter 2.

Characteristic Blade Passing Frequency (BPF) peaks associated with each shaft speed are also visible in the inlet spectra, although only for some speeds such as 160 krpm or 170 krpm.

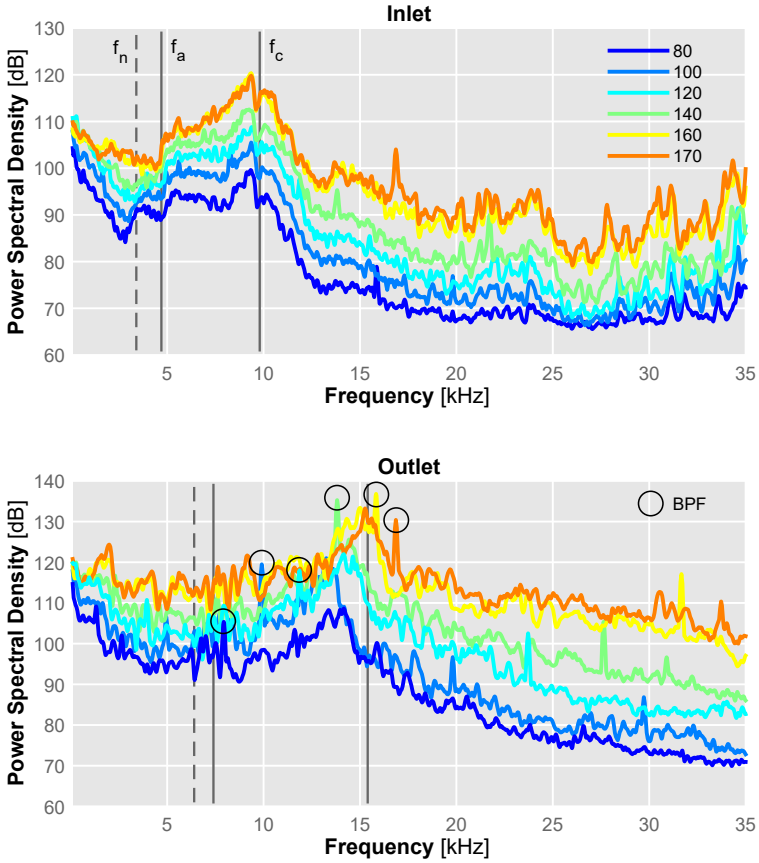

Figure 4.7: *Comparison of pressure spectra along the working line plotted in Fig. 4.1 up to 35 kHz, for both inlet (top) and outlet (bottom) ducts. Cut-off frequencies at 160 krpm for the spatial Nyquist criterion f_n, 1st asymmetric (f_a) and 1st circular (f_c) acoustic modes are also plotted as reference.*

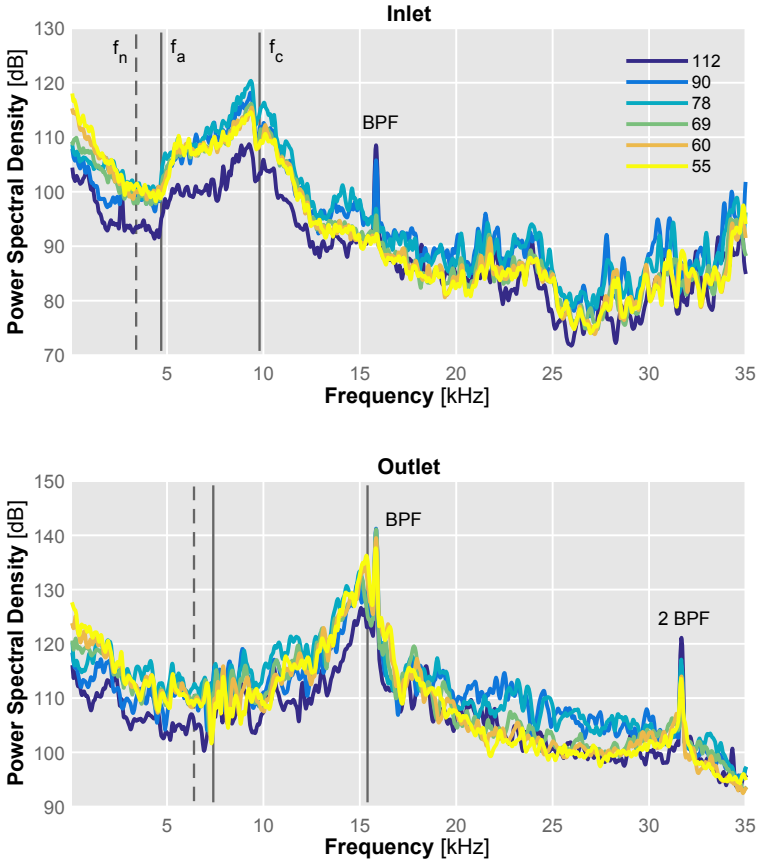

Figure 4.8: *Comparison of pressure spectra along the 160 krpm speed line plotted in Fig. 4.1 up to 35 kHz, for both inlet (top) and outlet (bottom) ducts. Cut-off frequencies for the spatial Nyquist criterion f_n, 1^{st} asymmetric (f_a) and 1^{st} circular (f_c) acoustic modes are also plotted as reference.*

Evolution of the spectral content in the outlet pressure signal shows also the previously discussed increase at plane wave frequencies, followed by a broadband at higher frequencies which again could be related to the so-called TCN. BPF peaks including some harmonics are visible in the outlet spectra, even for conditions where they were not apparent in the inlet spectra.

Similar evolution can be observed in Fig. 4.8 which tracks the spectral content of the raw pressure signal along the 160 krpm shaft speed line. Again, BPF peaks are much more visible in the outlet spectra. The plane wave broadband between is also noticeable in the outlet, along with other higher frequency broadbands after the first mode cut-off frequency.

4.1.2. Non-dimensional analysis

Further insight into the spectral content of the signal can be obtained through the use of non-dimensional analysis in order to identify the possible sources or mechanisms behind certain features of the spectra, as done by numerous authors such as Choi [24, 25], Mongeau [22, 23], Wolfram [26, 27] and Carolus [28] regarding specially the development of similarity laws for centrifugal pumps and fans [105].

In this way, non-dimensional power spectral density of the pressure signal $S(f)$ can be written [22, 24] as being the product of two functions:

$$\frac{\sqrt{S(f)}}{\rho V_{\text{tip}}^2 \sqrt{D_o/V_{\text{tip}}}} = G(He, \varphi) \cdot F(St, \varphi) \tag{4.1.1}$$

On the left hand side, ρ is the mean density of the flow, D_o is the outer diameter of the rotor and V_{tip} is the velocity of the blade tips. On the right hand side, $G(He, \varphi)$ is an acoustic frequency response function that depends on the Helmholtz number and comprises the influence of propagation effects such as duct resonances and directivity [22, 27].

The source spectral distribution $F(St, \varphi)$ depends on the Strouhal number and comprises the phenomena related to flow-induced acoustic generation such as flow fluctuations and near field acoustic interactions [23].

Both functions depend of the operating conditions of the system, as remarked by their dependence on the flow coefficient φ (flow rate divided by diameter, blade width and tip speed). They are however assumed to be independent of Re (Reynolds number). Definitions of the non-dimensional parameters can be found in table 4.1.

Two Strouhal numbers have been considered: one is related to the tip speed V_{tip} and is adjusted so that the blade passing frequency (BPF) has $St = 1$. The other takes into account the mean flow velocity U. Finally, the Helmholtz number takes into account the speed of sound a that is affected by temperature at each operating condition. All three are normalized with the outer diameter D_o of the rotor.

In Fig. 4.9 the non-dimensional spectra as computed in the left hand side of equation 4.1.1 as a function of the non-dimensional number has been plotted for the outlet duct, whose acoustic features appear more clear. Different mass flow rates are considered while shaft speed was kept constant at 160 krpm.

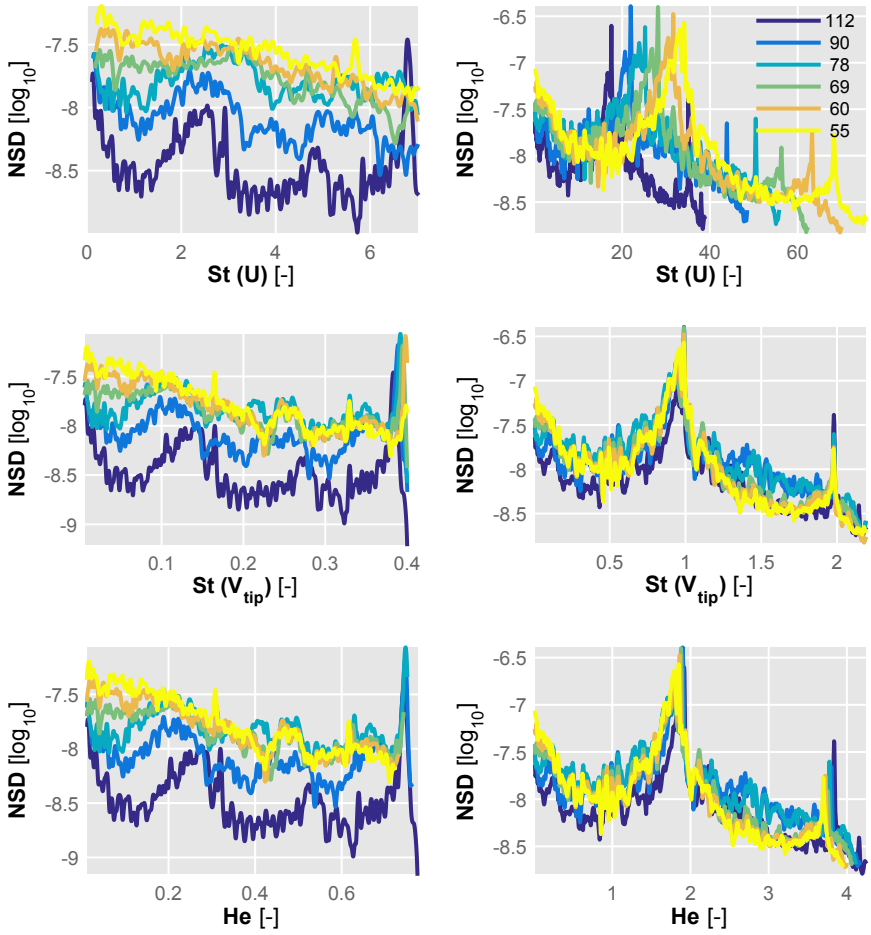

Figure 4.9: *Relationship of decomposed non-dimensional spectral density (NSD) in the plane wave range (left) and higher frequency spectra (right) with selected non-dimensional numbers for the different operating conditions of the 160 krpm speed line (outlet duct).*

It can be seen in Fig. 4.9 how when the spectra Strouhal number that takes into account the mean flow velocity $St(U)$ is used to normalize the spectra, the *whoosh* hump appears to align between 1 and 3. Broadband features at higher frequencies (right plots) however do not align.

However, when the Strouhal number takes into account the blade passing frequency these high frequency features appear more aligned, specially the tonal noise at the BPF and its harmonic at $St(V_{\text{tip}}) = 1$ and 2.

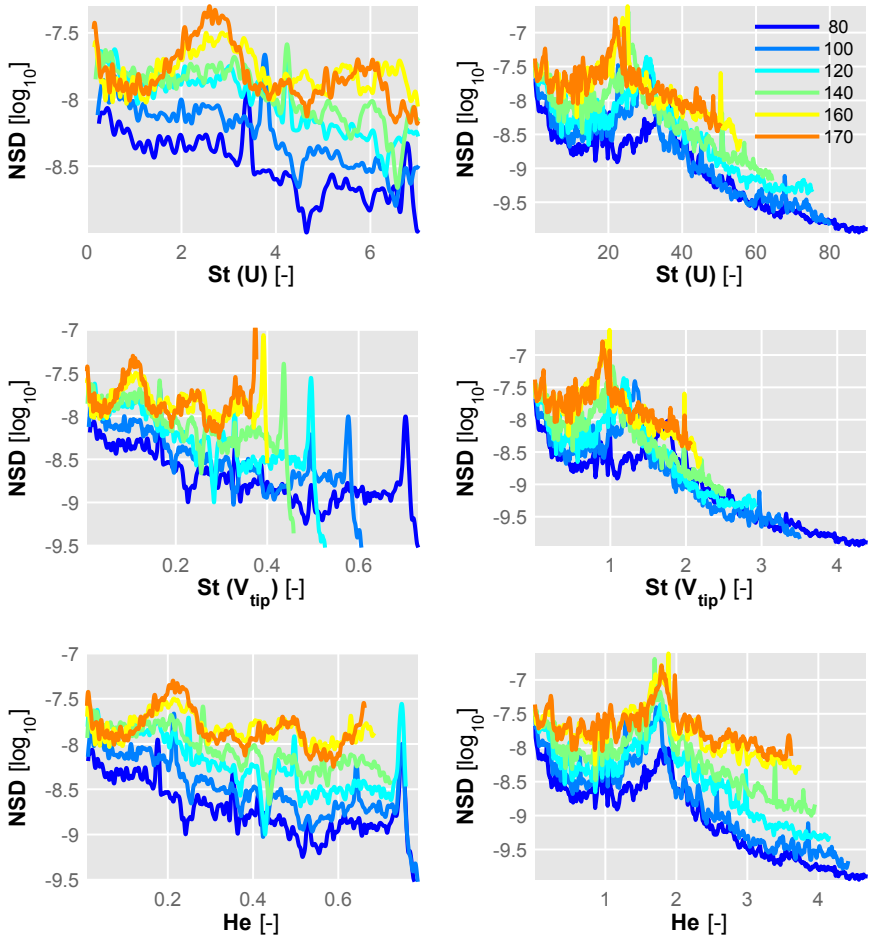

Figure 4.10: *Relationship of decomposed non-dimensional spectral density (NSD) in the plane wave range (left) and higher frequency spectra (right) with selected non-dimensional numbers for the different operating conditions of the engine working line (outlet duct).*

Helmholtz normalization appears to be quite similar, with the difference that in this case the BPF tones are not aligned. By inspecting the decomposed spectra on the left however, it can be seen that the spurious peak that limits the range of valid beamforming decomposition become aligned, as the spatial Nyquist criterion depends on the speed of sound.

Table 4.1: *Symbols and definitions of the three non-dimensional numbers considered in the analysis of acoustic spectra.*

Name	Symbol	Definition
Strouhal (tip speed)	$St(V_{\text{tip}})$	$\frac{f D_o}{V_{\text{tip}}} \frac{\pi}{N} = \frac{f}{BPF}$
Strouhal (mean flow)	$St(U)$	$\frac{f D_o}{U}$
Helmholtz	He	$\frac{f D_o}{a}$

In Fig. 4.10 a similar analysis is carried out considering the spectral information along the working line instead of along a fixed shaft speed. In this case the the results are similar, although in this case the Strouhal normalization that takes into account the tip velocity is more meaningful, as different shaft speeds are considered.

Again, the broadband hump in the plane wave range that is typically identified with *whoosh* appears to collapse when considering the mean flow Strouhal, albeit in this figure tracking of this effect is more complicated due to the simultaneous change in both shaft speed and mass flow rate.

In the case of the non-decomposed spectral information, it can be seen how the higher frequency TCN-like broadband is now only collapsing when the Helmholtz normalization is performed, whereas for both Strouhal normalizations clear differences can be seen between lower and higher shaft speeds. This could point to this broadband frequency being highly influenced by the speed of sound rather than by the flow mechanisms.

4.1.3. Interpolation

As described in section 3.3.2.4, the information contained in the discrete data points measured in this experimental campaign can be used to interpolate the results across the selected relevant section of the compressor map. This allows a clearer understanding into how the noise content varies across the different operating conditions of air mass flow and shaft speed.

4.1.3.1. Noise maps

In order to paint a general picture of the global sound emission of the compressor across the selected operating range, in-duct sound intensity has been computed through equation 3.3.2 for the described data points, and then overall level between frequencies of interest has been interpolated.

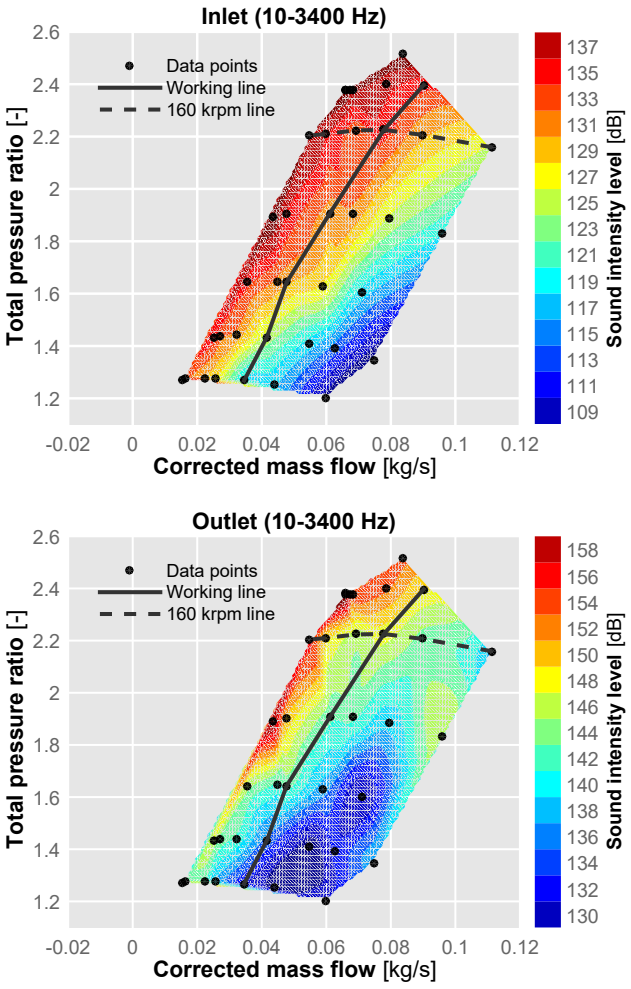

Figure 4.11: *In-duct Sound Intensity Level maps for inlet (top) and outlet (bottom) ducts between 10 and 3400 Hz, obtained through the interpolation procedure.*

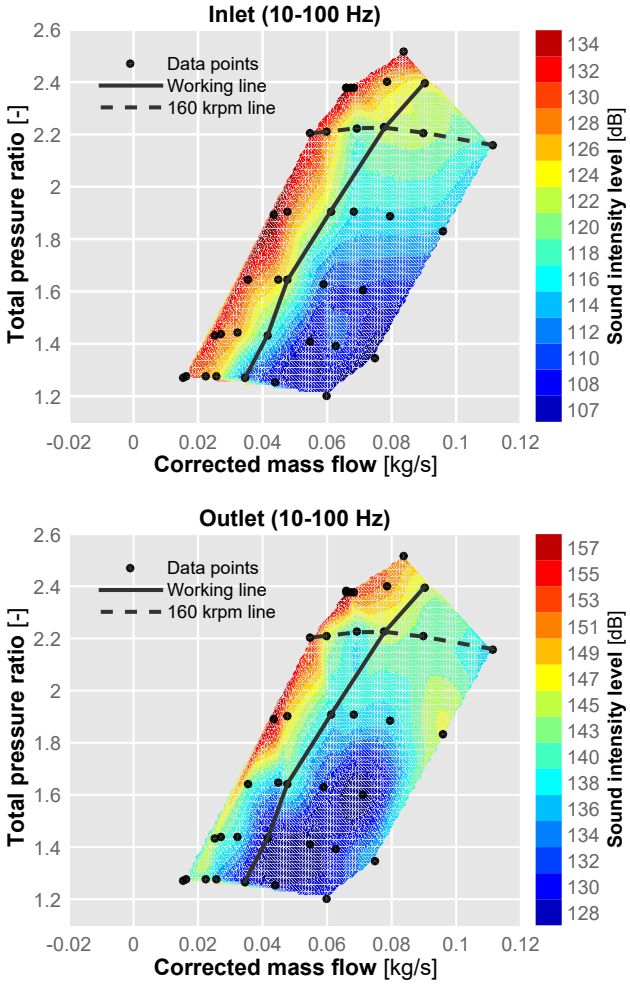

Figure 4.12: *In-duct Sound Intensity Level maps for inlet (top) and outlet (bottom) ducts between 10 and 100 Hz, obtained through the interpolation procedure.*

For instance, Fig. 4.11 shows global in-duct Sound Intensity Level (SIL) contours for both inlet and outlet in the frequency range where the plane wave assumption holds true for both ducts ($f < 3.4$ kHz).

It can be seen that, as previously observed when analysing the pressure spectra, sound intensity levels are generally higher in the outlet duct than in the inlet duct as pressure fluctuations are amplified.

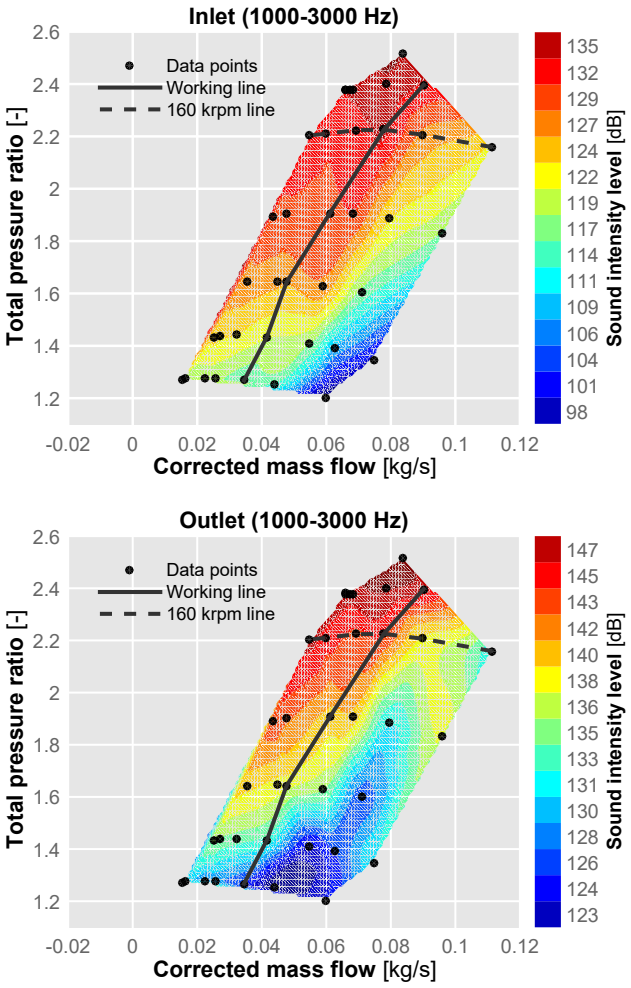

Figure 4.13: *In-duct Sound Intensity Level maps for inlet (top) and outlet (bottom) ducts between 1000 and 3000 Hz, obtained through the interpolation procedure.*

Distribution of SIL across the different conditions of the compressor map holds some similarities between both ducts, with SIL increasing towards the surge limit and with higher shaft speeds. However, the outlet seems to feature an abrupt increase in levels at the lower allowable air mass flow conditions, whereas the increase in the case of the inlet appears smoother.

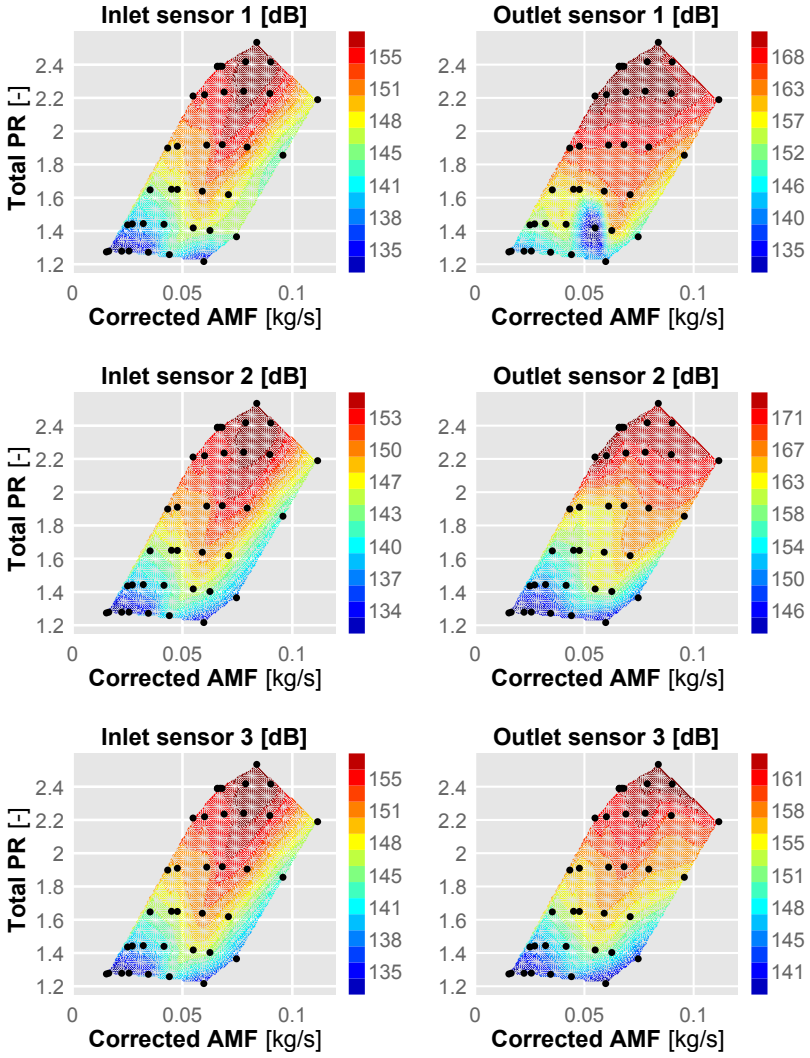

Figure 4.14: *In-duct Sound Pressure Level maps for the inlet (left) and outlet (right) ducts between 5 and 21 kHz, obtained through the interpolation procedure and considering the three sensors of each array.*

In order to provide a better insight into how frequency content is distributed across the compressor map, Fig. 4.12 shows sound intensity levels at very low frequency, between 10 and 100 Hz.

Comparing Fig. 4.12 with 4.11 it can be observed how, in the case of the inlet in-duct intensity, very low frequency content increase is parallel to the surge limit line, thus making the slope of the contours different in the two figures.

On the other hand, outlet intensity distribution is very similar between the two figures, highlighting the importance of the contribution of the low frequency content to the whole plane wave range.

In order to analyze the distribution of *whoosh* noise which, albeit still in the plane wave range, does not comprise so low frequency content, maps for intensity between 1 and 3 kHz have been plotted in Fig. 4.13.

Differences in the outlet in-duct SIL between this range and those shown previously in Figs 4.12 and 4.11 are noticeable. The slope of the SIL contours has changed, showing that the increase in this frequency band is more gradual with shaft speed, whereas in the two previous figures it rose abruptly for the 160 krpm line marked in the plots with dashes.

Finally, data from higher frequencies (above plane wave range) has been plotted in Fig. 4.14, showing the differences between the pressure levels recorded by each one of the three sensors of the arrays. This data shows a different pattern in the inlet duct: while still increasing with shaft speed, highest levels are located at medium mass flow settings, not at the lower ones.

As for the outlet, there are again differences when comparing against previously shown distributions in the plane wave range. In this higher frequency case, while content increases again with shaft speed, the point at which the maximum is located varies with mass flow rate.

It can also be seen that in the case of the outlet, there are more differences between the spectral content recorded by each of the sensors of the array that in the case of the inlet where differences are much more difficult to appreciate. This is probably due the flow presentation being much more uniform in the inlet as it is coming from the ambient, while in the case of the outlet it is leaving the compressor with all its associated flow phenomena such as increased swirl.

Furthermore, apart from the different distribution, it can be shown in the data from sensor 1 of the outlet that there was an operating conditions were a spurious low content is recorded, probably due a node affecting the sensors. This highlights the risk of using SPL to characterize compressor in-duct noise levels and the advantages of relying into sound intensity instead.

4.1.3.2. Spectrograms

Beside noise maps, an alternative way of analysing the spectral content across different conditions consists of processing the interpolated data to reconstruct spectrograms along lines of interest; in this case the working line and the 160 krpm lines have been selected as in the previously presented spectral content discussion.

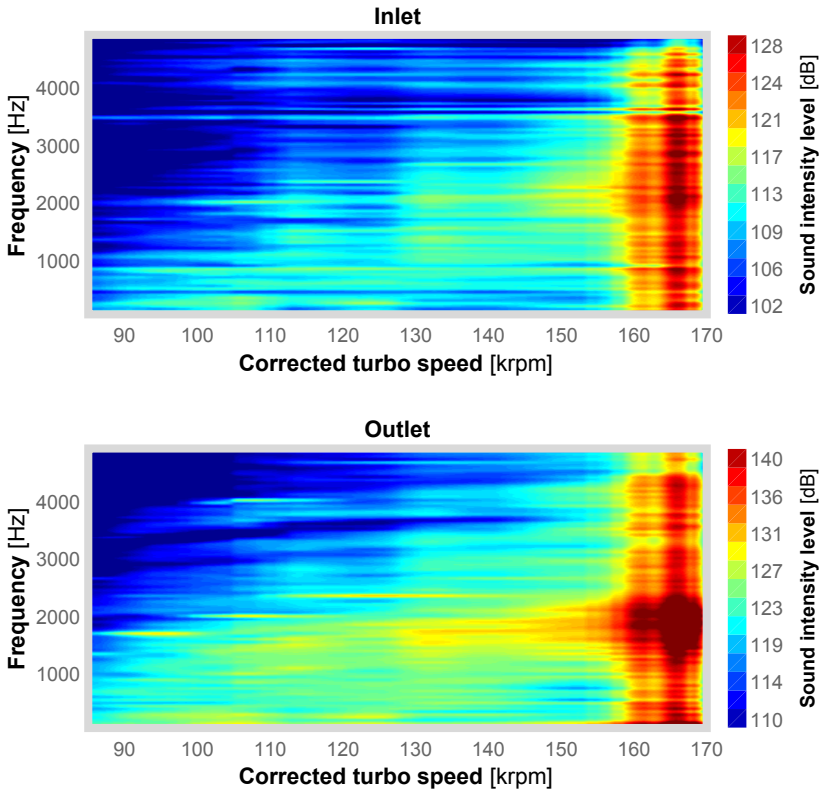

Figure 4.15: *Spectrograms for inlet (top) and outlet (bottom) in-duct SIL reconstructed from the interpolated spectral content along the working line.*

Figure 4.15 shows how the spectral content of the sound intensity changes along the path of the working line first shown in Fig. 4.1. This figure shows how, specially in the outlet, a certain, typical *whoosh* content (1 – 2.5 kHz) is present along the line. Intensity levels present a sudden step after 160 krpm of shaft speed.

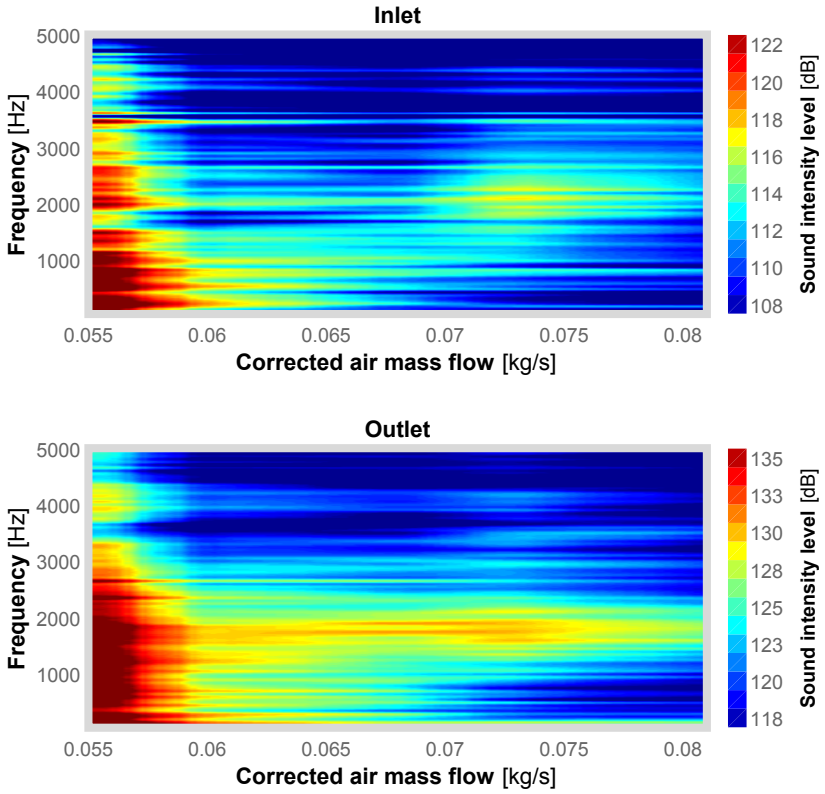

Figure 4.16: *Spectrograms for inlet (top) and outlet (bottom) in-duct SIL reconstructed from the interpolated spectral content along the 160 krpm line.*

In a similar manner, Fig. 4.16 shows the evolution of the intensity spectral content as air mass flow is reduced, while keeping a constant corrected shaft speed of 160 krpm. In this case, and again specially in the outlet duct, broadband content between 1 and 3 kHz consistent with *whoosh* noise is evident even at the highest considered mass flows which should be quite stable. This broadband then becomes masked by the rise in levels as mass flow rate is reduced.

It can also be seen in this figure how very low frequency content appears as operating conditions get close to the deep surge limit. In the inlet case this content under 1 kHz is dominant at these unstable conditions, whereas in the case of the outlet the content is more broadband. As for higher frequency content in the inlet duct, in both Figs. 4.15 and 4.16 spectral content is not as consistent as in the outlet duct.

4.2. External noise

Besides the measurement of in-duct sound pressure and intensity, external measurements of noise were performed during the experimental campaign as well, taking advantage of the anechoic conditions of the chamber where the turbocharger test rig was installed.

The equipment and methodology used in these experiments was described in section 3.4. As seen in the literature review presented in chapter 2, external measurements of noise are commonplace in the available scientific works, being also a common metric used by manufacturers. It is thus important to relate the obtained in-duct results with these kind of external measurements.

4.2.1. Orifice noise

External measurements of the orifice noise were carried out simultaneously with the in-duct measurements at the same data points, to ensure that the comparison between the two could be meaningful.

As previously detailed, data was captured with two free-field omnidirectional microphones placed perpendicular to the turbocharger axis line at distances of 10 and 20 mm from the inlet duct orifice.

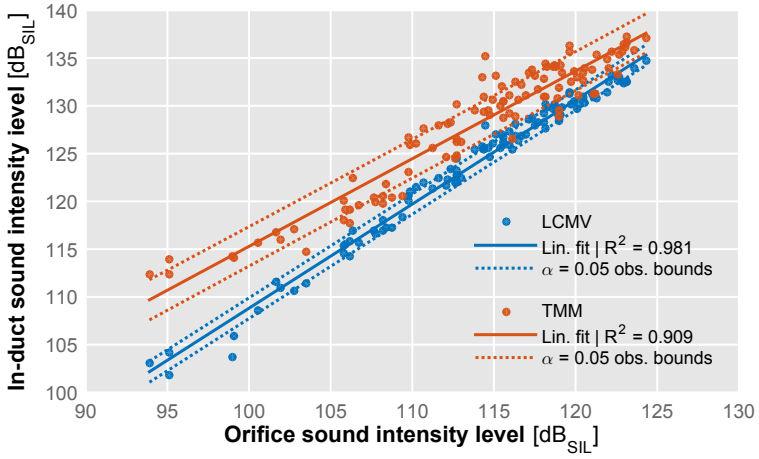

Figure 4.17: *Correlation between inlet in-duct sound intensity and orifice sound intensity considering both LCMV beamforming and the Two Microphone Method.*

In Fig. 4.17 a correlation is shown between the in-duct sound intensity levels measured in the inlet and those measured by the first microphone situated at 10 mm from the orifice by applying free-field conditions to compute intensity, as detailed in chapter 3. In the case of the in-duct SIL, the results from the LCMV beamforming method and the traditional Seybert's [93] Two Microphone Method (TMM) are shown, with the LCMV procedure showing a better statistical agreement in terms of R^2 with the free-field orifice data. Results from the second microphone offered a similar result.

4.2.2. Surface radiation

Apart from taking advantage of the anechoic environment to measure orifice noise, noise radiation data was also recorded by four additional free-field microphones distributed around the turbocharger assembly, as shown previously in chapter 3.

In this case however, unlike the previously described orifice measurements where acquisition was simultaneous with the compressor map characterization and thus they covered the whole selected region, measurements were restricted to the two characteristic lines used in this chapter: the engine working line and the 160 krpm speed line.

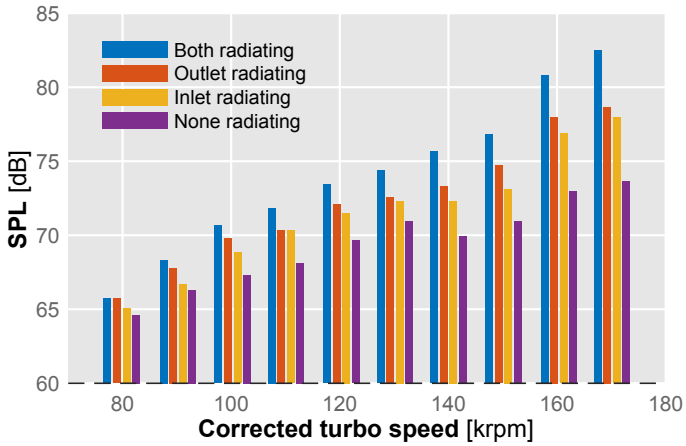

Figure 4.18: *Averaged RMS Sound Pressure Level as recorded during the sequential damping measurements for different corrected shaft speeds of the engine working line.*

Furthermore, a sequential damping of the different parts of the assembly (inlet duct, outlet duct and nothing at all) was performed using acoustic insulation blankets wrapped around them in order to isolate the distinct contribution of each part.

Results from this sequential testing procedure can be seen in Fig. 4.18 considering the operating conditions of the working line. In this case full spectrum SPL averaged between the four encircling microphones is shown in the figure.

As expected, radiated sound increases with shaft speed, following the previous in-duct measurements. In almost all conditions sound levels radiated by the outlet duct are higher that those radiated by the inlet duct.

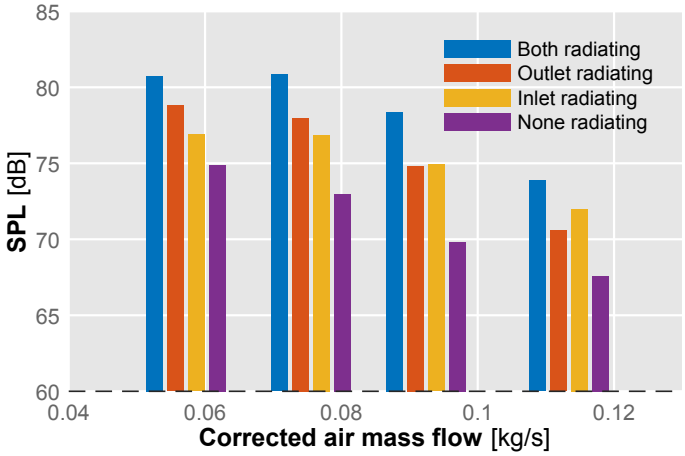

Figure 4.19: *Averaged RMS Sound Pressure Level as recorded during the sequential damping measurements for different air mass flow rates of the 160 krpm speed line.*

In Fig. 4.19 a similar analysis is carried out for four points of the 160 krpm speed line, from a higher flow rate stable point to a lower flow rate at more unstable conditions. In this case it can be seen again how, as expected, noise content rises towards deep surge.

However, at higher mass flow it is now the inlet duct the one exhibiting higher noise levels. As flow rate is reduced, the outlet duct takes again the lead on noise radiation. Between the last two points that are closer to surge, inlet duct, contribution does not increase, only that of the outlet duct.

4.3. Conclusions

In this chapter the main results of the experimental measurement campaign are presented. These concern specially the data gathered through in-duct measurements in both inlet and outlet pipes of the compressor, although some data from external measurements is also presented.

Analysis was first performed by considering the spectral signature of the pressure data in two sets of measurements: the working line of the engine which is representative of the different air flow rate and shaft speeds that the compressor may experience in normal operation, and a speed line or characteristic line where corrected shaft speed was maintained at 160 krpm, and mass flow rate was reduced from stable conditions to a point close to the deep surge limit.

Pressure wave decomposition was shown to be a helpful technique to enhance the spectral information coming from the compressor and filter out the reflections coming from the opposite ends of the pipes, thereby aiding to eliminate standing waves and offering cleaner spectral information.

In these improved results it became easier to identify relevant features such as the Blade Passing Frequency and its harmonics, along with a broadband hump between 1 and 3 kHz that is consistent with a broadband phenomenon known in the literature as *whoosh* noise, being of special concern due to its negative perception in automotive applications.

This particular noise phenomenon was more easily detected in the acoustic signature of the outlet duct, being more prominent at higher shaft speeds. At these higher speeds the hump was noticeable even at the more stable higher mass flow rate conditions. As flow rate was diminished, rising levels of lower and higher frequency phenomena masked the presence of this hump.

Non-dimensional analysis showed that the hump identified with *whoosh* was sensible to the mean velocity of the flow, rather than to the shaft speed or the sound speed, thus pointing to a flow-related generation rather than to a transmission-related one. The higher frequency TCN-like broadband on the other hand, seems to be heavily dependent of transmission factors such as the sound speed.

Furthermore, this later phenomenon shows an abrupt collapse at frequencies of plane wave transmission at all the considered points, suggesting that its source mechanism cannot propagate in this condition. This would confirm that this TCN-like phenomenon is indeed different from *whoosh*, which is a broadband noise that, on the other hand, does appear at the plane wave range.

Noise maps were also constructed from the interpolation of in-duct acoustic intensity across the different operating conditions considered in the study. In this way it was shown how onset of low frequency (<100 Hz) phenomena was parallel to the surge limit, whereas content on the *whoosh* band followed a different distribution, with its onset appearing more closely related to the null slope point of the characteristic line rather than to proximity of deep surge, indicating a difference between the two phenomena.

Analysis of the higher frequency maps became more difficult as pressure wave decomposition could not be performed due to the propagation of higher order acoustic modes that nullify the plane wave assumption required by the procedure. It was observed that while inlet PSD maps were similar for the three sensors of the array, distribution of the levels in the outlet presented important differences even considering the relatively small distance between each sensor, including in some cases spurious readings.

This reinforces the notion that PSD measurements with a single sensor, specially in the outlet duct where the flow is less uniform and features a high swirl, should be avoided if possible, preferring if feasible acoustic intensity measurements through wave decomposition.

In order to visualize how frequency content changed through the two different sets of conditions, spectrograms were constructed from the interpolated data of the maps for both inlet and outlet. Specially in the later it can be seen how content in the *whoosh* noise band is present even at lower shaft speeds and higher mass flow rate conditions.

Taking advantage of the anechoic environment in which the turbocharger was installed, orifice noise measurements performed with free-field microphones near the inlet mouth were used to compute a correlation with the in-duct intensity. In-duct intensity was calculated with both the beamforming procedure and the two microphone method, with the first resulting in better agreement and less dispersion, thereby confirming that the selected decomposition technique is suitable to estimate orifice noise without the need of an anechoic environment.

Finally, surface radiation was measured in a sequential test in which the different parts were damped: inlet and outlet ducts and turbocharger group. Results from these tests showed that the outlet duct featured generally a higher contribution than the inlet to the radiated noise, except at the higher mass flow rate conditions. It is worth noting that even if sound is generated in the turbocharger itself, the vibro-acoustic characteristics of the particular ducts can make them act as primary sources of sound radiation to the ambient.

CHAPTER 5

Validation on real engine conditions

While in the previous chapter results were obtained in an experimental campaign carried out in the controlled environment of an anechoic test chamber, with the turbine being powered by a flow rig, automotive turbochargers work paired with a reciprocating combustion engine.

Reciprocating engines produce a pulsating flow that carries the spectral content of the different cylinder firing sequence. This introduces a tonal noise in the pressure signal that includes the main firings and their harmonics, valve openings, and so on. It also means that power is provided to the turbine according to this pulsation, although the wheel inertia attenuates this last issue. In consequence, the operation of the compressor could become affected by these pulsations, an effect which could then influence the different flow phenomena occurring in the compressor such as stall, blade vortex shedding, etc.

Another important consideration is that robust methodologies are needed to perform acoustic characterization in the environment of production engine test cells, which are usually neither anechoic nor designed for acoustic measurements. In the previous chapter it was shown how SPL measurements performed with a single sensor in the outlet or inlet duct are vulnerable against reflections, standing waves, and other effects of the transmission and the pipe geometry, while acoustic intensity gives more robust results.

Acoustic intensity in the previous chapter was computed inside the ducts with flow using pressure wave decomposition, primarily through the use of a LCMV beamforming technique on the data collected by arrays of pressure transducers mounted flush in a straight duct section in both inlet and

---

Work in this chapter has been partly published in the following paper:

- *Acoustic characterization of automotive turbocompressors* [3]

outlet pipes. The classical Seybert's two microphone method [93] was also tested for comparison against orifice noise measurements, albeit the LCMV beamforming performed better.

In this chapter, an experimental campaign is described where acoustic measurements were taken in the engine test cell described in section 3.1.3. The objective of this experimental campaign was to test the application of the methodology laid out in chapter 3 in an engine environment and to ensure that conclusions and observations made in chapter 4 were still valid in this more realistic case.

5.1. Engine cell setup

Reviewing the available literature on noise characterization of turbocharger compressors, as done in chapter 2, it becomes readily apparent that due to the measurement limitations mentioned above and the difficulty of operating both the turbocharger and the engine at the same time to achieve precise operating conditions, most of the data comes from flow rig measurements.

However, some studies regarding the acoustic performance of turbocharger compressors on engine conditions can be found, such as those presented by Evans and Ward [30, 31], Teng and Homco [16], Pai et al. [40, 41] and Galindo et al. [69, 77, 106], the later specially concerned by low frequency surge noise.

Two different approaches for measuring turbocharger noise are found in these works. One of them is based on measuring radiated noise by means of exterior ambient microphones inside the engine test cell. In these conditions however, it is difficult to separate the radiation of the compressor group and pipes from the engine combustion noise and the auxiliary systems. Furthermore, as engine test cells are not usually anechoic, reflections will affect the data collected by ambient microphones, adding another important source of experimental error.

As an alternative, some authors have relied into a flow microphone or a pressure transducer situated inside the inlet duct of the compressor. However, as previously stated, this approach is affected by the particular geometry and reflections of the duct, as only Sound Pressure Level (SPL) can be computed from a single sensor in a duct with flow.

In this campaign it was thus decided to adapt the beamforming setup to the engine test cell, in order to apply the pressure wave decomposition that would allow the calculation of Sound Intensity Level (SIL).

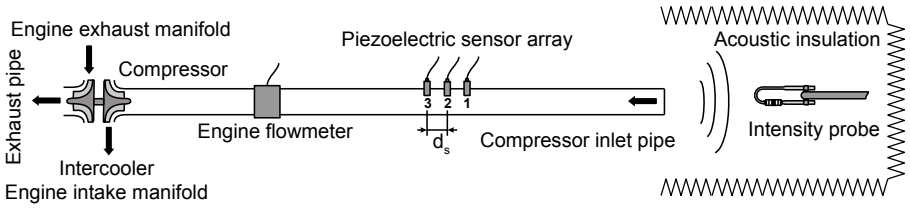

Figure 5.1: *Schematic of the experimental setup for the acoustic measurements carried out in the engine test cell.*

The experimental installation includes thus an array of piezoelectric pressure sensors flush-mounted in an extension of the compressor inlet pipe. These sensors were used to test the beamforming method and perform a comparison against the two-microphone method in engine conditions. Sound pressure level (SPL) of a single sensor as used frequently in the aforementioned literature was also computed to assess the difference with intensity results.

A commercial intensity probe (Brüel & Kjær Type 4197) consisting of two phase-matched 1/2" microphones was also installed at the inlet orifice as a reference, surrounded by acoustic insulation mats in order to avoid reflections from the walls or other components of the engine cell. Fig. 5.1 shows an schematic view of this experimental setup.

The engine used in this study was a 2 liter, 4-cylinder Diesel engine, very representative of common engines for automotive application, rated at a maximum power of 120 kW and maximum torque of 340 Nm. It featured a 16 valve system and a variable geometry turbine (VGT) turbocharger. The inlet duct of this turbocharger was modified and enlarged with an additional straight section in order to install the pressure transducer array and ensure proper development of the flow. In Fig. 5.2 some images of the modified inlet duct can be seen.

Also visible in this figure is the dynamometer that was used to control the power and torque of the engine, allowing the selection of the desired operating conditions of the engine. Due to the presence of this dyno, the enlarged inlet duct had to be provided with a flexible section so it could be angled slightly.

A particular feature of this engine test cell is that it allows the use of compressed air injection into the inlet manifold, after the intercooler. More details and schematics about this particular aspect of the setup can be found

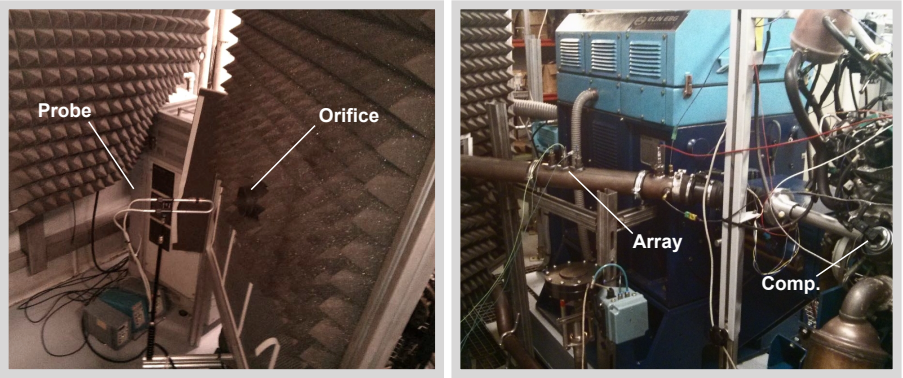

Figure 5.2: *Images of the experimental setup for the acoustic measurements, including the intensity probe and the transducer array mounted on the enlarged inlet pipe.*

in [69, 77]. A reservoir is added to smooth out irregularities that could be present in the injected flow. This reservoir can be seen in the bottom-right corner of Fig. 5.2.

In essence, by regulating the pressure and mass rate of this compressed airflow the engine cylinders are provided with additional air and as a result, less air is ingested by the compressor by effect of the variable geometry turbine.

This allows an additional degree of freedom in order to change the operating condition of the compressor without affecting the operation of the Diesel engine. A drawback of this method however, is that in this way constant pressure ratio lines are measured, not the characteristic, constant shaft speed lines that are usually plotted in the compressor map.

As done in the previous measurement campaigns, it is necessary to evaluate the restrictions that the chosen acoustic characterization methods impose in the frequency domain. While SPL is only limited by the frequency response of the particular sensor, the decomposition algorithms of both the two-microphone method and the beamforming method present some common additional restrictions which were discussed in chapter 3.

The first one is that both methods are formulated considering plane wave propagation, and are thus theoretically restricted to the frequency range below the onset of higher order modes, which can be computed according to the expressions provided by Eriksson [94].

Another restriction is the one related to the spatial resolution of the consecutive sensors [93], which imposes a cut-off frequency similar in concept to a Nyquist limit for spatial (rather than temporal) sampling, based on the separation d_s of the sensors. It is important to take into account that above this frequency limit, spurious spatial aliasing effects will be introduced.

5.2. In-duct measurement results

Using the setup described a measurement campaign was carried out where the region of the compressor map closer to surge was characterized by varying the injected additional air mass at different pressure ratios.

The interpolating procedure described in chapter 3 was used to build a noise level map between 1 and 3 kHz equivalent to those obtained in the anechoic chamber test rig, which is shown in Fig. 5.3.

In this figure, it can be seen how the intensity level distribution is similar to that obtained in the continuous flow test rig. Noise increase in this particularly concerning band is again located at higher shaft speeds and low mass flow rate, and again the contours are not parallel to the deep surge limit as it is the case with lower frequency content but grouped towards the upper left corner of the map.

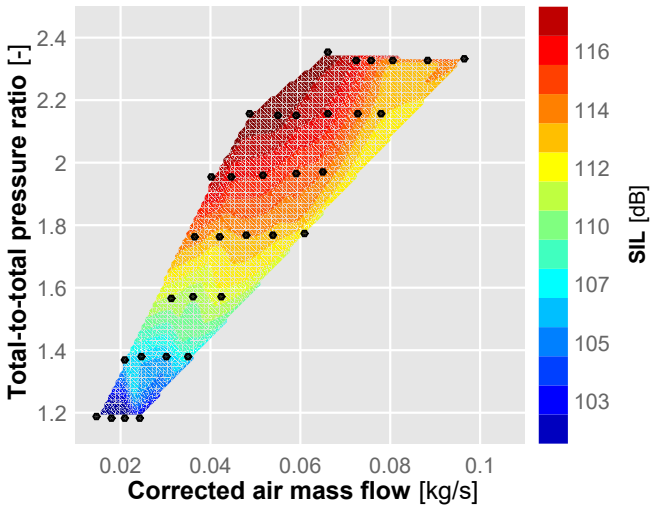

Figure 5.3: *Inlet in-duct sound intensity level map in the* whoosh *noise frequency band (1 – 3 kHz) as measured through the LCMV beamforming procedure in the engine test cell.*

As due to the different measurement procedure each line of data points is recorded at iso-pressure rather than iso-speed, it is not possible to judge whether the increase is again linked to the point of maximum pressure ratio. Still, it can be concluded that results in terms of noise level distribution are in line with those obtained in previous observations.

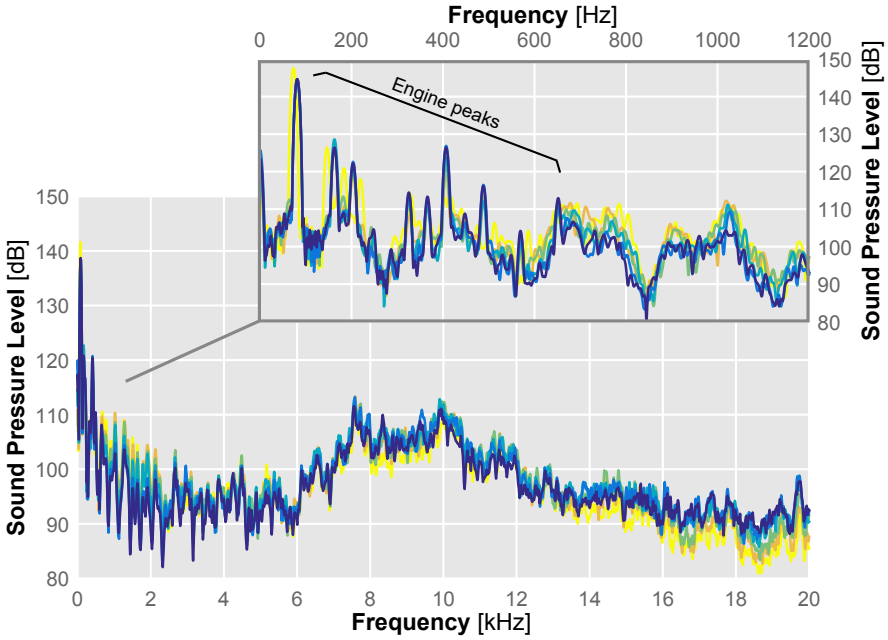

Figure 5.4: *Inlet in-duct SPL spectra for the different mass flow rates measured at 2.2 pressure ratio, including a low frequency zoomed view.*

Influence of the engine in the recorded in-duct spectral content can be seen in Fig. 5.4 where the raw sound pressure level measured by one of the array sensors is shown for the 2.2 pressure ratio data points. While the overall distribution is similar to those observed in the continuous flow test rig, featuring a slope in the plane wave range and a broadband at higher frequencies[1], a zoom at the lower part of the spectra shows a very clear peak at the cylinder firing frequency, accompanied by harmonics and other tonal noise phenomena produced by the engine, which could be related for instance with the air management system.

[1]Although in this particular case BPF is not being observed upstream of the compressor.

5.3. Methodology validation

Fig. 5.5 shows the in-duct sound spectra computed with the three discussed methods: SPL with one sensor, two-microphone approach, and LCMV beamforming. The spectra measured at the orifice by the reference probe is superimposed in blue. In this region, the beamforming method appears to follow the reference more closely.

It is also shown how spurious aliasing peaks occur at the frequency predicted by expression 3.3.6 when more than one sensor is used and how the onset of the 1st radial mode predicted by expression 3.3.7 marks the start of a clear difference between the in-duct sound field and the sound field radiated by the inlet orifice.

The results of applying the intensity equation 3.3.2 to compute SIL in the plane wave region of the spectra at different operating conditions of the compressor are shown in Fig. 5.6. Absolute levels at each working point were interpolated in order to get a continuous map. The beamforming and the two-microphone methods were used for in-duct SIL estimation and the intensity probe for measuring the reference orifice SIL. Correlations of these measurements are also provided, showing that in the plane wave range the beamforming method appears to perform up to 30% better in terms of R^2.

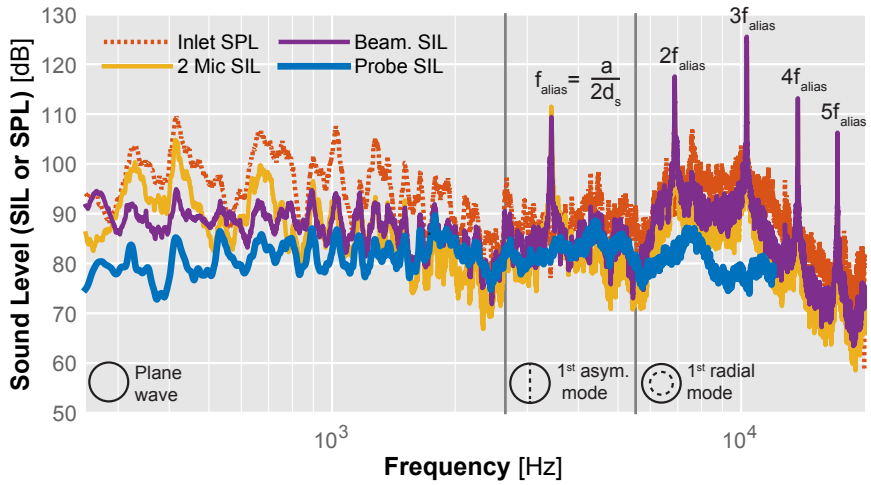

Figure 5.5: *Inlet in-duct sound spectra estimated by the three considered methods (SPL, beamforming and two-microphone) and orifice sound intensity spectrum as measured by the B&K intensity probe.*

Fig. 5.7 shows a comparison between the SPL computed by selecting only one sensor of the array and the reference SIL of the probe. The correlation of these two measurements is better in terms of R^2 than the two-microphone method but still worse than the beamforming method.

However, it should be noted that simple sound pressure level measurements can be influenced by the complex geometry of actual production pipes, which are remarkably more complex than the straight pipe used in this study. Also, it can be seen in Fig. 5.7 that, while at low pressure the sound maps are quite similar, SPL of one probe predicts a high sound level at high pressure

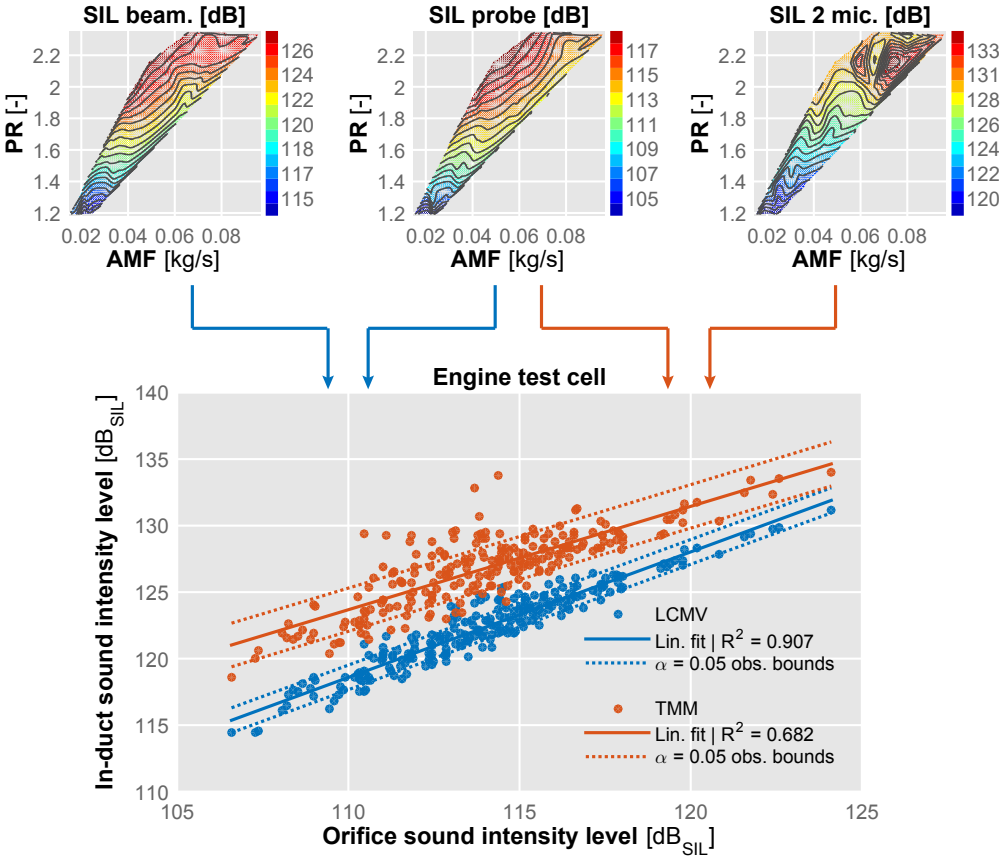

Figure 5.6: *In-duct SIL maps of the compressor noise estimated by the beamforming method (top left), two microphone method (top right) and SIL map of orifice noise as measured by the probe (top center) at plane wave range, including correlations between the three measurements (bottom).*

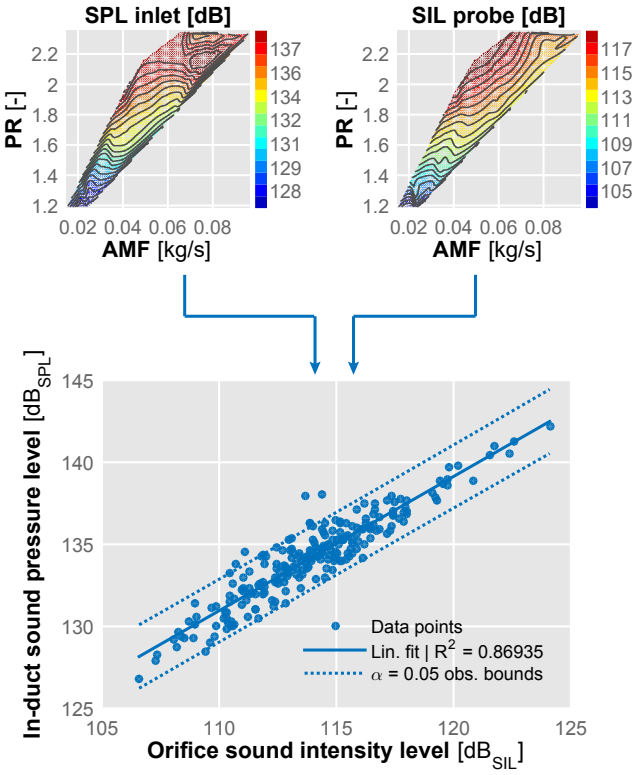

Figure 5.7: *Comparison of compressor sound maps (plane wave region) obtained through interpolation of SPL at the inlet 1st sensor and SIL at the probe at plane wave range, including a correlation between both.*

ratio and high mass flow conditions, which is not the case for the intensity probe. These high sound level points at high pressure ratio can be clearly seen as points lying outside the 95% observation confidence bounds of the correlation in Fig. 5.7.

A similar problem can be seen in the correlation of the two-microphone method in Fig. 5.6, in which some outliers appear to distort the map at some operation zones. The beamforming method, however, appears to be more robust, featuring less outliers than those detected with the use of one-sensor SPL and the Two Microphone Method decomposition.

5.4. Radiated noise

Besides in-duct measurements, another acoustic characterization approach consists in the measurement of noise radiated by the turbocharger and its pipes, in most cases using free field microphones at a given distance from the setup as it was discussed in the literature review.

This method has the advantage of allowing measurements with the real geometry, without any modification in the pipes to mount the in-duct measurement sensors. However, for accurate measurements it is desirable that the test cell be anechoic in order to prevent disturbances in measurements caused by reflections in the engine cell walls and resonances created by the cavities of the engine or its ducts that appear as other noise sources.

As testing the whole engine setup requires a large and expensive anechoic chamber, the setup is sometimes reduced to just the turbocharger group, which is powered by an external compressor or electric motor, losing in this way the possibility of performing on-engine tests.

However, a novel procedure based on measuring acoustic particle velocity level (PVL) may solve these issues [101] and enable on-engine testing in non-anechoic environments. This method, briefly introduced in chapter 3, makes use of two microscopic filaments acting as hot-wire flowmeters. Measuring the small voltage drop between the two, it is possible to derive the acoustic particle velocity in the plane of the sensor.

Such a method, in this case a commercial solution providing acoustic holography-like maps of radiated noise level [102], has been tested on the (non-anechoic) engine test cell. The measuring probe of this device houses

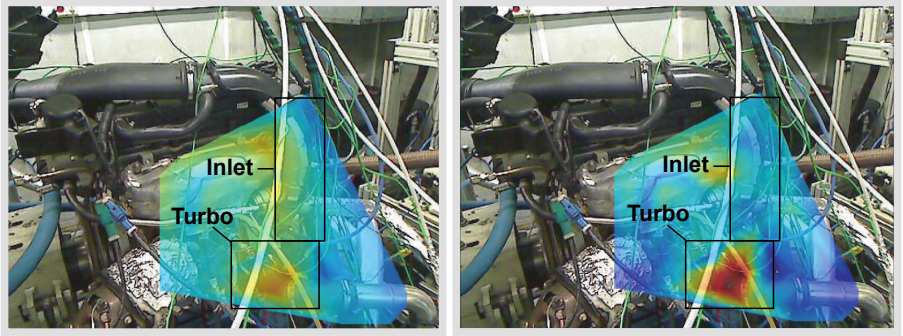

Figure 5.8: *Near field noise holograms (800 – 2000 Hz) obtained through SPL (left) and PVL (right), highlighting two regions of interest: turbocharger group and compressor inlet.*

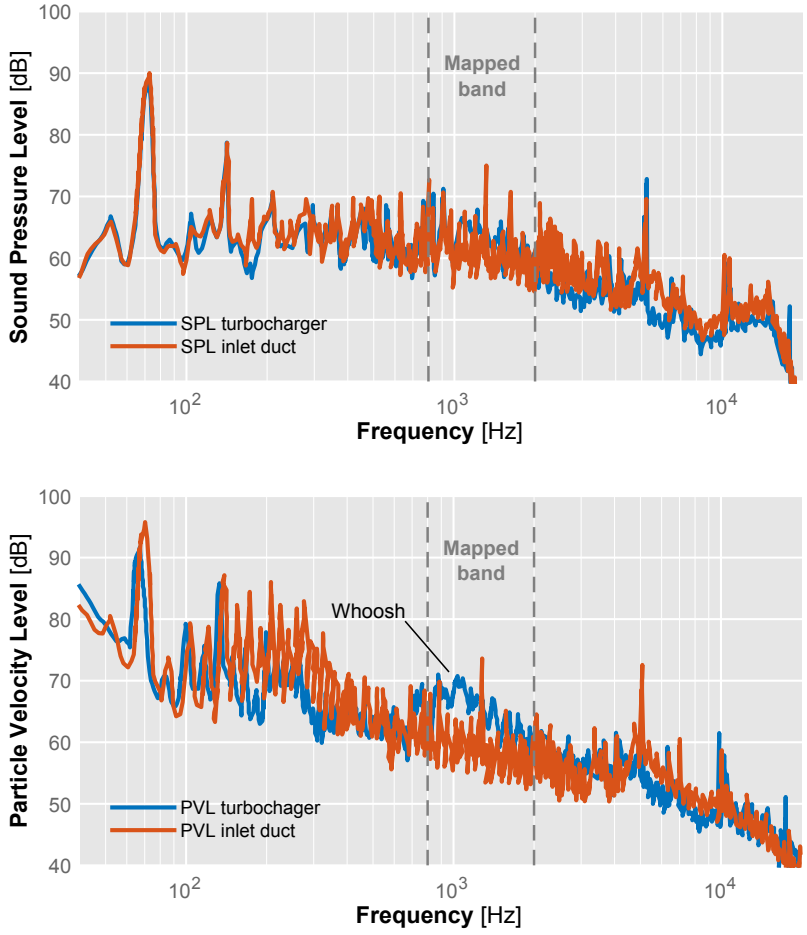

Figure 5.9: *Near field noise spectra in the full range obtained through SPL (top) and PVL (bottom), highlighting the frequency band that was mapped in Fig. 5.8.*

the two filaments on a MEMS chip and a traditional microphone, allowing the comparison of the performance of acoustic particle velocity measurements against traditional free-field sound pressure level (SPL) measurements.

Fig. 5.8 shows this comparison. SPL (left) and PVL (right) maps of the measured engine environment are provided by tracking the probe along the near field of the surfaces of interest. The frequencies considered in these maps have been restricted to the 800 – 2000 Hz range, where the broadband emission of *whoosh* noise was produced by the turbocharger. For

two particular regions (turbocharger group and inlet duct, marked on the maps) the full pressure (top) and particle velocity (bottom) spectra are also provided in Fig. 5.9.

The particle velocity technique clearly distinguishes the turbocharger as the source of a 700 – 2000 Hz broadband noise (at this particular operating condition) consistent with *whoosh*. The pressure method also appears to identify the turbocharger as the source, but the contrast with the surrounding areas is much less pronounced. This can be clearly seen in spectra of Fig. 5.9, in which the SPL level (top) of this frequency band is similar in both zones (turbocharger and inlet) while in the case of the PVL spectra (bottom), the turbocharger contribution is visibly higher, exhibiting the typical hump of *whoosh* noise.

The pressure method appears to be more sensitive to reflections in the near field and was thus unable to provide a clear identification. It should be noted that if characterization through in-duct techniques of this particular *whoosh* noise is intended, special attention should be placed on the outlet pipe, as this phenomenon is often found exclusively downstream of the turbo-charger.

5.5. Conclusions

Characterization of the acoustic performance of a given compressor under engine conditions must start with the definition of test means. If an anechoic chamber capable of housing the entire engine is available, then free field microphones can be used to estimate the acoustic radiation, but even in this case it would be difficult to isolate the contribution of the compressor.

In order to quantify the compressor noise emission, an intensity probe can be located at the inlet orifice. However, intensity probes are quite expensive, and sufficient acoustic insulation is necessary to prevent reflections. In addition to these issues, spectral characteristics of the internal field that are not externally propagated will be lost.

In this chapter it has been show that in-duct noise measurements offer a cost-effective way to characterize the sound field generated by the compressor, if the ducts can be modified so as to include straight measurement sections. Single-sensor SPL may be used to investigate the upper frequency bands, but generally sound intensity is a better and more meaningful metric of the acoustic power output of the source.

Calculation of in-duct sound intensity can be achieved by using an additional consecutive sensor and decomposing the waves through the two-microphone method. However, the addition of a third sensor and the decomposition through the beamforming method appears to be more reliable along the full plane wave range, and especially in the lower frequencies (250 – 1000 Hz).

As shown in previous chapters however, the restrictions of these intensity-based methods must be carefully considered, specially the influence of higher order modes and the aliasing frequency limit introduced by the spatial sampling imposed by the sensor spacing. In addition in this on-engine situation, the pulsation intrinsically imposed by the operation of the reciprocating engine must be taken into account as not only its main firing frequency but also its harmonics are present in the lower frequency part of the spectrum of the compressor inlet.

Regarding the external radiated noise, the particle velocity method has been able to provide more contrast than the pressure method and to correctly identify the turbocharger as the source of noise radiation at the particular *whoosh* noise band, in accordance with previous results.

The particle velocity method could therefore be useful to reconstruct noise maps similar to those obtained using in-duct measurements, isolating the signal from the acoustic near field of the area of interest at different working conditions, without the need of modifying the original duct geometry or ensuring anechoic conditions.

CHAPTER 6

Validation of numerical simulations

As stated in the initial literature review, numerical simulations of physical problems have been demonstrated to be a valuable tool for the analysis and understanding of phenomena that may be difficult to characterize exclusively through experimental means.

These kind of simulations are also very valuable in the development stage of engineering applications, where different prototype variations or operating conditions can be simulated simultaneously without the cost and risks of traditional experimental setups.

However, it is of the utmost importance to properly validate the results offered by these numerical tools in order to ensure that they correspond accurately enough with the physical reality. Small changes in the geometrical model, boundary conditions or numerical algorithms for solving the problem can have a great influence on the outcome of the simulation. Sometimes, it is even possible that the assumptions made in the physical models that are used in the simulation are such that they do not even allow the phenomena of interest to manifest.

In this chapter the use of experimental data and signal processing techniques to validate a numerical model of a turbocharger compressor is presented and discussed, including the comparison of global variables, local flow field, acoustic results and different operating conditions of the system.

Work in this chapter has been partly published in the following papers:

- *Methodology for experimental validation of a CFD model for predicting noise generation in centrifugal compressors* [1]
- *Simulations and measurements of automotive turbocharger compressor* whoosh *noise* [2]
- *Numerical and experimental analysis of automotive turbocharger compressor aeroacoustics at different operating conditions* [4]

6.1. CFD simulation setup

The development of this numerical model, including the assessment of the influence of spatial and temporal discretization, turbulence models, boundary conditions, tip clearance, etc. was performed in parallel of this thesis, in the framework of the doctoral thesis of R. Navarro [107], where full details about the model can be found.

In consequence, in this section only a brief description of the numerical model will be provided, covering only the most relevant details for the validation discussion and the use of simulation results in the analysis of the physical problem.

6.1.1. Computational domain

The first step in any numerical model is the decision on the extent at which the real setup will be included in the computational domain. In this case the real setup is the one described in section 3.3, this is, the turbocharger and pipes that were installed in the anechoic chamber rig.

In order to ensure that the fidelity of the simulated geometry to the real one was kept, a real compressor of the same exact model of the one installed in the experimental test rig was disassembled and digitized. A structured-light 3D scanner was used to obtain a point cloud, which was interpolated into a smooth CAD model through software post-processing.

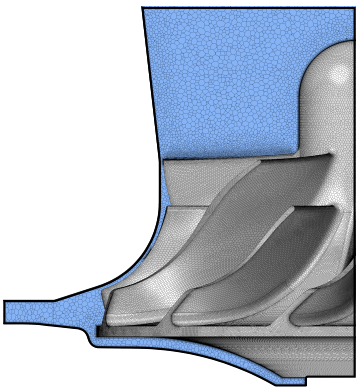

Figure 6.1: *Polyhedral mesh of the rotor walls (grey) and the surrounding fluid (blue) used in the CFD model.*

To avoid the influence of manufacturing differences that the real compressor could have had, only one main blade and one splitter blade were digitized, the rest of them being cloned into the final model. Tip clearance and backplate gap were also included in the digitized CAD model. The fluid domain was extracted by considering the spaces between the reconstructed surfaces. A sample of the resulting mesh can be seen in Fig. 6.1.

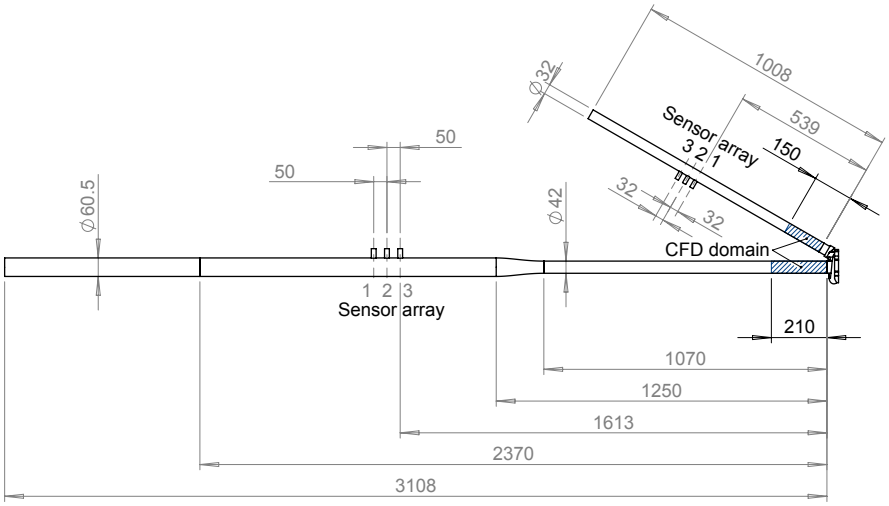

Figure 6.2: *Dimensional drawing of the real compressor inlet and outlet pipes, including the piezoelectric sensor arrays for the experimental wave decomposition and highlighting the CFD simulation domain.*

This non-structured mesh consisted of 9.5 million polyhedral cells arranged as to obtain y^+ values[1] close to 1 near the impeller walls. Inflation cell layers were used near the walls to enhance these values, with the size of the polyhedral cells being enlarged farther from the walls to reduce the total size of the mesh.

Once that the turbocharger compressor fluid volumes were obtained and meshed, inlet and outlet sections of the digitized compressor were used to create short inlet and outlet pipes by extruding these cross sections up to a distance of five of their diameters. Only these short pipes were considered, as simulating the full piping described in chapter 3 was considered too computationally expensive.

In Fig. 6.2 these short inlet and outlet ducts considered in the numerical simulations are compared with the real experimental setup as installed in the anechoic chamber test rig. It can be seen in the figure that the real pipes were much longer than the simulated ones.

[1]The so-called y^+ is a dimensionless parameter used in boundary layer theory. Some turbulence models work best when it is close to 1 in the first cell adjacent to the wall.

Table 6.1: *Boundary conditions of the CFD simulation as taken from the experimental data measured in the anechoic chamber test rig.*

Inlet boundary condition	$\dot{m} = 77$ g/s, $T_T = 293$ K
Outlet boundary condition	$p = 223$ kPa
Rotational speed	$N = 158763$ rpm

There was also a change in diameter in the inlet pipe mandated by the available measurement pipes and flow meter diameter. As this figure evidences, extending the CFD domain up to the limit of these ducts would have notably increased the simulation time.

6.1.2. Case setup

Once that the mesh was built, the case was solved using a segregated solver in the commercial CFD software package Star-CCM+ [108]. A DES (Detached Eddy Simulation) simulation was performed, using an SST $k-\omega$ turbulence model. This hybrid strategy [109] uses a combination of sub-grid-scale where possible taking into account grid size, and Reynolds-averaged equations where not [110], and should be helpful to resolve the finer flow structures that may be involved in noise generation. A similar solution was used by Mendonça et al. [45, 111].

Outlet pressure and inlet mass flow rate were chosen as boundary conditions for the simulations, with values for them taken from the experimental campaign described in previous chapters of this thesis. Specific operating conditions for the reference simulation can be found in table 6.1.

Rigid body motion simulation was chosen for the transient setup, with a time step adjusted to match 1° of rotation, which imposed a maximum frequency according to the Nyquist criterion above hearing range. At least 60 ms after steady state were stored. Regarding heat transfer, the problem is considered adiabatic, as heat transfer is less relevant at high loads [112–114]. Surface roughness, mechanical deformations and dynamic shaft eccentricity were also disregarded for simplicity.

6.1.3. Solution monitors

Besides other monitors dedicated to general fluid field visualization, some additional pressure monitors were added to the simulated inlet and outlet ducts in order to gather data for the specific purpose of acoustic validation of the numerical solution.

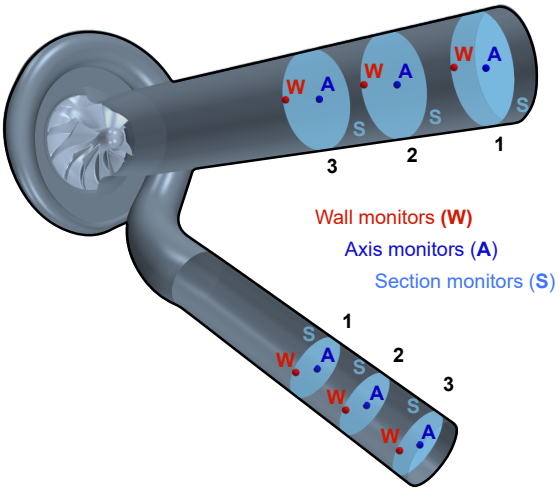

Figure 6.3: *Image of the CFD domain, highlighting the compressor wheel and including the three different kind of pressure monitors selected during the setup, at three different sections of the inlet and outlet ducts.*

Three different kinds of specific solution monitors were considered: a single-point pressure recording flush to the wall of the ducts, a similar single-point monitor in the centre of the duct, and finally an area-averaged pressure recording comprising the whole duct cross section.

Wall-flush pressure monitors were intended to replicate the position of the piezoelectric transducer used in the experimental campaign. Centerline monitors were used to assess differences between data recorded at this location, which could not be measured experimentally without perturbing the flow, and the data gathered by the wall-flush sensors.

As cross section area-averaged pressure monitors should produce the same results than the other two at the plane wave frequency range, they were introduced to test if the averaging of the pressure introduced differences.

The selected monitors can be seen in Fig. 6.3. It can be seen that all three types of monitors were replicated at three different cross sections in both inlet and outlet duct, in order to mimic the array installed in the real setup and also to assess the influence of the longitudinal distance to the compressor on the results. Full results of this assessment can be found in [1] and [107], but in essence the axial position demonstrated small influence.

6.2. Validation methodology

Once that enough iterations of the simulation solution were performed so that frequency resolution of the simulated pressure signal spectra was suitable for comparison, a validation effort was carried out in order to ascertain if the numerical model reproduced the compressor behaviour with enough accuracy as to use the simulation results to obtain exact information about flow features that are difficult to visualize experimentally.

6.2.1. Global variables

A first step of this validation methodology consisted in comparing global results of the variables that are normally used to characterize the performance of the compressor since if these simple checks were not good, the particular simulation setup should be further refined.

For instance, specific work W_u and isentropic efficiency η_s are two relevant parameters of the compressor operation, defined from the basic thermodynamic variables as follows:

$$\begin{aligned} W_u &= \frac{\dot{W}}{\dot{m}} = \frac{\Omega\tau}{\dot{m}} = c_p(T_{out,T} - T_{in,T}) \\ \eta_s &= \frac{\dot{W}_s}{\dot{W}} = \frac{T_{in,T}\left(\Pi_{TT}^{\frac{\gamma-1}{\gamma}} - 1\right)}{T_{out,T} - T_{in,T}} \end{aligned} \tag{6.2.1}$$

Here, Ω is the rotation speed in rad/s, τ is the torque as computed by the integration of simulated forces, c_p is the specific heat of air, Π_{TT} is the total-to-total pressure ratio, γ is the heat capacity ratio and the subscript T refers to total conditions in either inlet or outlet.

Furthermore, this total-to-total pressure ratio Π_{TT} is also a result of the simulation that must be validated. Since mass flow rate, outlet pressure and shaft speed were selected as boundary conditions, inlet pressure of the solution will give a pressure ratio that must be compared against the experimental data.

To avoid small variations in time, both experimental and CFD simulation variables such as pressures, temperatures and velocities were averaged in a 5 seconds window, before applying equations 6.2.1. Table 6.2 shows the results of the computed global variables in both cases, including the relative error between them, defined for each variable ψ as:

$$\varepsilon_R\,[\%] = \frac{\left|\psi_{CFD} - \psi_{exp}\right|}{\psi_{exp}}. \tag{6.2.2}$$

Table 6.2: *Comparison between compressor global variables as measured in the experimental test rig and as predicted by the CFD solution.*

	Π [-]	W_u [kJ/kg]	η_s [%]
Exp.	2.240	112.27	67.82
CFD	2.221	111.32	67.62
ε_R [%]	0.87	0.84	0.30

It can be seen in this table that the accuracy of global parameter prediction is good, with less than 1% of relative error between the CFD and experimental results, even taking into account the simplifying hypothesis considered for the numerical simulation.

This shows that the numerical model of the compressor is successfully reproducing the operating conditions of the real system so that averaged variables such as mean Mach number, temperatures and pressures that are needed for the acoustic analysis are well reproduced.

6.2.2. Acoustic results

However, the fact that these global time-averaged parameters are in good agreement does not guarantee that the simulation setup is precise enough to reproduce the kind of transient flow phenomena that are related to the acoustic behaviour of the compressor.

In a subsequent step of the validation analysis, the spectral content of the simulated pressure data gathered by the monitors described above was compared with the experimental data gathered by the fast piezoelectric sensors.

6.2.2.1. Total pressure spectra

First, comparison between experimental and numerical results was performed using the spectral content of the total pressure, this is, without applying the wave decomposition algorithm to any of the signals. In Fig. 6.4 this comparison is shown taking into account the three types of CFD monitors described in subsection 6.1.3.

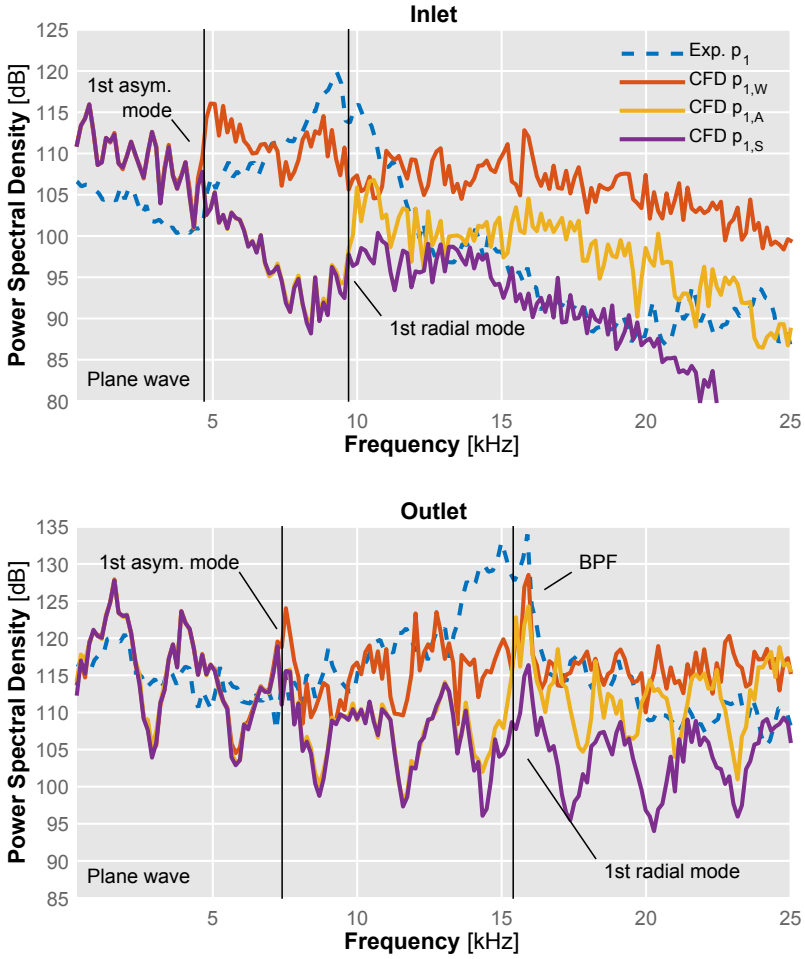

Figure 6.4: *Comparison of total spectral content between the experimental data recorded by one piezoelectric sensor and the simulation results for each type of monitor.*

It can be seen in this figure that as theoretically predicted, spectral content measured by the three different CFD monitors collapses in the plane wave frequency range for both inlet and outlet as pressure varies evenly in time across the cross-section.

This collapse of the signals ends when the wall monitor starts to show different spectral content after a certain frequency. This cut-off frequency almost exactly matches the theoretically predicted frequency at which the first asymmetric mode starts propagating.

Axis and surface monitor spectra remain collapsed until a higher frequency when another separation happens, again matching almost exactly the cut-off frequency of the first radial mode.

Explanation of how these different kind of monitors are affected by these two higher order modes can be found by considering Fig. 6.5. As the first asymmetric mode starts propagating, the axial monitor is located in its modal line, thus is not influenced by cross-section pressure fluctuations. The area average monitor evens out these fluctuations, thereby the only monitors being influenced being those located at the wall.

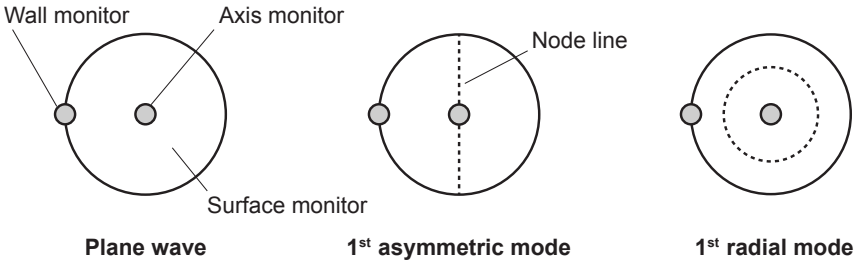

Figure 6.5: *Schematic of modal lines of the two relevant acoustic modes in relation to the different types of CFD monitors considered in the model.*

When the first radial mode starts propagating at a higher frequency, the axial monitor is not in the modal line any more, and thus its pressure spectral content separates from the surface monitor which continues to average the cross-sectional fluctuations.

Thereby it can be concluded that the CFD model is accurately predicting the cut-off frequencies at which higher order acoustic modes start propagating through the duct.

It can also be seen that BPF tonal noise peak is captured by the numerical model, although more clear in the outlet results that in the inlet ones. The pressure monitor located at the wall features the clearest BPF peak, even showing a small peak in the inlet case at the correct frequency of 16 kHz.

However, agreement between the CFD predicted signals and the experimental results is not so good in terms of PSD level and trend in the spectra, specially above the plane wave frequency range. The outlet pipe simulated spectra seems to feature an standing wave pattern, related to the short length of the pipe and lack of non-reflecting boundary conditions.

6.2.2.2. Decomposed spectra

As shown in chapter 4 the use of pressure wave decomposition can offer clearer spectra as the components coming from the compressor are more isolated from the reflections coming from the duct endings.

In the case of the experimental data, the decomposition was performed according to the three-sensor LCMV beamformer described in section 3.3.1.2. However, as CFD allows unfettered access to all of the flow variables at any point of the simulated domain, other pressure wave decomposition methods are available, such as the Method of Characteristic (MoC) that was implemented following the formulation proposed in [115–117]:

$$p_{\text{forw}} = p_{\text{ref}} \left[\frac{1}{2} \left(1 + \left(\frac{p}{p_{\text{ref}}} \right)^{\frac{\gamma-1}{2\gamma}} \left(1 + \frac{\gamma-1}{2} \frac{u}{a} \right) \right) \right]^{\frac{2\gamma}{\gamma-1}} \tag{6.2.3}$$

$$p_{\text{back}} = p_{\text{ref}} \left[\frac{1}{2} \left(1 + \left(\frac{p}{p_{\text{ref}}} \right)^{\frac{\gamma-1}{2\gamma}} \left(1 - \frac{\gamma-1}{2} \frac{u}{a} \right) \right) \right]^{\frac{2\gamma}{\gamma-1}}$$

Here, advantage is taken of the CFD ability to obtain instantaneous local values for sound speed a and flow speed u. Again, γ is the heat capacity ratio and p_{ref} is a suitable reference pressure. Fig. 6.6 shows the result of applying this algorithm to the wall CFD monitor.

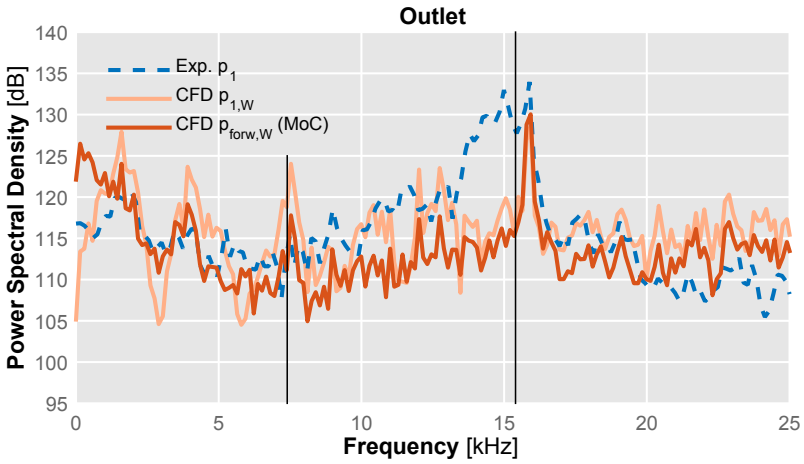

Figure 6.6: *Comparison of experimental and simulated total pressure against simulated decomposed pressure in the outlet case, using the Method of Characteristics and the wall monitor. Black lines indicate mode onset.*

As shown in the figure, the decomposed pressure spectra show a better agreement with the experimental data as the periodic oscillations present in the simulated pressure spectra are alleviated. The trend of both reference and simulated spectra are similar overall, although discrepancies can be observed, specially at lower frequencies below 2 kHz.

While the numerically simulated spectra is able to capture the characteristic peak of the Blade Passing Frequency (BPF) tonal noise at 16 kHz, the broadband noise that is visible in the experimental data between approximately 13 and 17 kHz is not reproduced by the CFD model, suggesting that the source mechanism of this particular phenomena is not being correctly considered in the simulation.

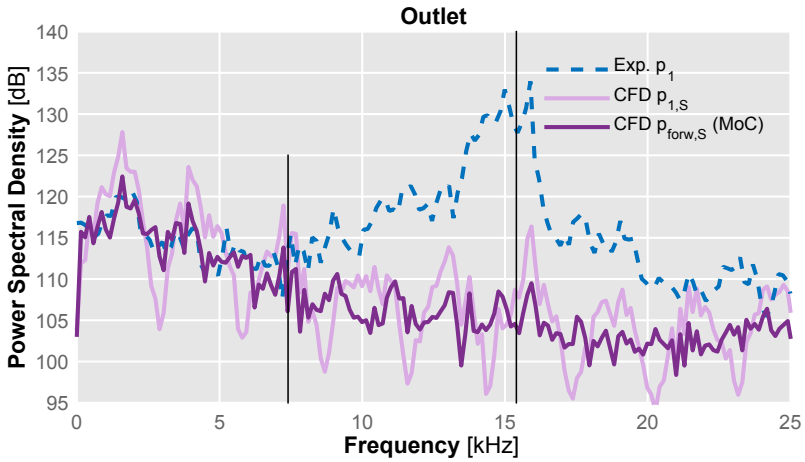

Figure 6.7: *Comparison of experimental and simulated total pressure against simulated decomposed pressure in the outlet case, using the Method of Characteristics and the section monitor. Black lines indicate mode onset.*

In Fig. 6.7 a similar comparison is made, but using instead the section monitor (area-averaged pressure). In this case the Method Of Characteristics decomposition procedure allows for a better match between experimental and simulated spectral content at the plane wave range, below the first asymmetric acoustic mode onset at 7.4 kHz.

However, using this monitor type, higher frequency content after the acoustic modes start propagating does not feature a good agreement with the reference experimental data. Blade Passing Frequency (BPF) tonal noise is not captured as clearly as with the single-point wall monitor, and neither is the broadband centred around 15 kHz.

Specially in the case of the BPF tonal noise, this could be due to the fact that the area-averaging process is neglecting the pressure differences across the cross-section, that are still picked up by the single-point CFD monitor.

Regarding the plane wave frequency range where the agreement between CFD and experimental data is better, Fig. 6.8 shows the comparison of decomposed pressure wave spectra in both inlet and outlet ducts.

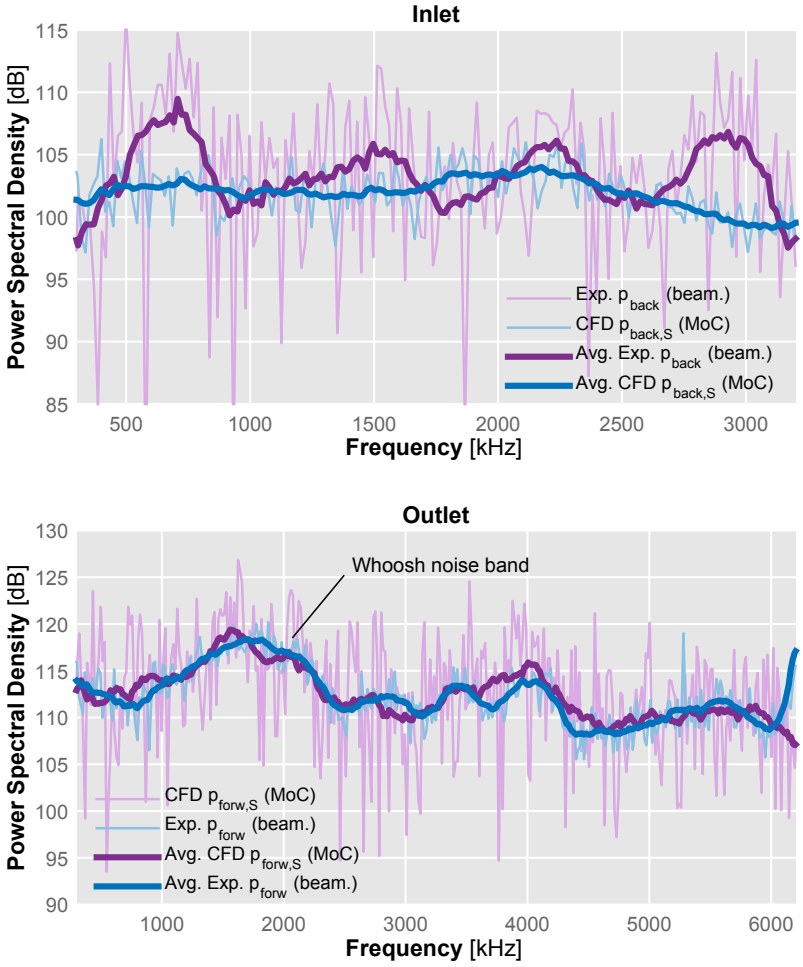

Figure 6.8: *Comparison of decomposed pressure spectral content between the experimental data (through beamforming) and the simulation results using the surface monitor (through the method of characteristics).*

Data from the decomposed signals is shown both at the highest frequency resolution available in the CFD calculation (∼16 Hz) and smoothed through a moving average filter in order to better show the shape of the spectra. As the experimental data is decomposed though the beamforming procedure described in chapter 3, frequency is limited not only by the onset of the first acoustic mode but also by the spatial Nyquist-like criterion.

In can be seen in this figure that the match between simulated and measured pressure waves coming back through the inlet from the compressor is not so good. While the experimental signal features an approximately plane spectra with only a slight "hump" of ∼4 dB at the *whoosh* noise frequency between 1.5 and 2.5 kHz, the simulated pressure wave features an oscillatory behaviour.

In the case of the outlet spectra however, a better agreement between the numerical prediction and the experimental data is found. The CFD simulation result appears to accurately follow the trend of the measurements, including the broadband between 1 and 2.5 kHz that is commonly associated with the *whoosh* noise phenomenon.

This ability of the numerical model to predict the *whoosh* noise phenomenon in the outlet duct while not completely matching the experimental inlet results seems to point to the primary source of *whoosh* noise not being located in the inlet flow structures but rather in a downstream point where simulations are more accurate.

Nevertheless, it is shown in Fig. 6.8 that the CFD model appears to contain a source of outlet broadband noise between 1 and 2.5 kHz that matches the experimental results. Thereby, post-processing of the CFD simulation data could be useful to locate the source mechanism of this phenomenon and, furthermore, the effect on *whoosh* noise of mitigating solutions could be simulated using this model before its physical implementation.

6.3. Operating conditions study

After performing the validation and optimization of the CFD model at the reference operating conditions (160 krpm of shaft speed and 77 g/s of corrected air mass flow), a further study was performed where two additional operating settings of the compressor were simulated by modifying the boundary conditions according to the experimentally measured data points, keeping the rest of the model parameters unchanged.

In order to analyze the differences in terms of pressure spectra and fluid field behaviour at different degrees of unstable operating conditions, the two additional simulations were performed at the same shaft speed of 160 krpm, in one case at a higher air mass flow (∼109 g/s) and in the other case at a lower air mass flow (∼60 g/s).

6.3.1. Global variables

While the original operating condition selected for the CFD study was chosen so that it matched the point at which the experimental measurements showed that the slope of the speed line reached zero, marking the start of the low-flow, marginal surge map zone, in this additional study the new operating conditions were chosen so that the lower flow one was well into this unstable zone and close to the deep surge limit, and the other was in the stable operating zone near the maximum efficiency point.

This would enable a comparison between the flow field of a stable point, the flow field at the point of the instability inception, and that of a point in which the unstable flow structures such as the inlet backflow would be already well developed.

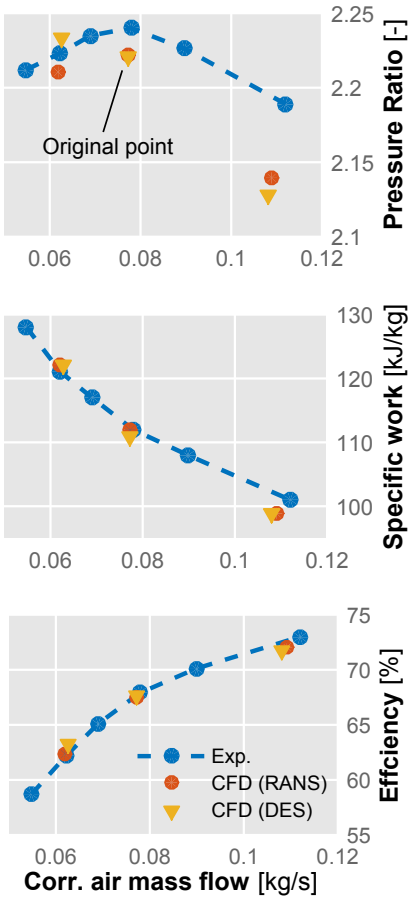

Figure 6.9: *Global compressor variables as measured experimentally and as simulated by CFD in the three selected operating conditions.*

Simulations carried out in this campaign were also performed using an unsteady RANS turbulence model in addition to the DES model that was considered for the reference study, to assess the influence that the turbulence model could have in the numerical results. Again, the first step of the validation process involved checking the same global parameters of the compressor performance that were analyzed for the reference case. In Fig. 6.9 the comparison of the numerical predictions for these parameters is shown against the previously measured experimental values.

It can be seen in this figure that while the prediction of isentropic efficiency (bottom plot) and specific work (middle plot) is in good agreement with the experimental data, in the case of the total-to-total pressure ratio (top plot) the agreement is not so good.

The least accurate prediction is that of the highest flow case, where the difference in terms of pressure ratio is larger. It should be noted as well that in this case, small variations in the predicted temperature and pressure resulted in a slight change in *corrected* air mass flow.

Regarding the differences between the two considered turbulence models, predictions in terms of isentropic efficiency and specific work are quite similar, with the larger differences in the case of the total-to-total pressure ratio.

This last difference between the two models is large enough so that it changes the slope of the speed line, with the RANS model correctly predicting a decrease in pressure ratio at lower mass flow and the DES model failing to do so, despite having less relative error.

Table 6.3: *Relative error between the compressor global variables measured in the experimental test rig and those predicted by the numerical model.*

Model	$\dot{m}$	$\varepsilon_{\Pi_{t,t}}$ [%]	ε_{W_u} [%]	ε_{η_s} [%]
RANS	60	-0.5	0.7	0.1
	77	-0.8	-0.6	-0.5
	109	-2.3	-2.1	-1.3
DES	60	0.4	0.6	1.6
	77	-0.9	-0.8	-0.4
	109	-2.8	-2.6	-1.5

Differences quantified in terms of relative error as defined by expression 6.2.2 are provided in table 6.3. It can be seen how, although larger that in the reference case of 77 g/s on which the setup was developed, relative errors are still smaller than 3% in the two additional operating settings as calculated with both DES and RANS turbulence models.

While this table shows how the use of an unsteady RANS model resulted in less relative error overall, specially in terms of isentropic efficiency at the lower flow operating point, it should be remarked that only the DES model correctly predicted the decrease in pressure ratio as flow was near surge conditions and impeller blades began stalling, suggesting that these unstable flow phenomena are better modelled using DES.

6.3.2. Pressure spectra

In addition to the validation of global variables, it is necessary to assess if the spectral content of the pressure signal simulated by the model at these new operating conditions still matches the trends observed during the corresponding experimental measurements. In this subsection only the data obtained using a DES model is presented.

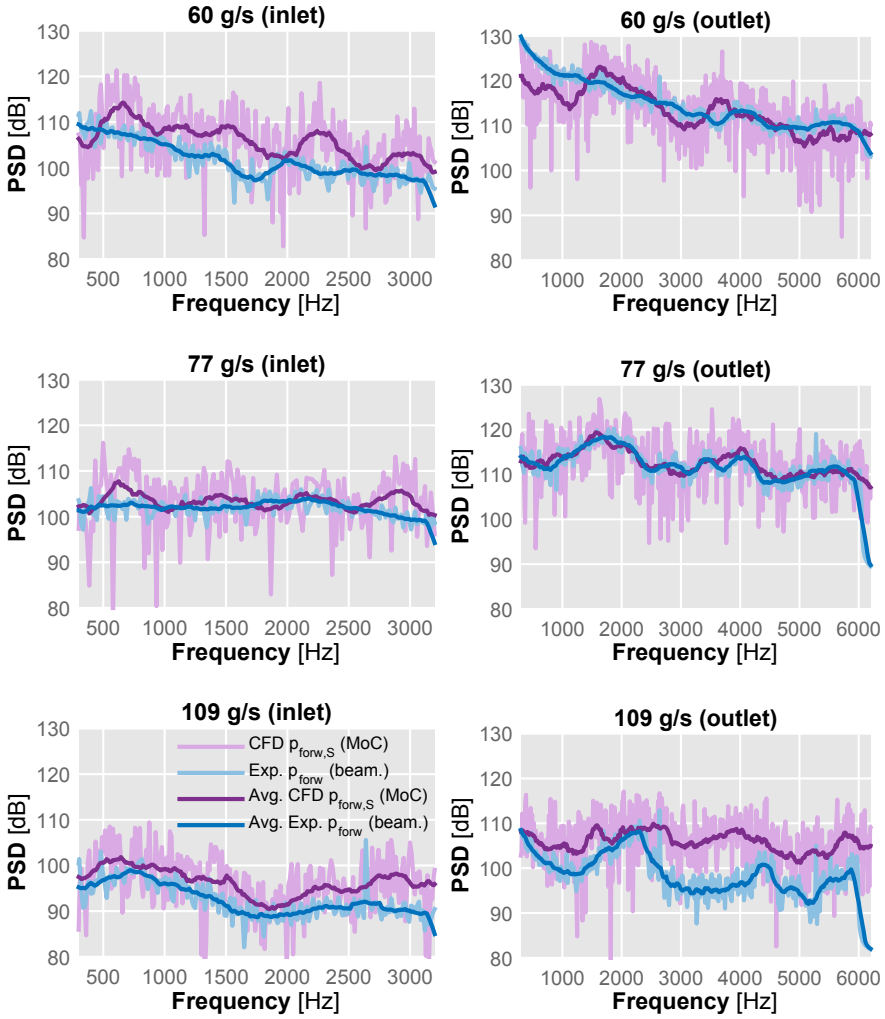

Figure 6.10: *Comparison of decomposed spectra in the plane wave range for all three operating conditions and both ducts against experimental results.*

In Fig. 6.10 a comparison is made in the same fashion as in Fig. 6.8 where decomposed experimental and numerical signals are compared, selecting the surface CFD monitor. The frequency range is thus limited by the experimental spatial criterion, not the first acoustical mode onset. It can be seen that, although not featuring as good match as in the 77 g/s case, the new simulations show a similar trend in spectral content compared against experimental results.

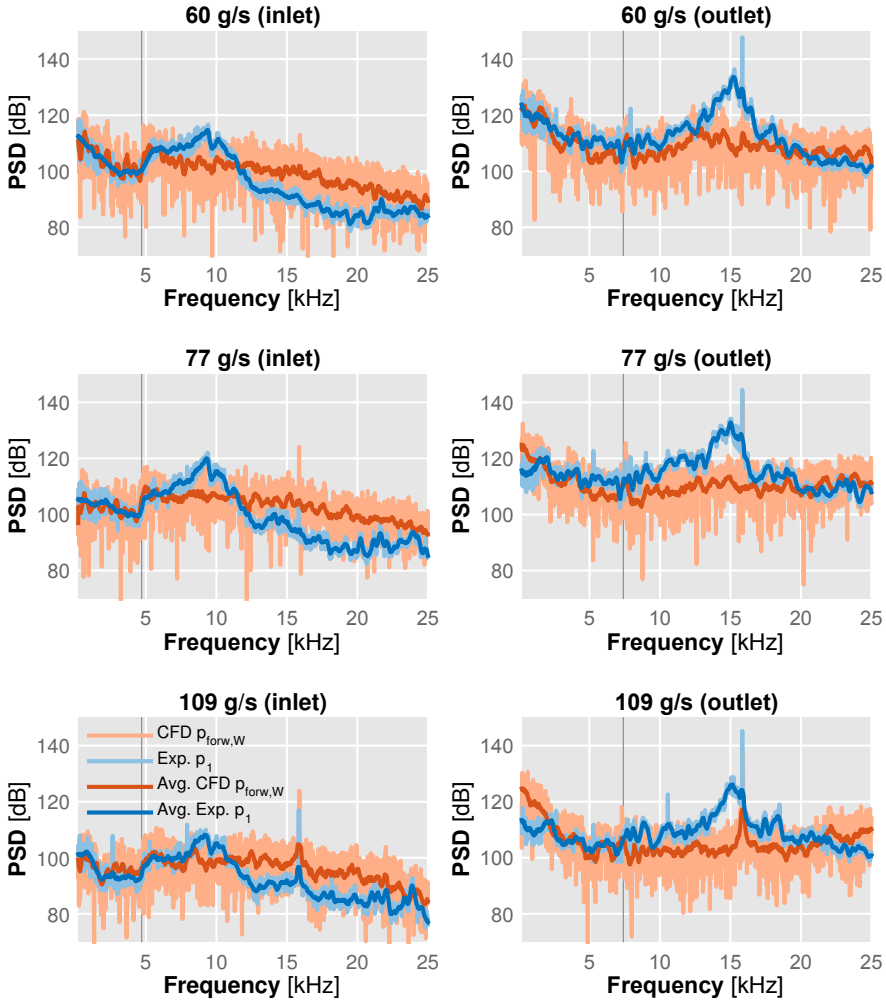

Figure 6.11: *Comparison of pressure spectra for all three operating conditions and both ducts against experimental results. In this figure, pressure wave decomposition is only performed in the CFD spectra.*

Regarding the full audible range of the spectrum, in Fig. 6.11 a comparison is presented where the decomposed signal of the CFD wall monitor (which was shown previously to result in better prediction of higher frequency spectral content) is compared with the experimental pressure spectra from a single sensor (as decomposition cannot be performed experimentally in the full frequency range). The plane wave range of each plot is shown enlarged in Fig. 6.12.

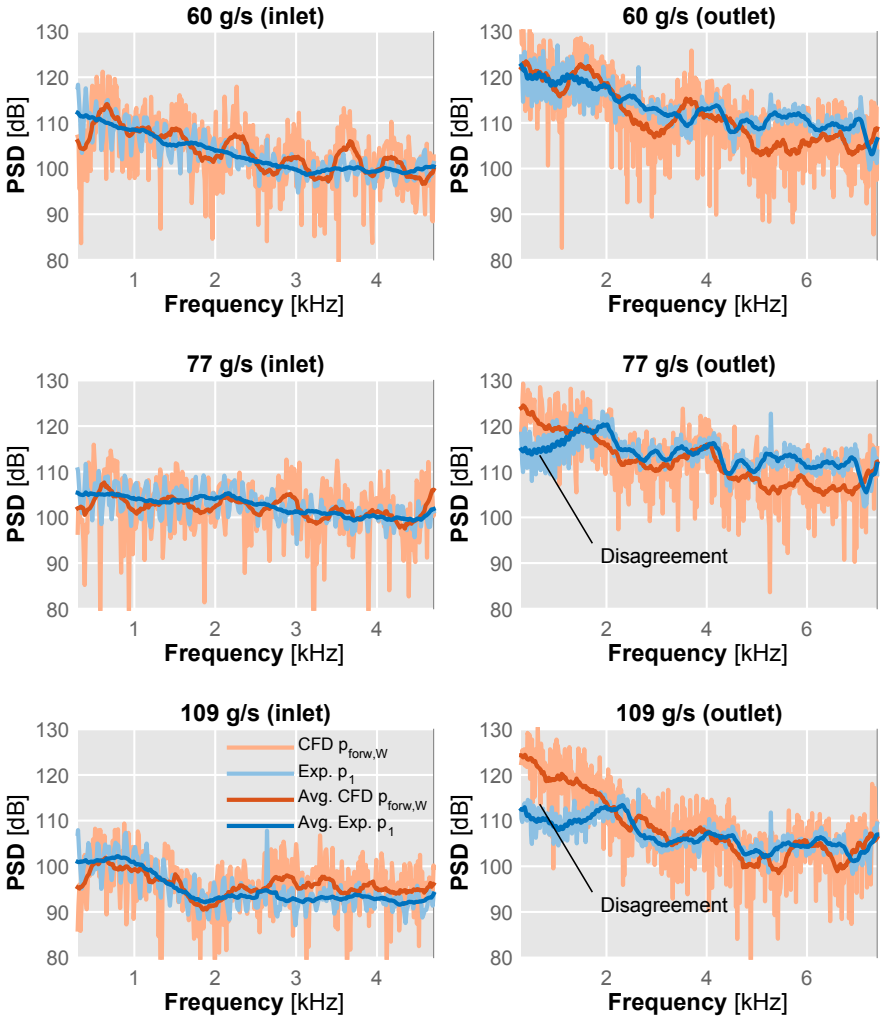

Figure 6.12: *Comparison of pressure spectra for all three operating conditions and both ducts against experimental results in the plane wave range. In this figure, pressure wave decomposition is only performed in the CFD spectra.*

Analysis of these last two figures shows that the prediction capability of the model in the higher frequencies is similar in the two new simulations that in the reference one of 77 g/s. The higher frequency broadband seen in both inlet and outlet ducts is still not reproduced by the CFD results, and the level of the high frequency content in the inlet duct is still over-predicted.

Inspecting the plane wave range seen in Fig. 6.12 it is apparent that in the case of the inlet, while still not a perfect match the trends of each flow rate operating point feature good agreement to the experimental data.

In the case of the outlet results, while the trend at the lowest flow condition is well predicted, for the two higher flow points of 77 and 109 g/s the simulated spectral content captured by the wall monitor does not reproduce correctly the *whoosh* noise hump between 1 and 2.5 kHz, over-predicting the level of the lowest frequencies.

6.3.3. Selected CFD results

While the prediction of spectral content is not totally accurate yet, specially in terms of levels, and thus more research should be devoted to enhance the numerical model of the compressor, it has been shown that the model is precise enough to reproduce the trends in spectral content, allowing some selected results to be presented in order to provide better insight into the flow conditions in the compressor.

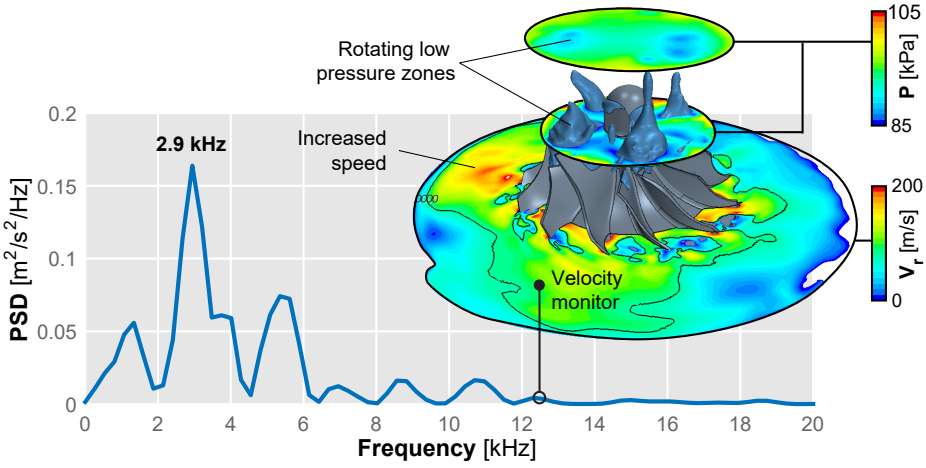

Figure 6.13: *Combination of selected CFD results for the lowest mass flow rate operating condition (60 g/s), including pressure and velocity field and diffuser frequency spectrum.*

The kind of results that can be extracted from the CFD simulation are exemplified in Fig. 6.13, which combines the 3D model of the compressor wheel with plane views of the pressure and velocity fields, and frequency information extracted from the time record of a particular position in the diffuser. Since the CFD setup is using a rotating mesh approach, the whole diffuser fluid domain is rotating, so this monitor is not stationary.

Pressure information is presented in two planes, at the top of the inducer and at the leading edge plane. 3D isosurfaces of $P = 85$ kPa are also shown, forming "bubbles" that move from one channel to the next at a frequency lower than that imposed by the wheel rotation. These recirculation "bubbles" have been sometimes linked to broadband acoustic phenomena of half rotating order (RO) [118, 119].

The radial velocity field is shown in the diffuser and the volute, revealing an asymmetrical field and the presence of a higher speed zone near the volute tongue. Frequency signature of the monitor is shown in the figure, peaking at 2.9 kHz (∼10% over RO) and presenting two sidelobes. These pulsations could also be related to *whoosh* noise generation.

Taking advantage of the three simulated flow rate conditions. in Fig. 6.14 the meridional velocity magnitude across the compressor wheel has been plotted into an extended isospan surface. Data to build this surface has been extracted from the inducer, the wheel, the diffuser and the volute, as shown in the accompanying graphic.

This allows to compare how the velocity field changes across the compressor in all three of the selected operating conditions. Differences are easily noticed between the point of higher flow and higher isentropic efficiency (bottom) and the other two points.

In the 109 g/s simulation the velocity field is more axisymmetric, with all blades and channels presenting a similar distribution. Flow in the inducer is very regular, being attached to the blades in all cases. Flow distribution in the diffuser and volute is no longer axisymmetric, featuring instead a wake trail for each blade. Also, vortex shedding can be appreciated even in these conditions close to the maximum efficiency point.

As mass flow rate of the CFD boundary condition was reduced to 77 g/s, a more irregular velocity field is shown in the middle plot of the figure. Flow in the inducer is not so regular as before, with some main blades featuring reversed flow at the suction side (SS) near the leading edge creating flow detachment. In the diffuser, a zone featuring increased velocity can be seen near the tongue, where the volute is smaller, with the wake of the blades not being so apparent as before.

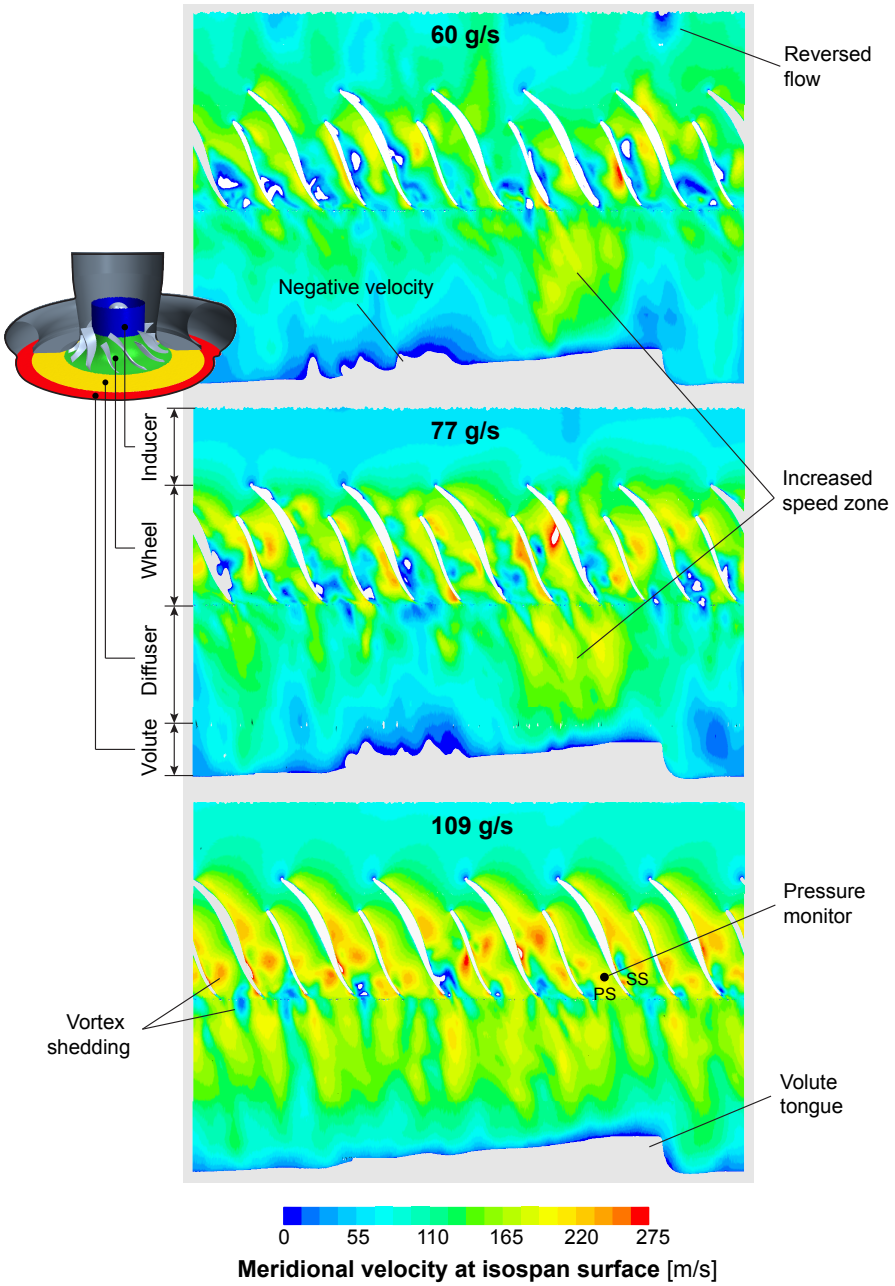

Figure 6.14: *Comparison of meridional velocity field in a blade-to-blade isospan surface, for the three selected operating conditions of the CFD model.*

For the lowest flow rate condition at 60 g/s, the flow field in the inducer became highly irregular, featuring some zone with reversed flow. Severe detachment of the flow can be appreciated in most of the blades, accompanied by a similar high velocity zone in the diffuser near the volute tongue.

The presence of this high velocity zone (which by continuity also affects pressure) can also be seen by attaching a moving pressure monitor to the pressure side of one of the blades (marked with a black dot in Fig. 6.14) and plotting the measured spectra, as seen in Fig. 6.15. Similarly to the previously discussed velocity spectra, a peak is shown at the frequency of the rotating order as the structure is seen by the blade once each revolution. A secondary peak appears also at 2 RO, but the sidelobes are not reproduced.

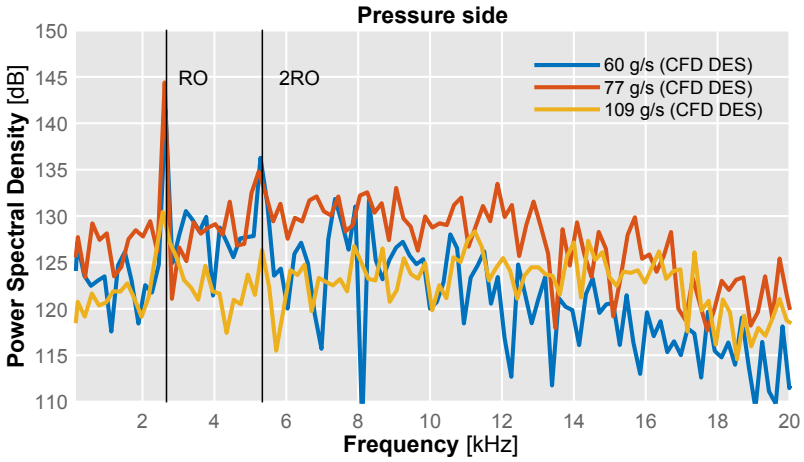

Figure 6.15: *Comparison of pressure spectral content recorded at the pressure side of the trailing edge of an impeller blade between the three simulated operating conditions.*

These peaks are much more pronounced for the two cases of lower mass flow rate where this zone was more easily identified, but still appears for the 109 g/s case, indicating that still some influence of the volute restriction affects the blades when they pass through this particular angular position.

Of particular interest among the different results that can be extracted from the CFD simulation is the opportunity to analyze the complex flow field that develops in the inducer and final part of the inlet duct as operating conditions reach the mild surge area of the compressor map and flow is reversed in direction.

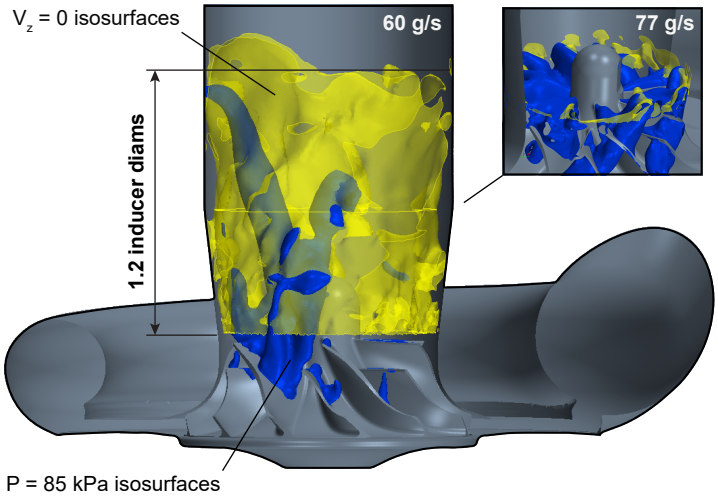

Figure 6.16: *Isosurfaces of null axial velocity in the compressor inducer/inlet showing the reversed flow extent and distribution, including isosurfaces of low pressure "bubbles" in the same region.*

In Fig. 6.16 this backflow is characterized for the 60 g/s condition (which is well inside the marginal surge area as demonstrated by the slope of the speed line) by plotting the isosurfaces where $V_z = 0$ m/s. At this operating condition some low pressure "bubbles" of stalled flow are also present in the inducer and are also plotted as isosurfaces, as in the previously seen Fig. 6.13.

The same data is also shown in an inset plot for the 77 g/s operating condition, which is the point that both experimental data and DES CFD simulations identify as the one where the slope of the speed line reaches zero and the marginal surge zone starts.

This 3D view of the pressure and velocity information shows how the low pressure bubbles extend up to the limit of the reversed flow, in both operating conditions. However, these low pressure zones are much more axisymmetric in the 77 g/s point, whereas in the lower flow rate case they become isolated and elongated. Time data shows also how they rotate inside the backflow-affected area in a tornado-like fashion.

Regarding the backflow itself as characterized by the null vertical velocity in the inlet, the figure shows the drastic evolution from an incipient recirculation at 77 g/s very close to the wheel, to the fully developed backflow at

60 g/s, reaching upstream up to 1.2 inducer diameters. It is also shown in the 77 g/s view how this backflow will start appearing close to the inducer walls, leaving the core flow still unperturbed.

6.4. Acoustic source location

While the analysis of raw pressure and velocity monitors can shed light into the behaviour of the compressor from the fluid dynamics point of view by identifying flow structures and spectral content at selected points of the domain, other data post-processing techniques can be used to obtain further insight into the acoustic behaviour of the system.

6.4.1. Fourier analysis

A way to explore the spatial distribution of the acoustic sources for different frequencies of interest is to perform the Fourier transform at each cell of different surfaces like walls and planes. Then, the amplitude of the transformed signal at the frequency of interest is used to color each cell of the selected surfaces, be it directly or through a smoothing interpolation.

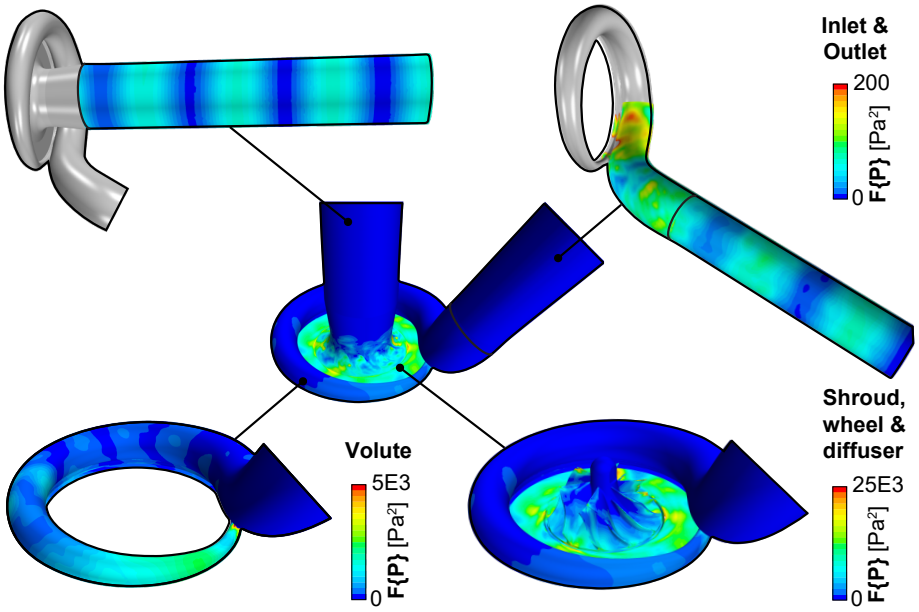

Figure 6.17: *Selected domain walls colored by the amplitude of the 3 kHz component of the simulated pressure signal at 160 krpm and 77 g/s.*

These kind of results are shown in Fig. 6.17 for some selected wall boundaries of the numerical domain. Simulated operating conditions are those of the medium flow rate point at 77 g/s. The chosen frequency component has been 3 kHz, as it is relevant in the phenomenon of *whoosh* noise issue that is of special concern regarding the identification of source flow mechanisms behind its inception.

From the figure it can be surmised that the pressure signal exhibits its stronger 3 kHz component at the diffuser and the downstream half of the blade chords, towards the trailing edges. Color scale needs to be magnified in order to appreciate the distribution in the volute, which is stronger at its narrower part near the tongue. The scale needs to be restricted again to see the pattern at the inlet and outlet ducts, in the form of a standing wave.

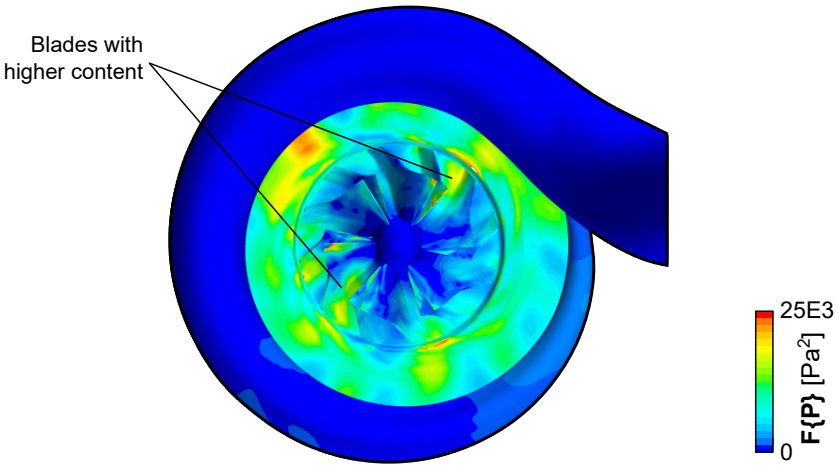

Figure 6.18: *Volute, wheel and diffuser walls colored by the amplitude of the 3 kHz component of the simulated pressure signal at 160 krpm and 77 g/s.*

Focusing in the diffuser and the wheel, Fig. 6.18 shows a perpendicular view of the diffuser plane. As it is apparent from the plot, distribution of the content amplitude is not axisymmetric neither in the diffuser nor in the wheel, with two opposite zones of the rotor appear to feature higher content at the selected frequency. It can also be seen how the trailing edges of the rotor blades seems to feature a higher amplitude that the leading edges, which could indicate an influence of the vortex shedding mechanism evidenced by Fig. 6.14.

6.4.2. Modal decomposition

However, while the Fourier analysis method allows the obtaining of interesting results in a simple, straightforward way which moreover can be found already implemented in some commercial CFD codes, it is not without disadvantages.

Among them is the need to manually select both the surfaces and the frequencies of interest, thereby having the risk of missing relevant regions or frequencies, which are not known beforehand. Also, in more complex geometries or flow structures it could be difficult to pinpoint exactly relevant features, requiring the placement of multiple planes in the domain to reconstruct these structures.

6.4.2.1. Proper Orthogonal Decomposition

In order to address these limitations, more sophisticated analysis can be carried out in the form of modal decomposition of the flow field. One of the most used among these is probably the Proper Orthogonal Decomposition (POD) or Karhunen–Loève expansion, which originated in the field of probability theory and was first applied to the analysis of turbulent flow in 1967 [120]. As (rather poetically) put by Aubry in the aptly named paper *"On the Hidden Beauty of the Proper Orthogonal Decomposition"* [121], the objective of this technique is that:

> *"The flow is decomposed into both spatial and temporal orthogonal modes which are coupled: each space component is associated with a time component partner. The latter is the time evolution of the former and the former is the spatial configuration of the latter."*

In this way, this decomposition allows the identification of which spatial structures comprise the most energy of the flow field, which is understood as the superposition of all modes. The ordering of the contribution of each mode however, allows in principle a simplified yet meaningful reconstruction of the flow field. This is realized by diagonalizing the time-averaged spatial correlation matrix assembled with temporal "snapshots" of the flow, obtained either numerically or experimentally [122, 123].

Principal drawbacks of this method include that in some cases energy may not be the most relevant metric in characterizing the relevance of flow structures [122], and that the use of second-order flow statistics can result in a loss of information such as phase [121], failing to capture the dynamics of the coherent structures of the flow [124].

Moreover, while modes resulting from POD exhibit spatial orthogonality, they can contain multi-frequency temporal content [125, 126]. This means that a particular flow structure can be excited by different phenomena and at different frequencies, yet remain spatially coherent in time and thus result in a higher energy POD mode.

Linking the spatial structures with a specific phenomena requires, as a consequence, some guesswork based on prior knowledge of the excitation mechanisms. A good example of this is the application of POD to the CFD simulation of an engine manifold presented by Sakowitz [126], where it can be seen how the first POD mode contains different frequency content originated from both the engine firing and the valve opening.

6.4.2.2. Dynamic Mode Decomposition

An alternative decomposition technique known as Dynamic Mode Decomposition (DMD) that addresses these shortcomings is also presented in the same work. A relatively recent technique for modal flow decomposition [122, 127, 128], DMD is a *data-based* procedure that aims to extract dynamic information from only the snapshots of a non-linear system while avoiding any need for previous knowledge [122].

This is done by computing the eigenvalues and eigenvectors of a linear model which approximates the underlying dynamics of a system, which may not be necessarily linear [128]. The DMD modes (eigenvectors) calculated using this technique represent again coherent spatial structures of the flow, in this case not necessarily orthogonal but each one featuring a single temporal frequency [125], in contrast with POD modes. DMD eigenvalues represent the rates of decay and growth of these modes, along with their associated frequency.

Evaluation of the relevance of each mode to the dynamics of the system is usually performed by computing the norm of the mode, although Dahan et al. reported [129] that in some cases it may be preferable to order the modes attending to their frequency rather that their norm, as some modes may feature a growth rate of less than the unity, and thus they may be damped over time.

Furthermore, another advantage of the DMD and POD techniques is that it can be proved [122, 124] that processing only subdomain data is possible, be it this subdomain a small region of the domain or even a projection of the 3D field into a 2D plane, as no spatial arrangement is assumed by either method. This is convenient as post-processing can be restricted to an area of the flow where relevant phenomena are expected, saving computational effort.

6.4.2.3. DMD implementation

As several variations for implementing a DMD strategy already exist in the literature only the basic concept originally proposed by Schmid [122] will be shown in this section. Generally, information on the flow field evolution coming from either numerical simulations or experimental measurements[2] will be naturally presented in a sequence of N vectors $\mathbf{v}_i$ representing temporal snapshots that can be gathered in a matrix $\mathbf{V}$:

$$\mathbf{V}_1^N = \{\mathbf{v}_1, \mathbf{v}_2, \ldots, \mathbf{v}_N\} \tag{6.4.1}$$

Each snapshot contains a quantity M of scalar flow magnitudes which in the case of experimental results usually represent the velocity information. In the case of numerical simulations these snapshots may represent other useful information such as pressure, species, etc. These snapshots should be separated by a constant time step Δt, and are assumed to be linearly related through a certain matrix $\mathbf{A}$, which is assumed to remain approximately constant during the time $N\Delta t$ spanned by the sequence:

$$\mathbf{v}_{i+1} = \mathbf{A}\mathbf{v}_i \tag{6.4.2}$$

Even if the flow field is non-linear, matrix $\mathbf{A}$ will provide a linear tangent approximation of the dynamic characteristics of the flow. The objective is now to extract its eigenvalues and eigenvectors which, will be the DMD eigenvalues and the DMD modes of the flow. Combining both expressions in matrix form we can write that:

$$\mathbf{V}_2^N = \mathbf{A}\mathbf{V}_1^{N-1} \tag{6.4.3}$$

[2] For instance, from experimental Particle Image Velocimetry (PIV) measurements that capture a sequence of velocity field snapshots.

Where $\mathbf{V}_2^N$ contains snapshots 2 to N and $\mathbf{V}_1^{N-1}$ contains snapshots 1 to $N-1$. As M for CFD simulations is usually in the order of 10^6 and N must comprise a sensible amount of time steps in order to ensure that the dynamic characteristics are well captured, directly performing the eigendecomposition of $\mathbf{A}$ is usually too computationally expensive.

In order to overcome this problem different strategies exist, such as reformulating 6.4.3 into a companion matrix that can be solved through a QR decomposition [123, 124, 127]. A more numerically stable method however is to make use of the Singular Value Decomposition (SVD) [122, 125, 126, 128] to obtain $\mathbf{V}_1^{N-1} = \mathbf{U}\mathbf{\Sigma}\mathbf{W}^T$. Then, 6.4.3 becomes:

$$\mathbf{V}_2^N = \mathbf{A}\mathbf{U}\mathbf{\Sigma}\mathbf{W}^T \tag{6.4.4}$$

From this expression it is now possible to manipulate the terms that are already known in order to define a new matrix $\widetilde{\mathbf{S}}$, which will be thus related to $\mathbf{A}$ in the following way:

$$\widetilde{\mathbf{S}} \triangleq \mathbf{U}^T\mathbf{V}_2^N\mathbf{W}\mathbf{\Sigma}^{-1} = \mathbf{U}^T\mathbf{A}\mathbf{U} \tag{6.4.5}$$

It can be seen that this relationship between $\widetilde{\mathbf{S}}$ and $\mathbf{A}$ matches the definition of *matrix similarity*. Thus, $\widetilde{\mathbf{S}}$ is similar to $\mathbf{A}$ and as a consequence their eigenvalues λ_i are the same, with the advantage that $\widetilde{\mathbf{S}}$ is of reduced size and easier to solve. The DMD modes Φ_i can finally be calculated from the eigenvectors y_i of $\widetilde{\mathbf{S}}$ as:

$$\Phi_i = \mathbf{U}y_i \tag{6.4.6}$$

The frequency associated with each spatial mode can be recovered by evaluating the imaginary part of each complex eigenvalue, and taking into account the time step Δt between snapshots:

$$f_i = \frac{\omega_i}{2\pi} = \frac{\Im\{\ln(\lambda_i)\}}{2\pi\Delta t} \tag{6.4.7}$$

As for ranking the contribution of each mode to the total flow field, several approaches can be followed. Since many eigendecomposition routines normalize the eigenvectors [130], simply computing their ℓ_2 norm is not always reliable.

The energy of the modes can be recovered by solving a linear system in which the DMD-reconstructed field multiplied by unknown amplitudes is compared against a selected snapshot [130]. It is also possible to optimize these amplitudes to promote a more sparse reconstruction of the field with fewer modes [125].

Another ranking metric was considered by Schmid [122] in his original DMD formulation, based on the computation of the modes' coherence in time. This can be done by first calculating matrix $\mathbf{G}$ [131]:

$$\mathbf{G} = \mathbf{V}_1^{N-1} \mathbf{\Sigma}^{-1} \mathbf{Y} \tag{6.4.8}$$

Where $\mathbf{Y}$ is the matrix that gathers the eigenmodes y_i of $\widetilde{\mathbf{S}}$. Then for each column $\mathbf{g}_{*,i}$ of $\mathbf{G}$, the coherence E_i of each DMD mode Φ_i can be obtained as the inverse of its norm:

$$E_i = ||\mathbf{g}_{*,i}||^{-1} \tag{6.4.9}$$

A disadvantage of this solution for ranking the modes is that the true magnitudes of the vectors for flow reconstruction purposes remain unknown. If flow reconstruction is desired, for instance aiming to simplify the application of the Ffowcs Williams-Hawkings acoustical propagation procedure [132] as done by Dahan et al. [129], solving the amplitudes in a reference snapshot as done by the `dymode` code [130] or the use of the sparsity-promoting procedure by Jovanović et al. [125] are recommended instead.

6.4.2.4. Sample DMD results

In order to provide an example of application of DMD to the CFD simulation considered in this chapter, preliminary work was done by implementing the original SVD-based DMD procedure with coherence ranking.

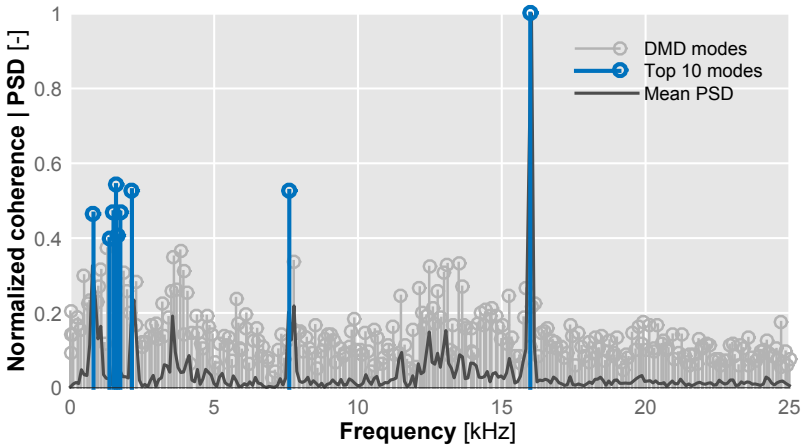

Figure 6.19: *Normalized coherence of the outlet surface DMD modes, highlighting the top 10 and including normalized magnitude of the average PSD.*

The procedure was applied to a limited subset of the available data, specifically to the dynamic pressure information at cells near the outlet wall, as in this particular CFD setup information about the pressure at every cell of the domain was not saved.

Due to the POD/DMD property that allows the selection of a subdomain instead of the whole domain, results in the selected zone should however be representative. Furthermore, data downsampling was performed both spatially and temporally by considering one in ten cells and one in ten snapshots, resulting in a spatial length of $M \sim 7 \times 10^3$ and a temporal length of $N \sim 10^3$.

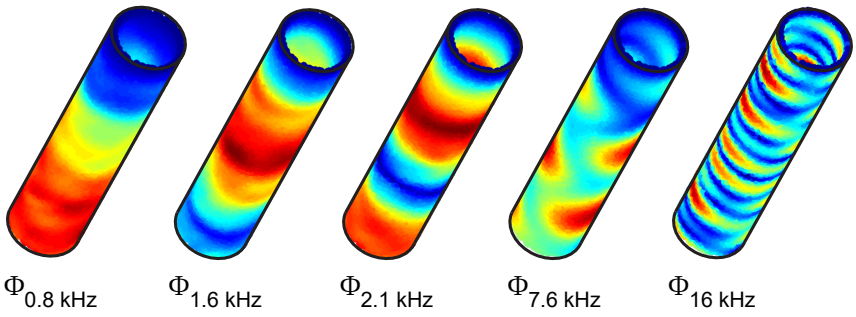

Figure 6.20: *Normalized amplitude (lower values in blue, higher values in red) of selected outlet surface DMD modes featuring a higher temporal coherence.*

In Fig. 6.19 the normalized coherence $E_i/E_{\max}$ of each DMD mode Φ_i has been plotted, highlighting the top 10 modes with the higher coherence. An average PSD of the pressure content is also presented, showing a good agreement with the mode coherence. In both cases the maximum is located at a frequency $f_i \sim 16$ kHz, which in the computed modal space corresponds to mode Φ_{323} and is related to the blade passing frequency (BPF).

Besides the BPF tonal noise, another relevant DMD mode appears at approximately half of this frequency (7.6 kHz). Coincidentally, this specific frequency is similar to the onset frequency of the first asymmetric acoustic mode (7.4 kHz). At lower frequency (<3kHz) several coherent modes appear, demonstrating the relevance of this particular frequency band, typical of *whoosh* noise. However, it appears that content in this band is not dominated by a particular mode. Finally, modes related to the TCN-like broadband noise seem to be less spatially coherent than those related to *whoosh* and BPF tonal noise.

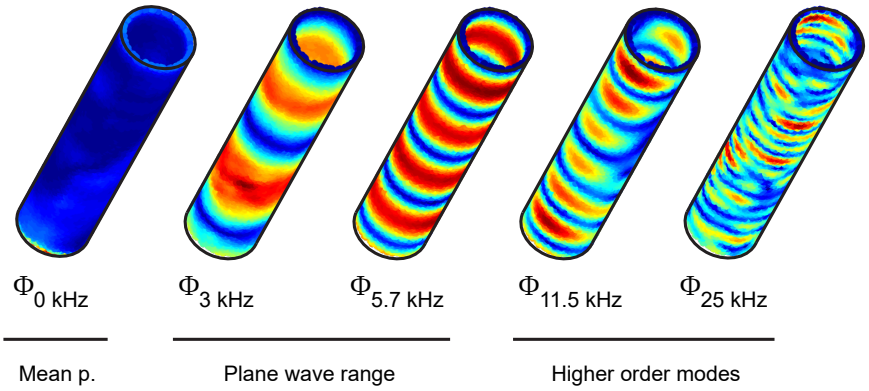

Figure 6.21: *Normalized amplitude (lower values in blue, higher values in red) of selected outlet surface DMD modes showcasing the effect of acoustic mode propagation.*

The spatial distribution of some DMD modes is plotted in Fig. 6.20. It can be seen in this figure how the content of the spatial modes is distributed along the outlet duct. The first three modes of lower frequency ($\Phi_{0.8\ kHz}$, $\Phi_{1.6\ kHz}$ and $\Phi_{2.1\ kHz}$) feature a distribution that is related to the plane wave propagation, with the modes at higher frequency showing a more complex distribution as a result of the onset of the different acoustic modes.

The influence of mode frequency and acoustic mode propagation in the distribution of the spatial content of the DMD modes can be seen in Fig. 6.21, where some DMD modes are selected to showcase this evolution.

In the leftmost plot the mode corresponding to the 0 kHz frequency has been selected, with the result showing the expected uniform distribution along the outlet duct (save for some small regions that are probably the result of numerical error). As frequency increases a pattern typical of a standing wave starts to appear in the simulated duct. Note specially the similarity between the distribution of the $\Phi_{3\ kHz}$ mode and the magnitude of the FFT in the compressor outlet duct shown in Fig. 6.17.

When higher order acoustic modes start propagating in the CFD simulation, the pattern changes. DMD mode $\Phi_{11.5\ kHz}$ shows the effect of the first asymmetrical mode, denoted as (0,1) in Eriksson's notation [94], as the content is no longer homogeneous in each section but dependant on the angle as well. Finally, mode $\Phi_{25\ kHz}$ features a very complex pattern as modes (0,1), (0,2), (0,3), (1,0) and (1,1) are propagating at these higher frequencies.

6.5. Conclusions

In this chapter a numerical simulation of the compressor characterized in chapter 4 has been validated regarding not only the global operating variables but specifically taking into account the acoustic point of view, which is usually not addressed in detail in many works regarding the simulation of automotive compressors.

It has been shown how the definition of the domain and boundary conditions has a large influence on the spectral information that can be recovered from the simulation results, by creating spurious reflections and standing waves that are not present in the experimental setup.

To address this issue while keeping the CFD domain and mesh within the limits of usual computational capacity the use of pressure wave decomposition has been shown both in numerical and experimental results, allowing enhanced isolation and recovery of the spectral information coming from the compressor and filtering spurious interferences.

Selection of the monitor type and location is also crucial from the acoustic point of view, as it is taking into account the propagation of higher order modes that may render results that are dissimilar from experimental reference data. Wall-flush pressure monitors demonstrated better agreement overall with the experimental measurements, although the area-averaged type of monitor showed better agreement in the outlet at plane wave frequencies, specially regarding the prediction of a *whoosh* frequency broadband at the operating condition of higher pressure ratio which signals the onset of marginal surge conditions and the appearance of reversed flow.

Analysis of the pressure and velocity fields simulated by the CFD models has been shown, in order to identify flow phenomena that may be related to the increased acoustic output at these unstable operating conditions. Contours of velocity and pressure at selected planes and surfaces show rotating low pressure “bubbles” that are linked to the zone of reversed flow, visualized through null axial velocity isosurfaces.

Inspection of these velocity isosurfaces offers a way of predicting the evolution of the backflow as operating conditions change. The point of maximum pressure ratio shows the inception of these backflows in the periphery of the wheel. At the same time, velocity information from a 50% isospan surface shows areas of increased velocity in the diffuser near the volute tongue, except for the case of the higher mass flow case. PSD from the velocity signal in the diffuser shows a peak at 2.9 kHz accompanied by two side peaks, which may be related to the *whoosh* phenomenon.

Moreover, vortex shedding from the compressor blades however is detected in the three simulated conditions, which may be linked to the acoustic emission as they induce a pressure fluctuation in the channels that is rotating with the shaft speed.

Further postprocessing techniques to inspect the location of acoustically-relevant flow features includes the use of the FFT of the pressure signal at selected spatial locations and frequencies of interest. An example has been presented regarding the 3 kHz frequency, showing special prominence of this frequency at the compressor wheel and diffuser.

Finally, in order to avoid the necessity of guessing which are the relevant frequencies and spatial locations, the use of modal decompositions of the flow field has been proposed, discussing advantages and disadvantages of different techniques. A limited-scope example of the formulation and implementation of the Dynamic Mode Decomposition has been shown, with the coherence of the model identifying relevant frequencies of the flow and their associated spatial distribution on the outlet duct wall cells, particularly related to *whoosh* and BPF tonal noise.

While implementation of the DMD technique over the full numerical domain is outside of the scope of this work, as it requires the implementation of computational tools to link Star-CCM+ snapshots with outside libraries that allow the manipulation of data in the order of gigabytes, it has been shown that further research on this topic could lead to a better identification of the spatial location of the most relevant frequency components of the flow field.

CHAPTER 7

Influence of the inlet flow field

As it was seen in the literature review of chapter 2, the inlet flow field immediately upstream of the compressor wheel has demonstrated a significant influence on parameters such as efficiency, maximum mass flow and characteristics of the noise output. CFD simulation results have show a complex flow field when the turbocharger operates in unstable conditions at the marginal surge region of the map.

While some measurements of flow variables have been performed in these conditions, they are often limited to a single sensor such as a thermocouple or pressure transducer, in order to use the reading as a metric for surge prediction. However, in order to validate CFD results and obtain a deeper knowledge of this unstable, reversed flow, in this chapter a measurement campaign is described where the spatial resolution of this phenomenon is taken into account.

7.1. Local measurements methodology

In this section the methodology used to characterize the reversed flow is presented, by measuring variables such as temperature, pressure and velocity at different locations.

7.1.1. Turbocharger modification

Prior to its installation in the gas stand, modifications were made to the selected compressor (similar to those used in previous chapters) in order to accommodate the required local temperature and pressure sensors used to measure these variables.

The compressor housing was modified by removing the original inducer up to the plane of the blade leading edges and substituting it by a removable adaptor piece which incorporates guides for a circumferential array of thermocouples and a miniaturized pressure probe. This adaptor is depicted in red in Figs. 7.1 and 7.2.

A detachable straight pipe section with a linear thermocouple guide was affixed to this adaptor. This configuration offers the possibility of easily substituting the straight section for others with different geometries such as elbows or tapered ducts.

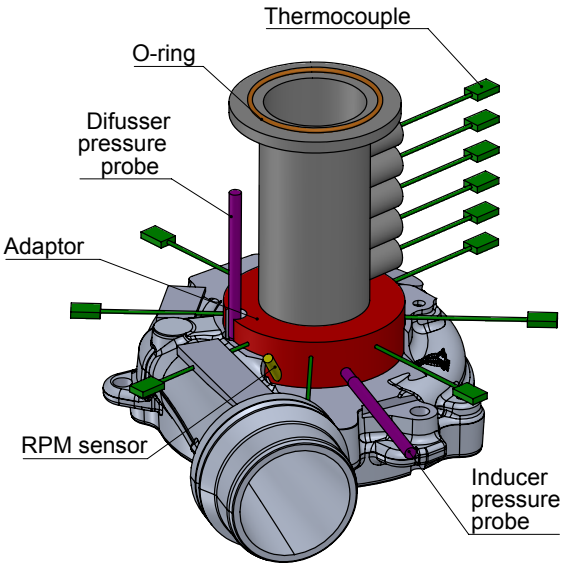

Figure 7.1: *CAD view of the proposed local temperature and pressure measurement instrumentation, showing the distribution of thermocouple arrays and pressure probes.*

7.1.2. Temperature

It is well established on the literature [106, 133] that flow reversing from after the impeller is one of the most telling phenomena signalling compressor instability and stall inception. As these backflows are coming from downstream the wheel they are thus at higher temperature, due to the non-isentropic compression process.

Consequently, not only pressure but also temperature measurement should provide a method for characterizing both the inception of these backflows and their upstream extent. For instance, Liu et al. [52] showed how the standard deviation of temperature and pressure measurements are good indicators of deep surge.

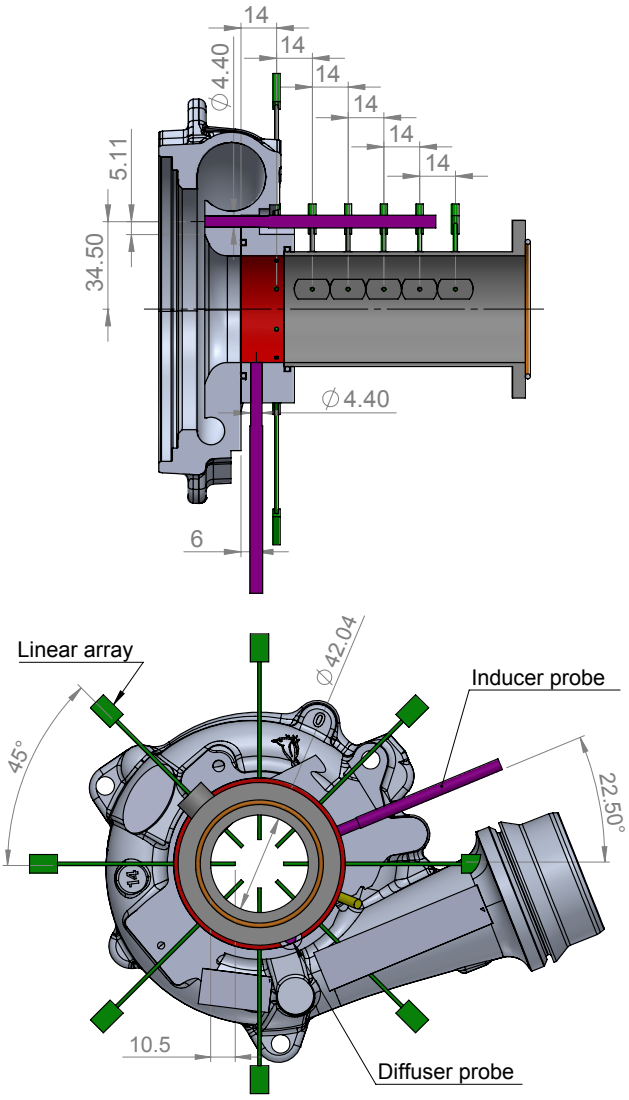

Figure 7.2: *Annotated section view of the pressure probes (purple) and thermocouples (green) location for local measurements (top) and front view of the turbocharger (bottom).*

Two 1.5 mm type K thermocouple arrays were thus installed on the compressor inlet in order to characterize the temperature distribution caused by this backflow. A circumferential array covers a cross section of the pipe just 14 mm from the compressor wheel plane, providing temperature measurements each 45º. The second array is linear, extending in the longitudinal direction of the pipe up to approximately 2 inlet diameters. Both arrays can be seen in Fig. 7.1 and specially in Fig. 7.2.

The first one was intended to tell if angular variations of temperature distribution existed, and the second one aimed to characterize the length of the recirculating backflows at each operating condition of the compressor.

Numerical simulations performed by Lang [49] suggested that backflows extend up to 2 – 3 diameters in length, with a thickness higher than half a radius. Andersen et al. [51]. selected a distance of half the duct radius for placing several thermocouples in the inlet pipe of the compressor, whereas Figurella et al [36] used thermocouples placed in the centre of the pipes and a single one at 14 mm from the blade tips, protruding 4 mm, to characterize the backflow.

Further measurements of temperature were taken, to provide reference points for the two arrays. Ambient temperature of the test chamber is recorded, being the that of the ingested flow. A surface thermocouple was affixed as well to the external wall of the aforementioned circular array adaptor.

All of the thermocouple measurements were captured with the same Yokogawa oscilloscope, and were averaged over one second.

Additionally, a thermographic camera was installed onto the turbocharger assembly, so that its view frame covered both the compressor volute and its inlet pipe duct. This provided a measurement of the external distribution of temperature, that proved useful to validate that the temperature profiles measured by the linear thermocouple array were not caused by heat transfer from the inlet pipe walls.

7.1.3. Pressure

While pressure measurements are usually carried out in both inlet and outlet ducts of the compressor, an effort has been made to characterize the spectral signature of the pressure in two critical locations: on the inducer, upstream the compressor wheel and on the diffuser, downstream of the wheel. Miniaturized Kistler type 6055C pressure probes, which are temperature-compensated up to 350ºC, were used in both locations.

The inducer probe was mounted flush to the wall, at a distance of 6 mm from the wheel leading edge to the centreline of the sensor. The diffuser probe was mounted 5 mm from its beginning and 34.5 mm from the turbocharger axis line. Both probes can be seen in Fig. 7.1 and Fig. 7.2.

7.1.4. Velocity

Besides isolated measurements of pressure and temperature, the characterization of the whole flow field is also crucial. Not only for understanding how the backflows interact with the downstream flow, but also to validate CFD predictions of macroscopic flow structures.

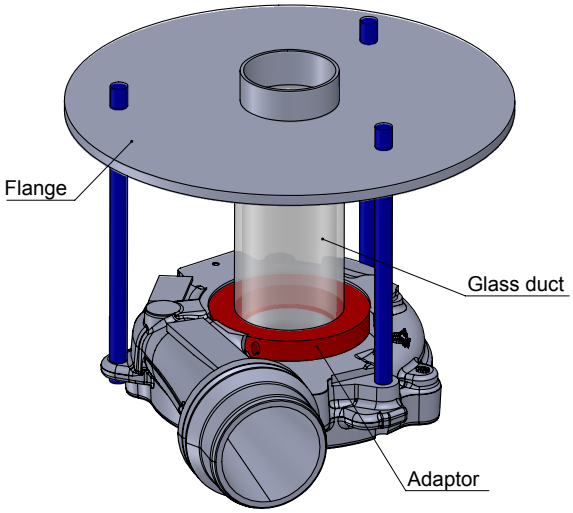

Figure 7.3: *CAD view of the proposed installation for PIV measurements, showing the adaptor piece, the glass tube and the mounting flange.*

7.1.4.1. Laser PIV measurements

In order to allow a characterization of these flow fields, a Particle Image Velocimetry (PIV) system was installed on the anechoic chamber. For PIV measurements, a laser sheet illuminates the measurement region, previously seeded with particles, by means of two consecutive laser shots of a Q-switched Nd:YAG laser. These two laser shots, produced at a user-defined time interval, illuminate the same flow field, so that light scattered by the particles is collected by a straddle CCD camera in two consecutive frames.

Based in these two frames particle position can be determined using cross-correlation algorithms. Hence, instantaneous two-dimensional velocity fields can be computed based on the displacement of particle groups within a given interrogation area of the image and the time step between frames.

Specifically in this study a standard 2D PIV system by TSI has been used for the measurement of the instantaneous two-dimensional velocity fields. It consists of a double-head 15 Hz Nd:YAG laser with 135 mJ/pulse @ 532 nm, a set of mirrors and lenses to drive the laser into the measurement plane and change the laser output 5 mm circular beam into a laser sheet with around 1 mm thickness at the measurement section, a 4Mpixel, 12-bit straddle CCD camera (PowerView Plus 4MP) and a synchronization device. The air flow was seeded with 1 µm oil droplets from an atomiser using the Laskin nozzle principle (TSI 9306A Six-jet atomizer). Figs. 7.3 and 7.4 show the experimental arrangement.

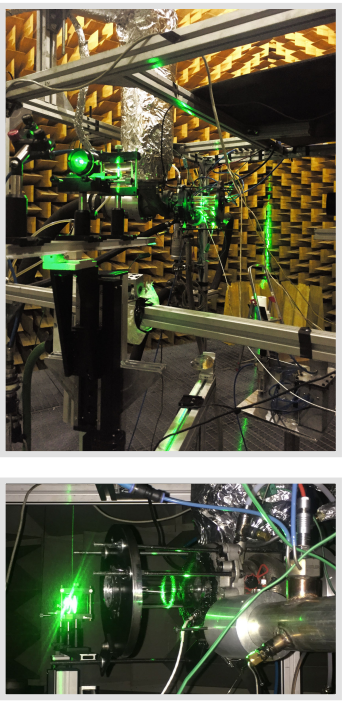

Figure 7.4: *Images of the laser sheet illuminating the glass duct in the transversal PIV setup.*

Images were processed with selected algorithms and validation criteria of the TSI Insight 3G software options. Post-processing, graphical output and analysis tools were complemented with additional processing routines developed in MATLAB for data extraction, comparison and validation.

The magnification of the images taken was around 30 pixel/mm (in fact, between 28 and 32 pixel/mm depending on the arrangement) and the size of the interrogation area for calculation of the cross-correlations was set to 64 × 64 pixels. This leads to the measurement of velocity fields with vectors separated a distance of 32 pixels, i.e. ∼1 mm. Time elapsed between the two laser shots was set to a value between 2 and 10 µs depending on the flow velocities at each test point in the experimental test matrix. Seeding control was proven to be critical, especially in the case of the longitudinal measurements that were made through the walls of the glass pipe.

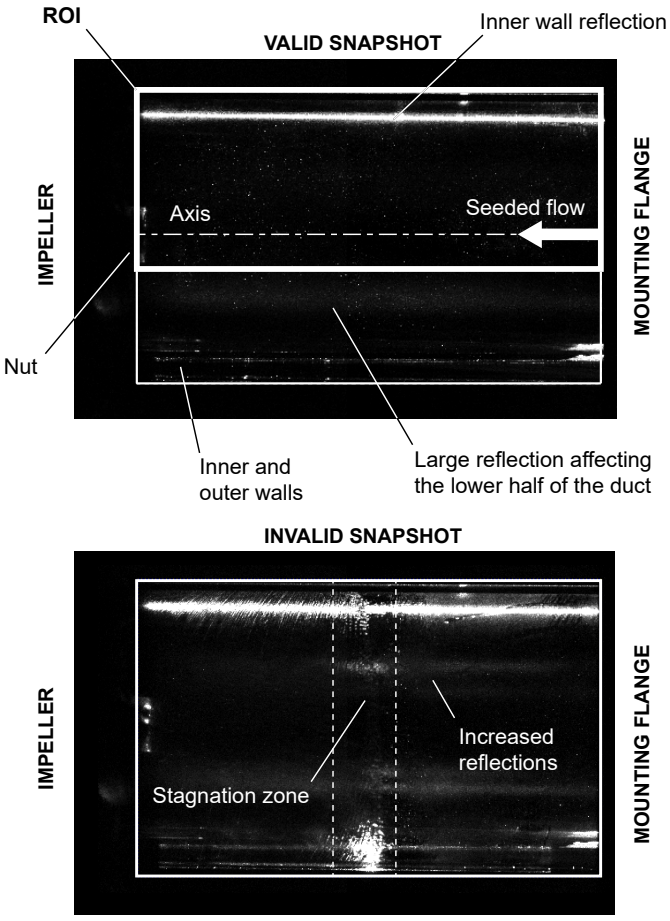

Figure 7.5: *Raw images of the longitudinal plane showing a valid snapshot (top) and an invalid one (bottom) due to oil soiling.*

Even during measurements of the longitudinal plane at stable conditions (high mass flow) where the stalled backflow does not reach upstream the leading edge of the blades, oil accumulated in the inner wall of the glass pipe, obstructing the view and enhancing reflections that rendered the measurement impossible through the affected parts.

Fig. 7.5 shows a raw longitudinal snapshot, detailing how the detrimental reflections reduced the available region of interest (ROI) in which the velocity can be resolved. These reflections were mainly caused by the laser sheet entering and exiting the walls of the glass duct, which are visible in the image.

The issue was aggravated when the backflow generated by the partially stalled compressor blades reached the glass pipe. As there is a zone where the axial velocity is null, oil particles become trapped and start to accumulate, forming a clearly visible fluid "ring" that blocks the view, as seen in Fig 7.5. Also, the high transversal velocity forces the particles to impinge onto the inner wall, forming visible helicoidal tracks along the surface.

As a consequence, a test procedure was followed where the turbo was settled at the desired operating conditions, and then seeding particles were introduced during at least 1 s. This allowed approximately 10 usable pairs of snapshots, after which the turbo was stopped and the glass pipe cleaned for the next run.

Measurement of the transversal planes was done pointing the camera directly towards the compressor, thereby avoiding the need to record through the glass. This allowed for longer test runs because the soiling of the wall did not affect the measurement.

However, measuring the transversal planes was not without issues. In this configuration, the rotor blades are illuminated by the scattered light as shown in the top image of Fig. 7.6, preventing the seeding particles from contrasting enough to be clearly correlated in some places, and generating bright spots that are misidentified as particles moving.

In order to mitigate this problem, a system was devised to feed the pulse train generated by the Hall effect rpm sensor into the laser and camera trigger controller, so that each pair of snapshots were taken at almost the same blade position.

This enabled a postprocessing technique where the average intensity of several non-seeded snapshots was subtracted from each seeded image, greatly reducing the brightness of the illuminated rotor and providing a better particle correlation, as shown in the bottom image of Fig. 7.6. In the case of the longitudinal measurements, this was not deemed necessary since the back of the glass was painted matte and thus provided a good background.

While this resulted in overall enhanced quality of the reconstructed field, small reflections such as that of a small notch at the axis nut could not be removed. Also, in some occasions small glitches in the operation of the sensor resulted in pairs where the two laser pulses were included in the first frame, thereby rendering the pair useless. Fortunately, those cases were easy to identify and remove.

Since apart from the influence of the background the transverse velocity flow was much more chaotic than the longitudinal flow field, the quality of each individual snapshot pair correlation was worse than those of the

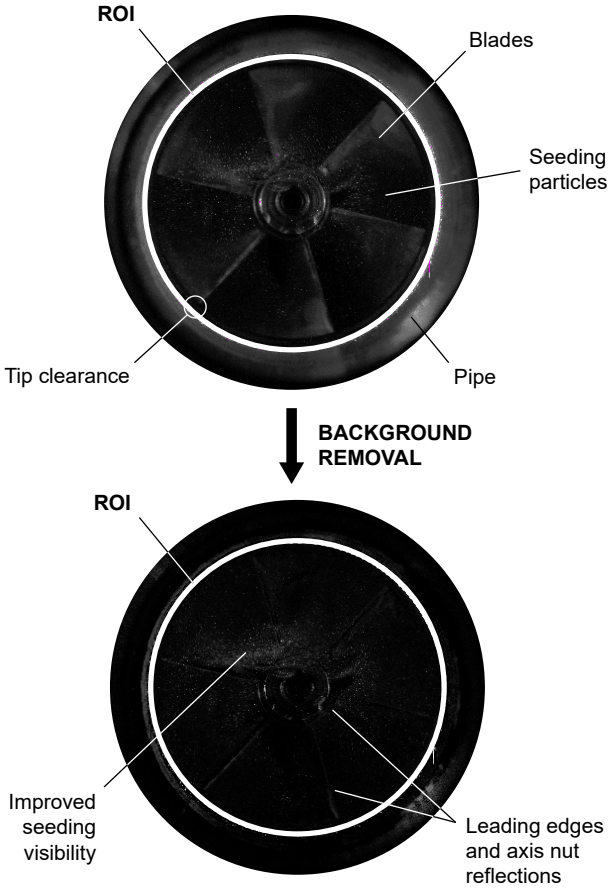

Figure 7.6: *Raw snapshot of the transversal plane (top) and the same snapshot after the background removal postprocessing (bottom).*

longitudinal case as the seeding particles were prone to "lump" together instead of homogeneously distribute, so only parts of the velocity field could be solved in each snapshot pair. This effect can be seen in Fig. 7.6.

However, as the oil soiling of the wall was not as problematic, a larger number of valid pairs could be captured so that the averaged velocity field could still be solved with confidence.

7.2. Results & discussion

Using both setups, data was captured at several turbocharger operating conditions. Different shaft speeds were kept constant while air mass flow was progressively reduced, from a stable operating point close to the compressor maximum efficiency region to an unstable point very close to the compressor deep surge limit. Figure 7.7 shows the recorded points for temperature and pressure measurements. PIV recording points had to be limited due to the time-consuming procedure required to extract valid data.

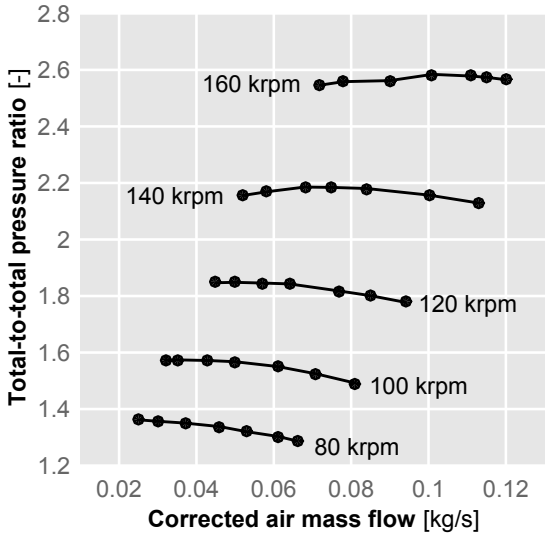

Figure 7.7: *Compressor map showing the operating conditions covered during the measurement campaign, from points close maximum efficiency to points close to deep surge, at different corrected speed lines.*

In order to prevent the appearance of deep surge, with its inherent danger to the integrity of the compressor, pressure signals were monitored to account for the onset of very low frequency components (5 to 20 Hz) which were shown by Galindo et al. [69] to be suitable indicators of deep surge.

7.2.1. Temperature

Different measurements of temperature were performed in this study: a radial profile at two selected locations at a single unstable condition, and a characterization of the circumferential and longitudinal temperature profiles across the selected region of the compressor map.

7.2.1.1. Radial profile

Before the measurement of the whole map, a sweep of temperature measurements along the inlet radius was performed for both the thermocouple located at 14 mm and the thermocouple located at 84 mm. For these measurements, the turbocharger compressor was brought to conditions close to deep surge at 80 krpm and 30 g/s.

The results can be seen in Fig. 7.8. As expected, overall temperature profile is higher at 14 mm (red) from the leading edge plane than at 84 mm (blue). Temperature seems to be approximately constant up to a distance of 0.2 radius from the internal wall, then decaying up to a distance of approximately 0.5 radius from the centreline (which is at 21 mm from the wall). From there onwards, temperature is again approximately constant.

Ambient temperature and surface temperature of the adaptor piece (seen in Figs. 7.1 and 7.2 in red) can also be seen in Fig. 7.8. As expected, centreline temperature at the most upstream point is almost coincident with the ambient, while fluid temperatures near the wall at the most downstream point (at just 14 mm from the wheel) are almost equal to those of the adaptor piece external wall, save for a small initial difference due to thermal loss.

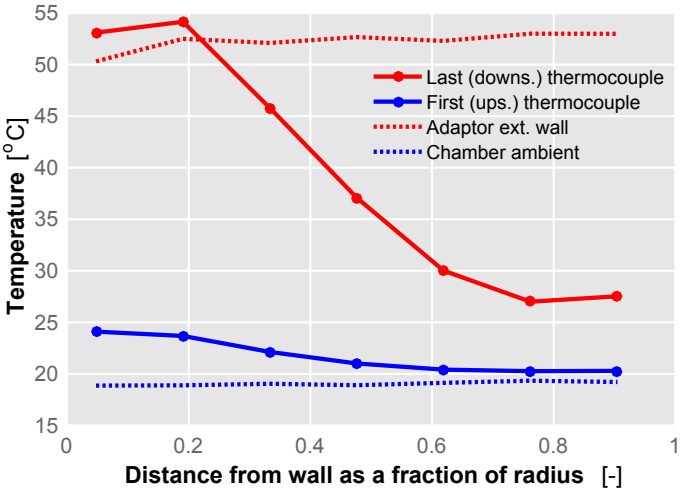

Figure 7.8: *Evolution of temperature measured by the first and last thermocouples of the linear array for different distances from the wall, including measurements of ambient temperature of the chamber and surface temperature of the adaptor.*

From this results it is apparent that measuring the fluid temperature near the wall is not practical due to the thermal transfer from the wall (which accumulates heat between measurements) to the thermocouple. Standardized procedures for characterization of flow temperature call for measurements at $r/2$ and $r/3$ where r is the duct radius. It can be seen in Fig. 7.8 that those distances show indeed a depart from wall-influenced temperatures. Ultimately, the distance of $r/2$ (10.5 mm in this case) was chosen for this study in accordance with the work of Andersen et al. [51].

Figure 7.8 also shows how even at the core of the flow there is a rise of temperature of about 8 degrees. It is expected that, even while the hot backflow is expelled near the walls, its high rotational speed contributes to the mixing with the cold core flow and the diffusion of the heat, causing the increase along all the profile.

7.2.1.2. Backflow growth

By analysing the evolution of temperature results over different operating conditions (speed and air mass flow) it is possible to estimate the growth of the recirculating backflow.

Figure 7.9 shows different profiles of temperature difference from the ambient, measured by the linear thermocouple array at a same shaft speed and different mass flows. It can be seen how at higher mass flows the temperature along the inlet pipe is approximately equal to that of the ambient.

When mass flows is reduced a temperature increase coming from the compressor wheel starts to be noticeable, denoting the presence of air heated by the compression process which is reversing in direction due to flow instabilities on the wheel channels. The operating condition of backflow onset appears to approximately correspond to that of maximum pressure ratio at each shaft speed.

Temperature increase grows both in difference from the ambient and distance from the wheel. However, this growth appears to be highly dependent of the particular shaft speed. At lower shaft speeds, growth reaches greater distances from the wheel at lower air flows, but maximum temperature difference is lower. Conversely, at higher shaft speed temperature difference is greater (due to higher pressure ratio) but backflow extent along the inlet pipe is more constrained.

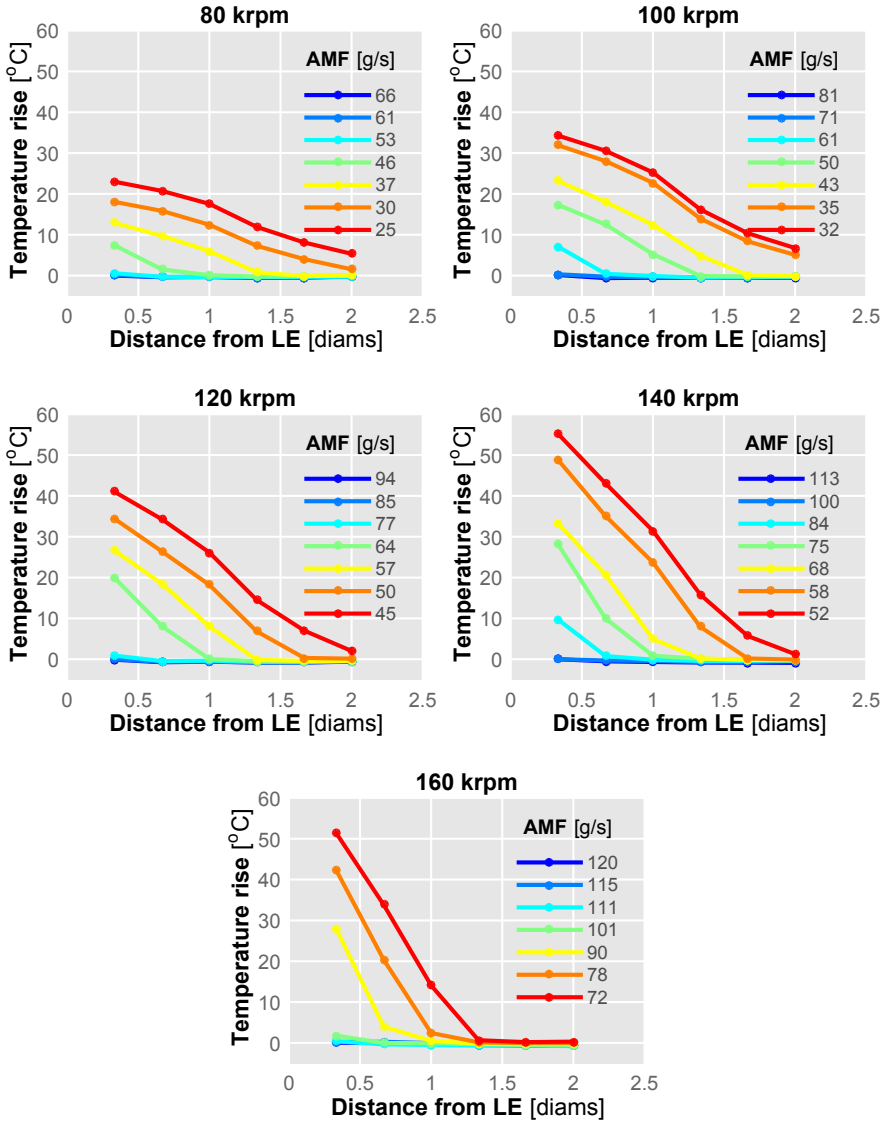

Figure 7.9: *Evolution of temperature rise measured by the linear array thermocouples for different mass flow settings and different shaft speeds, taking the most upstream temperature as reference.*

The reason for this constriction of backflow length at higher shaft speed could be probably attributed to higher inlet flow momentum at those operating conditions. Reduced momentum at lower shaft speeds would instead allow the compressed hot backflow to reach farthest into the inlet line when backflow occurs.

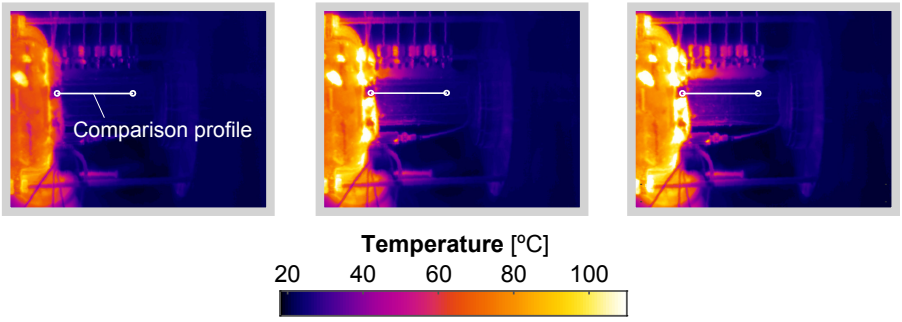

Figure 7.10: *Thermographic (infrared) measurement of the compressor at 140 krpm of shaft speed and different air mass flows, showing the progressive rise of temperature with diminishing air flow. From left to right 111, 71 and 57 g/s. White line indicates the temperature profile compared in Fig. 7.11.*

In order to ensure that the temperature increase along the inlet pipe measured through the thermocouples is indeed caused by compressor backflow and not by thermal diffusion from the compressor housing through the metallic pipe, an additional test run was performed where external thermographic images of the compressor and inlet pipe were captured during the measurements, as shown in Fig. 7.10.

These snapshots were synchronized with the operating conditions at which flow temperatures were measured inside the duct. Inlet pipe radiated wall temperature profiles were extracted to compare their growth against those of the internal flow. Figure 7.11 shows this comparison.

Considering first the higher flow operating condition (blue lines) where there is no backflow exiting the compressor, it is apparent that while the wall temperature follows a typical heat diffusion process where the external wall temperature profile (dotted line) is continuously decaying, the flow temperature measured by the thermocouples (solid line) remains constant through the pipe.

When the flow is restricted (orange lines) the backflow can be clearly seen as the internal thermocouples register a temperature increase up to one diameter upstream. Further upstream of this point the flow temperature remain equal to the most upstream point, whereas the external wall profile shows no such clear turning point.

As for the lowest flow condition (red lines) the temperature increase as measured by the internal thermocouples is higher that the temperature registered by the thermographic camera, so in this case heat would transfer from the hot backflow to the walls and not the other way around.

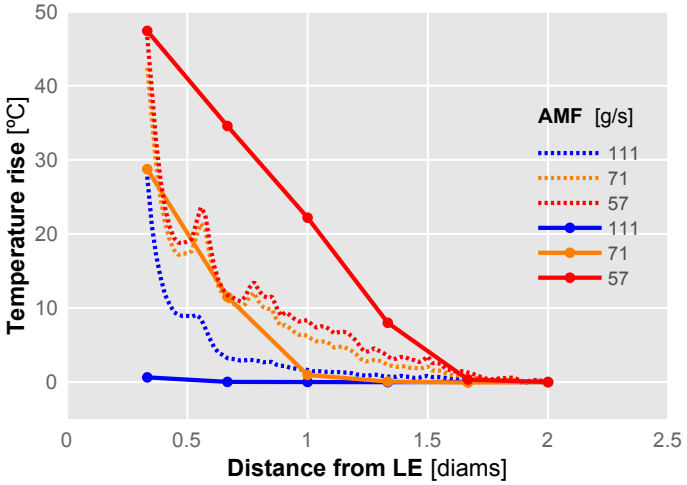

Figure 7.11: *Comparison of the temperature rise measured by the thermographic camera (dotted line) and the internal thermocouples (solid line) for different mass flow settings, taking the most upstream temperature as reference.*

7.2.1.3. Circumferential profile

As previously described, temperature measurements were also recorded using the circumferential thermocouple array situated at 14 mm from the compressor leading edge. The objective in this case was to characterize the angular distribution of temperature near the impeller at different operating conditions.

The result for this study can be seen in Fig. 7.12, where the circumferential temperature profiles at each measured air mass flow regime are plotted for the different shaft speeds considered. These air mass flow regimes were the same as those previously plotted in Fig. 7.9 where the linear array temperatures were shown.

It can be seen that the skewness of the circumferential profile grows with the reduction of mass flow. At higher flow, skewness is practically zero, the profile being completely regular as the temperatures remain similar for all angular positions. However, again at the point of higher pressure ratio, some skewness starts to appear along with an increase in temperature due to the high temperature backflow.

As air mass flow is further decreased towards compressor surge limit, both overall temperature and profile skewness increased. The pattern of the increased skewness appeared to be similar at all conditions: temperature

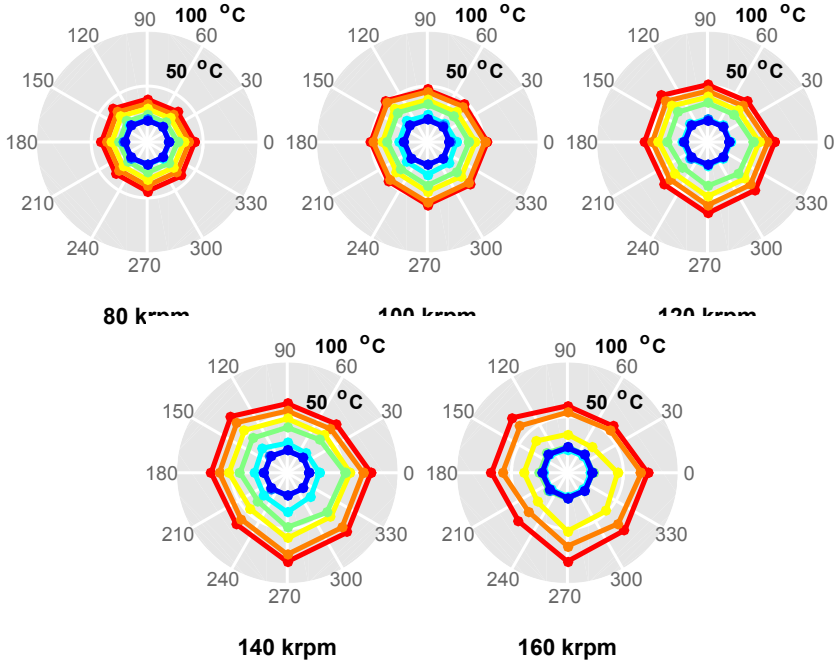

Figure 7.12: *Evolution of temperature measured by the circumferential array thermocouples as air mass flow was reduced keeping shaft speed constant. A polar temperature plot is shown for each speed, colors indicating mass flow from higher (blues) to lower (reds). Legends for colors at each speed are available in Fig. 7.9. See Fig. 7.2 for reference position of the compressor volute.*

was higher at angles corresponding to the tongue and the end of the volute, where its cross-section is larger, and smaller at the angles where the volute cross-section is still small.

Again, while minimum temperatures (corresponding to higher air mass flows) remain similar for all shaft speeds and approximately equal to ambient temperature, maximum temperatures increase with shaft speed. This is coherent with the backflow being hotter due to increased compression ratio.

However, the increased the angular differences of these maximum temperatures is notable, with almost 20°C difference between the 90° and the 270° angular positions at the lower air mass flow regime of the 160 krpm test (red line in the rightmost plot of Fig. 7.12).

7.2.1.4. Temperature compressor maps

In order to visualize how the previously presented temperature results varied with the compressor operating condition, some selected results have been mapped to the compressor map presented in Fig. 7.7 through an interpolation procedure. The result of these mappings can be seen in Fig. 7.13.

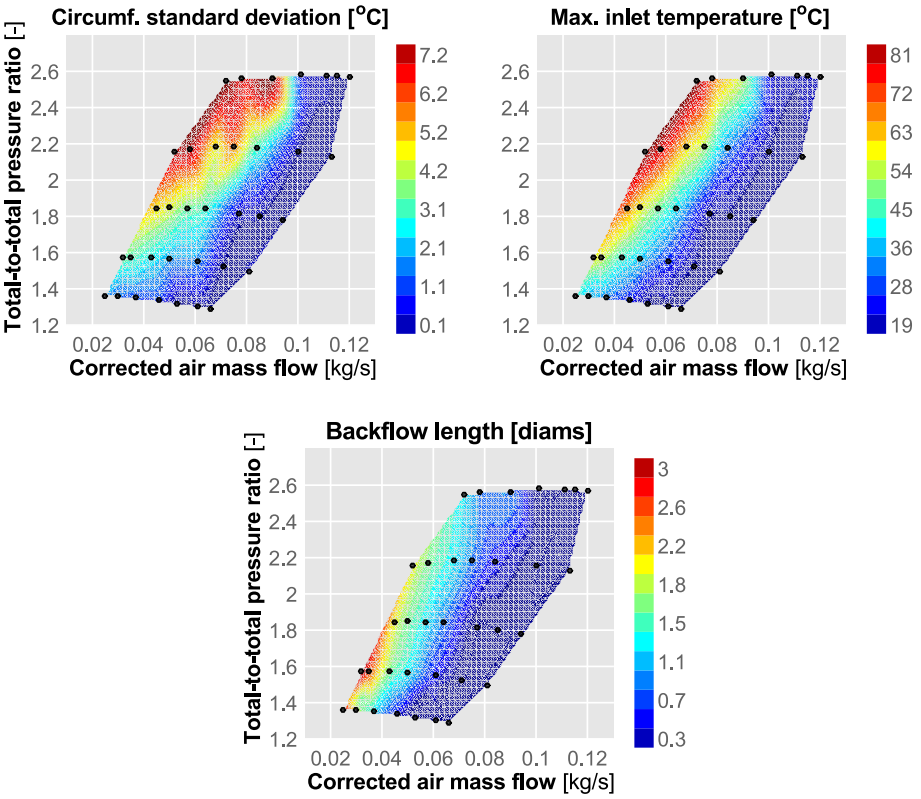

Figure 7.13: *Maps summarizing the results obtained through temperature measurements across the different operating conditions. On the top row results of circumferential skewness (left) and maximum temperature (right) are presented, while estimated backflow length is presented at the bottom plot.*

The top-left map shows how the skewness of the circumferential temperature distribution varies along the different operating conditions. Standard deviation has been chosen as a metric to quantify the magnitude of the skewness. It can be shown in the leftmost map of Fig. 7.13 how skewness rises with higher shaft speed and instability caused by lower air mass flows.

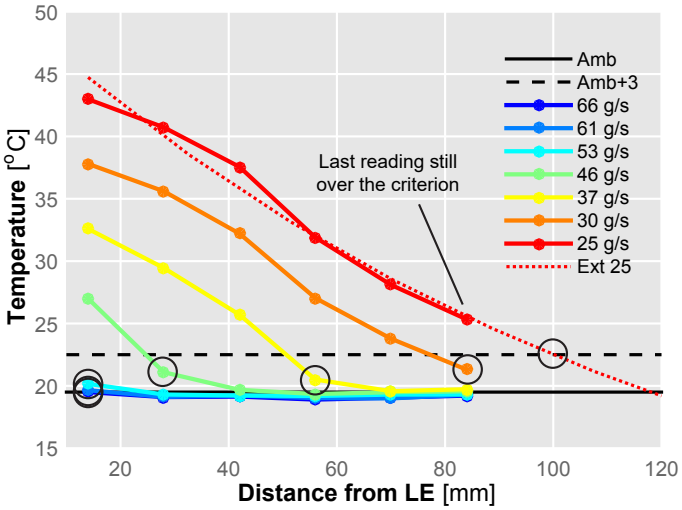

Figure 7.14: *Temperature readings at the inlet linear array for a constant shaft speed (80 krpm) and different mass flows. Circles indicate the estimated limit of the backflow for each mass flow using the proposed criterion.*

Top-right map of Fig. 7.13 shows the overall maximum temperature measured by the thermocouples. The distribution along the map is similar to that of the skewness albeit less pronounced at higher speeds. Temperatures remain close to the ambient temperature (∼20°C) at higher mass flow and increase after the isospeed slope approaches zero. This increased temperature can reach up to 80°C at 160 krpm and conditions close to surge.

Lastly, an estimation of the backflow upstream extent is provided in the bottom map of Fig. 7.13. This was done postprocessing the raw data from the linear array displayed in Fig. 7.9. The temperature profile for each measurement point (shaft speed and air mas flow) was automatically processed with the following algorithm:

Starting from the thermocouple closer to the impeller, each thermocouple reading of the linear array is compared with the ambient temperature; the first that reads less than 3°C above is selected as the backflow extent.

The following step checks if the maximum temperature difference between linear thermocouples is more than 3°C; if not, a constant temperature profile has been detected. If the maximum temperature of the profile is less that 10°C above ambient temperature, backflow length is assumed to be minimum (0.3D), the deviation caused by previous prolonged operation at

high temperature points. If not, it is assumed to be maximum (2D), meaning that a very large backflow is present. This situation only occurred when the compressor entered deep surge conditions.

If the profile still does not satisfy the previous criteria, this means that the backflow is extending beyond the length of the linear thermocouple array, but it is not so high as being uniform. In this case a linear-log extrapolation of the measured profile is performed. The backflow maximum length is assumed to be located where the extrapolated profile intercepts a threshold of 3°C above ambient temperature. A graphical example of this processing is shown in Fig. 7.14.

The resulting map plotted in Fig. 7.13 shows that no backflow is apparent at higher mass flows, with its length only reaching the thermocouple array near the point of null slope of the isospeed line. However, contrary to the case of the previous two maps, backflow length is higher at low shaft speeds, as lower mass flows provide less momentum to counteract the backflow.

7.2.2. Pressure

Two sets of pressure information were recorded during this experimental campaign. Local pressure in both inducer and diffuser was acquired in order to provide more insight into the flow conditions at those areas of interest and to validate CFD results. In addition, in-duct pressure as recorded by the piezoelectric arrays in order to compare with this local pressure and to compute sound intensity by means of the beamforming wave decomposition procedure.

7.2.2.1. Local pressure

As shown in Figs. 7.1 and 7.2, miniature pressure probes were fitted in both the inducer and the diffuser of the compressor in order to characterize the behaviour of the pressure as the operating conditions changed.

In figure 7.15, the top row shows the sound pressure level spectra for both inducer and diffuser probes at a certain constant shaft speed of 160 krpm and different air mass flows. The frequency range is 0 to 35 kHz, an upper bound which is well beyond human hearing range but nonetheless shows relevant information. As the behaviour at the rest of the tested shaft speeds was similar, the discussion will be presented only for this condition.

It can be seen in these two plots that pressure spectra in the diffuser (right) remains approximately constant through the different air mass flow regimes, with a marked increase only in frequencies below 5 kHz.

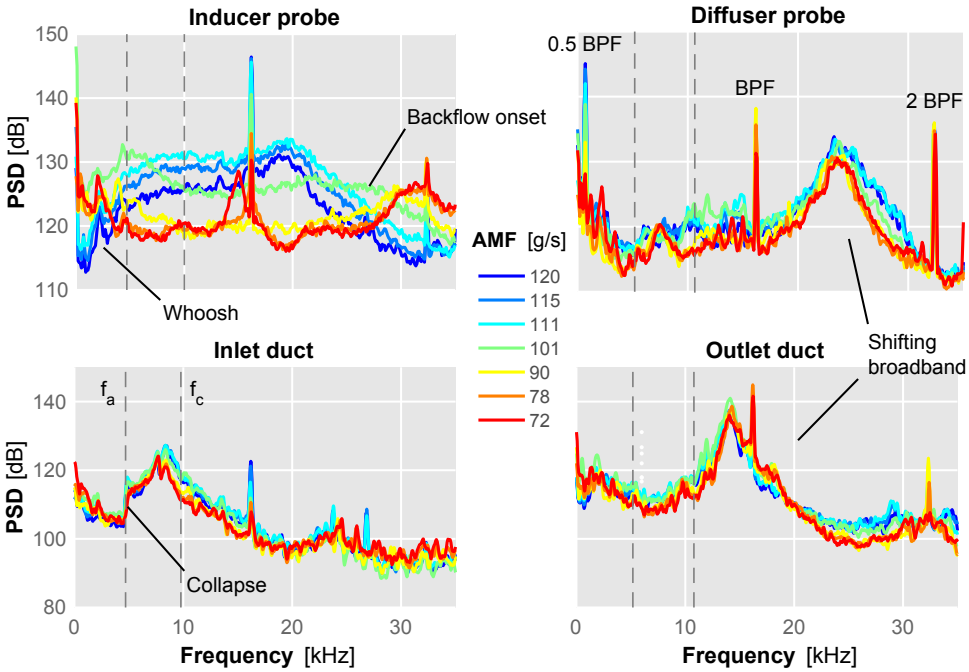

Figure 7.15: *Top row: pressure spectra at the inducer (left) and diffuser (right) measured by the local pressure probes at different air mass flows while the shaft speed was kept constant. Bottom row: pressure spectra at the inlet (left) and outlet (right) ducts, including the onset of the first and second acoustic modes.*

A broadband noise centered around 2 kHz becomes apparent at low flow conditions, with two sidelobes. A characteristic Blade Passing Frequency can be clearly seen as a peak at 16 kHz, along with higher and lower frequency harmonics. A very notable TCN-like broadband is also present at high frequency, peaking around 23 kHz and thereby higher than BPF.

Data from the inducer pressure probe on the left top plot, on the other hand, shows very different spectra depending on the compressor operating condition. At higher flow conditions, frequency content below 5 kHz is lower than the rest of the audible content between 5 kHz and 22 kHz. A slight broadband can be seen peaking around 20 kHz. As the flow is reduced from 120 to 115 and 111 g/s all the frequency content raises in level but the distribution is similar, with the broadband being more pronounced, but still peaking around the same 20 kHz frequency.

As seen in Figs 7.13 and 7.9, the next measurement point at 101 g/s is the first where the hot backflow reaches the first thermocouple at 1/3 diameters from the impeller. Recall from Fig. 7.2 that the inducer pressure probe is located between this thermocouple and the impeller, thus the fact that the backflow is reaching the thermocouple implies that the probe readings are starting to be affected by this backflow.

The backflow causes a radical change in the pressure spectrum of this point: in contrast with the previous operating point, at 101 g/s (line colored in teal) the highest level is now located below at and below 5 kHz with a steady decrease up to 10 kHz and a more or less constant content until level starts to fall after 28 kHz.

As air mass flow was again decreased to 90 g/s, the backflow extended upstream to at least the second thermocouple at 1 diameter distance from the impeller leading edges. This changes again the spectrum, with now the higher levels descending from 0 to 8 kHz, constant level from 8 to approximately 25 kHz and a broadband peaking at approximately 30 kHz.

The following two operating points where air mass flow was still reduced (to 78 and 72 g/s) and the backflow keeps extending upstream (as seen in the thermocouple readings presented in Fig. 7.9) exhibit spectra similar to the previously described, but with the higher frequency broadband slightly shifting upwards in frequency up to approximately 32 kHz.

As it was the case with the measurement from the diffuser pressure probe, the Blade Passing Frequency peak at 16 kHz and its lower and higher frequency harmonics can be clearly distinguished at all operating points.

Lastly, the lower frequency broadband at around 1 – 3 kHz that is usually associated with *whoosh* noise can be clearly distinguished at all mass flow conditions specially in the inducer spectra, even at the higher flow point were the backflow still has not reached the probe location. This could be related to the phenomena observed by Liśkiewicz [134] where some frequencies characteristic of unstable fluid structures were shown to be present in damped form even at stable conditions.

7.2.2.2. In-duct pressure

In addition to the miniature pressure probes at the inducer and the diffuser of the compressor, pressure was also measured by piezoelectric transducer arrays in the straight inlet and outlet ducts. While these arrays were mainly used to compute plane wave sound intensity, the spectrum of the first sensor of each array was plotted in the bottom row of Fig. 7.15 to compare the pressure signature in the ducts with those measured by the probes.

Comparing the pressure spectra measured in the outlet duct (bottom right plot) with the previously described spectra measured in the diffuser (top right plot) it can be seen that the results are similar except for the shifting of the high frequency broadband, from approximately 23 kHz to 15 kHz. Again, levels increase with lower mass flow at the lower frequencies and descend at the higher frequencies, in this case the turning point being around 8 kHz. BPF peaks are still clearly visible except for the lower frequency harmonic.

Contrasting with the notable differences between the spectra at different mass flow conditions that were captured by the inducer probe, the inlet sensor shows an evolution similar to that of the outlet. Clear increases in levels can be seen for frequencies lower than 5 kHz as mass flow is reduced, whereas levels at higher frequencies remain similar or diminishing slightly.

The broadband in this case appears to be centered around 7 kHz, but most interestingly, in all the spectra this TCN-like broadband collapses with a deep decrease in level at 5 kHz. Again, by using expression 3.3.7 as proposed by Eriksson [94] for the onset of the first asymmetric mode, and expression 3.3.8 for the first circular mode, we can estimate their onset frequencies for the inlet and outlet ducts.

These have marked with grey dotted lines in Fig. 7.15. As it can be seen the onset of the first mode, and thus the limit of the plane wave range, is around 5 kHz with slight differences due the variation in temperature, diameter and Mach number from the inlet to the outlet. The TCN-like broadband appears to be unable to shift lower than this frequency.

While in the case of the inlet duct f_a appears to coincide with the abrupt lower bound of the mentioned TCN-like broadband, it appears that in the case of the outlet duct the broadband has shifted enough so that its lower frequency limit is higher than f_a and thus the broadband content is symmetric, without the collapse at the plane wave limit observed at the inlet.

However (unlike what previous results of subsection 4.1.1.3 seemed to suggest) no correlation with the first circular mode is evident in this case. It becomes thus apparent that while the TCN-like higher frequency broadband propagates above plane wave conditions, it is not related to the onset of a certain acoustic mode.

As for the pressure probes, both turning points appear to be more related to the first mode onset at 5 kHz, but specially in the case of the diffuser it should be taken into account that the given expression for a circular pipe does not apply and the acoustic modes will depend on the particular geometry of the compressor.

7.2.2.3. Noise

Following the interpolation procedure described in [5] it is possible to construct "noise maps" that allow for an easy visualization of how the sound intensity level in a given band varies with the operating condition of the compressor. Such maps were calculated for the 1 – 3 kHz, the result shown in Fig. 7.16.

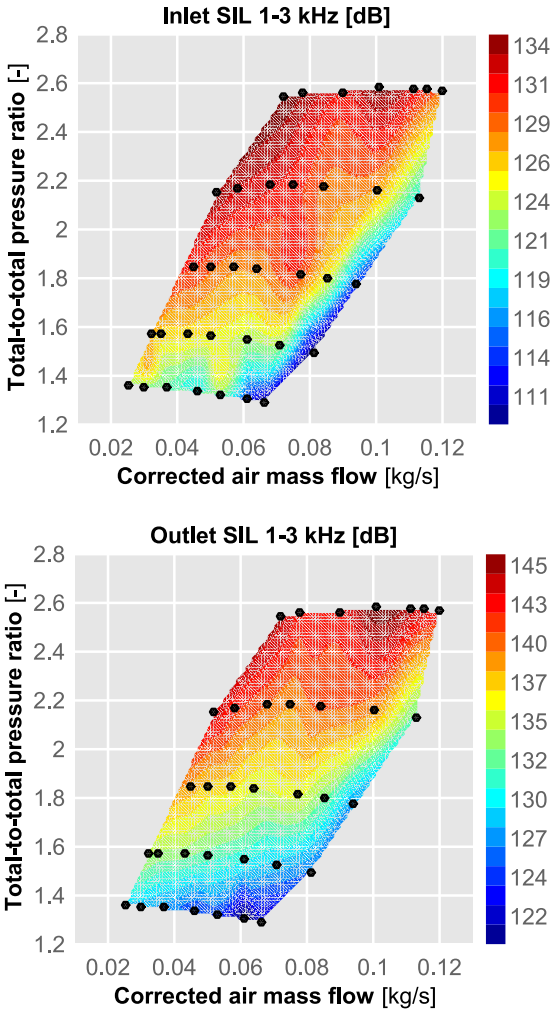

Figure 7.16: *Sound intensity level maps for both inlet (top) and outlet (bottom) ducts in the 1 – 3 kHz frequency band, interpolated from the measured operating points.*

This band was chosen as it is usually associated with the *whoosh* noise [29, 30] phenomenon that was discussed in previous chapters. Indeed, a broadband peaking around 2 kHz was found specially in the spectra measured by the inducer and diffuser probes at higher shaft speeds and low mass flow conditioı

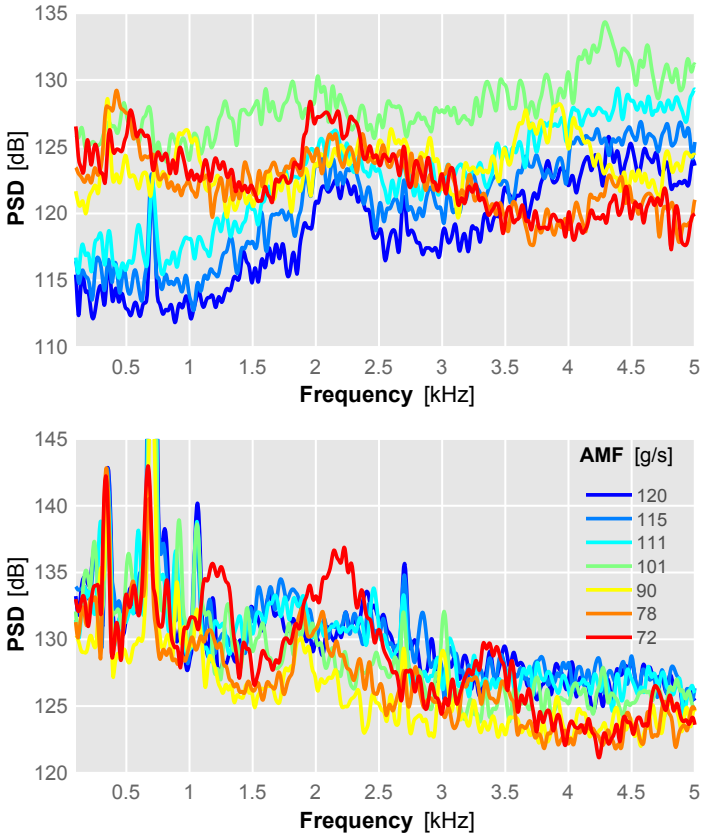

Figure 7.17: *Lower frequency pressure spectra at the inducer (top) and diffuser (bottom) measured by the local pressure probes at different air mass flows while the shaft speed was kept constant at 160 krpm.*

It can be seen in Fig. 7.16 that sound intensity is higher in the outlet than in the inlet duct. Also, at higher mass flow where the isospeed curve still is changing in slope, there are low levels for almost all the shaft speeds. While in both cases noise levels rise with shaft speed and and lower air mass flow, distribution is however not the same.

Operating conditions with higher level are more extended in the inlet duct both in terms of shaft speed and mass flow. Except for the top shaft speed, noise levels rise sooner in the inlet than in the outlet. Considering for instance the 140 krpm line, it can be seen that in the inlet, high levels (red colors) are reached just at approximately 80 g/s whereas in the outlet red contours are not reached until nearly the deep surge limit at around 60 g/s.

Slope of the sound intensity contours is also different between inlet and outlet. Level increase is more progressive in the outlet but in the inlet the increase happens suddenly at mass flows just before to the point where the backflow reaches the inlet thermocouples.

This suggest that the *whoosh* broadband noise naturally propagates downstream but the upstream propagation is only boosted when the backflow extends pass the impeller and into the inlet duct, pointing to the generation flow mechanism being located after the impeller rather than being caused by the instabilities of the hot backflow at the inlet duct.

7.2.3. Velocity

Once that temperature data was processed to estimate the backflow extent across the area of interest of the compressor map, the experimental setup of the turbocharger was modified to fit the glass pipe that confined this backflow and the laser optics were installed in order to proceed with the PIV measurements.

7.2.3.1. Longitudinal plane

As described in the methodology section, longitudinal plane measurements were the most difficult since the seeding oil particles blocked the line of sight of the camera. However with the right combination of seeding flow, oil dilution and quick operation of the system, valid snapshot pairs were obtained that were suitable for postprocessing.

To capture the difference between stable and partially stalled conditions (also called mild surge or marginal surge conditions) two back-pressure valve positions were tested, while maintaining the same shaft speed of 140 krpm, so that high and low flow rate conditions could be attested.

In this particular case PIV postprocessing was carried out for 7 snapshot pairs for each condition. This was the maximum snapshots that could be recorded before the oil film ring shown in Fig. 7.6 started to form at the stagnation zone of the backflow in the unstable condition test, obscuring the images.

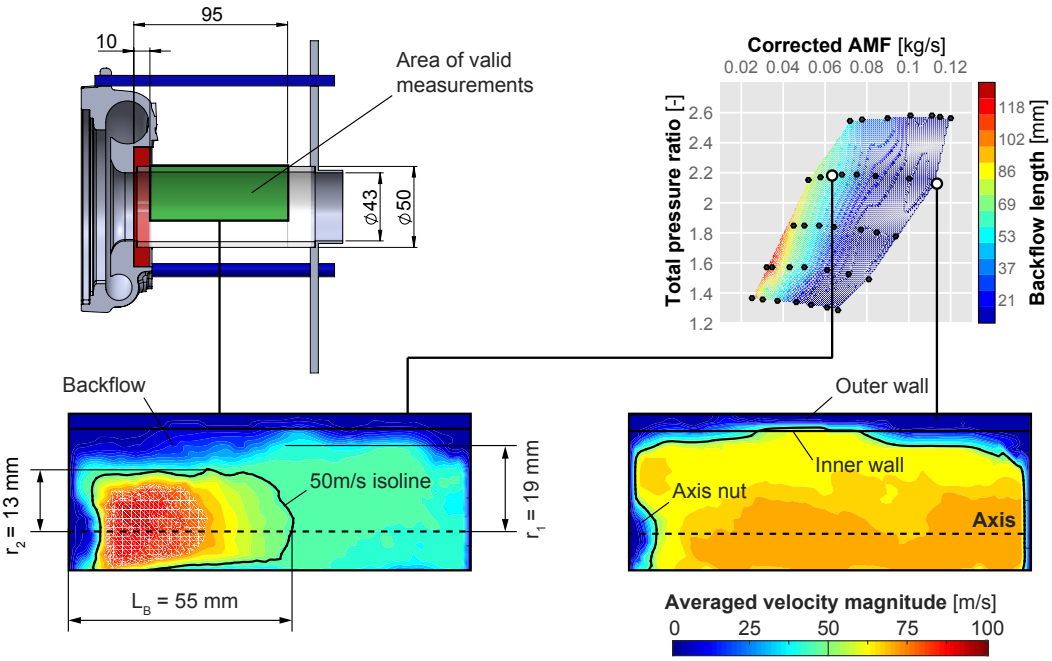

Figure 7.18: *Results of the axial velocity field measurement (longitudinal plane) for the two operating points considered: low air mass flow (left) and high air mass flow (right), indicated along the estimated backflow length in the compressor map.*

While the lower third of the frames were obscured by a reflection, at least 2/3 of the longitudinal plane could be resolved in sufficient quality. The two resulting averaged velocity fields can be seen in Fig. 7.18. A 50 m/s isoline has been added in both cases for clearer identification.

In these tests there was no direct measurement of inlet air mass flow, so an average of the measured velocity field in the upstream area of the duct was taken to identify the precise operating point of the compressor.

At the higher mass flow, it can be seen that the velocity field is approximately homogeneous along the duct and only near the wall the velocity diminishes. However, when flow is reduced, the spatial distribution of velocity changes. The expected compressor backflow is apparent as the low velocity region near the wall increases in thickness, reducing the useful diameter from ∼19 mm to ∼13 mm.

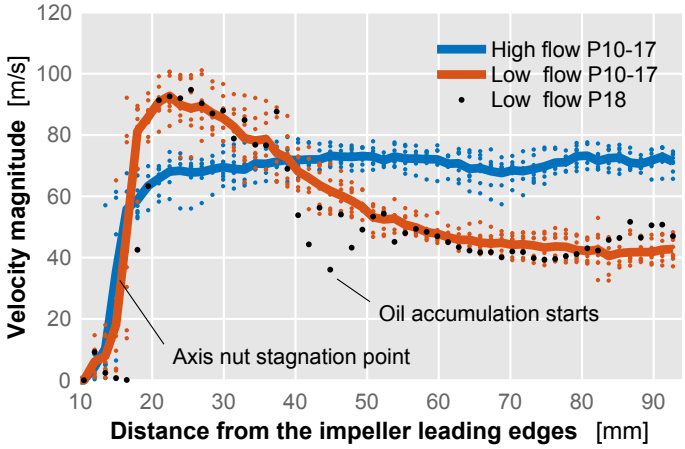

Figure 7.19: *Velocity magnitude over the centreline of the longitudinal plane at high and low flow. Solid line indicates the mean and points correspond to individual snapshot pairs. Pair 18 is presented separately as it starts showing the effect of the oil fouling. Note that distances below 10 mm are obscured by the adaptor piece.*

This apparent reduction in velocity magnitude is probably caused by the highly transversal velocity of the backflow, that makes the transit time of the particles through the laser sheet too small to be captured in consecutive snapshots and thus makes the correlation impossible, leading to no velocity being detected in the processed results.

The reduction in diameter extends to approximately ∼55 mm, this is, approximately half of the transparent glass length. This distance is consistent with the prediction made through temperature measurements as shown in the backflow length map of Fig. 7.13, which is included for convenience.

It can also be seen in Fig. 7.18 how this reduction in the useful diameter appears to be paired with an increase in the flow velocity. A similar but lower increase can be seen in the work of Fike et al. [60] where a single channel of an axial flow fan was tested. Also, a similar constriction and acceleration of the flow is correctly predicted by the compressor numerical model developed by Lang [49].

To better quantify the increase in speed in the core flow, velocity data along the turbocharger axis line (marked with dashed line in Fig. 7.18) from each valid snapshot has been plotted in Fig. 7.19 for both operating conditions. The first invalid snapshot pair has also been plotted (black dots) to show how the oil film accumulating in the pipe wall due to the backflow starts to affect the measurements.

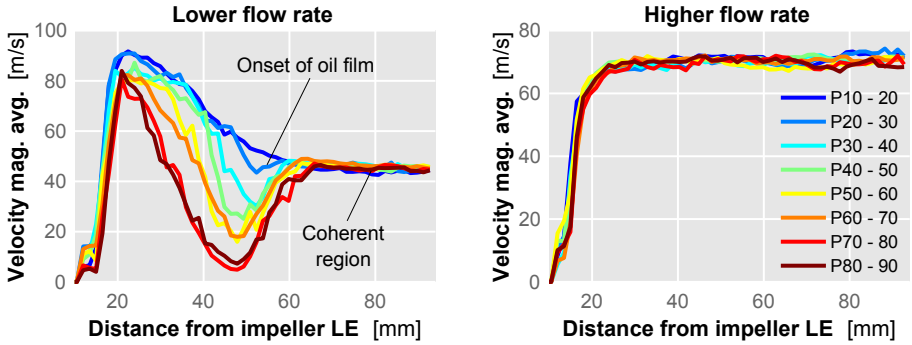

Figure 7.20: *Velocity magnitude averages over the centreline of the longitudinal plane at high and low flow, considering different consecutive sets of snapshots.*

In order to assess if the flow field is stationary enough so that this approximate number of snapshot pairs accurately reflects the velocity profile, in Fig. 7.20 the profiles shown in Fig. 7.19 have been recreated for different consecutive snapshot sets taken during the same measurement run. Note that pairs 0 – 10 are omitted as seeding particles have not yet fully reached the laser sheet in those.

It can be seen that for the higher flow rate case (right) where conditions are stable, the calculated velocity profile is approximately the same for any snapshot range, showing that the flow field is not changing from one set to the next. In the case of the unstable conditions however, this coherence only holds true for the part of the pipe which is upstream of the backflow stagnation point.

As oil starts accumulating (in snapshot pair 18 as seen in Fig. 7.19) velocity readings diminish until the point that almost no velocity can be measured (last two sets of snapshots). Further downstream of the oil ring velocity readings tend to recover to the same point.

Looking then at the selected pairs (10 – 17) in Fig. 7.19 it can be observed how, while at higher flow rate the flow exhibits an approximately constant velocity along the line (which only decreases adjacent to the axis nut) at the lower flow condition and after a steady initial segment the velocity increases to a top average speed of 91.7 m/s. The average speed at the initial segment between 80 and 90 mm was found to be 43.7 m/s.

Using this data it is possible to draw a simple correlation between the area constriction and the increase of speed. By applying the mass conservation equation between the initial segment (denoted by the subscript 1) and the top speed point (denoted by the subscript 2):

$$\dot{m}_1 = \dot{m}_2 = \rho_1 U_1 \pi r_1^2 = \rho_2 U_2 \pi r_2^2 \tag{7.2.1}$$

If a small enough increase of temperature between point 1 and point 2 is assumed so that $\rho_1 \sim \rho_2$ the expression can be rearranged to obtain the velocity change:

$$\frac{U_1}{U_2} = \frac{r_2^2}{r_1^2} \tag{7.2.2}$$

If now the aforementioned approximate values for radii and velocities are substituted into the equation, we can obtain an estimation of the relative error ε between the theoretical value and the experimental observation:

$$\varepsilon\,(\%) = \left| \frac{U_1/U_2 - r_2^2/r_1^2}{r_2^2/r_1^2} \right| \cdot 100 \approx 1.7\% \tag{7.2.3}$$

The small relative difference between the prediction and the observation supports the assumption that the measurement technique is in fact able to characterize the reduction in useful area associated with the backflow and its associated increase in velocity, even if the axial speed of backflow itself cannot be quantitatively measured.

7.2.3.2. Transversal plane

After the measurement of the axial velocity field at the longitudinal plane, the setup was modified to measure transversal planes. The camera was moved to point directly through to the compressor short inlet pipe, while the cylindrical lenses were rotated 90º to create a vertical laser sheet.

During this test, the contrast between a high flow and a low flow operating condition was again measured as in the transversal test, in order to ensure that the method allowed for a clear differentiation between the backflow coming from downstream the impeller and the unperturbed, non-rotating flow coming upstream from the compressor.

As mentioned earlier, in contrast with the longitudinal case, the background of the snapshots for these transversal measurements had to be necessarily the rotating, polished turbocharger impeller itself instead of the back of the glass pipe. This caused an increased amount of bright reflections that made tracking of the seeding particles more difficult.

To reduce the severity of this issue, snapshots were synchronized with the blades' position through the existing shaft speed Hall effect sensor. However, the data transfer rate of the particular camera used in this test limited the time between snapshots and thus the shaft speed at which the synchronization mechanism operated correctly. A speed of 100 krpm was selected as a compromise between safe operation of the synchronization mechanism and adequate expected length of the backflow.

Using this setup a first test was carried out where the transversal plane illuminated by the laser sheet was located at approximately 50 mm (or 1.2 inducer diameters) from the compressor impeller leading edges, since at this distance it was expected to adequately capture the backflow.

Approximately 90 valid snapshots pairs were captured for both the low flow and the high flow operating conditions. Since in this case the accumulation of oil along the walls of the duct was not such a relevant issue, they were all averaged after subtracting a reference background image made from the average of 10 snapshots pairs captured before the seeding started as shown in Fig. 7.6. The results of this process are shown in Fig. 7.21.

In this figure, the two operating conditions are marked on a compressor map that estimates the length of the hot backflow. As expected, the transversal velocity at the high flow case is low, albeit some reflections from the impeller blades are showing up in the correlation.

For the low flow rate case, which makes the compressor operate at a condition where a high backflow is expected, a clearly different flow field can be observed.

In this case there was a highly rotational field near the walls that diminishes in the direction of the core flow, coherent with the backflow coming back through the stalled tips of the impeller blades and through the tip clearance.

As expected, the laser PIV postprocessing method cannot resolve the flow field up to the glass pipe wall, as there is a small zone where the correlation does not give valid results, since the rectangular grid does not contain enough seed particles as they are slowed down by the boundary layer and obscured by the wall reflection.

After attesting that the experimental setup was able to capture the rotating backflow, a final test was made where the turbocharger was kept at an approximately constant low flow operating condition and the laser sheet was placed at different distances along the glass inlet pipe in order to measure how the backflow-induced rotational field evolved along the pipe.

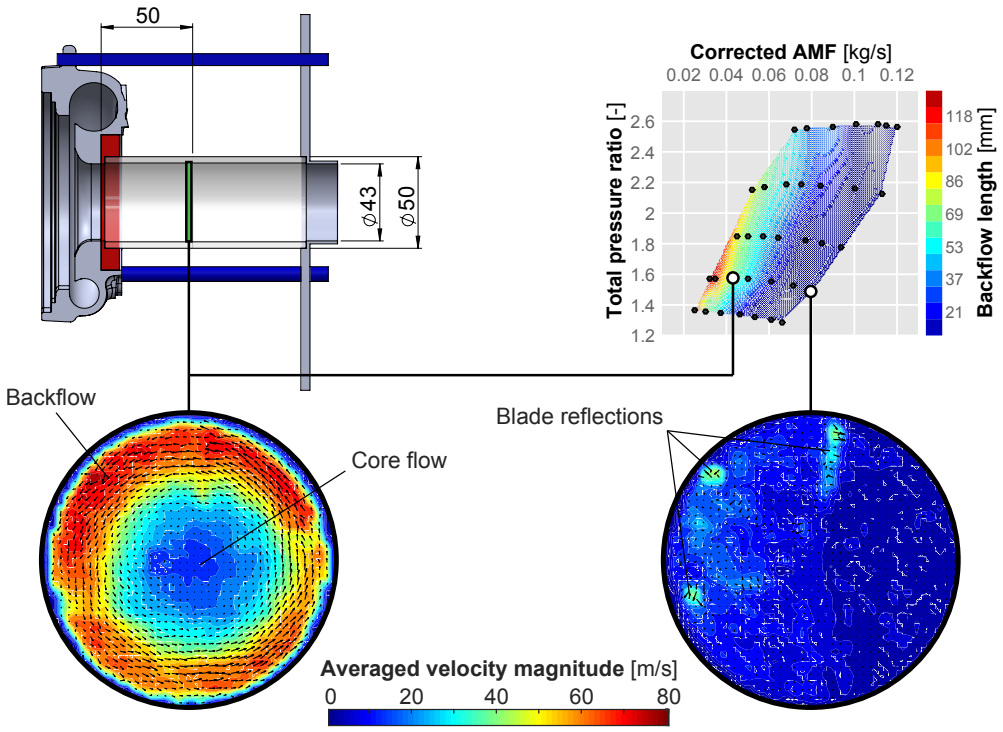

Figure 7.21: *Results of the averaged transversal velocity field for two operating points: low air mass flow (left) and high air mass flow (right), indicated along the measured inlet backflow length in the compressor map.*

The selected operating condition was again at 100 krpm of shaft speed and a low flow point similar (but not equal) to that of Fig. 7.21. Three different snapshots sets were taken with the laser sheet at distances of 20, 45 and 85 mm from the leading edges of the impeller blades. Expected length of the compressor backflow at these conditions was around 70 mm. The results of this study can be seen in Fig. 7.22.

In this figure, two of the slices (left and center) are inside the backflow as expected by the temperature measurements discussed before, while the third one (on the right) is clearly situated outside the backflow as the rotational velocity is almost null.

It is also apparent that the slice closest to the impeller (20 mm) exhibits a thicker zone of stronger rotational velocity, starting from the wall and diminishing towards the centre. A reflection coming from a dent in the axis nut (probably for balance) and some slight reflections from the blades are also visible.

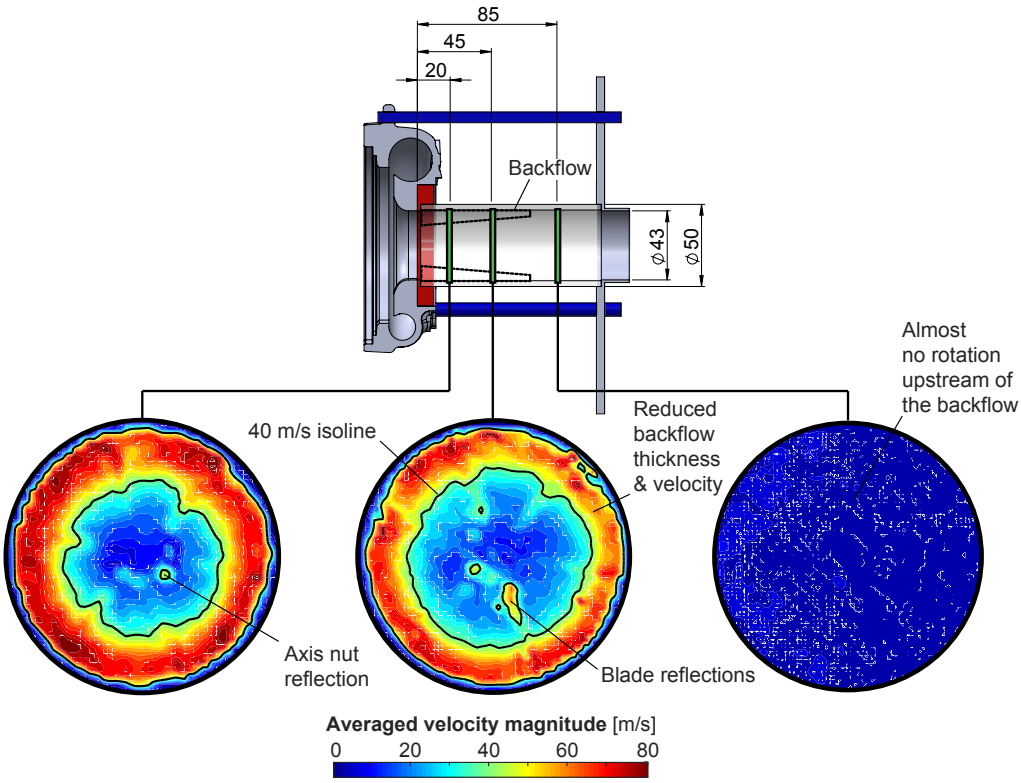

Figure 7.22: *Results of the averaged transversal velocity magnitude for three slices at different distances from the compressor impeller leading edges. From left to right 20, 45 and 85 mm. Same compressor operating condition for all slices.*

The second slice at 45 mm from the leading edges features a similar velocity field, albeit a slight reduction in both the speed and the thickness of the backflow is appreciable. The effect of erroneous reflections from the blades is also stronger in the core flow section.

To quantitatively compare the velocity profiles of the three slices, velocity magnitude data was extracted from the horizontal centreline of each slice. Fig. 7.23 shows the velocity data for each individual snapshot (points) and the averaged magnitude (solid line).

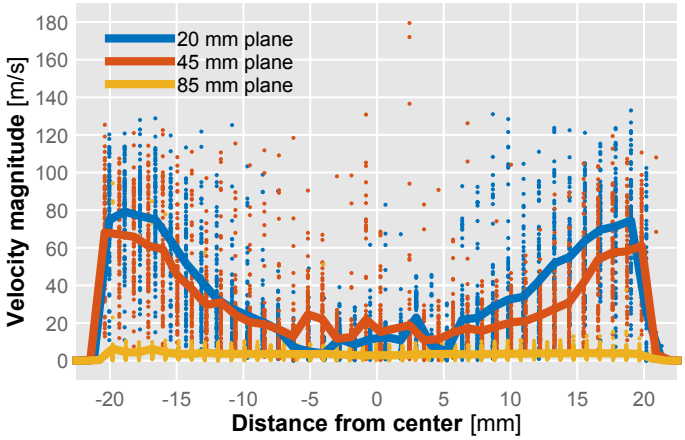

Figure 7.23: *Velocity magnitude over the centreline of three transversal planes. Solid line indicates the mean and points correspond to individual snapshot pairs.*

Dispersion at each point of the line is much higher that in the previously discussed case of longitudinal plane measurements, but it can be confirmed that in average the 45 mm slice presents lower top speed and less thickness: any given speed (for instance, 50 m/s) is achieved closer to the wall than in the 20 mm slice.

In the case of the 85 mm slice which as predicted was located outside of the backflow, velocity and dispersion are much lower, the profile being constant at an approximate magnitude of 4 m/s, probably due to pure momentum diffusion upstream.

Core rotation velocity appears to be similar in the three measured slices, at least at radius of less than 8 mm, although the reflections of the blades and the axis nut introduce some perturbations in the 20 and 45 mm slices. On the other side, velocity could not be resolved at locations with radius greater than 20 mm, leaving a gap of missing data of about 1.5 mm from the pipe wall.

7.2.4. Correlations

As all the captured temperature, pressure and velocity data has been gathered using the same compressor and equivalent straight inlet ducts, some correlations of interest can be drawn between the different variables.

7.2.4.1. Backflow and sound intensity

In order to further attest for a linkage between these inlet flow instabilities at marginal surge conditions and the *whoosh* broadband noise at plane wave frequencies, it is possible to correlate the aforementioned thermal phenomena with total sound level in that frequency range.

Figure 7.24 shows a plot of inlet sound intensity level against standard deviation of temperature in the circumferential thermocouple array. It can be seen how for higher temperature deviation sound intensity appears to be correlated following an ascending trend.

However, below approximately 1.1°C of deviation sound level appears to still increase with shaft speed at low mass flows, even if no hot backflow is being detected by the circumferential thermocouple array.

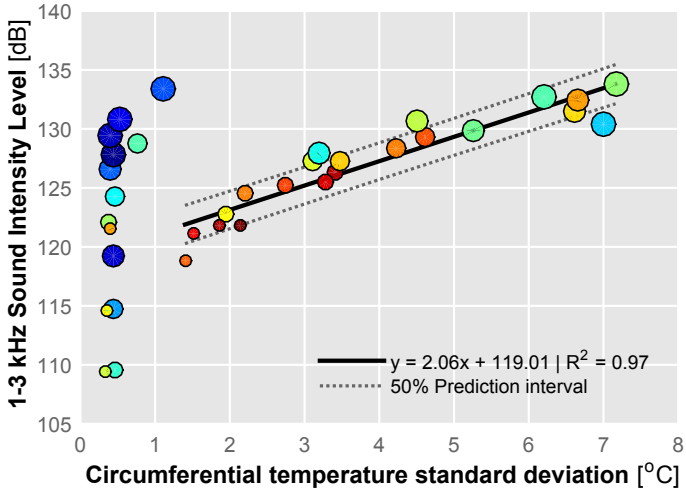

Figure 7.24: *Correlation between standard deviation σ at the circumferential thermocouple array and inlet sound intensity level in the 1 – 3 kHz band. Size indicates shaft speed from low to high and color indicates mass flow from higher (blues) to lower (reds).*

A least squares linear fitting was performed, showing that there is a good correlation between increase in sound intensity at the selected frequency band and increase in the skewness of the inlet circumferential temperature distribution, thereby suggesting a link between the two phenomena.

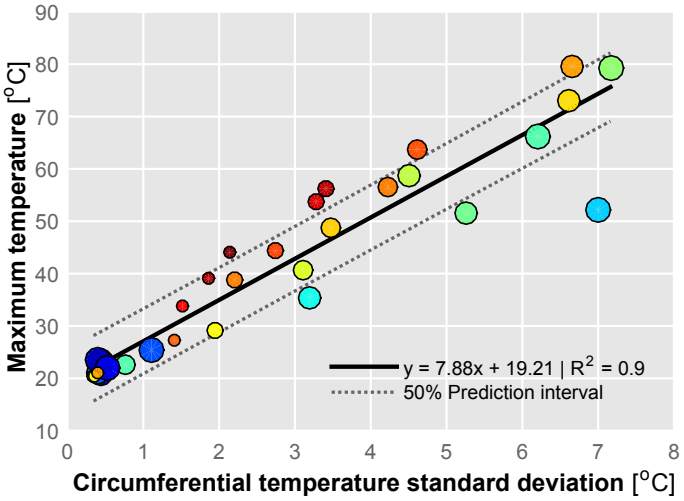

Figure 7.25: *Correlation between standard deviation at the circumferential thermocouple array and maximum temperature measured by the thermocouples. Size indicates shaft speed from low to high and color indicates mass flow from higher (blues) to lower (reds).*

Coupled with the fact that the increase in sound level happens even at operating conditions at which the backflow containing the skewness has not reached the thermocouples yet, this again points to the generation of *whoosh* happening in or after the impeller, with the phenomena being amplified upstream the impeller as the backflow extends into the inlet.

Another linear correlation was performed between circumferential standard deviation of temperature and maximum temperature of the backflow, as shown in Fig. 7.25. The good agreement of this correlation showed that a relative or dimensionless standard deviation (this is, raw standard deviation divided by a representative temperature) is approximately constant: the backflow is skewed similarly along the compressor map and is augmented linearly with the increase of temperature caused by higher pressure ratios.

7.2.4.2. Velocity and temperature profiles

Besides using the thermocouples described in section 7.1.1 for estimating the backflow extent across the different operating conditions, a comparison was performed between the recorded temperature profiles and the velocity profiles obtained through PIV.

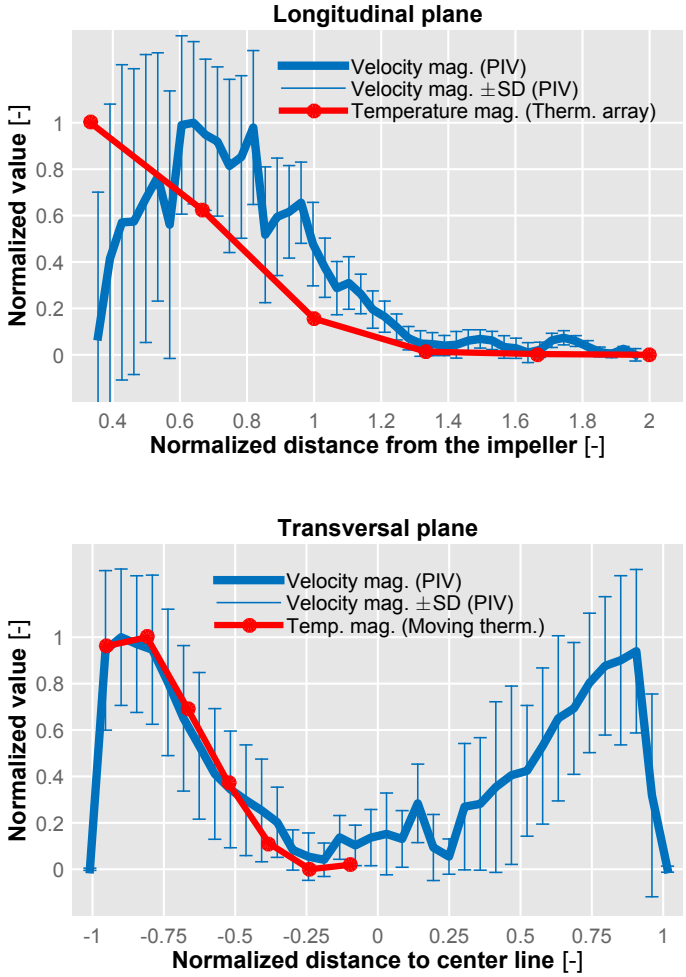

Figure 7.26: *Normalized profile comparison between temperature measurements and PIV results on both the transversal plane (bottom plot) and the longitudinal plane (top plot).*

First a velocity profile was extracted from the longitudinal plane at a line separated ½ radius from the wall, which was the distance at which the thermocouples were installed. This velocity magnitude profile was then normalized between 0 and 1, and the same was done with the thermocouple array data that most closely matched the operating point at which the PIV test was performed. The results can be seen in the top plot of Fig. 7.26.

In addition to the temperature profile and the averaged value of the velocity magnitude, error bars indicating the standard deviation values are included.

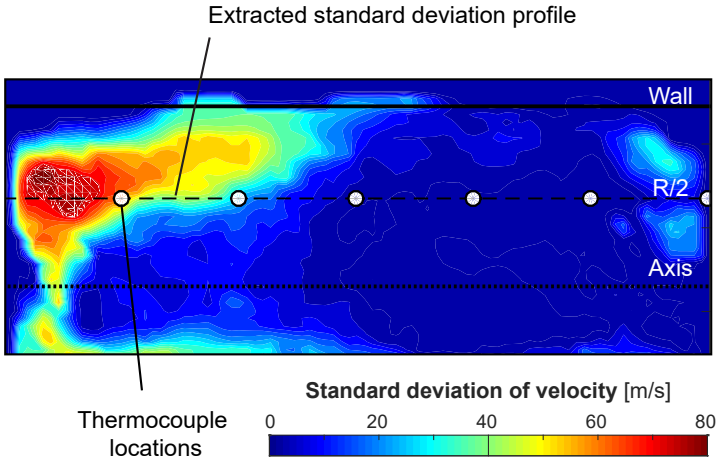

Figure 7.27: *Standard deviation of velocity between selected snapshots in the longitudinal plane, showing the location of the thermocouples used in the temperature measurements.*

Contrasting with Fig. 7.19 where the centerline profile was shown to have a relatively small dispersion, at the thermocouple array location (half a radius from the wall) the profile suffers from a much larger deviation at locations where the velocity increases towards the compressor.

Compared with the normalized longitudinal temperature profile measured by the thermocouple array however, it can be seen that there is a good agreement in the maximum extent of the backflow influence on velocity and temperature, with the turning point located around 1.3 diameters from the impeller and velocity and temperature then increasing towards the impeller.

To compare the radial profile of the backflow in terms of velocity and temperature, a test was performed where the turbocharger was kept at a certain fixed operating condition while the thermocouple closer to the impeller was progressively inserted into the air stream, from close to the wall to the centerline. Again, data was normalized so that both variables ranged between 0 and 1. Results can be seen in the bottom plot of Fig. 7.26.

In this case the concordance between temperature and transversal velocity profiles is even better than in the axial case: near the wall there is a small section where temperature and velocity are maximum and then both diffuse towards the center, reaching a stable value corresponding approximately to the core flow at ±¼ of the radius away from the centerline.

When instead of focusing into the average velocity values the standard deviation (represented with bars in Fig. 7.26) of velocity between the selected snapshot datasets is compared, other interesting findings emerge.

In the case of the transversal velocity field the deviation remains quite high along the entire profile except for a reduction near the center, since as previously explained perturbations from the blades in the background and seeding particles lumping together have a higher impact on each individual snapshot. Averaging a large number of them correctly estimates the average velocity but the deviation remains high.

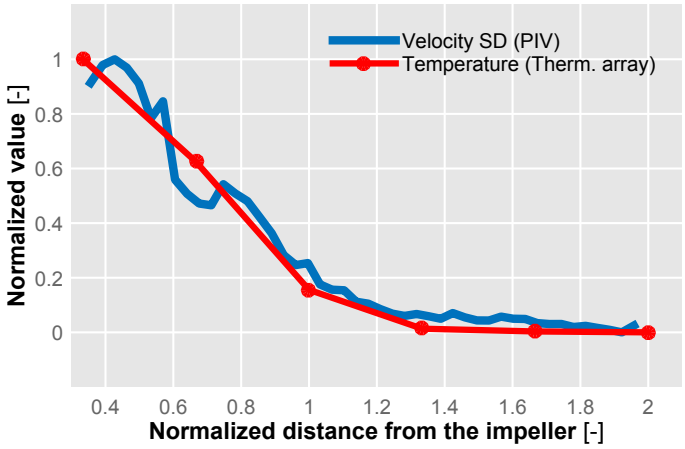

Figure 7.28: *Normalized profile comparison between temperature measurements and velocity standard deviation in the longitudinal plane as seen in Fig. 7.27.*

On the other hand, the evolution of the velocity standard deviation in the case of the longitudinal profile shows a clear difference between a very low standard deviation upstream and a significant increase in standard deviation downstream and towards the impeller, which seems well correlated with the increase in temperature caused by the backflow.

In Fig. 7.27 the spatial distribution of standard deviation has been plotted, showing how its increase is related to the backflow-affected zone. The location of the linear array thermocouples has been added, along with the path of the standard deviation profile selected for the different line plots in this subsection. Furthermore, in Fig. 7.28, the same longitudinal temperature profile is depicted along the normalized magnitude of the velocity standard deviation.

A very good match between the two distributions is obtained in this manner, further attesting how the reversed flow at high temperature also boosts the variability and complexity of the velocity field near the compressor impeller at unstable working conditions.

This conclusion is in line with the results of Liu et al. [52] who successfully showed how the standard deviation of temperature, pressure and mass flow measured at selected locations abruptly increased near deep surge conditions. Now, it is possible to link these increases to the properties of the velocity field measured by PIV, showing how the backflow extends the deviation as it progresses further upstream.

7.3. Conclusions

In this chapter, an experimental study is described with the objective of accurately characterizing the behaviour of the inlet flow instability of a turbocharger compressor when marginal surge conditions are reached. Specifically, focus has been put on the high-temperature compressed flow that reverses direction and extends upstream of the impeller and into the final section of the inlet duct when marginal surge conditions are reached.

The rotation, vortex shedding and reintegration of this backflow into the main flow coming through the core of the inlet duct have been regarded as possible sources of acoustic noise and several methods such as ported shrouds and different casing treatments have been proposed to mitigate its occurrence and extension [135, 136].

During this investigation the setup described in section 7.1.1 has been used to measure the distribution of temperature associated with marginal surge, this is, conditions with low air mass flow but not as low as to cause that the compressor goes into deep surge.

By using the two thermocouple arrays installed into the compressor inlet, both axial and circumferential temperature measurements were obtained for several operating conditions. A test was also performed in order to characterize the radial distribution of temperature caused by the hot backflow. The robustness of these internal flow measurements against radiation from the inlet pipe walls was verified through external thermographic imaging.

The analysis of these temperature distribution allowed the identification of the backflow length along the compressor chart, together with the maximum temperature rise in the inlet and also the skewness of the circumferential temperature distribution of the flow.

Mass flow rate has been shown to be the most influencing factor when predicting how far the hot backflow extends upstream of the compressor impeller. At high rotational speeds, where surge occurs at relatively high mass flows, the backflow temperature is higher (due to higher compression ratio) but the length of the backflow is shorter. As for circumferential skewness, it has been shown to increase linearly with backflow temperature, while it appears to be similar in relative terms for all the different operating conditions considered.

In order to gain further understanding of the generation and evolution of the local flow behaviour, miniaturized pressure probes where placed in the compressor inducer and diffuser. Analysis of the data provided by these two probes, and specially by the former, showed that the pressure spectral information in the inducer abruptly changed when the backflow reached the upstream side of the impeller and the probe, as predicted with the aforementioned temperature data.

Whoosh noise humps are detected at their usual frequencies, along with a higher frequency TCN-like broadband which features large shifts in frequency, that could be related to the change in sound speed due to the large difference in thermodynamic conditions at the selected measurement locations. The shift of this broadband, however, appears to be limited by the plane wave frequency.

Furthermore, a correlation of sound intensity in the *whoosh* characteristic frequency band that was analyzed in previous chapters and the increase in temperature skewness due to the backflow was found. Comparison of inlet and outlet sound intensity charts shows a more smooth evolution in the outlet and a more sudden rise in the inlet, linked to conditions where the backflow starts to appear.

In conjunction with the analysis of inlet temperature and pressure data, this suggests that *whoosh* noise in the inlet is boosted by the convective effect of the reversed flow structures at the inlet in marginal surge conditions, but it is not caused by them. Still, strategies aiming at the control of these backflow structures could influence noise transmission to the downstream side and potentially alleviate its adverse effects on vehicle NVH perception.

A following experimental effort was carried out with the objective of measuring the reversed flow at the turbocharger compressor in unstable conditions when this backflow is confined and fully developed in a straight duct. In order to do this, the straight duct containing the thermocouples was

substituted with a transparent glass pipe in order to allow the illumination of the seeded flow with a laser sheet and the imaging of the particles with a camera.

First, an attempt was made to measure the axial velocity field by imaging a longitudinal plane introducing the laser sheet aligned with the turbocharger axis and positioning the camera in a perpendicular way so that images would be captured through the glass duct.

This proved difficult as the oil particles deposited into the walls of the duct, obstructing the view of the camera and enhancing the detrimental reflections that made the correlation difficult or even impossible in some areas. The effect was found to be even worse when conditions close to surge were reached, as the highly rotational backflow forced the oil particles into the walls and also created an stagnation zone where particles formed a liquid film ring.

As a result of these issues, few valid snapshots of the longitudinal plane could be captured, leading to the conclusion that further research of other seeding mechanisms (such as the alumina dispersion used by Wernet [56] or the fluorescent particles used by Wu et al. [59]) or other coating of the pipe (such as the fluorescent coating used by Gancedo et al. [68]) is required if a larger number of snapshots is required.

In any case, the increase of core speed resulting of the reversed flow along the periphery predicted by Lang's simulations [49] was observed, and shown to be coherent with the apparent reduction in useful diameter and also with prior temperature measurements.

Comparison with higher mass flow rate conditions leads to the conclusion that the difference between an stable axial flow field and the unstable one caused by reversed flow in a confined pipe can be characterized through PIV, albeit with difficulty.

A similar comparison between unstable and stable working conditions was performed in the transversal plane, keeping the distance to the impeller equal in both cases. Again a clear difference was observed with a highly rotational flow appearing at unstable conditions.

To test that transversal plane measurements can be used as well to estimate the length that the backflow reaches when confined in a straight pipe, an experiment was performed measuring three "slices" of the flow field: two inside the predicted length of the backflow and one outside.

This experiment successfully showed a clear difference between the transversal flow field directly caused by the highly rotating backflow and the relatively unaffected field upstream, allowing the conclusion that this slicing method

can be successfully used to externally characterize the length and radial distribution of a confined backflow without perturbation as long as images can be captured from the inlet.

Regarding difficulty, measurements in this transversal planes were easier as the images could be captured directly through the inlet pipe mouth instead of through the glass, thereby avoiding the oil fouling problem. However, a higher ensemble of snapshot pairs was needed since the seeding particles tended to lump together and leave gaps in each snapshot.

Finally, a comparison between the PIV results and the previous temperature measurements was performed in order to ensure that both methods were in agreement. Measurements were normalized in order to meaningfully compare the profiles.

Comparison of the radial profile was done extracting data from the slice closer to the compressor, and the closer thermocouple was introduced step by step into the flow until the inlet duct axis. A good agreement between the two results was found, reinforcing the conclusion that the high transversal speed profile measured by PIV is caused by the hot reversed flow and it is accurately capturing its velocity distribution.

Comparison in terms of axial velocity profile was also performed. While the non-disturbed upstream flow and the maximum length of the backflow appeared to match, profiles inside the backflow were more different than in the transversal case, probably due to the aforementioned difficulties regarding the PIV measurement through the glass in the presence of confined backflow. However if the standard deviation of velocity in the recorded snapshots is analyzed, a good agreement can be found between the rising in deviation and the raising in temperature.

In conclusion, it has been shown that PIV measurements can be used to successfully characterize the flow field in the presence of a confined backflow in the compressor inlet, with the added advantage of avoiding the disturbances that thermocouples or other sensors can introduce. Temperature measurements with thermocouple arrays can be used to measure the extent of this backflow and also characterize its circumferential distribution, which presents good correlation with the increase in *whoosh* noise levels.

Future works using the flow field characterization techniques presented in this chapter would be useful in order to visualize the effect of different inlet configurations designed to mitigate unstable flow issues such as guiding vanes, tapered ducts, nozzles, etc. and to provide better validation of CFD simulations.

CHAPTER 8

Influence of the inlet geometry

As discussed in the literature review performed in chapter 2, different geometric variations of the inlet line near the impeller have been proposed and tested in order to mitigate the negative effect of the flow instabilities.

While mainly aimed at obtaining a more stable flow to delay deep surge onset to enhance the usable zone of the map and keep compressor thermodynamic efficiency even at low air mass flow operating conditions, the impact of these solutions in the generated and transmitted noise must be also considered.

In this chapter different experimental measurement campaigns are described, where some of the geometries most commonly proposed in the literature were tested both in the continuous flow test rig and in real engine conditions.

8.1. Simple geometries

The first of these experimental campaigns was carried by manufacturing a sample of each one of the simplest proposed geometries: a 90º sharp elbow, a tapered duct, and a reservoir. In addition, a short straight pipe was also used as a reference. All of these four geometries can be seen in Fig. 8.1.

These simple geometries were installed on the anechoic chamber flow test rig described in chapter 3. Both the orifice noise measurement free-field microphone and the radiated noise setup with four equally distributed free-field microphones were kept in order to evaluate the acoustic emission in this preliminary investigation.

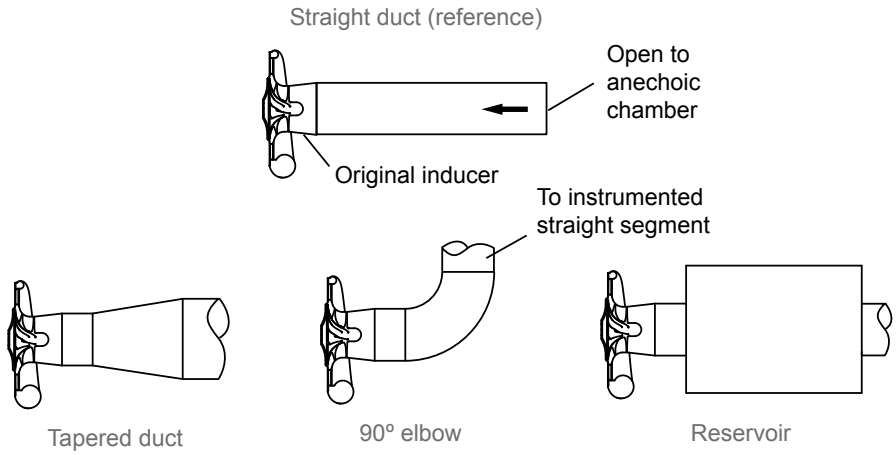

Figure 8.1: *Drawing of the selected simple geometries. The straight pipe at the top was used standalone as a reference and also attached upstream of each geometry in order to measure the instantaneous pressure except for the tapered duct that used a wider pipe.*

In order to simulate more realistic inlet conditions a short straight pipe was added upstream of each tested geometry. This short pipe included a three piezoelectric sensor array in order to obtain validation pressure data for CFD simulations, but no acoustic intensimetry could be performed as the pipes were too short for proper flow development.

8.1.1. Surge margin

Furthermore, raw pressure data from one of these fast sensors was used to characterize with high precision the air mass flow at which the compressor entered into deep surge conditions. In this way not only the acoustic output of each geometry could be measured but also their influence regarding the stability of the flow and thus the enlargement of the usable operating conditions.

As in the previously described experimental campaigns, this fast pressure data was recorded by a Yokogawa digital oscilloscope, along with the mass flow and shaft speed data. The rest of the ancillary information about the turbocharger operation was recorded by the in-house DAQ system.

Measurements with each inlet geometric variant were carried out at different air mass flow settings and a constant shaft speed of 160 krpm, from higher mass flow to lower mass flow.

When conditions were judged to be close enough to deep surge, a continuous recording of the variables started where the mass flow was gradually decreased by slowly closing the backpressure valve until the violent oscillations of deep surge began and the valve was opened completely to stabilize the turbocharger.

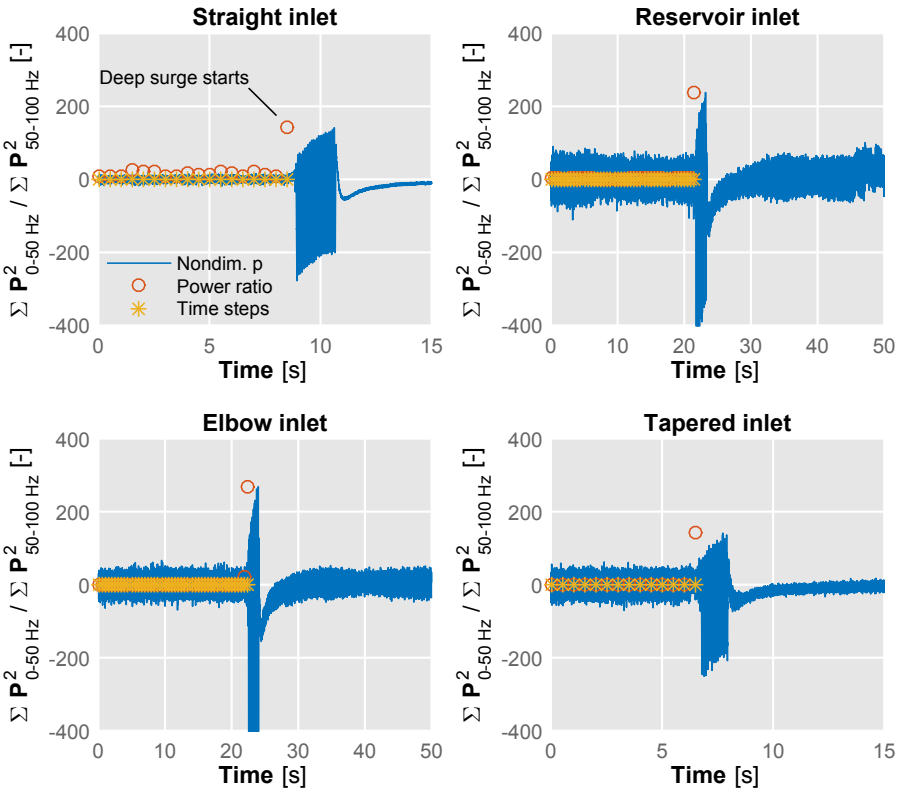

Figure 8.2: *Non-dimensional pressure recording of each geometry when air mass flow was progressively decreased until deep surge condition was reached.*

This pressure recording was then post-processed following a procedure similar to that described in chapter 3. In steps of 0.5 s, FFT was applied to obtain the pressure spectra and then a frequency ratio R_f was computed between the power at 0 – 50 Hz and the power at 50 – 100 Hz:

$$R_f = \frac{\sum_{f=0}^{50} |\mathbf{P}(f)|^2}{\sum_{f=50}^{100} |\mathbf{P}(f)|^2} \tag{8.1.1}$$

When this power ratio reached values over 100, it was considered that deep surge had started at that time. Data was then averaged between the two previous time steps in order to obtain the corresponding value of lowest allowable air mass flow. Time steps and power ratios can be together with non-dimensional pressure tracks in Fig. 8.2. The lowest allowable mass flow obtained through this method can be seen in Fig. 8.3.

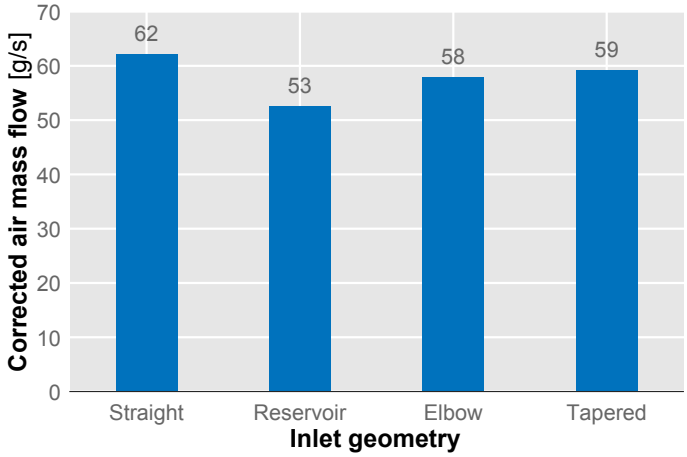

Figure 8.3: *Lowest allowable air mass flow for the different simple geometries tested, obtained through the described algorithm.*

As seen in this figure, the straight duct is the first one to reach deep surge conditions. The tapered duct and the 90º elbow pipe have similar but higher margins until surge, while the reservoir delays this damaging condition even more, allowing approximately 10 g/s of further air mass flow reduction.

8.1.2. Noise levels

In addition to the effect on surge margin, the effect on external noise levels was evaluated. As described in previous chapters, two different measurements systems were available in the anechoic chamber.

To capture the orifice noise, one free-field omnidirectional microphone was situated at a distance of 10 mm from the inlet opening. In this case the microphone had to be repositioned each time the geometry was changed as they had different lengths and, in the case of the elbow, orientation of the orifice.

The second system for measuring externally radiated noise, consisting in the four equispaced free-field microphones placed at 1 m distance form the center of the inlet assembly was kept in the same place for all the tested geometries.

In both cases the microphones were calibrated using a Brüel & Kjær piston-phone prior to the measurements and data was captured using a PULSE™ DAQ system. Fig. 8.4 shows the result of both measurements at the stable operating point closer to surge as characterized by the aforementioned procedure, since it is the point of maximum noise emission.

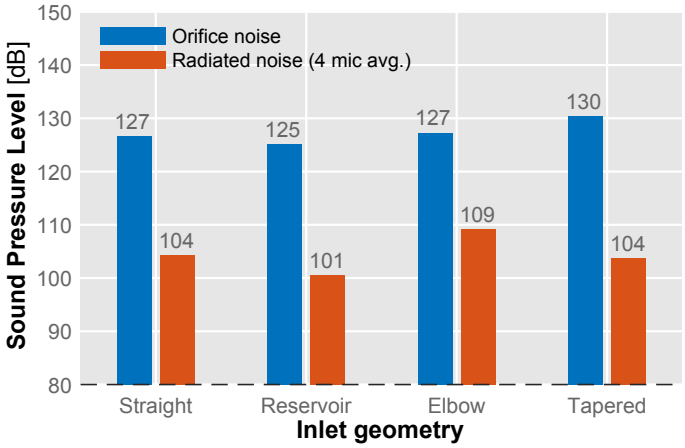

Figure 8.4: *Comparison of orifice noise and averaged radiated noise measured in the anechoic chamber for each of the simple inlet geometries at the stable operating point closer to surge.*

It can be seen that again there are significant differences between the inlet geometries tested. These differences were higher when measuring the radiated noise through the average of the four microphones, with the reservoir featuring a 3 dB reduction compared to the reference straight duct.

On the other hand, the 90º elbow inlet reached a 5 dB increase over the straight inlet level, but this particular result could be influenced by the fact that the direction of the orifice was not perpendicular to the plane of the four microphones. Finally, the tapered duct seemed to radiate at the same level that the straight pipe.

Regarding orifice noise, the reservoir featured again a reduction in noise level of 2 dB. However, in this case the elbow featured the same level as the reference straight pipe, being the tapered duct the one with a higher level at 130 dB, 3 dB more than the reference geometry.

In Fig. 8.5 the different spectra recorded by the orifice microphone during each geometry test are plotted to look in detail at these level differences. It can be seen how levels for the tapered duct are higher along the whole frequency range, while the inlets featuring the elbow and the reservoir remain closer to the reference straight pipe.

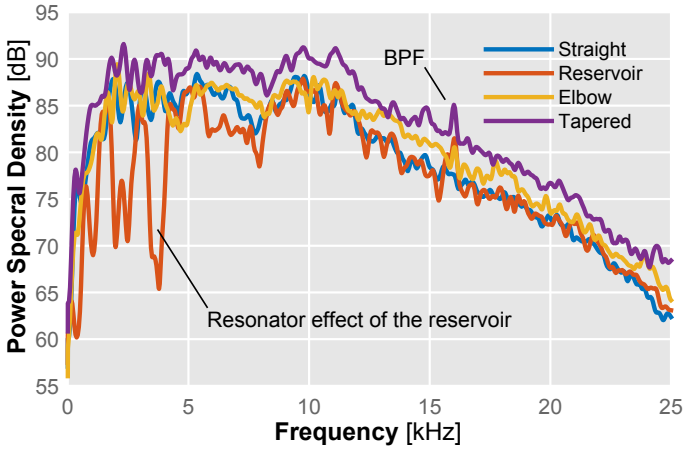

Figure 8.5: *Comparison of orifice noise spectra for each of the simple inlet geometries at the stable operating point closer to surge.*

The most noticeable difference however, is the resonator effect of the reservoir, that provides an important attenuation at frequencies in the plane wave region of the spectrum. Compare this against the tapered duct spectrum which raises levels over the whole spectrum. Finally, a small peak can be noticed at 16 kHz, correspondent to the Blade Passing Frequency associated to the 160 krpm shaft speed that was used during these measurements.

8.2. On-engine tests

In the scope of the on-engine tests described in chapter 5, a follow-up experimental campaign was carried out in order to characterize the effect that different geometric variations of the turbocharger inlet line had in performance, surge margin and noise emission.

8.2.1. Measurement setup

The selected geometric variations of the inlet line were chosen taking into account realistic packaging size restrictions of commercial vehicles, so in this case the reservoir case was not tested as it was not possible to fit it to the available compressor inlet.

Similarly, elbow inlets were not tested as they would require to re-route the inlet line, being its design already frozen at the time of the testing. Focus was then put into small changes like tapered ducts, rotation devices and nozzle-like additions to the inlet pipe.

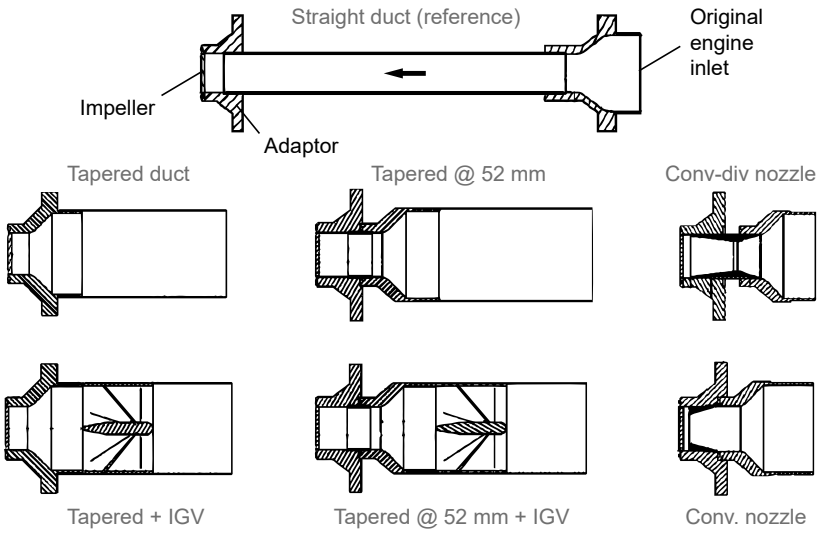

Figure 8.6: *Longitudinal section view of the inlet geometries that were considered for the on-engine experimental campaign.*

Figure 8.6 shows the selected geometry variations based on these selection criteria. On top of the figure the reference geometry is depicted. The turbocharger inducer was milled and substituted by an adaptor to which a straight duct was coupled. At the end of this duct a pipe of the original diameter was then affixed with a tapered transition.

The simplest inlet geometry tested consisted in a tapered duct situated as close as possible to the compressor impeller leading edge. This can be seen at the center left in the figure. Below, it is shown how this tapered duct was complemented with an inlet guide vanes (IGV) device.

This was done in order to increase the swirl of the incoming air flow. The device stators featured 0° leading edge angles and ∼ 70° trailing edge angles, and it was directly 3D-printed from the CAD design. The device can be seen fitted into the inlet pipe in Fig. 8.7.

Figure 8.7: *Image of the 3D-printed IGV device fitted to the compressor inlet duct, looking towards the impeller.*

To analyze how the closeness of the tapered duct to the impeller influenced the behaviour of the compressor, the two following geometric variations (center column of Fig. 8.6) were the same except for the separation between the tapered duct and the impeller, which was increased to 52 mm. Again, one of the measurements was performed with an IGV and the other without it.

Lastly, two nozzles were tested (right column of Fig. 8.6): a convergent-divergent nozzle between the tapered adaptor and the impeller (top) and a convergent nozzle (bottom) just after the tapered duct, with its throat as close as possible to the impeller wheel.

In order to evaluate the influence of these geometric variation on the noise output of the compressor, the acoustic measurement setup used in chapter 5 was maintained, consisting in the straight inlet extension featuring the pressure decomposition array for in-duct intensimetry and the intensity probe aligned with the inlet orifice.

Measurement operating conditions for the noise characterization campaign were chosen as to be representative of the most common real-life conditions. This was done in order to test if these simple inlet variations could modify the noise output not only on the most extreme conditions but also when more conservative settings are applied.

8.2.2. Results

Since the objective of this experimental campaign is the comparison between geometries, in this subsection only the results from the orifice intensity probe will be presented for the sake of brevity, as it was shown in section 5.3 that they were well correlated with in-duct noise.

In Fig. 8.8 the interpolated intensity level map is presented, indicating the points at which each measurement was made. The interpolation of sound intensity was performed between frequencies of 1 and 3 kHz, which are specially relevant regarding the aforementioned *whoosh* issue.

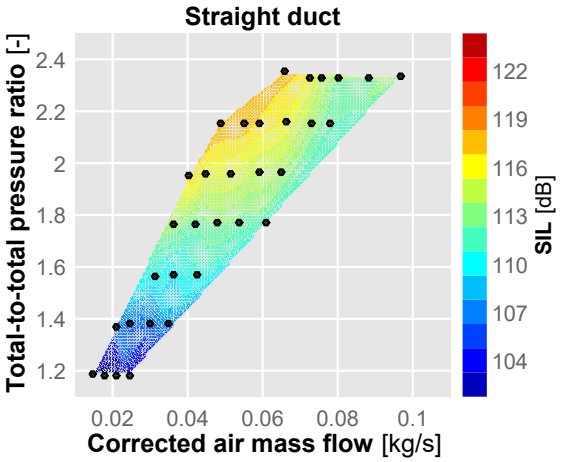

Figure 8.8: *Sound intensity level map between 1 – 3 kHz for the straight inlet used as a reference in the on-engine inlet geometric variation test.*

Note as well that because of the particular regulation mechanism of the facility based on the injection of compressed air into the inlet line, the depicted operating conditions do not represent constant shaft speed lines[1], so no judgement about the slope of these lines should be made.

However, it can be seen in this figure that the noise levels in the selected band behave as expected, based on results described in previous chapters. Noise levels increase as pressure ratio increases and air mass flow diminishes, with the dependency on air mass flow being much more noticeable at higher pressure ratios that at lower ones.

Figure 8.9 shows the results for the same frequency band when the reference straight duct was substituted by each of the geoetric inlet variants previously described in Fig. 8.6.

It is apparent from the figure that different operating conditions were measured in each one of the tests, as the goals in this campaign were to characterize the sound emission across the selected map region and to test how each geometry impacted the performance in regards of surge margin and maximum ingested air mass flow.

In this regard, the figure shows how the geometry changes have an impact on surge margin (left frontier of the map), as some of the modified inlet lines increase the range of low flow operating conditions that can be safely

[1]For reference, shaft speed varied between 65 and 170 krpm in the depicted map.

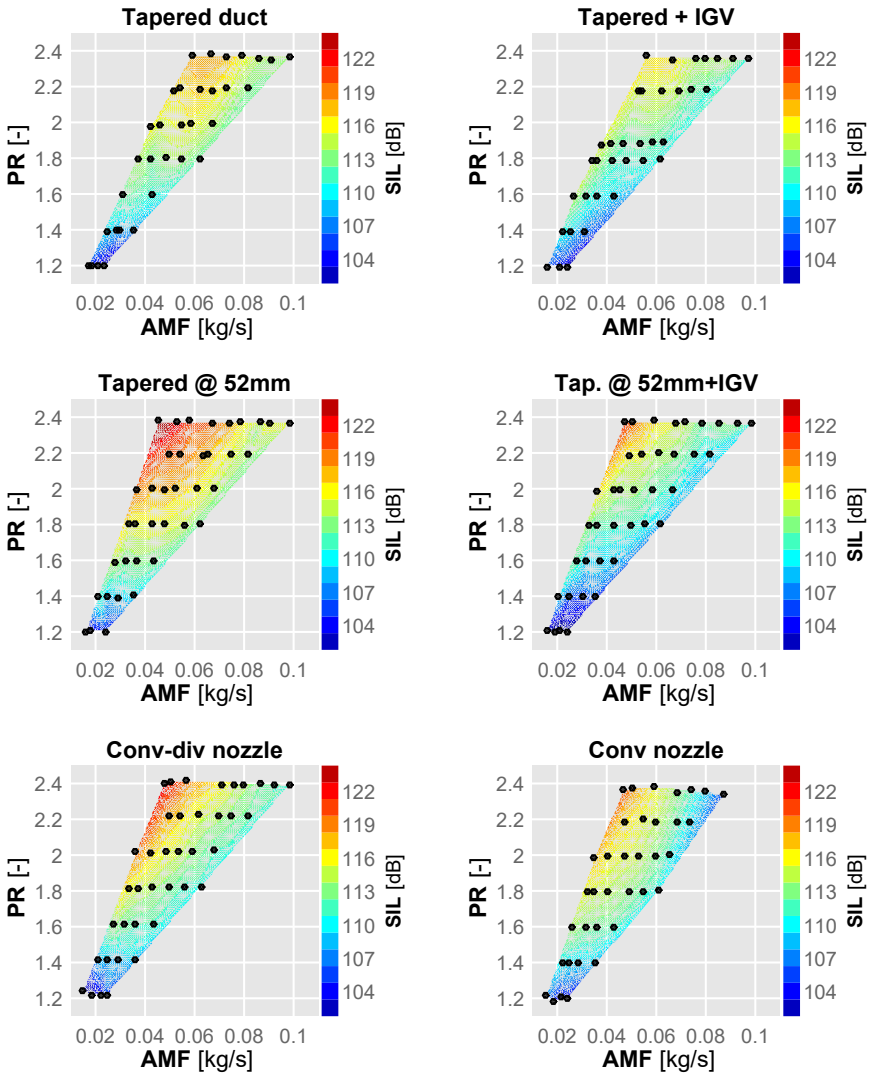

Figure 8.9: *Sound intensity level maps between 1 – 3 kHz for the different geometries used in the on-engine test.*

used before going into deep surge, specially at higher shaft speeds; compare for instance the highest row of points of the straight inlet in Fig. 8.8 and that of the convergent-divergent nozzle (bottom left plot of Fig. 8.9).

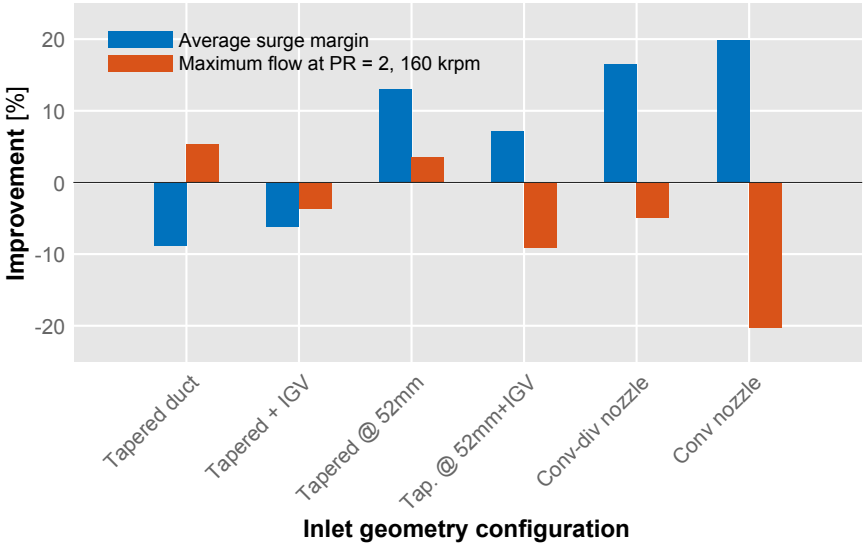

Figure 8.10: *Comparison of performance variation for each of the inlet geometries across the normal operating range of the engine.*

Impact of the geometry variation on air mass flow was also tested in regards of maximum flow at 160 krpm, as it is not only important to increase surge margin but also to maintain the possibility of operating the turbocharger at high mass flow levels.

A comparison of the performance of each geometry in both aspects is presented in Fig. 8.10 where the percentages of improvement from the straight duct reference inlet are plotted. An inverse correlation between maximum flow and surge margin is apparent, only the tapered duct at 52 mm from the impeller improving both factors at the same time and only the tapered duct closer to the impeller and featuring an IGV worsening both.

Largest amount of surge margin improvement was found with the convergent nozzle, but at the cost of an equally large air mass flow reduction at $\Pi_{TT} = 2$ and 160 krpm of shaft speed, so in order to implement this solution in real-life applications it should be necessary to mechanically open the nozzle throat at these high flow conditions.

To similarly quantify the influence of the geometries in noise emission at the selected frequency band, in Fig. 8.11 an average sound intensity level (SIL) is presented, as measured by the Brüel & Kjær intensity probe located pointing directly to the inlet orifice.

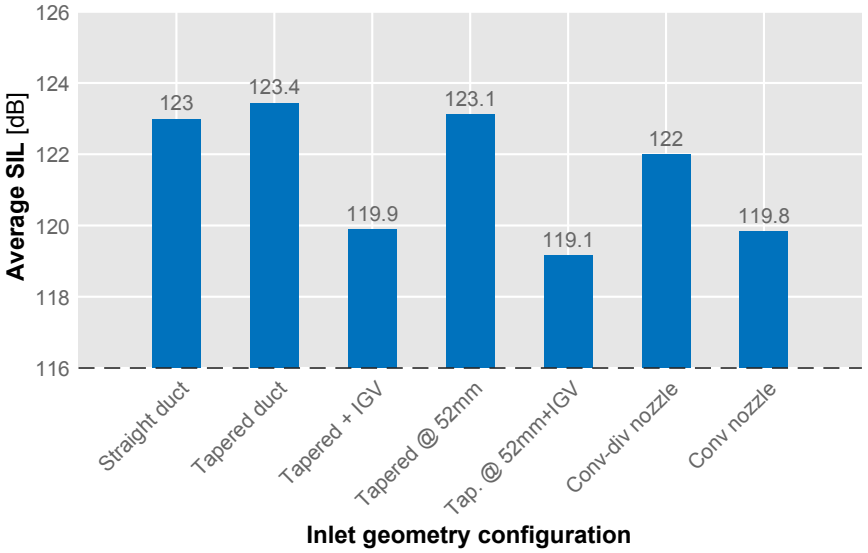

Figure 8.11: *Comparison of mean sound intensity level for each of the inlet geometries across the normal operating range of the engine.*

Intensity level of the tapered duct is very similar to that of the reference straight pipe; both when located as close as possible to the compressor wheel and when separated 52 mm from it. The addition of the described IGV to those tapered inlets notably reduces noise levels by 3 and 4 dB respectively.

Regarding the nozzle configurations, it can be seen that the convergent-divergent nozzle reduces noise output in the selected frequency band by 1 dB, whereas the convergent nozzle features a notable reduction of approximately 3 dB compared to the reference.

8.3. Elbow parametric study

Having attested the influence of the inlet geometries not only in surge margin and maximum flow but also regarding acoustic performance, it was decided to use the turbocharger test rig used for the inlet local flow measurements described in chapter 7 to study the effect of these geometric variations not only in the global aspects of sound intensity and air mass flow but also regarding local aspects like temperature distribution, skewness, etc.

The gathering of local flow experimental data will also be useful if CFD simulations of these kind of inlet modifications are undertaken, in order to provide a validation reference to check for the correct solving of not only global values but also local flow field characteristics.

Since neither during the previously described on-engine experimental campaign nor during the preliminary testing described at the beginning of the present chapter was it possible to properly measure the sound intensity caused by elbow geometries, it was decided that the study should start with this kind of geometry variation.

Another reason to consider this geometry is that it introduces non-uniformities in the flow field that completely axisymmetric geometries such as tapered ducts and nozzles do not, so it would provide a good contrast to check the influence on circumferential temperature distribution skewness and correlation with noise generation.

In order to increase the available data on the relation between inlet-induced flow distortion, temperature skewness and noise output, it was decided that a parametric campaign should be carried out where three 90º elbows of different radius would be designed, manufactured and tested.

8.3.1. Geometry design

Requirements for the design of the elbow inlets were such that they could be easily installed into the existing setup used for local measurements, coupling to the adaptor piece and existent measurement pipe featuring the in-duct intensity sensor array.

In addition, they needed to house the available linear thermocouple arrays in order to measure the high temperature reversed flow (it should be noted that the circumferential thermocouple array was installed into the adaptor piece) approximately keeping the distance between tips and distance from the wall that were selected for the straight pipe study.

Finally, to assess the influence of the flow distortion, the three selected variants were as follows: a very tight elbow with a central radius of 0.75 compressor inlet diameters (marked as D in Fig. 8.12), a medium elbow with 1D of radius and finally an elbow with a central radius of 1.5D that would provide a smoother transition and less distorted flow.

To fulfil these design requirements, a decision was made to manufacture the elbow prototypes using 3D printing instead of traditional workshop means. This way, the guiding slots for the thermocouples and retention

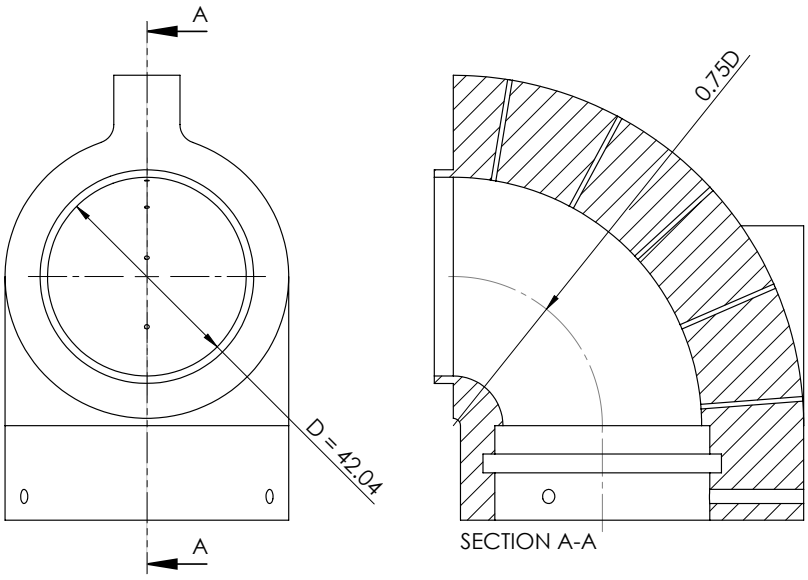

Figure 8.12: *Mechanical drawing of the 0.75D elbow inlet designed to fit into the compressor inlet adaptor and house the linear thermocouple array.*

screws could be directly embedded in the piece, along with the slots for the sealing O-rings. Fig. 8.12 shows the mechanical drawing of the most abrupt elbow with 0.75D of radius.

This design was implemented in a parametric CAD model to easily modify the central radius. Also, a locking system was put into place so the elbow could be affixed tightly to the compressor adaptor using a flange and a set of threaded rods, similarly to the procedure performed for the local flow characterization. The three prototypes generated in this way are shown in Fig. 8.13.

Once that the three CAD models were generated, they were sent to a commercial partner for verification and manufacturing. It should be noted that the elbow prototypes were expected to withstand the high temperature backflow coming from the compressor in unstable operating conditions close to deep surge, without undertaking deformations that would have misaligned the thermocouple array.

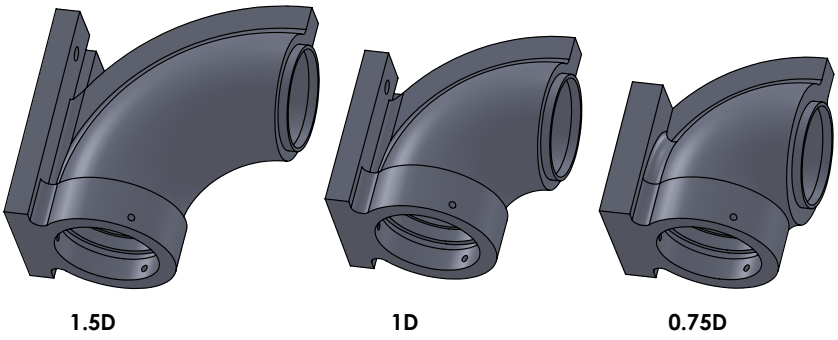

Figure 8.13: *CAD models of the compressor elbow inlets of different radius (decreasing in radius from left to right) that were used to create the 3D-printed prototypes.*

Taking into account these concerns, it was decided to manufacture the elbow prototypes using an aluminium-filled polyamide through a process known as Selective Laser Sintering (SLS), a technique in which a laser beam is focused onto the surface of a tray containing the powdered material, binding it together in layers to create the desired shape.

Specifications of the selected material can be found in table 8.1. Of special relevance is the heat deflection temperature, also called sometimes heat distortion temperature. It is defined as the temperature at which a sample,

Table 8.1: *Specifications of the aluminium-filled polyamide used for the laser-sintering of the elbow inlet prototypes.*

Property	Normative	Unit	Value
Tensile Modulus	DIN EN ISO 527	MPa	3800 ± 150
Tensile Strength	DIN EN ISO 527	MPa	48 ± 3
Elongation at Break	DIN EN ISO 527	%	3.5 ± 1
Flexural Modulus	DIN EN ISO 178	N/mm^2	3600 ± 150
Charpy – Impact strength	DIN EN ISO 179	MPa	29 ± 2
Charpy – Notched Impact Strength	DIN EN ISO 179	MPa	4.6 ± 0.3
Shore D/ A-hardness	DIN 53505	-	D 76 ± 2
Heat Deflection Temp	ASTM D648 (1.82MPa)	°C	130
Vicat Softening Temperature B/50	DIN EN ISO 306	°C	169
Density	N/A	g/cm^3	1.36 ± 0.05

under a defined load of 1.82 MPa, will start to deflect at least 0.25 mm. Since in this case the inlet line is approximately at ambient pressure no problem is expected until more elevated temperatures.

8.3.2. Setup

After SLS manufacturing and delivery, the prototype elbows were instrumented with thermocouples and installed into the anechoic chamber test rig. Fig. 8.14 shows the assembly of the narrower elbow variant.

It should be noted that the narrow holes for the thermocouple alignment became filled with residual dust during the sintering process, and had to be finished with a manual drill. This presented no problem as the chosen material is easily mechanized.

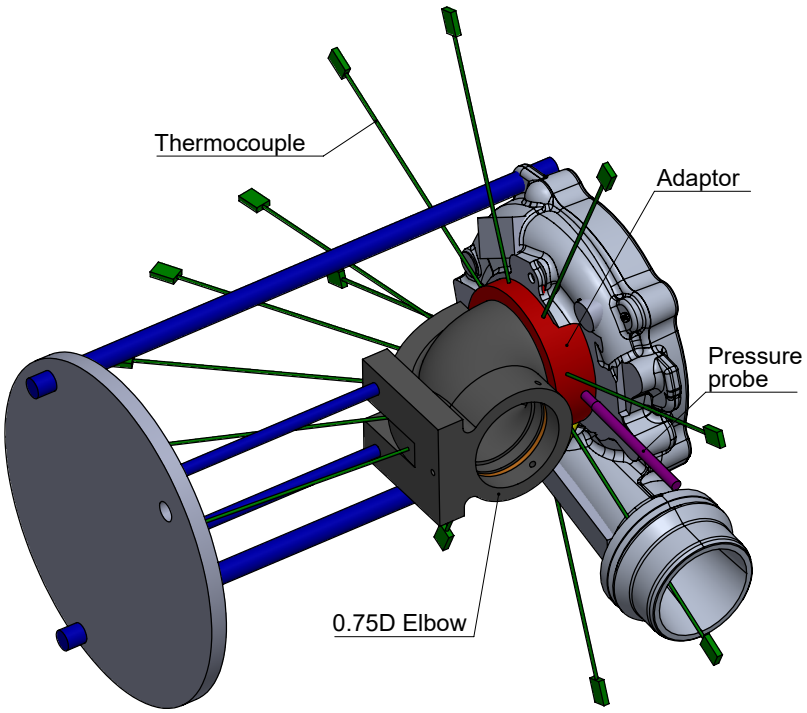

Figure 8.14: *CAD model of the compressor assembly featuring the 0.75D elbow inlet attached to the common adaptor, including the pressure and temperature instrumentation and the mounting system.*

As it can be seen in Fig. 8.14 the previously used adaptor piece housing the circumferential temperature array, the inducer miniature pressure probe and a sealing O-ring was kept in place, and the holes in the plane surface added to the elbow were used to align the elbow parallel to the outlet and tighten it using the threaded rods depicted in blue.

8.3.3. Results

During this experimental campaign, operating conditions were selected to mirror those used in the local flow characterization chapter that featured a straight inlet pipe, in order to allow the reconstruction of interpolated maps that were as close as possible to the original reference map.

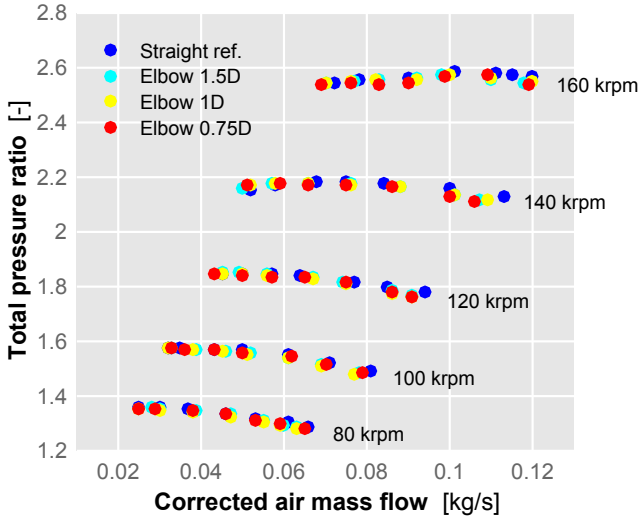

Figure 8.15: *Operating conditions at which data was recorded during the inlet flow characterization tests with a straight duct (as reference) and during the parametric elbow campaign. This data points will be used in the present section for every map.*

Fig. 8.15 shows the operating conditions of each measured data point, for both the straight inlet pipe used as reference, and for the three described elbow prototypes. It can be seen that repeatability was achieved in most conditions up to a few g/s of air mass flow and ∼100 corrected rpm.

The most adverse conditions were those of maximum allowable flow, specially at higher pressure ratios where the flow distortion and pressure loss caused by the elbows made difficult to achieve exactly the same conditions.

8.3.3.1. Sound intensity

Using the in-duct piezoelectric sensor arrays, sound intensity level was computed through the wave decomposition method outlined in chapter 3 for each operating conditions. In order to focus into the previously described *whoosh* noise problem, sound intensity level was averaged between 0.7 and 3 kHz. and then the interpolating procedure was used in order to reconstruct noise maps for each geometry.

To highlight the differences between the reference straight duct noise map and the result obtained for each elbow prototype, and taking into account the aforementioned slight differences between operating conditions at higher air mass flow settings, difference maps were produced by subtracting the reference levels to each one of the newly obtained elbow maps.

It should be remarked that this subtraction procedure was not performed between the raw levels at each measurement setting but between each interpolated data point, and only where such interpolated data existed in both noise maps (elbow and reference), as to avoid erroneous differences due to the different operating conditions.

The results of this procedure can be seen in Fig. 8.16, where the difference maps for the three elbow configurations regarding inlet and outlet in-duct intensity are presented. Color scale has been kept constant in order to allow a meaningful comparison between each map.

It can be seen in the maps, examining for instance some of the highest mass flow rate points, that some information is missing around the black dot that indicates the original measurement point before interpolation. This missing data comes from slight differences in measurements between the two geometries being compared, as the subtraction process is only performed where data exists for both of them.

As for the evolution of level difference with the variation of the elbow radius, the figure shows how in the case of the inlet sound intensity differences appear to be higher than in the case of the outlet. This increase is specially evident at lower flow conditions and medium-low shaft speeds, reaching up to 6 dB in level increase.

There also appears to be a particular point with an small increase in level for both inlet and outlet ducts, at medium air mass flow and medium to hight shaft speeds, its relevance diminishing along with the reduction of the elbow radius.

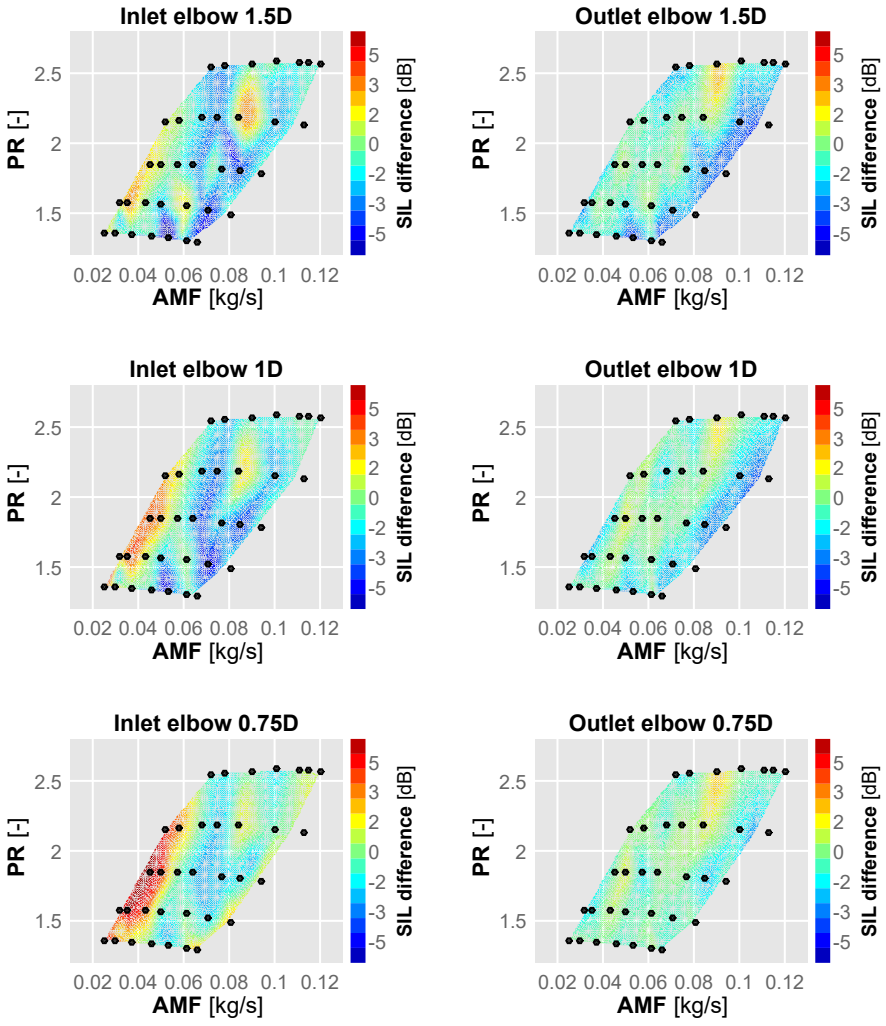

Figure 8.16: *Difference map of inlet (left) and outlet (right) in-duct sound intensity levels for each of the selected inlet elbows compared against the reference straight duct. From top to bottom: 1.5D, 1D & 0.75D.*

Finally, some operating conditions in both the inlet and outlet present reduced noise output in the selected frequency band, specially at medium-higher mass flows and lower shaft speeds. As with the case of the increases, these reductions are more significant in the inlet duct, whereas positive and negative variations are of smaller magnitude in the outlet duct.

In order to better quantify the SIL differences that these maps reveal, histograms that represent the distribution of the differences have been computed and presented in Fig. 8.17 for both inlet (top) and outlet (bottom) sound intensity results.

It can be seen in the figure how the different elbow configurations affect the distribution of the intensity level differences. In the case of the inlet, the less narrow elbow (1.5D) and the medium elbow (1D) present a similar, almost symmetric distribution with a mean around -1 dB.

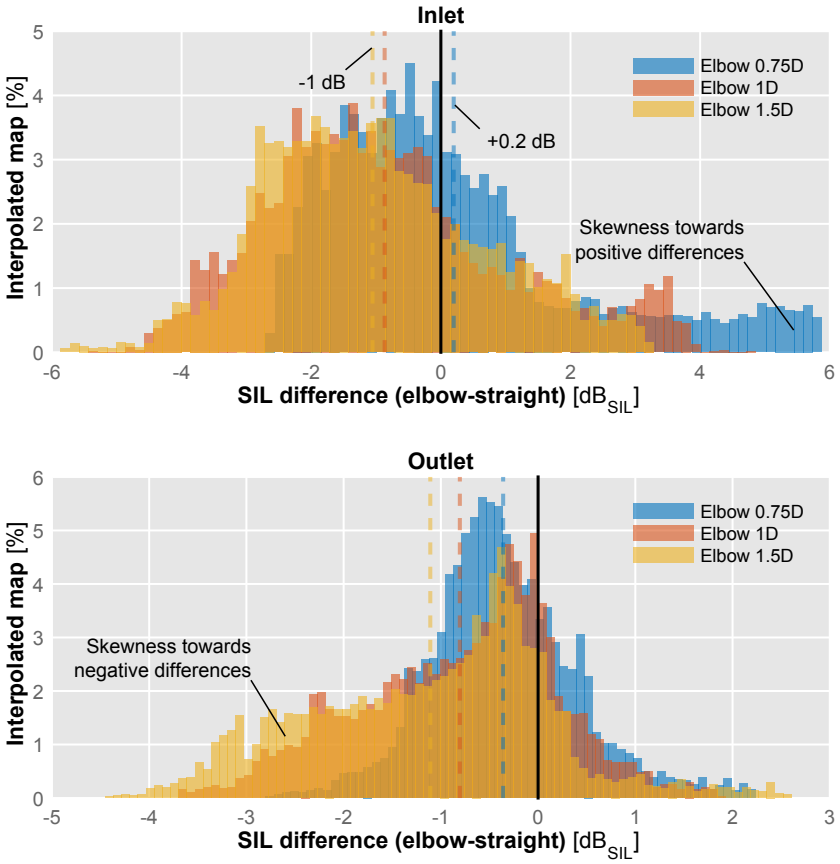

Figure 8.17: *Histograms of inlet (top) and outlet (bottom) sound intensity level differences between each one of the tested elbow variants and the reference straight inlet pipe. Y axis indicates the percentage of the interpolated compressor map at which each difference level occurred. A dashed line indicates the average of each configuration.*

The distribution of the most narrow elbow (0.75D) appears to feature a marked skewness towards positive differences of up to 6 dB that correspond with the low flow, medium-low speed region identified in the aforementioned intensity maps. These points shift the mean up to approximately 0.2 dB of increased level.

Regarding the outlet difference distributions, the situation appears to reverse, with the narrower elbow now featuring the most symmetric distribution and the other two variations presenting a marked skewness towards intensity reduction values, again up to a mean of around 2 dB in the most favo

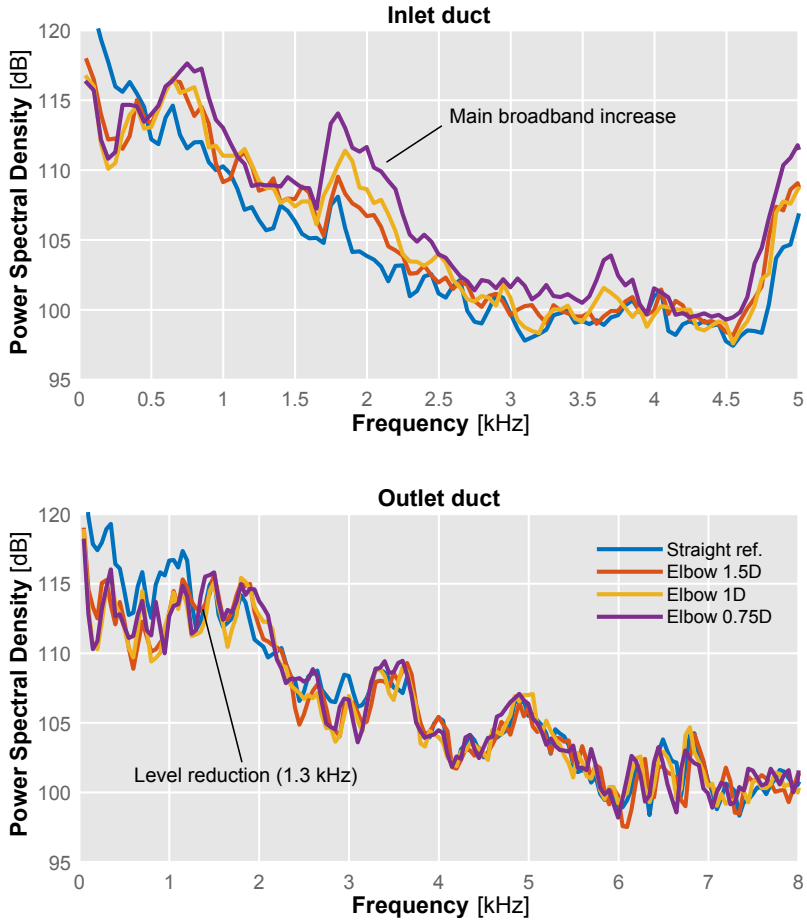

Figure 8.18: *Comparison of plane wave range spectra from both inlet and outlet, highlighting the differences between the straight reference duct and each elbow configuration at 140 krpm and 45 g/s.*

Focusing now into the detailed aspects of the sound level variation, it is possible to compare the pressure spectra in different points to assess the frequency distribution of the level variation. For instance in Fig. 8.18 the PSD in the plane wave region recorded by inlet and outlet piezoelectric sensors is shown for the different inlet geometries at an operating condition where differences were high (140 krpm, 45 g/s).

In the case of the outlet duct, spectra are very similar up to a cut-off point at approximately 1.3 kHz, below which the straight duct presents higher levels than all of the elbows.

On the other hand, spectra on the plane wave region of the inlet duct shows higher differences, consistent with the data already presented in the maps and histograms.

It is interesting to note however that this increase is not homogeneous in frequency; it can be seen how the small peak at 1.7 kHz present in the straight duct gradually increases with elbow radius reduction, up to a clearly visible broadband between 1.5 and 2.5 kHz.

These are flanked by another two smaller broadband elevations at 0.75 and 3.6 kHz that are also visible in the case of the outlet spectra, and were also very clearly present in the pressure spectra recorded by the diffuser pressure probe, shown for instance in Fig. 7.17 of the previous chapter.

It should be noted as well that, while levels for the detected broadband in the inlet show an increase up to 5 dB, at these frequencies all of the outlet spectra plotted in the lower graph remain at the same levels, indicating that while changes in the inlet configuration seem to boost the upstream transmission of the so-called *whoosh* broadband noise, no influence on the outlet duct spectra is detected at these frequencies.

8.3.3.2. Temperature

Besides the described differences in terms of acoustic intensity produced by the different inlet configurations, it is possible to follow a similar processing procedure in order to assess the differences in terms of temperatures in the inlet section that are related to the hot reversed flow coming from after the compressor impeller.

As in the previous experimental campaign, data from the two thermocouple arrays (longitudinal and circumferential) was processed in order to compile maps of the backflow length and flow temperature skewness, respectively.

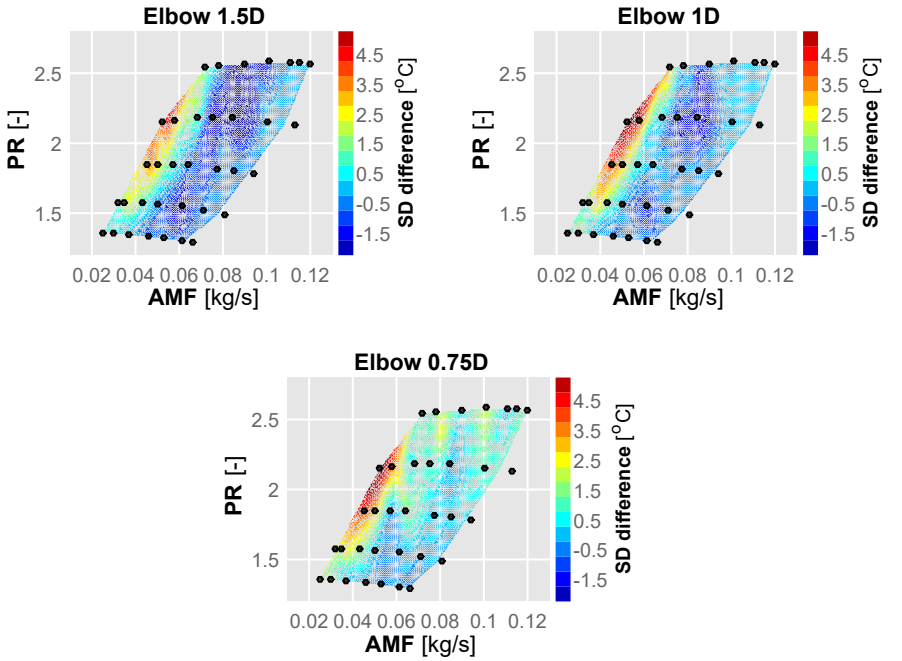

Figure 8.19: *Difference maps of temperature circumferential standard deviation for each of the selected inlet elbows compared against the reference straight duct.*

These maps were then compared with the original reference map measured with a straight inlet duct, and difference maps were produced for each elbow variant. The resulting difference (elbow minus straight) maps can be seen in Fig. 8.19. The same color scale has been kept in all of them to provide a suitable comparison.

It can be seen that for the three cases a similar patters appears. An increase in temperature skewness is consistently detected at the lower air mass flow settings, specially at medium shaft speed operating conditions.

At higher air mass flow settings however, a slight reduction in flow temperature skewness is apparent, being much more pronounced in the less narrow elbow configuration (1.5D, top left map).

This reduction area spans approximately the same conditions for the 1D elbow, but the magnitude of the temperature skewness difference is lower than in the previous case, becoming nearly zero in the case of the most reduced elbow variant (0.75D).

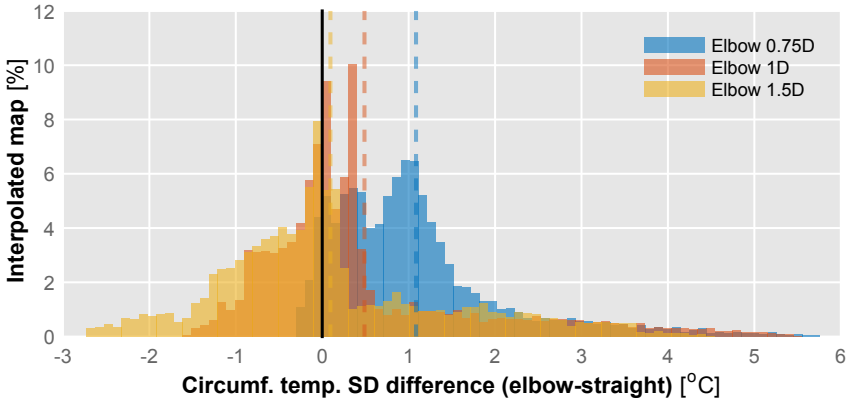

Figure 8.20: *Histograms of temperature standard deviation differences between each one of the tested elbow variants and the reference straight inlet pipe. Y axis indicates the percentage of the interpolated compressor map at which each difference level occurred. A dashed line indicates the average of each configuration.*

As in the case of sound intensity level differences, it is possible to combine these maps in the form of histograms in order to better quantify the distribution of these differences. These histograms can be seen plotted in Fig. 8.20.

Distributions shown in this figure appear similar in shape, but shifted in mean value. In all three cases the right tail of the distribution is longer but less populated, indicating that the difference increase happens abruptly in a small region of the compressor map.

On the contrary, the left tails are more populated but shorter, meaning that more regions of the compressor map feature points with slightly lower differences than the average. These averages reach up to 1°C in the case of the most narrow elbow configuration (0.75D), while the average is almost zero for the case of the less narrow elbow (1.5D).

As mentioned earlier, by processing the temperature profiles measured by the longitudinal thermocouple array that was added to the design of each elbow prototype, it is also possible to estimate the length of the hot reversed backflow that travels upstream of the impeller and into the inlet in unstable operating conditions.

When designing the prototypes, care was put to ensure that the separation between the thermocouples remained equal to that of the straight inlet duct, taking into account their inserted length of half a radius and the varying radius of each elbow pipe.

In Fig. 8.21 the estimated length along the exterior edge of the elbow (where the thermocouple array was installed, as shown in Fig. 8.12) is mapped for the three elbow configurations.

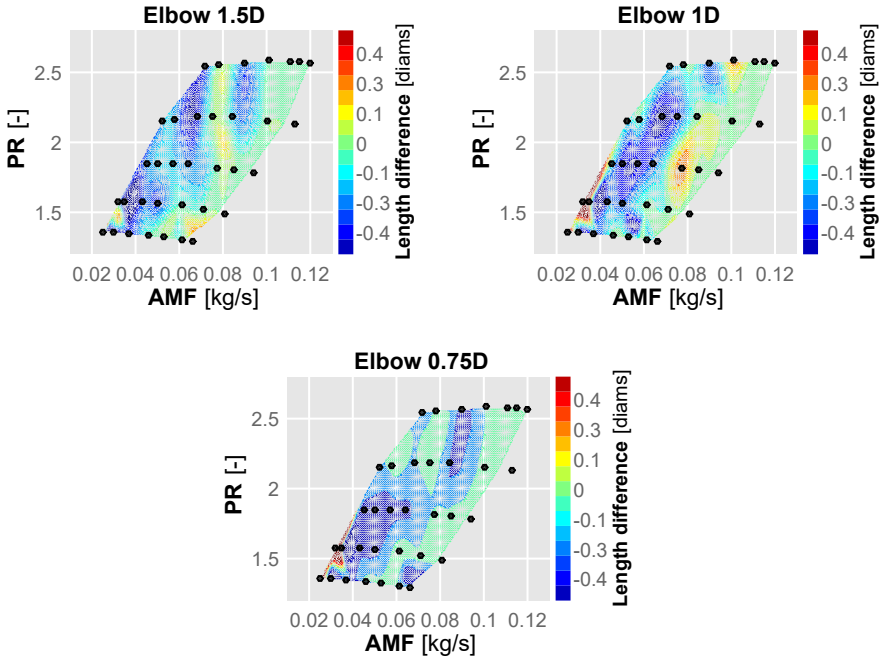

Figure 8.21: *Difference maps of high temperature backflow extent for each of the selected inlet elbows compared against the reference straight duct.*

In this case, differences range from minus half a diameter up to plus a diameter when compared with the reference straight pipe. The patterns of these differences along the compressor map appears to be similar for the three geometric variations: a slight reduction at lower mass flow conditions and a slight increase at higher mass flow conditions for all shaft speeds.

Exceptions to this pattern are some of the lowest air mass flow data points at 100 and 120 krpm for the two narrower elbows (0.75D and 1D), where the backflow length appears to feature a large increase. However it is possible that those are spurious results from the interpolation procedure, since the increase region is very small.

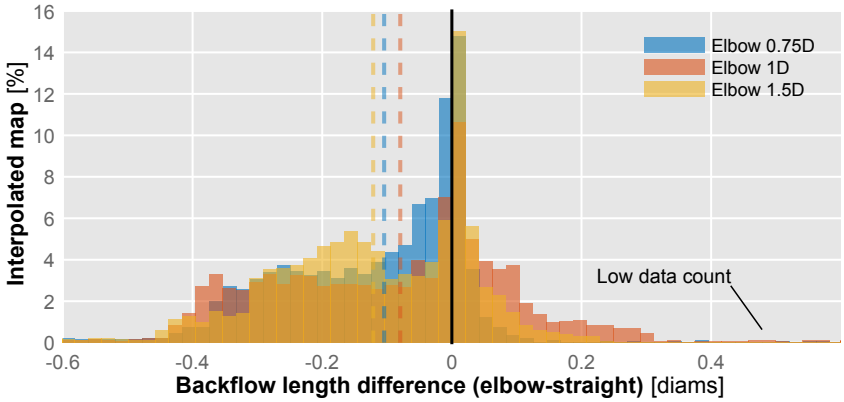

Figure 8.22: *Histogram of high temperature backflow extent differences between each one of the tested elbow variants and the reference straight inlet pipe. Y axis indicates the percentage of the interpolated compressor map at which each difference level occurred. A dashed line indicates the average of each configuration.*

These low count points are best shown when the data is put into histogram form as seen in Fig. 8.22. In this figure it can be seen how the three backflow length difference distributions are quite similar in shape and values.

The three distributions feature approximately the same mean, around 0.1 diameters of backflow length reduction from the straight inlet case. However, the most usual difference (that is, the statistical mode) is practically zero. It must be also considered that the estimation of backflow is only performed along the outer edge of the elbow, while the modified flow pattern could mean that a very non-symmetric backflow is propagating upstream.

8.3.3.3. Correlations between SIL and temperature

In Fig. 8.23 the correlation between sound intensity level and circumferential temperature skewness has been performed again for the three elbow inlet cases as it was already made in chapter 7 for the case of the straight pipe. This correlation has been included as a reference, keeping the same axis limits of the elbow cases.

It can be seen in this figure how for the straight pipe and the more straight elbow (that with an central radius equal to 1.5D), both pictured on the top plots, a clear separation is maintained between higher flow rate conditions

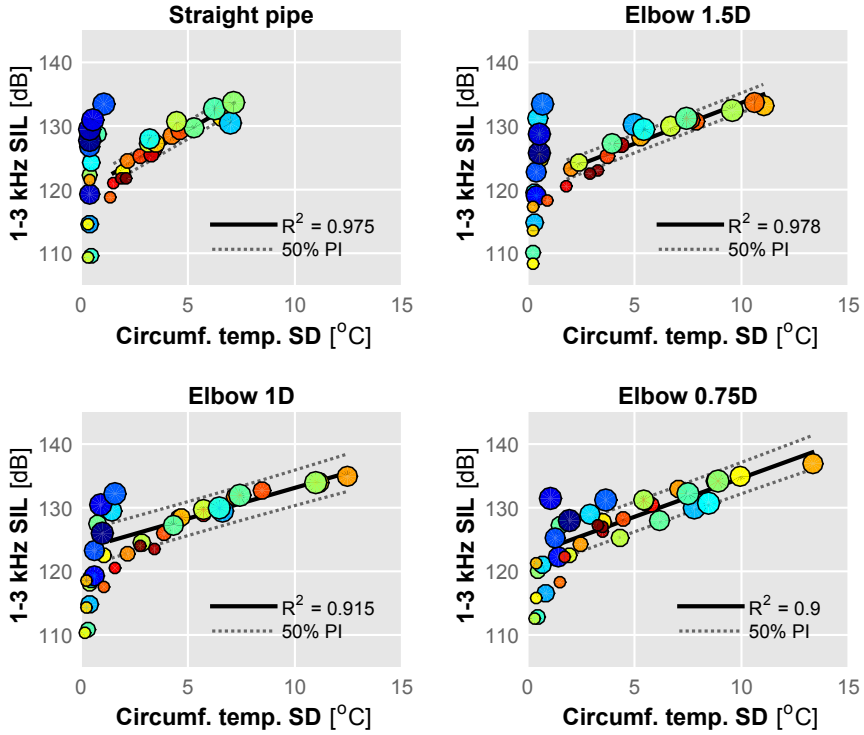

Figure 8.23: *Correlations between standard deviation at the circumferential thermocouple array and inlet sound intensity level in the 1 – 3 kHz band for the straight pipe and the three elbow inlets. Size indicates shaft speed from low to high and color indicates mass flow from higher (blues) to lower (reds).*

(indicated as blue circles) which exhibit higher noise levels even when no skewness is detected, and those of lower flow rate where skewness is well correlated with the increase in noise levels.

In the case of the more narrow elbows, pictured in the bottom plots of the figure, the difference between the higher and lower flow rate cases becomes blurred, as even points of the higher flow rate demonstrate measurable temperature skewness as the elbow radius decreases.

By comparing the four plots of the figure, it can also be seen how the maximum values of temperature skewness increase as the radius of the pipe decreases, with the same trend being followed by the sound intensity level in the selected frequency band, as was clearly seen previously in Fig. 8.17

where the characteristic "hump" of *whoosh* noise becomes more pronounced as the radius of the elbow gets narrower (while a similar influence is not observed in the outlet spectra).

8.4. Conclusions

Through this chapter, three different experimental campaigns aimed at assessing the influence of the inlet geometry in the turbocharger acoustic output have been presented. While different in scope and means, the results shown in this chapter allow some global conclusions to be drawn.

First, a series of tests was carried out where simple geometric variants were added to the compressor inlet, with a straight duct of the same diameter than the compressor inducer being as a reference. This reference was maintained for the three described experimental campaigns. Both orifice noise recorded with a free-field microphone and orifice noise averaged between four microphones were recorded.

Results of this first test series showed that, apart from an effect in the turbocharger surge margin that had been previously pointed out by Galindo et al. [70], influence of the geometries on both orifice and radiated noise could be found. The tapered duct appeared to increase the orifice noise, while the reservoir acted as a resonator and not only increased surge margin but lowered both orifice (2 dB) and radiated noise (3 dB). Meanwhile, the elbow increased kept the same orifice noise levels.

Another series of geometry tests were carried out in an engine cell and introduced more complex geometry combinations, with tapered ducts featuring an IGV device and the addition of two nozzles to the inlet line, besides the reference straight pipe. In this case noise output was measured by a commercial intensity probe aligned with the inlet orifice and with the in-duct intensimetry method based on beamforming wave decomposition described in chapter 3.

Acoustic data from this on-engine campaign confirmed that the selected tapered duct, while revealing an improvement in surge margin and maximum flow when located at a certain distance from the impeller, did not evidence a significant effect in orifice noise intensity and in any case these differences were harmful with a slight increase in levels, albeit of less than 0.5 dB.

The addition of an IGV device to boost incoming flow swirl proved interesting as it decreased the acoustic intensity recorded by the orifice probe by 3-4 dB depending on the position of the tapered duct. However this device negatively impacted the maximum flow and, depending on the position of the downstream tapered section, also the surge margin.

In the case of the inlet geometries equipped with a nozzle, a decrease of orifice noise was found ranging from 1 dB (converge-divergent nozzle) to 3 dB (convergent nozzle). These nozzles also improved surge margin up to 20%, but, specially the convergent one, decreased the maximum available air mass flow.

Finally, a more through experimental campaign was carried out where a family of 90º elbow inlets with different radii (that were not tested on the engine due to packaging constraints) were installed on the anechoic test ring and instrumented to measure not only in-duct noise but also temperature distribution through the thermocouple arrays described in chapter 7.

Results from this campaign provided higher in-depth insight into the influence of the elbow radius; as in the aforementioned first testing campaign the very sharp elbow showed equal or slightly higher mean sound intensity in the inlet. However, this increase was not uniformly distributed across the compressor map but concentrated on the lowest allowable air mass setting for each shaft speed. This pattern was shared among the three tested elbow configurations, although as the radius grew sound intensity levels in both inlet and outlet reduced up to 1 dB in average.

Regarding the influence of the inlet elbow variants on the temperature distribution, a similar pattern of circumferential skewness increase towards the lowest allowable flow conditions for each shaft speed could be reconstructed. However, reversed flow length appears similar in all cases, with differences of less than 0.5 inlet diameters.

Correlations of *whoosh* noise content and temperature skewness indicated an increase of both variables as the elbow radius became narrower. Reasons for these correlated increases could be related to the uneven presentation of the air flow caused by the progressively narrow 90º elbows[2]. These created a region of lower pressure that facilitated the upstream propagation of reversed flow and thus enhanced the convection of *whoosh* noise content from the diffuser to the inlet duct, while also increasing the differences in temperature across the different zones.

[2]See the work of Kalpakli et al. [137, 138] for an in-depth numerical analysis of the particular flow field caused by these kind of 90º elbows, including its POD decomposition.

This would explain why elbow radius shows a clear effect on the *whoosh* noise content in the inlet spectra shown in Fig. 8.18 but not in the outlet, and also why this effect is restricted to the lower mass flow rate zones of the compressor map (see Fig. 8.16 for the effect on sound intensity and Fig. 8.19 for the effect on temperature skewness) where reversed flow is more prominent, as instabilities grow while inflow momentum diminishes.

In any case, further research, specially if performed together with CFD simulations, is needed to characterize the effect of the inlet flow field at unstable conditions and its relation to coherent flow structures acting as noise sources.

CHAPTER 9

Conclusions and future works

In this chapter the concluding remarks of this doctoral thesis are presented, gathering together the main findings that have been obtained during the research described in the previous chapters and the global contributions that have been made to the state of the art in the field of the acoustic characterization of turbocharger compressors, specially focusing on the different methodological procedures and the results that their application has offered.

To conclude, some future works of interest are suggested, that could be pursued in order to expand the knowledge obtained during this investigation applying both the experimental techniques that have been described in the previous chapters and the numerical tools that have been validated as part of this thesis.

9.1. Conclusions

The main conclusions of the work performed during the development of this doctoral thesis can be globally categorized by the point of view of methodology procedures that have been presented, validated and discussed and, on the other hand, by the results about the acoustic output of the compressor that the application of these procedures has provided.

These conclusions fulfil the objectives that were outlined for this work, increasing the available knowledge on the acoustic behaviour of turbocharger compressors and the methodologies that are useful for its characterization.

It is hoped that this knowledge aids in the development of better turbocharger designs and implementations, thereby contributing to the mitigation of the concerns raised by noise emission caused by automotive applications with quieter and more efficient engines.

9.1.1. Methodology

Along the different chapters of this doctoral thesis, several techniques have been described that are useful to characterize the noise emission of turbocharger compressors, mainly experimentally but also by analyzing the results of numerical simulations. The main findings, contributions and conclusions about these methodologies can be summarized as follows:

- Beamforming wave decomposition has been proved to be a useful technique to obtain experimental measurements of in-duct sound intensity in turbocharger compressor inlet and outlet pipes. A methodology has been presented in order to use this information to build noise maps and spectrograms that characterize the acoustic performance of the compressor along the region of interest of its operating conditions map.

- Comparisons made with inlet orifice noise measurements performed on an anechoic chamber show that in-duct sound intensity results are well correlated with orifice noise information, which is a metric of interest in automotive applications. External acoustic radiation measurements were also performed, coupled with sequential insulation in order to assess the contribution of each part of the turbocharger system.

- Further validation of this methodology in an engine test cell equipped for turbocharger characterization including an orifice intensity probe has shown that the technique is robust even in the case where pulsations from the reciprocating internal combustion engine are present in the spectral content of the compressor duct pressure, leading to more coherent results that other wave decomposition techniques. External near field measurements performed with an Acoustic Particle Velocity probe demonstrated promising potential to isolate the specific acoustic contribution of the turbocharger.

- Usefulness of beamforming wave decomposition has also been shown regarding the validation of results coming from CFD simulations of the compressor. In conjunction with numerical MoC decomposition, validation of simulated pressure spectra against experimental data has been shown. Other post-processing techniques such as Fourier analysis and Dynamic Mode Decomposition have also been demonstrated to offer valuable information regarding the identification of

acoustical sources, specially concerning complex flow phenomena in the compressor inlet, inducer and diffuser at unstable operating conditions.

- In order to investigate these complex flow features a methodology for experimental measurements of local temperature, pressure and velocity has been developed and presented, showing how these unstable phenomena evolve as air mass flow rate is reduced. Specifically, processing of the temperature readings were used to characterize the growth of the reversed flow in order to perform Particle Image Velocimetry in selected operating conditions.

- Different approaches to successfully apply the PIV procedure to longitudinal and transversal planes of the glass pipe confining the reversed flow were found and described. Results from these velocity field characterization were found to be in good agreement with data measured by thermocouple arrays, with the growth of this backflow also correlated with increased sound intensity propagation in the *whoosh* frequency band.

- A methodology for accurate assessment of the influence that different inlet geometries have on the compressor performance regarding not only surge margin but also regarding acoustic output has been presented, including the implementation of an experimental installation that allows the fast acoustic testing of custom 3D-printed inlet geometries up to 1/3 diameters from the compressor wheel.

9.1.2. Results

During the development and application of the aforementioned methodological procedures, valuable results regarding the acoustic behaviour of turbocharger compressors were found, being the most relevant among them as follows:

- Analysis of the in-duct decomposed pressure spectra correctly identified acoustic features that were described in the initial literature review such as tonal noise caused by the blade passing, broadband *whoosh* noise at plane wave frequencies, and a TCN-like broadband at higher frequencies. Non-dimensional analysis of these phenomena suggested the first being related to flow effects and the later ascribed

to transmission effects. Furthermore, the TCN-like broadband appeared to be unable to propagate at plane wave frequencies, unlike the *whoosh* noise band which appears at these conditions. This demonstrates a clear difference between these two broadband phenomena and provides a simple criterion to tell them apart.

- Sound intensity level maps measured in the anechoic chamber flow rig were compiled for different frequency bands, reproducing for instance the relation between very low frequency content and deep surge onset. In contrast, *whoosh* noise level isocontours were not parallel to deep surge onset but more related to the inception of mild surge at the maximum pressure ratio condition for each constant speed characteristic line.

- Inspection of selected spectra and specially the spectrograms reconstructed from the interpolated map results clearly demonstrated however the presence of typical *whoosh* noise content even at conditions close to the maximum efficiency region of the compressor map and well before the inception of mild surge, pointing to the source flow mechanism of *whoosh* noise not being rotating stall or large reversed flow vortices that only appear after mild surge onset.

- Once that validation of CFD simulations attested that numerical data correctly followed experimental results, specially regarding the presence of the *whoosh* noise band in simulated pressure spectra, post-processing of CFD results at different operating conditions (that were simulated using experimentally-measured boundary conditions) indicated that reversed flow did not appear until the maximum pressure ratio point, although vortex shedding in the diffuser was present for all conditions. Fourier analysis also showed that for a typical *whoosh* band frequency, amplitude is higher at the diffuser than at the ducts. DMD analysis of the outlet wall cells identified modes related to BPF and *whoosh* noise frequencies as the most relevant in terms of coherence.

- Experimental results from the local variable characterization provided experimental data on the backflow growth across the compressor map through the analysis of temperature evolution, confirming that stable, high flow rate conditions where no backflow was detected through temperature nor through velocity measurements still presented *whoosh* noise content, measured not only through the beamforming arrays but also through the inducer and diffuser probes, where the characteristic

hump was detected even for the higher flow rate condition, thereby pointing to an origin for this noise phenomenon not related to reversed or stalled inlet flow.

- Analysis of the influence of inlet geometry demonstrated that the acoustic performance of the compressor can be modified with the addition of different elements such as 90º elbows, tapered ducts, reservoirs, nozzles, etc. Effect of the elbow radius was specifically investigated, showing how sound intensity level and circumferential temperature skewness differences were particularly significant at the lower mass flow rates where inlet flow carries less momentum. This was also hinted by the preliminary results as nozzles and IGVs which highly affect the flow presentation have the larger effect on noise in the *whoosh* band. Coupled with the correlation analysis and the conclusions from previous chapters, this seems to reinforce the hypothesis of *whoosh* noise being generated by flow interaction in the diffuser, its level in the inlet at unstable conditions being raised by convection effects as the reversed backflow carries its spectral content upstream.

9.2. Future works

In order to confirm these hypotheses and gain further information on the influence of geometry and flow presentation on the different acoustic phenomena that are of concern regarding turbocharger compressors, some future works are suggested in this section, from the point of view of both experimental research and numerical simulations.

9.2.1. Experimental research

By taking advantage of the experimental techniques and the facilities developed in the framework of this doctoral thesis, a follow up investigation could be envisaged where the following points could be of interest:

- An exploratory analysis of different simple geometries could be performed, taking special interest in how the inlet flow is affected at unstable conditions in the mild surge region and how the modification of this flow pattern, as described with the aid of the presented local measurement techniques, influences the transmission of *whoosh* noise and other concerning acoustic emissions.

- Acoustic Particle Velocity measurements could be used to characterise the detailed spatial distribution of the near-field noise radiated by the turbocharger assembly, thus assisting in locating the most relevant sources for each acoustic phenomena identified in the already obtained spectral content.

- The turbocharger facilities could be modified with the addition of compression drivers[1] in order to provide external excitations which could be used to measure acoustical properties of the compressor assembly such as the full scattering matrix, with the aim of building realistic acoustic models of the compressor at different operating settings.

9.2.2. Numerical simulations

These experimental works could also provide valuable information to initialize and validate further numerical simulations that could provide a deeper insight in how the flow field interacts inside the compressor and how it evolves with the different working conditions, such as:

- Modification of the initial CFD model with more realistic inlet and outlet ducts, improved boundary conditions and heat transfer models that could be useful to enhance the identification of spectral content generated by the turbocharger compressor and better compare against experimental temperature data.

- Use of this improved model to analyze the effect of different inlet geometries and how the flow pattern is affected by these additions. This study would be specially relevant if carried out conjunction with experimental measurements performed using the setup presented in this work.

- Implementation of advanced post-processing routines such as the Dynamic Mode Decomposition technique outlined in chapter 6, mainly if coupling with existing solvers could be achieved by use of streaming DMD algorithms that avoid the need for large data storage and processing. These techniques would allow easier matching between relevant flow structures and their corresponding frequency contribution.

[1] Essentially, special loudspeakers featuring a strong titanium diaphragm.

- Extension of the numerical setup beyond uncoupled internal flow, encompassing vibro-acoustic and noise radiation simulations by means of one-way or fully coupled fluid/solid interaction modelling. This extended setup could be validated through near- and far-field experimental measurements as described in this work, thereby developing a comprehensive model of the turbocharger compressor acoustics that would be useful for faster simulation-based design cycles.

Bibliography

[1] A. Broatch, J. Galindo, R. Navarro, and J. García-Tíscar. "Methodology for experimental validation of a CFD model for predicting noise generation in centrifugal compressors". *International Journal of Heat and Fluid Flow* 50, 2014, pp. 134–144 (cited in pp. 52, 97, 101).

[2] A. Broatch, J. Galindo, R. Navarro, J. García-Tíscar, A. Daglish, and R. K. Sharma. "Simulations and measurements of automotive turbocharger compressor whoosh noise". *Engineering Applications of Computational Fluid Mechanics* 9 (1), 2015, pp. 12–20 (cited in pp. 55, 97).

[3] A. Torregrosa, A. Broatch, R. Navarro, and J. García-Tíscar. "Acoustic characterization of automotive turbocompressors". *International Journal of Engine Research* 16 (1), 2015, pp. 31–37 (cited in p. 83).

[4] A. Broatch, J. Galindo, R. Navarro, and J. García-Tíscar. "Numerical and experimental analysis of automotive turbocharger compressor aeroacoustics at different operating conditions". *International Journal of Heat and Fluid Flow* 61, Part B, 2016, pp. 245–255 (cited in p. 97).

[5] A. J. Torregrosa, A. Broatch, X. Margot, and J. García-Tíscar. "Experimental methodology for turbocompressor in-duct noise evaluation based on beamforming wave decomposition". *Journal of Sound and Vibration* 376, 2016, pp. 60–71 (cited in pp. 27, 153).

[6] A. J. Torregrosa, A. Broatch, X. Margot, J. García-Tíscar, Y. Narvekar, and R. Cheung. "Local flow measurements in a turbocharger compressor inlet". *Submitted to Experimental Thermal and Fluid Science*, 2016.

[7] A. J. Torregrosa, A. Broatch, J. V. Pastor, J. García-Tíscar, R. K. Sharma, and R. Cheung. "Measuring turbocharger compressor inlet backflow through laser particle image velocimetry". *Submitted to Experimental Thermal and Fluid Science*, 2016.

[8] G. Daimler. "Gas- bezw. Petroleum-Kraftmaschine". N°34926 (Kaiserliche Patentamt). 1885 (cited in p. 2).

[9] L. Renault. "Perfectionnements aux moteurs à quatre temps". N°327452 (Office National de la Propiété Industrielle). 1902 (cited in p. 2).

[10] A. Büchi. "Verbrennungskraftmaschinenanlage". N°204630 (Kaiserliche Patentamt). 1905 (cited in p. 2).

[11] J. O. de Beeck, J. Thompson, and N. Booth. "Upcoming Emission Regulations for Passenger Cars: Impact on SCR System Requirements and Developments". *SAE Technical Paper* 2013-01-1072, 2013 (cited in p. 4).

[12] F. Schumann, F. Sarikoc, S. Buri, H. Kubach, and U. Spicher. "Potential of spray-guided gasoline direct injection for reduction of fuel consumption and simultaneous compliance with stricter emissions regulations". *International Journal of Engine Research* 14 (1), 2013, pp. 80–91 (cited in p. 4).

[13] K. S. Peat, A. J. Torregrosa, A. Broatch, and T. Fernández. "An investigation into the passive acoustic effect of the turbine in an automotive turbocharger". *Journal of Sound and Vibration* 295 (1-2), 2006, pp. 60–75 (cited in p. 4).

[14] B. Lecointe and G. Monnier. "Downsizing a Gasoline Engine Using Turbocharging with Direct Injection". *SAE Technical Paper* 2003-01-0542, 2003 (cited in p. 4).

[15] H. Stoffels and M. Schroeer. "NVH Aspects of a Downsized Turbocharged Gasoline Powertrain with Direct Injection". *SAE Technical Paper* 2003-01-1664, 2003 (cited in p. 4).

[16] C. Teng and S. Homco. "Investigation of Compressor Whoosh Noise in Automotive Turbochargers". *SAE Int. J. of Passeng. Cars-Mech. Syst.* 2 (1), 2009, pp. 1345–1351 (cited in pp. 4, 11, 13, 16, 50, 84).

[17] A. Stodola and L. Loewenstein. *Steam and gas turbines: with a supplement on the prospects of the thermal prime mover*. McGraw-Hill, 1927 (cited in p. 4).

[18] C. J. da Silveira Brizon and E. B. Medeiros. "Combining subjective and objective assessments to improve acoustic comfort evaluation of motor cars". *Applied Acoustics* 73 (9), 2012, pp. 913–920 (cited in p. 5).

[19] M. Nor, M. Fouladi, H. Nahvi, and A. Ariffin. "Index for vehicle acoustical comfort inside a passenger car". *Applied Acoustics* 69 (4), 2008, pp. 343–353 (cited in p. 5).

[20] J. Němec. "Noise of axial fans and compressors: Study of its radiation and reduction". *Journal of Sound and Vibration* 6 (2), 1967, pp. 230–236 (cited in p. 9).

[21] J. Griffiths. "The spectrum of compressor noise of a jet engine". *Journal of Sound and Vibration* 1 (2), 1964, pp. 127–140 (cited in p. 9).

[22] L. Mongeau, D. Thompson, and D. McLaughlin. "Sound Generation by Rotating Stall in Centrifugal Turbomachines". *Journal of Sound and Vibration* 163 (1), 1993, pp. 1–30 (cited in pp. 10, 34, 66).

[23] L. Mongeau, D. Thompson, and D. Mclaughlin. "A method for characterizing aerodynamic sound sources in turbomachines". *Journal of Sound and Vibration* 181 (3), 1995, pp. 369–389 (cited in pp. 10, 34, 66).

[24] J.-S. Choi. "Aerodynamic noise generation in centrifugal turbomachinery". *KSME Journal* 8 (2), 1994, pp. 161–174 (cited in pp. 10, 66).

[25] J.-S. Choi, D. K. McLaughlin, and D. E. Thompson. "Experiments on the unsteady flow field and noise generation in a centrifugal pump impeller". *Journal of Sound and Vibration* 263 (3), 2003, pp. 493–514 (cited in pp. 10, 66).

[26] D. Wolfram and T. H. Carolus. "Experimental and numerical investigation of the unsteady flow field and tone generation in an isolated centrifugal fan impeller". *Journal of Sound and Vibration* 329 (21), 2010, pp. 4380–4397 (cited in pp. 10, 66).

[27] D. Wolfram and T. Carolus. "Detection and Analysis of Blade Tone Sources at Centrifugal Impellers Without Casing". In: *Aeroacoustics Conferences*. American Institute of Aeronautics and Astronautics, 2009 (cited in pp. 10, 66).

[28] T. H. Carolus, D. McLaughlin, and R. Basile. "Experimental investigation of the unsteady discharge flow field and the noise of a centrifugal fan impeller". In: *The Seventh International Congress on Sound and Vibration Garmisch-Partenkirchen, Germany*. 2000 (cited in pp. 10, 66).

[29] E. P. Trochon. "A new type of silencers for turbocharger noise control". *SAE Technical Paper* 110 (6), 2001, pp. 1587–1592 (cited in pp. 11–13, 15, 154).

[30] D. Evans and A. Ward. "Minimizing Turbocharger Whoosh Noise for Diesel Powertrains". *SAE Technical Paper* 2005-01-2485, 2005 (cited in pp. 11, 13, 15, 84, 154).

[31] D. Evans and A. Ward. "The reduction of turbocharger whoosh noise". In: *Proceedings of the 8 th International Conference on Turbochargers and Turbocharging, London, UK*. 2006, pp. 29–42 (cited in pp. 11, 84).

[32] R. Kabral, H. Rammal, and M. Åbom. "Acoustical methods for investigating turbocharger flow instabilities". *SAE Technical Paper* 2013-01-1879 (cited in p. 11).

[33] R. Kabral and M. Åbom. "Investigation of flow-acoustic interaction in automotive turbocharger". In: *26th International Conference on Noise and Vibration Engineering, ISMA 2014*. KU Leuven. 2014, pp. 1327–1331 (cited in p. 11).

[34] Y. Lee, D. Lee, Y. So, and D. Chung. "Control of Airflow Noise From Diesel Engine Turbocharger". *SAE Technical Paper* (2011-01-0933), 2011 (cited in pp. 11, 13, 17, 19, 20).

[35] E. Guillou, R. DiMicco, E. Gutmark, A. Mohamed, and M. Gancedo. *Characterization of a Ported Shroud Compressor using PIV Measurements*. Tech. rep. 2010-01-1225. SAE Technical Paper, 2010 (cited in pp. 12, 13, 17, 22, 24).

[36] N. Figurella, R. Dehner, A. Selamet, K. Tallio, K. Miazgowicz, and R. Wade. "Noise at the mid to high flow range of a turbocharger compressor". *Noise Control Engineering Journal* 62 (5), 2014, pp. 306–312 (cited in pp. 12, 13, 18, 21, 34, 134).

[37] N. Figurella, R. Dehmer, A. Selamet, K. Tallio, et al. "Effect of inlet vanes on centrifugal compressor acoustics and performance". *Noise Control Engineering Journal* 62 (4), 2014, pp. 232–237 (cited in pp. 12, 13, 18).

[38] G. Gaudé, T. Lefèvre, R. Tanna, K. Jin, T. J. B. McKitterick, and S. Armenio. "Experimental and computational challenges in the quantification of turbocharger vibro-acoustic sources". In: *Proceedings of the 37th International Congress and Exposition on Noise Control Engineering (INTER-NOISE 2008)*. Vol. 2008. 3. Institute of Noise Control Engineering. 2008, pp. 5754–5767 (cited in pp. 12–14, 34, 58).

[39] T. Raitor and W. Neise. "Sound generation in centrifugal compressors". *Journal of Sound and Vibration* 314, 2008, pp. 738–756 (cited in pp. 12, 13, 15).

[40] A. V. Pai, S. J. Walsh, D. J. O'Boy, and R. Chen. "Air intake system noise in a turbocharged petrol engine during transient operation". In: *INTER-NOISE and NOISE-CON Congress and Conference Proceedings*. 2013, pp. 3656–3663 (cited in pp. 13, 84).

[41] A. V. Pai, S. J. Walsh, D. J. O'Boy, and R. Chen. "Turbocharger surge noise measurement and solution using experimental techniques". In: *Proceedings of the 22nd International Congress on Sound and Vibration*. 2015, pp. 2433–2441 (cited in pp. 13, 18, 84).

[42] H. Tiikoja, H. Rämmal, M. Abom, and H. Boden. "Investigations of Automotive Turbocharger Acoustics". *SAE International Journal of Engines* 4 (2), 2011, pp. 2531–2542 (cited in pp. 13, 17, 34).

[43] F. Kameier and W. Neise. "Rotating blade flow instability as a source of noise in axial turbomachines". *Journal of Sound and Vibration* 203 (5), 1997, pp. 833–853 (cited in p. 15).

[44] A. Karim, K. Miazgowicz, B. Lizotte, and A. Zouani. "Computational Aero-Acoustics Simulation of Compressor Whoosh Noise in AUtomotive Turbochargers". *SAE Technical Paper* (2013-01-1880), 2013 (cited in pp. 19, 24).

[45] F. Mendonça, O. Baris, and G. Capon. "Simulation of Radial Compressor Aeroacoustics using CFD". In: *Proceedings of ASME Turbo Expo 2012*. GT2012-70028. ASME. 2012, pp. 1823–1832 (cited in pp. 19, 100).

[46] F. Hellström, E. Guillou, M. Gancedo, R. DiMicco, et al. *Stall Development in a Ported Shroud Compressor using PIV Measurements and Large Eddy Simulation*. Tech. rep. SAE Technical Paper 2010-01-0184, 2010 (cited in pp. 20, 22).

[47] E. Guillou. "Flow characterization and dynamic analysis of a radial compressor with passive method of surge control". PhD thesis. University of Cincinnati, 2011 (cited in p. 20).

[48] X. Margot, A. Gil, A. Tiseira, and R. Lang. "Combination of CFD and Experimental Techniques to Investigate the Flow in Centrifugal Compressors Near the Surge Line". *SAE Technical Paper Series* 2008-01-0300, 2008 (cited in p. 20).

[49] R. Lang. "Contribución a la Mejora del Margen de Bombeo en Compresores Centrífugos de Sobrealimentación". PhD thesis. Universitat Politècnica de València, 2011 (cited in pp. 21, 23, 134, 157, 171).

[50] J. Galindo, A. Tiseira, R. Navarro, and M. López. "Influence of tip clearance on flow behavior and noise generation of centrifugal compressors in near-surge conditions". *International Journal of Heat and Fluid Flow* 52, 2015, pp. 129–139 (cited in p. 21).

[51] J. Andersen, F. Lindström, and F. Westin. "Surge definitions for radial compressors in automotive turbochargers". *SAE International Journal of Engines* 1 (1), 2009, pp. 218–231 (cited in pp. 21, 134, 142).

[52] A. Liu and X. Zheng. "Methods of surge point judgment for compressor experiments". *Experimental Thermal and Fluid Science* 51, 2013, pp. 204–213 (cited in pp. 21, 133, 169).

[53] N. Pedersen, P. S. Larsen, and C. B. Jacobsen. "Flow in a centrifugal pump impeller at design and off-design conditions-part I: particle image velocimetry (PIV) and laser Doppler velocimetry (LDV) measurements". *Journal of Fluids Engineering* 125 (1), 2003, pp. 61–72 (cited in p. 21).

[54] J. M. F. Oro, E. B. Marigorta, K. M. A. Díaz, and R. Ballesteros-Tajadura. "Forced and unforced unsteadiness in an axial turbomachine". *Experimental Thermal and Fluid Science* 33 (3), 2009, pp. 449–459 (cited in p. 21).

[55] A. K. Vester, S. S. Sattarzadeh, and R. Örlü. "Combined hot-wire and PIV measurements of a swirling turbulent flow at the exit of a 90° pipe bend". *Journal of Visualization*, 2015, pp. 1–13 (cited in p. 21).

[56] M. Wernet. "Development of digital particle imaging velocimetry for use in turbomachinery". *Experiments in Fluids* 28 (2), 2000, pp. 97–115 (cited in pp. 21, 22, 171).

[57] B. Liu, X. Yu, H. Liu, H. Jiang, H. Yuan, and Y. Xu. "Application of SPIV in turbomachinery". *Experiments in fluids* 40 (4), 2006, pp. 621–642 (cited in pp. 21, 22).

[58] A. Dazin, G. Cavazzini, G. Pavesi, P. Dupont, et al. "High-speed stereoscopic PIV study of rotating instabilities in a radial vaneless diffuser". *Experiments in fluids* 51 (1), 2011, pp. 83–93 (cited in p. 21).

[59] Y. Wu, S. Liu, H. Yuan, and J. Shao. "PIV measurement on internal instantaneous flows of a centrifugal pump". *Science China Technological Sciences* 54 (2), 2011, pp. 270–276 (cited in pp. 21, 171).

[60] M. Fike, G. Bombek, M. Hriberšek, and A. Hribernik. "Visualisation of rotating stall in an axial flow fan". *Experimental Thermal and Fluid Science* 53, 2014, pp. 269–276 (cited in pp. 21, 157).

[61] M. P. Wernet. "Application of DPIV to study both steady state and transient turbomachinery flows". *Optics & Laser Technology* 32 (7), 2000, pp. 497–525 (cited in pp. 21, 22).

[62] M. P. Wernet, M. M. Bright, and G. J. Skoch. "An investigation of surge in a high-speed centrifugal compressor using digital PIV". *Journal of turbomachinery* 123 (2), 2001, pp. 418–428 (cited in p. 21).

[63] M. Voges, M. Beversdorff, C. Willert, and H. Krain. "Application of particle image velocimetry to a transonic centrifugal compressor". *Experiments in Fluids* 43 (2-3), 2007, pp. 371–384 (cited in p. 22).

[64] S. Ohuchida, H. Tamaki, K. Tomoki, K. Yamada, and M. Maruyama. "Internal Flow Measurements of Turbomachinery using PIV". *IHI Engineering Review* 46 (1), 2013, pp. 22–28 (cited in p. 22).

[65] B. Cukurel, P. B. Lawless, and S. Fleeter. "Particle image velocity investigation of a high speed centrifugal compressor diffuser: spanwise and loading variations". *Journal of Turbomachinery* 132 (2), 2010, p. 021010 (cited in p. 22).

[66] E. Guillou, M. Gancedo, R. DiMicco, E. Gutmark, et al. "Surge characteristics in a ported shroud compressor using PIV measurements and large eddy simulation". In: *9th International Conference on Turbochargers and Turbocharging*. 2010 (cited in p. 22).

[67] E. Guillou, M. Gancedo, E. Gutmark, and A. Mohamed. "PIV investigation of the flow induced by a passive surge control method in a radial compressor". *Experiments in fluids* 53 (3), 2012, pp. 619–635 (cited in p. 22).

[68] M. Gancedo, E. Gutmark, and E. Guillou. "PIV measurements of the flow at the inlet of a turbocharger centrifugal compressor with recirculation casing treatment near the inducer". *Experiments in Fluids* 57 (2), 2016, pp. 1–19 (cited in pp. 22, 171).

[69] J. Galindo, A. Tiseira, F. J. Arnau, and R. Lang. "On-Engine Measurement of Turbocharger Surge Limit". *Experimental Techniques* 37 (1), 2013, pp. 47–54 (cited in pp. 22, 32, 44, 84, 86, 140).

[70] J. Galindo, J. R. Serrano, X. Margot, A. Tiseira, N. Schorn, and H. Kindl. "Potential of flow pre-whirl at the compressor inlet of automotive engine turbochargers to enlarge surge margin and overcome packaging limitations". *International journal of heat and fluid flow* 28 (3), 2007, pp. 374–387 (cited in pp. 23, 24, 200).

[71] J. R. Serrano, X. Margot, A. Tiseira, and L. M. García-Cuevas. "Optimization of the inlet air line of an automotive turbocharger". *International Journal of Engine Research* 14 (1), 2013, pp. 92–104 (cited in p. 23).

[72] L. Wang, C. Yang, B. Zhao, D. Lao, C. Ma, and D. Li. "The change of the inlet geometry of a centrifugal compressor stage and its influence on the compressor performance". *Journal of Thermal Science* 22 (3), 2013, pp. 197–208 (cited in p. 23).

[73] E. M. Greitzer. "Surge and rotating stall in axial flow compressors—Part I: Theoretical compression system model". *Journal of Engineering for Power* 98 (2), 1976, pp. 190–198 (cited in p. 23).

[74] K. Hansen, P. Jorgensen, and P. Larsen. "Experimental and theoretical study of surge in a small centrifugal compressor". *Journal of Fluids Engineering* 103 (3), 1981, pp. 391–395 (cited in p. 23).

[75] A. Engeda, Y. Kim, R. Aungier, and G. Direnzi. "The inlet flow structure of a centrifugal compressor stage and its influence on the compressor performance". *Journal of fluids engineering* 125 (5), 2003, pp. 779–785 (cited in p. 23).

[76] D. Li, C. Yang, M. Zhou, Z. Zhu, and H. Wang. "Numerical and experimental research on different inlet configurations of high speed centrifugal compressor". *Science China Technological Sciences* 55 (1), 2012, pp. 174–181 (cited in p. 23).

[77] J. Galindo, F. Arnau, A. Tiseira, R. Lang, H. Lahjaily, and T. Gimenes. "Measurement and Modeling of Compressor Surge on Engine Test Bench for Different Intake Line Configurations". *SAE Technical Paper* (2011-01-0370), 2011 (cited in pp. 23, 84, 86).

[78] J. M. Desantes, J. M. Luján, B. Plá, and J. A. Soler. "Potential of using a nozzle at the compressor inlet of a high-speed direct-injection diesel engine". *Proceedings of the Institution of Mechanical Engineers, Part D: Journal of Automobile Engineering* 225 (2), 2011, pp. 178–189 (cited in p. 23).

[79] N. Kyrtatos and N. Watson. "Application of aerodynamically induced prewhirl to a small turbocharger compressor". *Journal of Engineering for Gas Turbines and Power* 102 (4), 1980, pp. 943–950 (cited in p. 24).

[80] M. Coppinger and E. Swain. "Performance prediction of an industrial centrifugal compressor inlet guide vane system". *Proceedings of the Institution of Mechanical Engineers, Part A: Journal of Power and Energy* 214 (2), 2000, pp. 153–164 (cited in p. 24).

[81] B. Semlitsch, V. JyothishKumar, M. Mihaescu, L. Fuchs, E. Gutmark, and M. Gancedo. "Numerical Flow Analysis of a Centrifugal Compressor with Ported and without Ported Shroud". *SAE Technical Paper* 2014-01-1655, 2014 (cited in p. 24).

[82] H. Chen and J. Yin. "Turbocharger compressor development for diesel passenger car applications". In: *8th International Conference on Turbochargers and Turbocharging*. Ed. by C. E. F̃. G. Institution of Mechanical Engineers. Woodhead Publishing, 2006, pp. 15–27 (cited in p. 24).

[83] J. Luján, V. Bermúdez, J. R. Serrano, and C. Cervelló. "Test bench for turbocharger groups characterization". *SAE Technical Paper* (2002-01-0163), 2002 (cited in p. 29).

[84] G. Piñero, L. Vergara, J. M. Desantes, and A. Broatch. "Estimation of velocity fluctuation in internal combustion engine exhaust systems through beamforming techniques". *Measurement Science & Technology* 11 (11), 2000, pp. 1585–1595 (cited in pp. 35, 36).

[85] C. L. Morfey. "Sound transmission and generation in ducts with flow". *Journal of Sound and Vibration* 14 (1), 1971, pp. 37–55 (cited in p. 35).

[86] E. Dokumaci. "On calculation of acoustic power". *Journal of Sound and Vibration* 238 (5), 2000, pp. 869–876 (cited in p. 35).

[87] B. Van Veen and K. Buckley. "Beamforming: A versatile approach to spatial filtering". *ASSP Magazine, IEEE* 5 (2), 1988, pp. 4–24 (cited in p. 35).

[88] J. E. Piper. *Beamforming narrowband and broadband signals*. Ed. by N. Kolev. INTECH Open Access Publisher, 2011 (cited in p. 35).

[89] K. Holland and P. Davies. "The measurement of sound power flux in flow ducts". *Journal of Sound and Vibration* 230 (4), 2000, pp. 915–932 (cited in p. 38).

[90] A. Torregrosa, A. Broatch, V. Bermudez, and I. Andres. "Experimental assessment of emission models used for IC engine exhaust noise prediction". *Experimental Thermal and Fluid Science* 30 (2), 2005, pp. 97–107 (cited in p. 38).

[91] A. P. Dowling and J. E. F. Williams. *Sound and Sources of Sound*. Ellis Horwood publishers, 1983 (cited in p. 39).

[92] M. Åbom and H. Bodén. "Error analysis of two-microphone measurements in ducts with flow". *Journal of the Acoustical Society of America* 83 (6), 1988, pp. 2429–2438 (cited in p. 39).

[93] A. F. Seybert. "Two-sensor methods for the measurement of sound intensity and acoustic properties in ducts". *Journal of the Acoustical Society of America* 83 (6), 1988, pp. 2233–2239 (cited in pp. 39, 78, 84, 87).

[94] L. J. Eriksson. "Higher order mode effects in circular ducts and expansion chambers". *Journal of the Acoustical Society of America* 68, 1980, p. 545 (cited in pp. 40, 86, 128, 152).

[95] F. Payri, J. M. Desantes, and A. Broatch. "Modified impulse method for the measurement of the frequency response of acoustic filters to weakly nonlinear transient excitations". *Journal of the Acoustical Society of America* 107 (2), 2000, pp. 731–738 (cited in p. 41).

[96] J. Galindo, J. R. Serrano, C. Guardiola, and C. Cervelló. "Surge limit definition in a specific test bench for the characterization of automotive turbochargers". *Experimental Thermal and Fluid Science* 30 (5), 2006, pp. 449–462 (cited in pp. 42, 44).

[97] J. Galindo, H. Climent, C. Guardiola, and A. Tiseira. "On the effect of pulsating flow on surge margin of small centrifugal compressors for automotive engines". *Experimental Thermal and Fluid Science* 33 (8), 2009, pp. 1163–1171 (cited in p. 48).

[98] F. Jacobsen. "Active and reactive, coherent and incoherent sound fields". *Journal of Sound and Vibration* 130 (3), 1989, pp. 493–507 (cited in p. 51).

[99] S. Elliott. "Errors in acoustic intensity measurements". *Journal of Sound and Vibration* 78 (3), 1981, pp. 439–443 (cited in p. 51).

[100] H.-E. de Bree, P. Leussink, T. Korthorst, H. Jansen, T. S. Lammerink, and M. Elwenspoek. "The μ-flown: a novel device for measuring acoustic flows". *Sensors and Actuators A: Physical* 54 (1), 1996, pp. 552–557 (cited in p. 51).

[101] F. Jacobsen and H.-E. de Bree. "A comparison of two different sound intensity measurement principles". *The Journal of the Acoustical Society of America* 118 (3), 2005, pp. 1510–1517 (cited in pp. 51, 92).

[102] D. F. Comesaña, S. Steltenpool, G. Carrillo Pousa, H.-E. de Bree, and K. R. Holland. "Scan and Paint: Theory and Practice of a Sound Field Visualization Method". *ISRN Mechanical Engineering* 2013, 2013 (cited in pp. 51, 92).

[103] O. Wolff, E. Tijs, and H.-E. de Bree. "A PU Probe Array Based Panel Noise Contribution Analysis Whilst Driving". In: *SAE Technical Paper*. SAE International, 2009 (cited in p. 51).

[104] I. Andrés. "Contribución al estudio y caracterización de la generación de ruido de flujo en el sistema de escape (in Spanish)". PhD thesis. Universidad Politécnica de Valencia, 2003 (cited in p. 53).

[105] W. Neise and B. Barsikow. "Acoustic similarity laws for fans". *Journal of Engineering for Industry* 104 (2), 1982, pp. 162–168 (cited in p. 66).

[106] J. Galindo, J. Serrano, H. Climent, and A. Tiseira. "Experiments and modelling of surge in small centrifugal compressor for automotive engines". *Experimental Thermal and Fluid Science* 32 (3), 2008, pp. 818–826 (cited in pp. 84, 132).

[107] R. Navarro García. "A numerical approach for predicting flow-induced acoustics at near-stall conditions in an automotive turbocharger compressor". PhD thesis. 2014 (cited in pp. 98, 101).

[108] *STAR-CCM+*. Version Release 8.04. CD-Adapco. 2013 (cited in p. 100).

[109] M. L. Shur, P. R. Spalart, M. K. Strelets, and A. K. Travin. "A hybrid RANS-LES approach with delayed-DES and wall-modelled LES capabilities". *International Journal of Heat and Fluid Flow* 29 (6), 2008, pp. 1638–1649 (cited in p. 100).

[110] A. Travin, M. Shur, M. Strelets, and P. Spalart. "Detached-eddy simulations past a circular cylinder". *Flow, Turbulence and Combustion* 63 (1-4), 2000, pp. 293–313 (cited in p. 100).

[111] O. Baris and F. Mendonça. "Automotive Turbocharger Compressor CFD and Extension Towards Incorporating Installation Effects". In: *Proceedings of ASME Turbo Expo 2011: Power for Land, Sea and Air*. ASME, 2011, pp. 2197–2206 (cited in p. 100).

[112] J. Serrano, P. Olmeda, F. Arnau, M. Reyes-Belmonte, and A. Lefebvre. "Importance of Heat Transfer Phenomena in Small Turbochargers for Passenger Car Applications". *SAE International Journal of Engines* 6 (2), 2013, pp. 716–728 (cited in p. 100).

[113] J. R. Serrano, F. J. Arnau, R. Novella, and M. Á. Reyes-Belmonte. "A Procedure to Achieve 1D Predictive Modeling of Turbochargers under Hot and Pulsating Flow Conditions at the Turbine Inlet". *SAE Technical Paper* (2014-01-1080), 2014, 13pp (cited in p. 100).

[114] J. Serrano, P. Olmeda, F. Arnau, A. Dombrovsky, and L. Smith. "Methodology to characterize heat transfer phenomena in small automotive turbochargers: Experiments and modelling based analysis". In: *ASME Turbo Expo 2014: Turbine Technical Conference and Exposition*. American Society of Mechanical Engineers. 2014, pp. 1–13 (cited in p. 100).

[115] F. Payri, J. M. Desantes, and A. J. Torregrosa. "Acoustic boundary condition for unsteady one-dimensional flow calculations". *Journal of Sound and Vibration* 188 (1), 1995, pp. 85–110 (cited in p. 106).

[116] A. Torregrosa, P. Fajardo, A. Gil, and R. Navarro. "Development of a non-reflecting boundary condition for its application in 3D computational fluid dynamic codes". *Engineering Applications of Computational Fluid Mechanics* 6 (3), 2012, pp. 447–460 (cited in p. 106).

[117] J. Galindo, A. Tiseira, P. Fajardo, and R. Navarro. "Coupling methodology of 1D finite difference and 3D finite volume CFD codes based on the Method of Characteristics". *Mathematical and Computer Modelling* 54 (7-8), 2011. Mathematical models of addictive behaviour, medicine & engineering, pp. 1738–1746 (cited in p. 106).

[118] E. Sundström, B. Semlitsch, and M. Mihaescu. "Centrifugal compressor: The sound of surge". In: *21st AIAA/CEAS Aeroacoustics Conference*. 2015 (cited in p. 116).

[119] E. Sundström, B. Semlitsch, and M. Mihaescu. "Assessment of the 3D Flow in a Centrifugal compressor using Steady-State and Unsteady Flow Solvers". In: *SAE Technical Paper*. SAE International, 2014 (cited in p. 116).

[120] J. L. Lumley. "The structure of inhomogeneous turbulent flows". In: *Atmospheric Turbulence and Radio Wave Propagation – Proceedings of the International Colloquium*. Nauka, Moscow, 1967, pp. 166–178 (cited in p. 122).

[121] N. Aubry. "On the hidden beauty of the proper orthogonal decomposition". *Theoretical and Computational Fluid Dynamics* 2 (5-6), 1991, pp. 339–352 (cited in pp. 122, 123).

[122] P. J. Schmid. "Dynamic mode decomposition of numerical and experimental data". *Journal of Fluid Mechanics* 656, 2010, pp. 5–28 (cited in pp. 122–126).

[123] S. Bagheri. "Koopman-mode decomposition of the cylinder wake". *Journal of Fluid Mechanics* 726, 2013, pp. 596–623 (cited in pp. 122, 125).

[124] P. J. Schmid, L. Li, M. P. Juniper, and O. Pust. "Applications of the dynamic mode decomposition". *Theoretical and Computational Fluid Dynamics* 25 (1-4), 2011, pp. 249–259 (cited in pp. 123–125).

[125] M. R. Jovanović, P. J. Schmid, and J. W. Nichols. "Sparsity-promoting dynamic mode decomposition". *Physics of Fluids (1994-present)* 26 (2), 2014, p. 024103 (cited in pp. 123, 125, 126).

[126] A. Sakowitz, M. Mihaescu, and L. Fuchs. "Flow decomposition methods applied to the flow in an IC engine manifold". *Applied Thermal Engineering* 65 (1), 2014, pp. 57–65 (cited in pp. 123, 125).

[127] C. W. Rowley, I. Mezić, S. Bagheri, P. Schlatter, and D. S. Henningson. "Spectral analysis of nonlinear flows". *Journal of fluid mechanics* 641, 2009, pp. 115–127 (cited in pp. 123, 125).

[128] K. K. Chen, J. H. Tu, and C. W. Rowley. "Variants of dynamic mode decomposition: boundary condition, Koopman, and Fourier analyses". *Journal of nonlinear science* 22 (6), 2012, pp. 887–915 (cited in pp. 123, 125).

[129] J. Dahan, R. Futrzynski, C. O'Reilly, and G. Efraimsson. "Aero-acoustic source analysis of landing gear noise via dynamic mode decomposition". In: *21st International Congress on Sound and Vibration*. 2014 (cited in pp. 123, 126).

[130] R. Futrzynski and G. Efraimsson. *Dymode: A parallel dynamic mode decomposition software*. KTH Royal Institute of Technology. 2015 (cited in pp. 125, 126).

[131] Y. T. Delorme, A.-E. M. Kerlo, K. Anupindi, M. D. Rodefeld, and S. H. Frankel. "Dynamic mode decomposition of Fontan hemodynamics in an idealized total cavopulmonary connection". *Fluid Dynamics Research* 46 (4), 2014, p. 041425 (cited in p. 126).

[132] J. F. Williams and D. L. Hawkings. "Sound generation by turbulence and surfaces in arbitrary motion". *Philosophical Transactions of the Royal Society of London A: Mathematical, Physical and Engineering Sciences* 264 (1151), 1969, pp. 321–342 (cited in p. 126).

[133] S. Koff and E. Greitzer. "Axisymmetrically stalled flow performance for multistage axial compressors". *Journal of Turbomachinery* 108 (2), 1986, pp. 216–223 (cited in p. 132).

[134] G. Liśkiewicz, L. Horodko, M. Stickland, and W. Kryłłowicz. "Identification of phenomena preceding blower surge by means of pressure spectral maps". *Experimental Thermal and Fluid Science* 54, 2014, pp. 267–278 (cited in p. 151).

[135] H. Chen and V. Lei. "Casing treatment and inlet swirl of centrifugal compressors". In: *Proceedings of ASME Turbo Expo 2012*. GT2012-69340. ASME. 2012 (cited in p. 169).

[136] L. Ding, T. Wang, B. Yang, W. Xu, and C. Gu. "Experimental investigation of the casing treatment effects on steady and transient characteristics in an industrial centrifugal compressor". *Experimental Thermal and Fluid Science* 45, 2013, pp. 136–145 (cited in p. 169).

[137] A. Kalpakli, R. Örlü, and P. Alfredsson. "Vortical patterns in turbulent flow downstream a 90° curved pipe at high Womersley numbers". *International Journal of Heat and Fluid Flow* 44, 2013, pp. 692–699 (cited in p. 201).

[138] A. K. Vester and R. Örlü. "Turbulent pipe flow downstream a 90° pipe bend with and without superimposed swirl". *International Journal of Heat and Fluid Flow* 41, 2013, pp. 103–111 (cited in p. 201).

UNIVERSITAT POLITÈCNICA DE VALÈNCIA

DOCTORAL THESIS

EXPERIMENTS ON TURBOCHARGER COMPRESSOR ACOUSTICS

Jorge García Tíscar

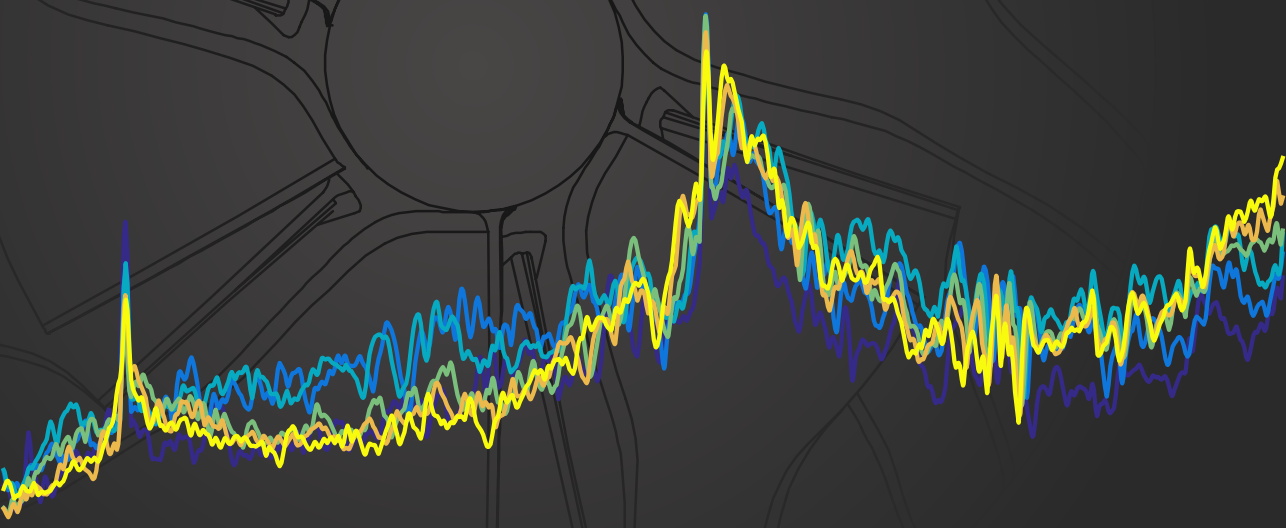

January 2017

DEPARTAMENTO DE MÁQUINAS Y MOTORES TÉRMICOS